Delayed and Swelling Behaviour of Damaged/Fractured Callovo-Oxfordian Claystone

Hao Wang

Dissertation presented for the degree of

Doctor of Ecole des Ponts ParisTech

Discipline: Geotechnical engineering

by

Hao WANG

Delayed and swelling behaviour of damaged/fractured Callovo-Oxfordian claystone

Date: 1 February 2021

Jury

Prof. Farimah Masrouri	Université de Lorraine (France)	Présidente
Prof. Jianfu Shao	Université de Lille (France)	Rapporteur
Prof. Philippe Cosenza	Université de Poitiers (France)	Rapporteur
Dr. Xiang-ling Li	Ondraf/Euridice (Belgique)	Examinatrice
Dr. Minh-ngoc Vu	Andra (France)	Examinateur
Prof. Yu-jun Cui	Ecole des Ponts ParisTech (France)	Directeur de thèse

Résumé

Pour le stockage géologique des déchets radioactifs, l'Agence Nationale pour la Gestion des Déchets Radioactifs (ANDRA) a construit un laboratoire de recherche souterrain (URL) à Bure, France, dans une formation d'argilite du Callovo-Oxfordien (COx). L'excavation réalisée pendant la construction de l'URL a entraîné des fractures à proximité des ouvertures. Dans la zone fracturée, les propriétés hydromécaniques d'argilite étaient significativement affectées. Afin d'assurer la sûreté à long terme du stockage, il est nécessaire d'étudier le comportement hydromécanique de l'argilite COx endommagée/fracturée.

La présente étude est consacrée au comportement de compression, de gonflement et de fluage de l'argilites endommagées/fracturées. Les méthodes de préparation des argilites endommagées/fracturées sont d'abord développées en laboratoire. Ensuite, des essais oedométriques sont effectués sur de l'argile fracturée. Les résultats obtenus montrent que la fracture peut influencer significativement le comportement de gonflement, de compression et de fluage de l'argilite COx. L'auto-colmatage de l'argilite fracturée dans le processus de gonflement est causé par le remplissage des minéraux argileux gonflants. L'effet de fracture sur la compressibilité dépend de l'orientation de la fracture et du niveau de contrainte. En outre, l'effet possible de broyage des grains sur le comportement de compression est mis en évidence. Afin de clarifier ce phénomène du broyage de grains, une série d'essais oedométriques est réalisée sur l'argile Téguline naturelle et sur un mélange sable-argile artificiel. Les résultats confirment que le broyage de grains peut se produire durant le chargement, dépendant de la fraction des fines.

Les effets de la succion sur le gonflement et la compression de l'argilite COx endommagée sont étudiés au moyen d'essais oedométriques à succion contrôlée. Il est observé que la compressibilité diminue et la limite élastique augmente avec l'augmentation de la succion. L'effet de la vitesse de chargement sur le comportement volumique de l'argilite COx endommagée est étudié par des essais de compression à déformation contrôlée. En se basant sur les résultats obtenus, les paramètres mécaniques sont déterminés, permettant de caractériser le comportement différé de l'argilite COx endommagée.

Enfin, en tenant compte de l'effet de l'endommagement, une loi de comportement est proposée permettant de modéliser le comportement viscoplastique de l'argilite COx non saturée. Le mécanisme d'endommagement est d'abord clarifié, permettant la définition d'un coefficient d'endommagement. Cette loi est validée par les résultats expérimentaux obtenus dans cette

étude de thèse et par des résultats de la littérature. Un bon accord est obtenu entre les simulations et les résultats expérimentaux, montrant la performance du modèle proposé.

Mots clés: argillite COx; excavation; dommages et fracture; propriétés hydromécanique; compression; gonflement; fluage; mécanisme de dommage ; modélisation viscoplastique

Abstract

For the geological storage of radioactive waste, the French National Radioactive Waste Management Agency (ANDRA) built an underground research laboratory (URL) at Bure, France, in the Callovo-Oxfordian (COx) claystone formation. The excavation of drafts and drifts in URL results in fractures inside the host rock around the openings. In the fractured zone, the hydro-mechanical properties of the host rock were significantly affected. To ensure the long term safety of repository, it is necessary to investigate the hydro-mechanical behaviour of damaged/fractured COx claystone.

The present study focuses on the compression, swelling and creep behaviour of damaged/fractured claystone. The preparation methods of damaged/fractured claystone were first developed in the laboratory. Then, oedometer tests were conducted on fractured claystone. Results show that the fracture can significantly affect the swelling, compression and creep behaviour. The self-sealing of fractured claystone upon wetting is caused by the filling of the swollen clay minerals. The compression results show that the fracture effect is dependent on its orientation and the stress level. Besides, the possible grain breakage effect was identified during compression. To clarify such effect, a series of oedometer tests were conducted on Teguline clay and artificial sand-clay mixture. Results confirm the effect of grain breakage on the compressibility of soils, depending on the fine fraction.

In addition, suction effects on the swelling and compression behaviour of damaged COx claystone were investigated through oedometer tests with controlled suction. It is observed that the compressibility decreases and the yield stress increases with the increase of suction. The rate-dependent behaviour of damaged COx claystone was investigated through constant rate strain compression tests. Based on the results, the related mechanical parameters were determined, allowing characterization of the time-dependent behaviour of damaged COx claystone.

Finally, accounting for the damage effect, a constitutive model was proposed allowing description of the viscoplastic behaviour of unsaturated COx claystone. The damage mechanism of COx claystone is clarified, allowing definition of a damage coefficient. The model is validated based on the results obtained in this study and some results from literatures. A good agreement is obtained between the simulations and the experimental results, showing the performance of the model proposed.

Keywords: COx claystone; excavation; damage and fracture; hydro-mechanical properties; compression; swelling; creep; damage mechanism; viscoplastic modelling

Acknowledgements

As time goes by, three years have passed since I came to France. To date, the work planned in my thesis has been completed. After I studied at Ecole des Ponts ParisTech for three years, I would like to take this opportunity to thank all those who have contributed to this research in all aspects. Without their help, the completion of this thesis cannot be possible.

First and foremost, I would like to thank my supervisor, Prof. Yu-jun Cui, sincerely and deeply. He made great contributions to the present work from the experimental design to the result analysis. Besides, his spirit of constant pursuit and exploration of scientific research encouraged me throughout the whole period of my Ph.D. candidate. Under his supervision, I learned how to use critical and logical thinking to study scientific problems. His systematic guidance and great effort in my thesis will also benefit me a lot in the future.

I would also like to express my deepest gratitude to all my colleagues in the geotechnical group, Dr. Youssouf Abdallah, Dr. Patrick Aimedieu, Zhixiong Zeng, Yu Su, Zi Ying, Zhixiong Zeng, etc. I am really thankful for their useful suggestions and sincere help to my research. A special mention is addressed to Dr. Feng Zhang. He gave me a lot of valuable suggestions when we discussed my subject in regular meetings. Besides, this thesis is also significantly benefited from the comments and suggestions made by Dr. Nathalie Conil, Dr. Jean Talandier, and Dr. Minh-ngoc.VU, who work in ANDRA and participate in this project. I gratefully acknowledge the help and encouragement from them.

On the other hand, I would like to especially thank the jury of this thesis. As the reviewers, Prof. Jianfu Shao at Université de Lille and Prof. Philippe Cosenza at Université de Poitiers took much time to review my thesis carefully and to offer valuable comments on my thesis. Moreover, the jury president Prof. Farimah Masrouri at Université de Lorraine, and the examiners Dr. Xiangling Li at ESV EURIDICE GIE and Dr. Minh-ngoc Vu at ANDRA, are also greatly acknowledged for the advice proposed to this thesis.

Most of the content in this thesis is associated with experiments. Therefore, I also grateful for the supports from the technical team of CERMES, including Emmanuel De Laure, Xavier Boulay, Baptiste Chabot, Marine Lemaire, and Loïc Lesueur. Without their assistance, my experiments would not have been finished successfully. I will always remember their uncountable help and happy times with them. The support from the China Scholarship Council (CSC) is also greatly acknowledged.

Finally, the deepest appreciation is given to my mother, sister, and girlfriend Yangzi Qiu. Their love and support gave me the motivation to overcome the difficulties in my life. I owe my sincere gratitude to them for understanding and supporting in the past days. In the future, I will be braver to pursue the truth in the scientific field.

Contents

Introduction

Context

Over the past decades, the deep geological storage concepts have been proposed for nuclear waste disposal in many countries, such as Belgium, Switzerland, France, USA, Germany, China, Japan, Canada, etc (IAEA, 2009). Many underground research laboratories (URL) were built prior to constructing the nuclear waste repository, in order to investigate the potential host formations in terms of long-term thermo-hydro-mechanical and chemical (THMC) behaviours in the field conditions. Generally, the radioactive wastes were classified on the basis of their radiation levels and periods (OECD/NEA, 1995; NEA, 2008; IAEA, 2009). In France, the radioactive waste classification is detailedly described in Fig. 0.1. To safely store the nuclear radioactive wastes with long radiation periods and intermediate/high levels, the URLs are usually constructed in the host rocks at the depth up to several hundreds of meters. For instance, the depth is around 500 m in France and in China (ANDRA, 2005; Chen et al., 2012, 2014; Armand, 2013). The host rocks which have been considered are: clay-based formations (France, Belgium and Switzerland), salt formations (USA and Germany) and granite formations (Japan, Canada and China) (Yoshida et al., 2000; Gens et al., 2003; Fairhurst, 2004; ANDRA, 2005; Mayor et al., 2005; Wang, 2010; Molinero-Guerra, 2018). The feedbacks from the excavation of URL and from the different in situ experiments in the URL are of paramount importance for the construction and exploitation of the nuclear waste repository.

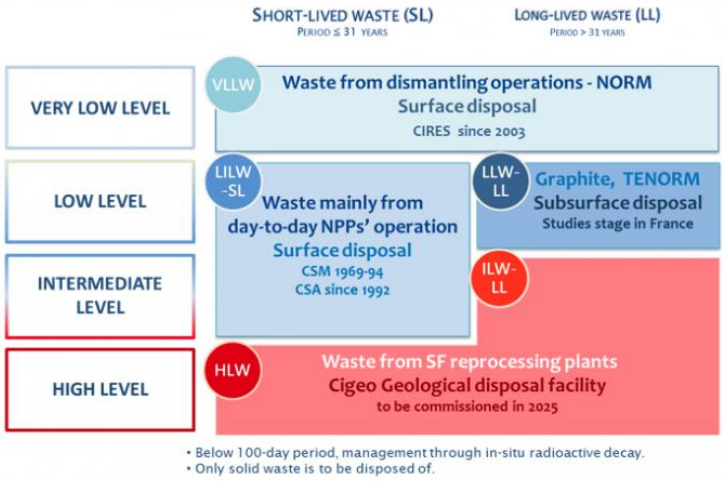

Fig. 0.1. The radioactive waste classification in France (https://international.andra.fr/radioactive-waste-france/waste-classification)

In France, the French National Radioactive Waste Management Agency (Andra), is in charge of studying the disposal of high-level and intermediate-level long-lived waste (HLW and ILW-LL) in a deep geological repository (Cigéo project). This possible nuclear waste disposal will be located at the border of the Meuse and Haute-Marne departments, nearly 300 km East of Paris. The host formation consists of a claystone (Callovo-Oxfordian argillaceous rock – COx) lying between 420 m and 550 m in depth and exhibiting very favorable conditions for a repository of radioactive waste, as they generally have a very low hydraulic conductivity, small molecular diffusion and significant retention capacity for radionuclide. In 2000, Andra started to build the Meuse Haute-Marne underground research laboratory (MHM URL), which aims to demonstrate the feasibility of constructing and operating the Cigéo project (Armand et al, 2016). During the construction of MHM URL, it was observed that the excavation of galleries and drafts induced significant disturbances on the host formation, leading to the creation of the fractured zone (Armand et al., 2014). In the fractured zone, a lot of shear and traction fractures were generated, resulting in degradation of thermo-hydro-mechanical properties in particular the increase in permeability (de la Vaissière et al., 2015).

To days, many in situ experiments have been conducted within the MHM URL to investigate the thermo-hydro-mechanical (THM) behaviour of the COx claystone as a geological barrier (e.g., Armand et al., 2016). In the meanwhile, a series of tests at smaller scales were performed in laboratory (e.g., Armand et al., 2017; Conil et al., 2018). The key aspects identified from the field and laboratory tests are briefly summarized below:

(i) Short term mechanical behaviour - Excavation induces the redistribution of in situ stress and the change of pore water pressure in the vicinity of the galleries. The fractures in the fractured zone lead to significant increase of hydraulic conductivity and convergence of drifts. The anisotropic initial stress state and anisotropic properties have considerable influences on the short term mechanical behaviour. The main features of the shear behaviour of COx claystone, evidenced by laboratory test, can be summarized as: (a) a linear elasticity under low deviatoric stress; (b) a plastic hardening and/or diffuse damage before the peak stress; (c) the strain softening characterizing the post-peak behaviour where macrocracks are generally observed; (d) a residual domain where the claystone behaves as a cohesion-less completely fractional material corresponding to the behaviour of the formed macro-cracks; (e) a transition from a brittle towards a ductile behaviour when the confining pressure increases

(ii) Long term mechanical behaviour - The in situ convergence measurements on the drifts indicate that the time-dependent deformation of host formation is pronounced. In laboratory, the creep of COx claystone can occur at a very low stress, showing a negligible stress threshold for creep. COx claystone can exhibit significant time-dependent deformation. The creep behaviour also depends on the applied stress path. Besides, with consideration of the decay duration of radioactive wastes, time effect needs to be investigated in depth.

(iii) Swelling/shrinkage behaviour - The ventilation in the galleries can change the relative humidity of air, further dehydrating the COx claystone in the fractured zone. Furthermore, the fractured zone will be progressively resaturated due to the infiltration of water from the farther intact zone. With almost half of clay minerals in its mineral composition, COx claystone can exhibit significant swell/shrink in the wetting/drying process.

(iv) Thermal behaviour - The nuclear wastes emplaced within the storage can release heat, which makes increase the temperature of host formation and thus the thermomechanical stress and the thermal pressurization within the saturated host rock and concrete structure.

Many research teams have investigated the COx claystone by considering the coupled THM aspects. Many factors jointly affecting the hydro-mechanical behaviours were taken into account, including the damage, the creep, the unsaturation, etc. Though it has been recognized that the fractured zones dominate the long term hydro-mechanical behaviour, the experimental investigations with respect to the effects of water infiltration and damage on the time dependent behaviour are relatively few. Besides, the modelling methods of damage in most constitutive models are mathematical-based. The damage mechanism of COx claystone needs to be further investigated to propose a more reasonable damage model.

Objectives and organization of the thesis

The thesis aims at studying the long term hydro-mechanical behaviour of unsaturated damaged/fractured COx claystone through experimental investigation and constitutive modelling. The specific objectives are as follows:

(i) To investigate the effect of artificial fracture on the swelling, compression and creep behaviours of COx claystone by performing high pressure oedometer compression tests and hydraulic conductivity tests.

(ii) To clarify the role of granular inclusions inside the COx claystone on its compressibility. The effect of clay fraction on the volume change behaviour of artificial sand-clay mixture was specifically investigated.

(iii) To define an appropriate damage criterion through the investigation of the damage behaviour of COx claystone with high pressure triaxial tests, X-ray tomography tests and mercury intrusion porosimeter tests.

(iv) To study the effect of suction on the swelling, compression and creep behaviours of the damaged claystone and the evolution of cracks during the compression process.

(v) To further investigate the strain rate-dependent volume change behaviour of unsaturated damaged claystone by carrying out suction-controlled constant rate of strain (CRS) tests.

(vi) To propose an elasto-viscoplastic (EVP) model for unsaturated claystone with consideration of damage effect, to describe the long-term hydro-mechanical behaviour.

Correspondingly, there are six chapters in the thesis.

The first chapter presents an overview of the Meuse\Haute-Marne site and the hydro-mechanical behaviour of COx claystone. The basic information about the Meuse\Haute-Marne site was presented, including the location of the site, EDZ of the URL. Besides, the mineral composition, microstructure and wetting/drying properties are reviewed and summarized. Subsequently, the mechanical behaviours and the influencing factors are discussed and analyzed with respect to the water content, temperature, anisotropy, etc. The main features of the existing EVP models are evaluated.

The second chapter is devoted to the description of the basic physical properties of COx claystone and the experimental techniques adopted in this study. The experimental devices used are presented in detail, including high pressure oedometer, high pressure triaxial cell, pressure-volume controller, μ-computed tomography device, etc. In addition, the sample preparation method of fractured claystone is described. Following that, the test programs are presented, aiming at investigating the hydro-mechanical behaviours of COx claystone with respect to fracture orientations, granular inclusion, suction, strain rate, etc.

The third chapter is devoted to the preparation of fractured and damaged COx claystone samples. Triaxial and intact oedometer samples are first prepared. Then, the sample preparation method of fractured COx claystone is described. For the preparation of damaged COx claystone, triaxial tests were first performed to study the damage behaviour of COx claystone. Based on the

triaxial results in laboratory, a novel method is developed to prepare the damaged claystone with an appropriate damage criterion.

The fourth chapter focuses on the hydro-mechanical behaviours of fractured and intact COx claystone. Firstly, an uncommon compression phenomenon is pointed out with respect to the possible grain breakage effect on COx claystone volume change behaviour. Then, a series of oedometer tests were conducted on artificial sand-clay mixture, verifying the effect of grain breakage on the compressibility of soils with granular inclusions. The tests on fractured claystone illustrate the significant fracture effect on the swelling, compression and creep behaviours of COx claystone. The self-sealing mechanism of fractured claystone is summarized. Fracture effect is found to be dependent on the fracture orientation and stress level.

The fifth chapter investigates the effects of suction and strain rate on the compression behaviour of damaged COx claystone. The suction effects on the swelling and compression behaviours are first studied by conducting suction controlled oedometer tests. Then, the microstructure changes are analyzed by X-ray tomography and Mercury Intrusion Porosimetry (MIP) tests. Moreover, the rate-dependent compression behaviours are investigated through constant rate strain consolidation tests. Based on the results, the related mechanical parameters were determined, allowing the time-dependent behaviour of damaged COx claystone be to characterised.

The sixth chapter deals with the modeling of elasto-viscoplastic behaviour of unsaturated COx claystone, accounting for the damage effect. A new EVP constitutive model for unsaturated soils is first proposed without consideration of the damage effect. Then, the damage mechanism with respect to COx claystone is analyzed and discussed. Based on the MIP results, a damage coefficient is proposed. Incorporating the damage effect, an EVP-damage model for unsaturated damaged COx claystone is built to describe the time-dependent behaviour. Finally, this model was validated based on the experimental results from this study and from the literatures.

Chapter 1. Literature review

In this chapter, the Meuse\Haute-Marne site and the in situ investigation on excavation damage are first presented. Then, the hydro-mechanical properties of Callovo-Oxfordian (COx) claystone, including damage, microstructure, mineralogy, hydraulic behaviour, short- and long-term mechanical behaviours of COx claystone are summarized. In addition, the elasto-viscoplastic (EVP) constitutive models for general geomaterials are reviewed.

1.1 The Meuse\Haute-Marne site and excavation damage

To demonstrate the feasibility of constructing and operating a High Level Waste (HLW) disposal facility in the Callovo-Oxfordian (COx) claystone formation and to improve it, the French National Radioactive Waste Management Agency (ANDRA) has run an underground research laboratory since 2000 at Bure, Meuse/Haute-Marne (nearly 300 km east of Paris, as presented in Fig. 1.1 (Armand et al. 2013). The COx claystone was selected as the host formation for the construction of URL, lying between depths 420 m and 550 m (ANDRA, 2005).

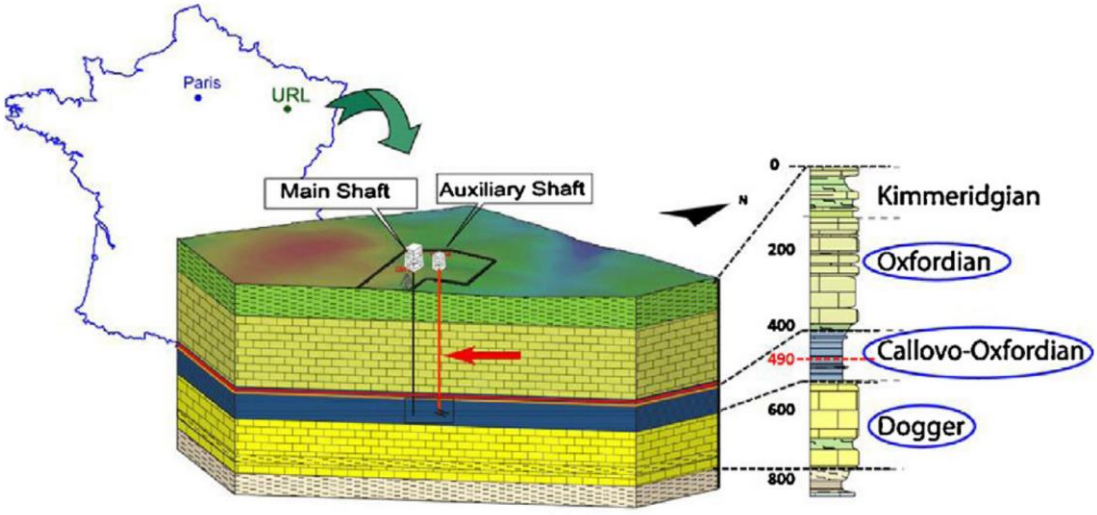

Fig. 1.1. The MHM URL: location and geological profile (Armand et al. 2013)

The COx claystone layer is sandwiched between poorly permeable carbonate formations. In-situ monitoring and investigations were performed for assessing the performance of COx claystone in ensuring the feasibility of the storage of radioactive waste (Delay et al., 2007). At the depth of 490 m (main level of the URL), drifts were excavated along different directions, as shown in Fig. 1.2. Different excavation technologies and support methods were tested to study the effect of excavation on the hydro-mechanical behaviour of COx claystone under different conditions. These drifts were entitled GED, GCS, GCR, etc. (Seyedi et al., 2017).

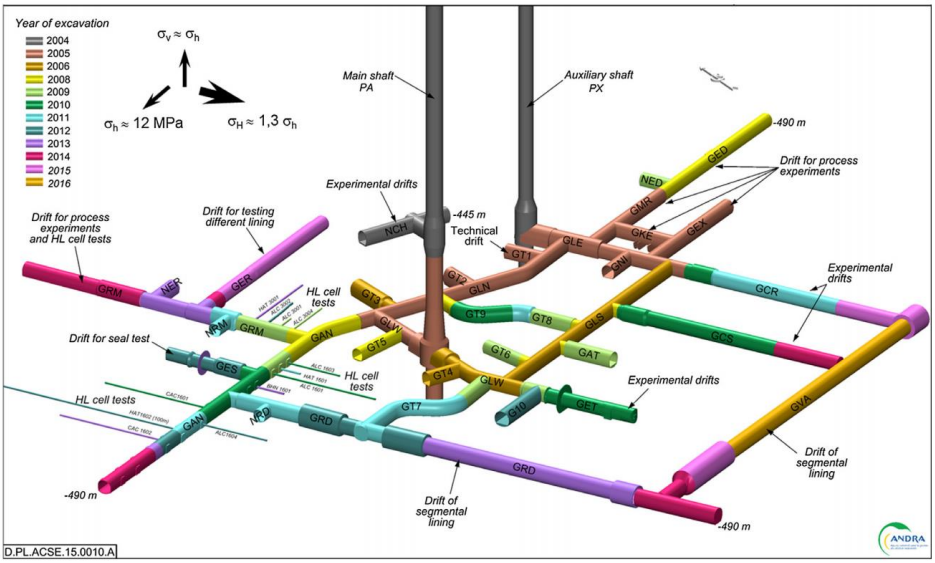

Fig. 1.2. The MHM URL plan and principal stress directions (Seyedi et al., 2017)

At −490 m, the anisotropic stress state of COx claystone was determined by Wileveau et al. (2007). The major stress σ_H (16.1 MPa) is horizontally oriented at NE150◦. The vertical stress σ_v (12.7 MPa) is nearly equal to the horizontal minor stress σ_h (12.4 MPa) (Seyedi et al., 2017):

$$\sigma_v = \rho g Z;\ \sigma_h \approx \sigma_v \tag{1-1}$$

where Z is the depth, ρ is the unit mass and g is the gravity. The ratio σ_H/σ_h is close to 1.3 and varies with locations and mineralogical characteristics.

Fairhurst and Damjanac (1996) and Tsang et al. (2005) used the excavation damaged zone to describe the region of rock adjacent to an underground opening that has been significantly damaged due to the redistribution of stresses and the change in permeability. In Meuse/Haute-Marne URL, different excavation damaged zones were created by the constructions of drifts and galleries at the main level. There are mainly two types of fractured zones, along the horizontal major stress direction and the horizontal minor stress direction, as presented in Fig. 1.3. The in-situ investigations conducted by Armand et al. (2014) indicated that there are around 4,000 excavation-induced fractures based on the analysis of 400 boreholes. Most data about fractures was obtained from drilling performed on the walls of the drifts parallel to the major stress. Based on the data obtained, a 3D representation of the fracture plan in the drift parallel to the major horizontal stress was obtained (Fig. 1.4). Two different zones of excavation induced fractures can be clearly distinguished, including the near zone (a zone) with traction and shear fractures and the far zone (b zone) with only shear fractures. The shear fractures dominated in the whole zone, as demonstrated by the fracture density shown in Fig. 1.5.

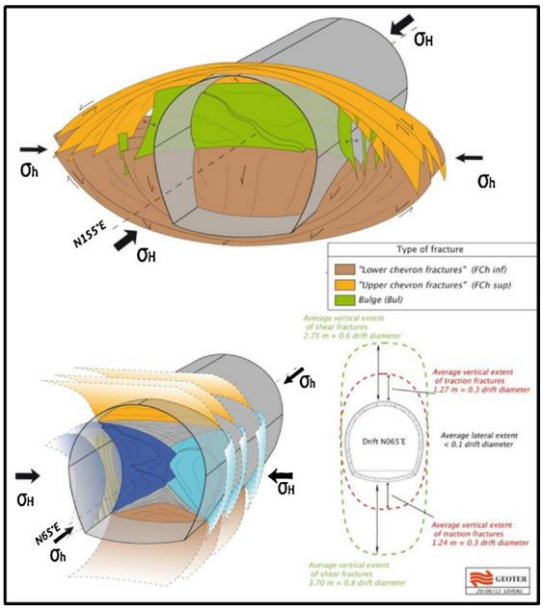

Fig. 1.3. Induced fracture networks at the main level of MHM URL for the drifts parallel and perpendicular to the horizontal major stress (Armand et al. 2013)

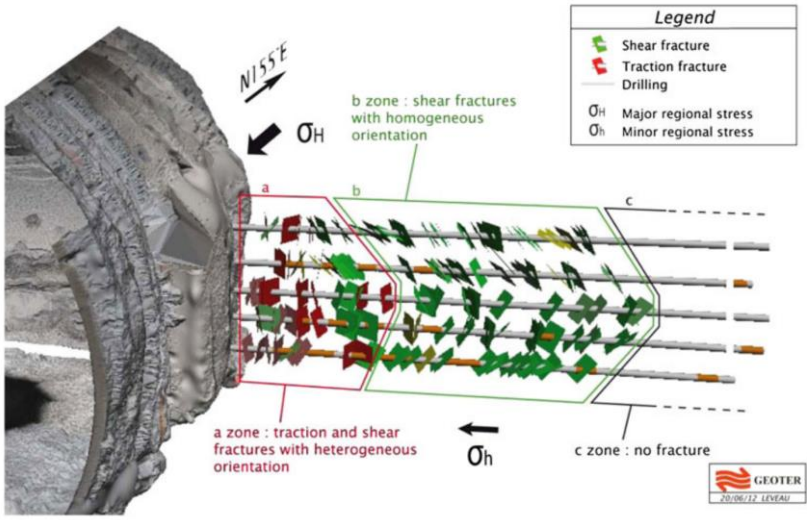

Fig. 1.4. 3D visualisation of the fractures network (Armand et al., 2014)

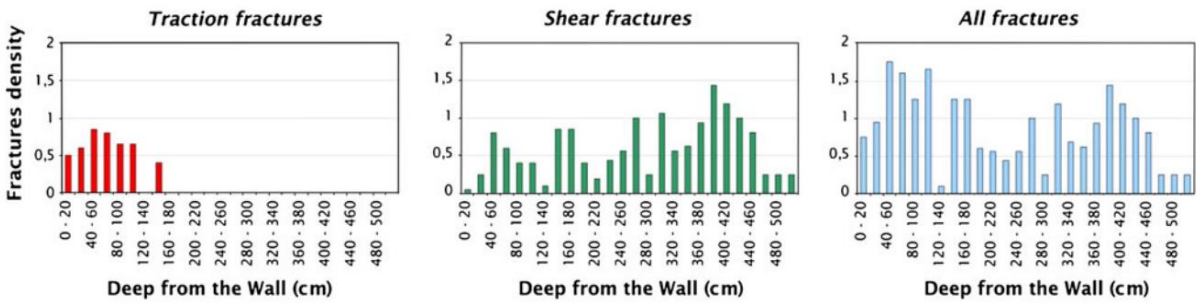

Fig. 1.5. Fracture density around the drifts (Armand et al., 2014)

It appears from the drilled cores shown in Fig. 1.6 and Fig. 1.7 that all fractures and slickensides can be classified into two types: shear fracture or unloading tensile fractures. These fractures show different shapes and thicknesses, and there are many complex shear bands on the fracture surfaces. In borehole CDZ1331, apertures up to 0.8 mm were observed. Generally, in the shear zone, the aperture of fractures is between 0.1 and 0.7 mm. But it is worth noting that the fractures larger than 1 mm and smaller than 100 µm cannot be identified by the resin injection method employed.

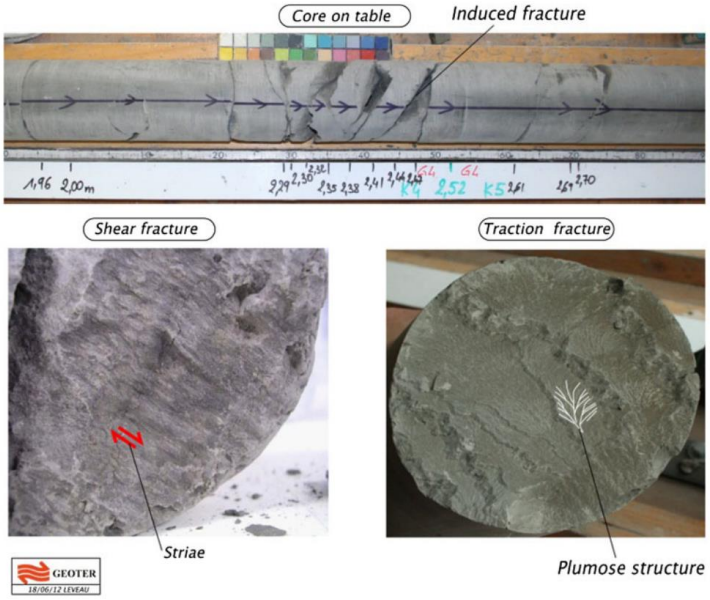

Fig. 1.6. Observed drill core structures: shear and extensional fractures (Armand et al., 2014)

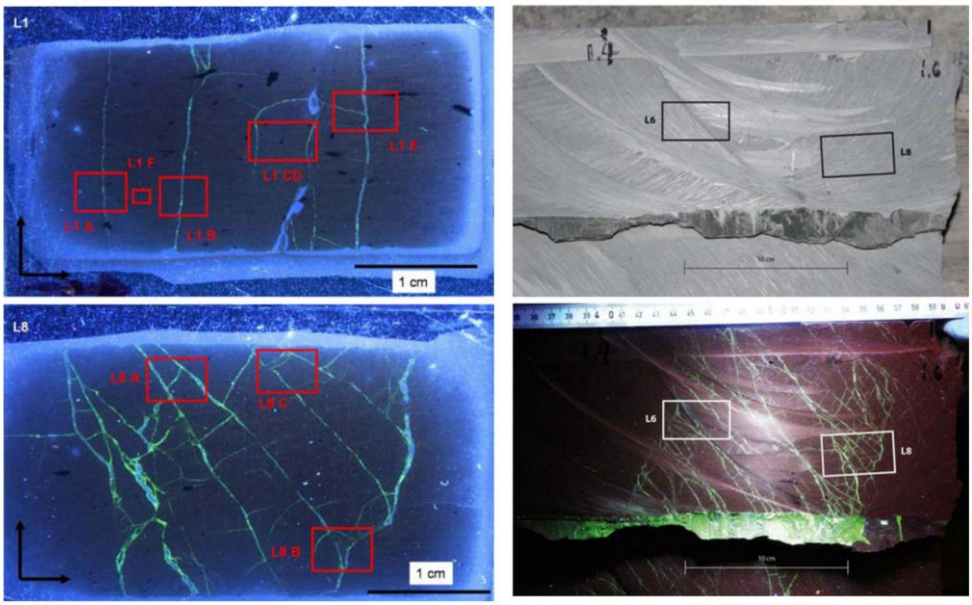

Fig. 1.7. View of the shear fractures of borehole CDZ1331 (Armand et al., 2014)

On the other hand, the in-situ measurements in the vicinity of drift revealed a hydraulic conductivity lower than 10^{-10} m/s even in the fractured zone, as shown in Fig. 1.8a. Far from the wall, the shear fractures exhibited low transmissivity which did not significantly affect the average hydraulic conductivity. In addition, the drift wall converged with time due to the effect of creep of COx claystone. In Fig. 1.8b, the horizontal convergence of a GED drift excavated along σ_h increased faster than the vertical one because of the discrepancy of stress state and anisotropy of COx claystone. In addition, the horizontal convergence is about two times larger than the vertical one for the drifts parallel to σ_H (GCS) due to the quasi-isotropic initial in situ stress (Guayacan-Carrillo et al., 2016).

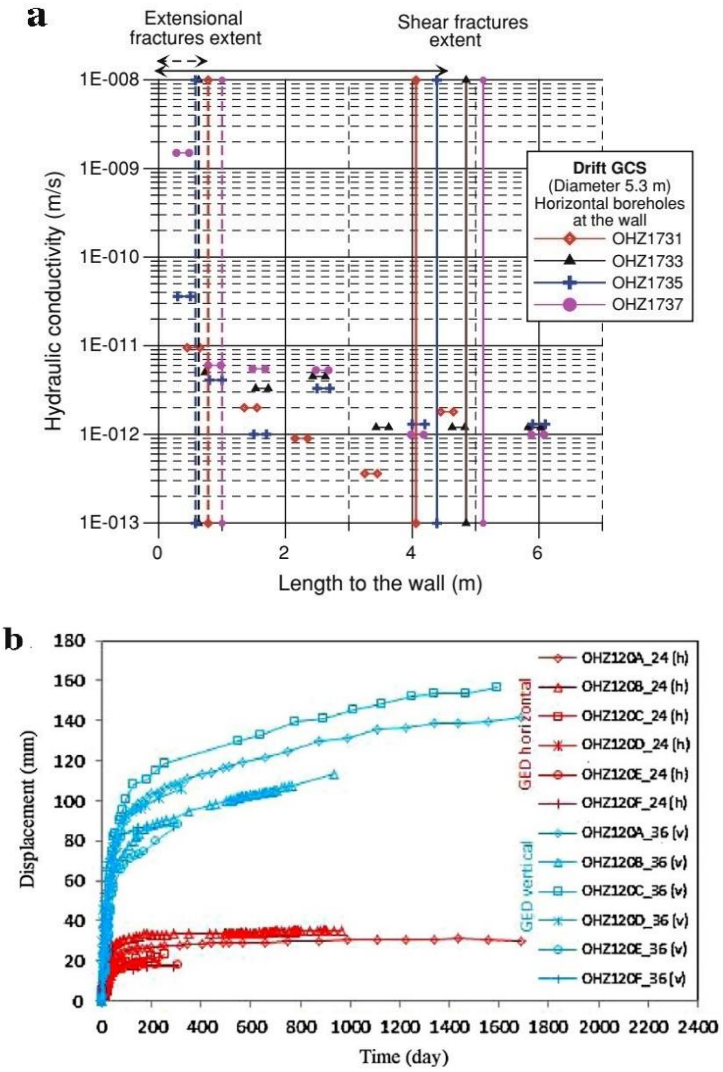

Fig. 1.8. (a) Hydraulic conductivity measured in drift GCS parallel to σ_H (after Armand et al., 2014); (b) Convergence of GED drift parallel to σ_H (Armand et al., 2013);

In summary, many experiments have been carried out to characterize the hydro-mechanical behaviour of the excavation induced damage zone within COx claystone, as well as the effect

of excavation method and support system, which is a key issue for the repository safety assessment (Blumling et al. 2007).

1.2 Mineral composition and microstructure of COx claystone

COx claystone is a kind of sedimentary rock, deposited for 155 million years between two layers of limestone Dogger and Oxfordian limestone with hundreds of meters thick, as shown in Fig. 1.9. The MHM URL is located in the layer of 130 m thick, between the depths 420 and 550m, corresponding to Unit C2, which was subdivided into four lithofacies: C2a, C2b, C2c and C2d, according to the differences of lithological units (Yven et al., 2007). The upper units

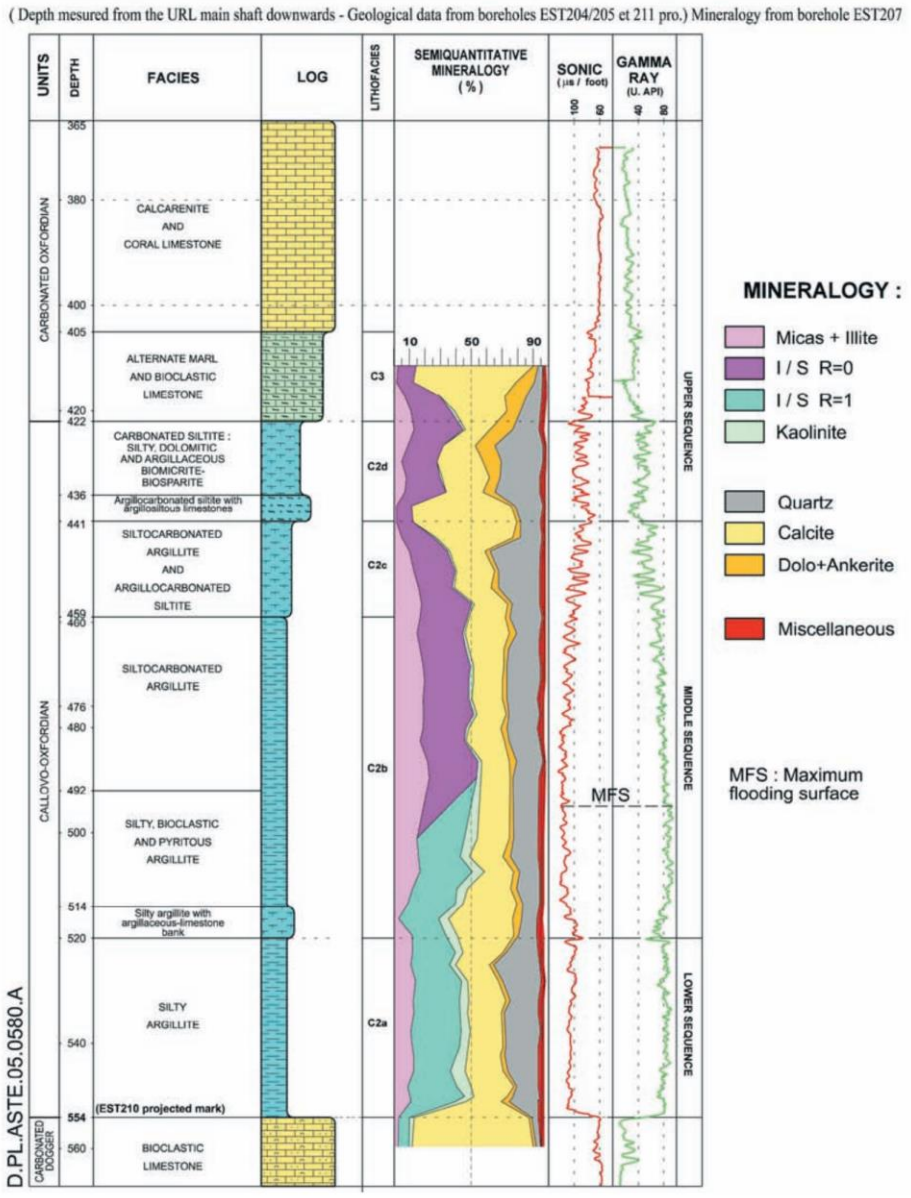

Fig. 1.9. Lithology and mineralogy of COx claystone at right angle with the Bure URL (Meuse/Haute-Marne) (Yven et al., 2007)

C2c and C2d are composed of silty-limestone and claystone, including silty fraction of 20 to 60% and carbonates of 25 to 80% at the top of the formation (Andra, 2012). For the lower units C2a and C2b, they occupy 3/4 of the formation thickness, which are relatively more clayey and homogeneous with clay fraction up to 50%. Most excavations were executed in this unite C2b, chosen as the main level.

Fig. 1.10 presents the distributions of clay, carbonates and pores. The image was generated by autoradiography. The intensity of grey level is proportional to the absolute porosity, with CLA zone (rich in clay minerals) and CCA zone (rich in carbonates). In Fig. 1.10b, it is observed that the porosity is divided into three zones (blue, green and red) which have the porosities lower than 13%, from 13 to 20% and from 20 to 30%, respectively. The mineralogy is mainly defined by clay, calcite and quartz. Other secondary minerals such as feldspar, chlorite, iron sulphur and organic material are also present. At the main level 490 m, there are 40-50% clay, 28% and 23% quartz (Gaucher et al., 2004; Andra, 2005; Yven et al., 2007; Robinet, 2008). The mineral composition of COx claystone reported in literatures is summarized in Table 1.1.

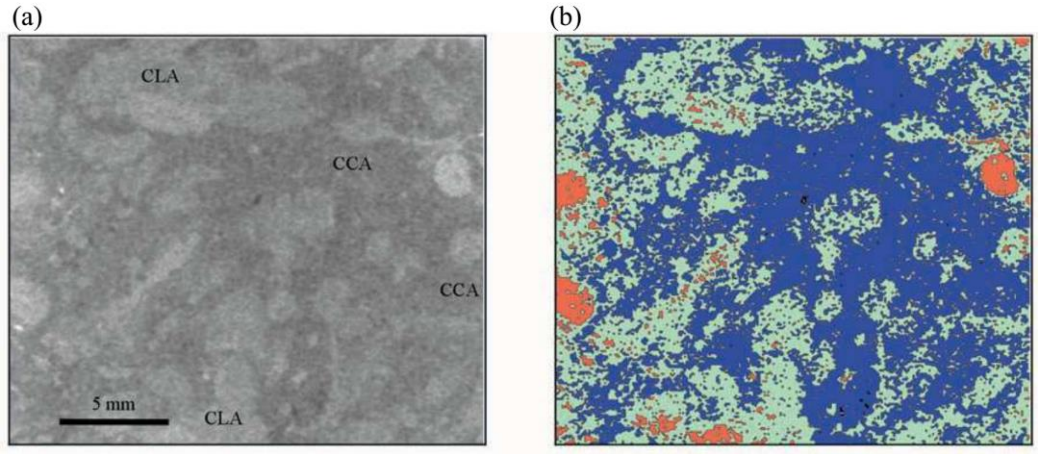

Fig. 1.10. Porosity map generated by autoradiography of C2c (borehole HTM102) (Sammartino et al. 2003).

Table 1.1. Mineralogy composition of COx claystone

Source	Clay (%)	Carbonates (calcite) (%)	Quartz (%)	Others (%)
Bauer Plaindoux et al. (1998)	40-50	20-30	25-30	＜10
Ghoreychi (1999)	30-60	20-40	-	＜5
Wright (2001)	40-45	30	25	0-5
Guéry et al. (2008)	45	28	23	4

The clay part mainly includes two types of illite/smectite interlayer with: (1) 20-40% smectite at the upper part of the formation; (2) 50-70% of smectite at the lower part of the formation. The content of smetite in clay fraction at the level of URL is between 40-50%, and the clay content can reach 50% (Menaceur, 2014).

Generally, the clay particles have a size smaller than 2 µm. The properties of clay minerals are significantly related to their plate-like microstructure shown in Fig. 1.11. There are three main clay groups (Table 1.2): kaolinite, illite and smectite (Wang, 2012). They have different swelling capacities due to their different structures. Kaolinite is a TO type clay mineral without substitution and it has a low swelling capacity. Illite is a TOT type clay mineral for which substitutions take place principally in tetrahedral sheets. The smectite group is also of TOT type, but with less organization in the arrangement of layers. There is a wide variety of smectite according to exchangeable cations. The nature of the various counter cations directly affects the interpolation of water molecules. However, for the clay in COx claystone, the special mixed layer clay is mainly the interstratified illite/smectites, other minerals being illite, mica, chlorite and kaolinite.

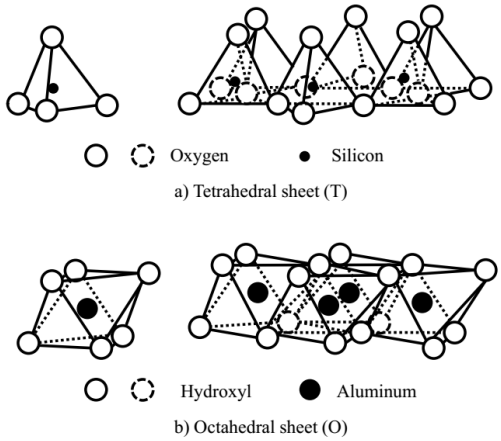

Fig. 1.11. Basic unities of clay minerals: a) Tetrahedral sheet; b) Octahedral sheet (Mitchell, 1993)

Table 1.2. Basic properties of the three main groups of clay minerals (Wang, 2012)

Groups of clay minerals	**Kaolinite**	**Illite**	**Smectite**
Layer	1 :1 (TO)	2 :1 (TOT)	2 :1 (TOT)
Exchangeable cation	-	K^+	Ca^{2+}, Na^+
CEC (meq/100g)	3 - 15	10 -40	70 - 100
Arrangement of particles	Isolated crystal	Mecaceosus aggregate	Quasi-crystal
Swelling property	Hardly swelling	Moderate swelling	Great swelling

For COx claystone, the microstructure is significantly related to the spatial distribution and geometry of minerals (Yven et al., 2007). Fig. 1.12 presents the conceptual model proposed by Yven et al. (2007) based on the combination of different experimental techniques, including scanning electron microscope, autoradiography, mercury porosimetry, petroleum, helium and nitrogen adsorption. It shows that the inclusions of calcite and quartz are embedded in the clay matrix which occupies 45-50% of the mineral composition with interconnected pores. It is also observed that the swelling minerals, especially interstratified illite/smectite, are found in some platelets with a clear distinction between swelling and non-swelling layers (Menaceur et al., 2016). It appears from Fig. 1.12 that the pores in COx claystone can be divided into two different groups: (1) the pores located at the interface between the clay matrix and the other minerals are micrometric ones (between the clay matrix and the quartz inclusions) and submicron ones (between the matrix clay and inclusions of calcite), occupying approximately 20 to 40% of the total pores; (2) the pores in the clay matrix is characterized by sub-micrometric and nano-metric ones, representing about 60 at 80% of the total pores (Menaceur, 2014).

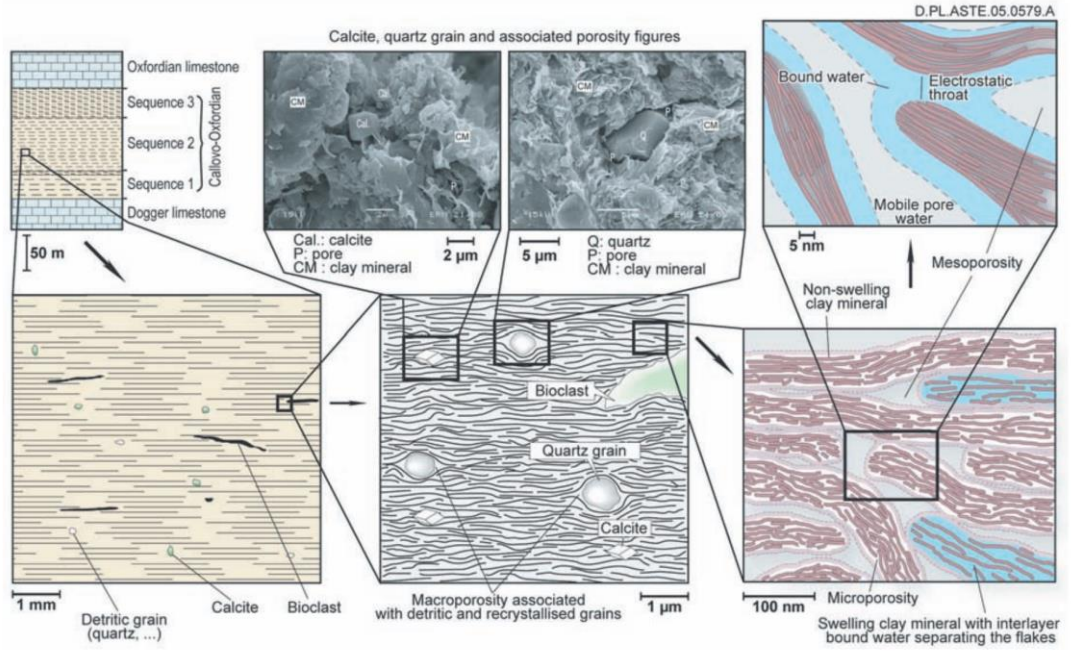

Fig. 1.12. Diagram of the organization of porosity in COx claystone (Yven et al. 2007)

Robinet et al. (2012) also obtained a 3D spatial distribution of mineral components in COx claystone (Fig. 1.13) using Scanning Electron Microscopy (SEM), showing that the clay matrix had a porosity of 0.23 by assuming that all pores exist in the clay and the clay fraction accounts 60% of mineral composition, corresponding to the total porosity 0.14 in COx claystone. Other studies on the microstructure of the COx claystone using mercury intrusion porosimetry (MIP)

showed that the average pore diameter is around 20 nm (Fig. 1.14) (Chiarelli 2000; Yven et al. 2007; Boulin et al. 2008).

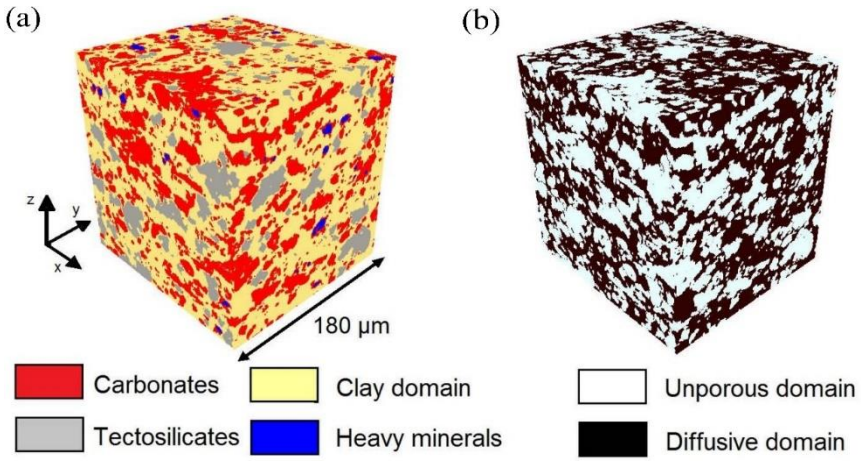

Fig. 1.13. Three-dimensional mesostructure of COx claystone obtained using X-ray tomography: (a) spatial distribution of mineral groups; (b) spatial distribution of unporous and diffusive domains (Robinet et al., 2012)

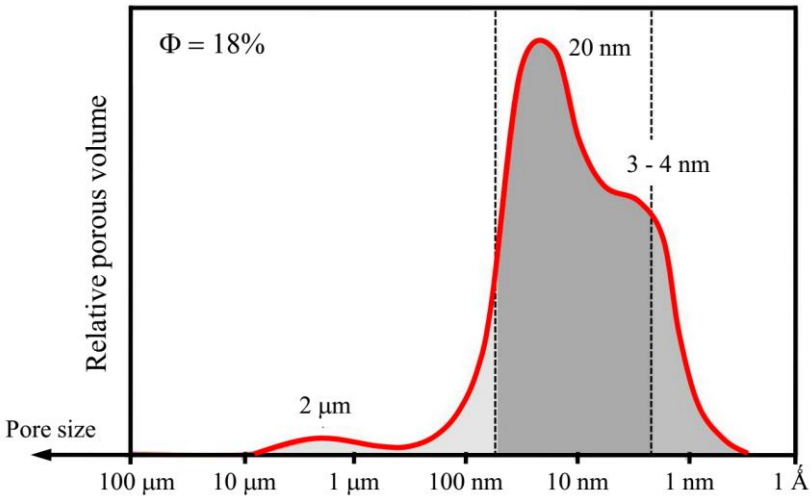

Fig. 1.14. Pore size distribution (PSD) of air-dried COx claystone (Andra, 2005)

Moreover, Delage et al. (2014) and Menaceur et al. (2016) indicated that the average diameter obtained on freeze-dried COx claystone sample is 32 nm for core EST44584. Fig. 1.15 shows a typical density curve with a single peak at the initial state. It appears that the PSD density function curve at 9 MPa suction is similar to that of initial state, indicating that the volumes of infra-pore for initial state and 9 MPa are close. The change of microstructure is thus negligible in terms of the porosity intruded by mercury. On the contrary, significant difference is observed between the initial state and 0 MPa in terms of peak density values. For the PSDs at suctions

higher than the initial state, the pore diameter corresponding to the peak density decreases with increasing suction.

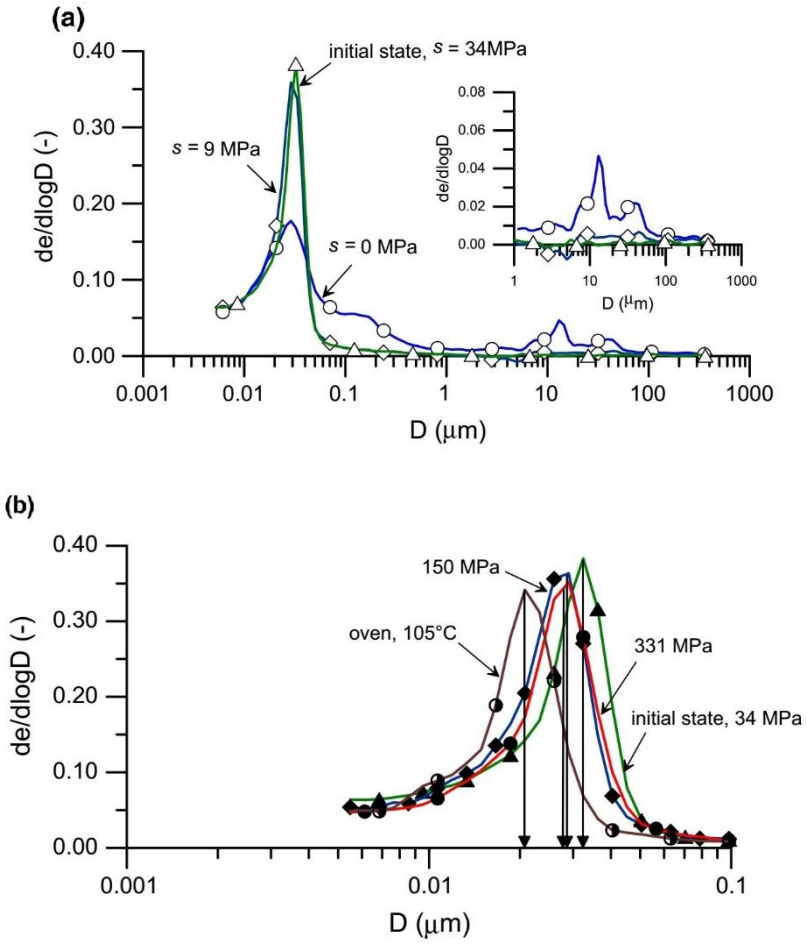

Fig. 1.15. Pore size distribution curves of samples (EST44584) at different suctions: (a) comparison among initial state, 9 and 0 MPa; (b) comparison among initial state, 150 MPa, 331 MPa and oven dried state (Menaceur et al., 2016).

1.3 Hydraulic behaviour and self-sealing properties

As mentioned before, the hydraulic behaviour of COx claystone is closely related to its mineral composition and microstructure. Under hydraulic loading, the mechanical property and microstructure of COx claystone can significantly change because the clay minerals are sensitive to water. For instance, wetting/drying cycles can cause significant microstructure and volume changes. In this section, the hydraulic and the self-sealing behaviours of COx claystone are reviewed and discussed.

1.3.1 Swelling mechanism

The swelling potential of clay materials is closely related to the clay minerals (Delage et al., 1998; Arifin, 2008; Mitchell, 1993). For pure clays, the factors influencing their swelling properties include the structure, the mineralogy, the fabric, as well as the clay-water interaction (Samingan, 2005). For instance, the inter-layer space of kaolinite and illite cannot be hydrated and the particles of these clays are rigid or quasi rigid (Wang, 2012). The swelling is mainly induced by the rearrangement of clay particles. By contrast, for smectite, its interlayer space can be hydrated due to crystalline swelling and diffuse double layer (DDL) swelling, as presented in Fig. 1.16.

The crystalline swelling corresponds to the change of inter-layer space due to the adsorption of water molecules by interlayer cations inside the clay particles (Laird et al., 1995; Karaborni et al., 1996). The layer can adsorb one to four layers of water molecules, corresponding to the inter-layer space 9.6 Å, 12.6 Å, 15.6 Å, 18.6 Å and 21.6 Å, respectively. Saiyouri et al. (2004) indicated that the number of adsorption layers of water molecules and number of layers per particle changed with suction for FoCa7 clay and MX80 bentonite, as shown in Fig. 1.17. The crystalline swelling is controlled by the combination of repulsion (hydration energy of interlayer cation) and attraction (van der Waals forces and Coulomb force).

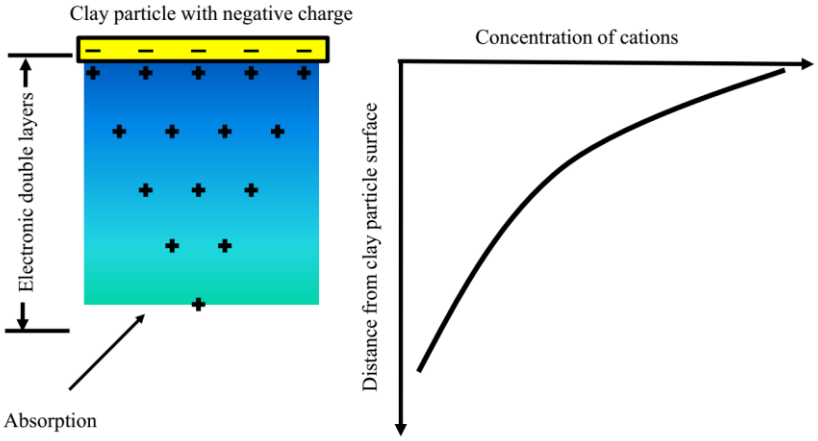

Fig. 1.16: The diffuse double layer created at the surface of a clay particle (Cernica, 1995).

For the swelling of DDL, it is mainly related to the evolution of inter-particle space (Barbour and Fredlund, 1989; Bolt, 1956; Delville and Laszlo, 1990; Dormieux et al., 2003; Wersina et al., 2004), because negative charge on the external surface of the clay particle can attract water

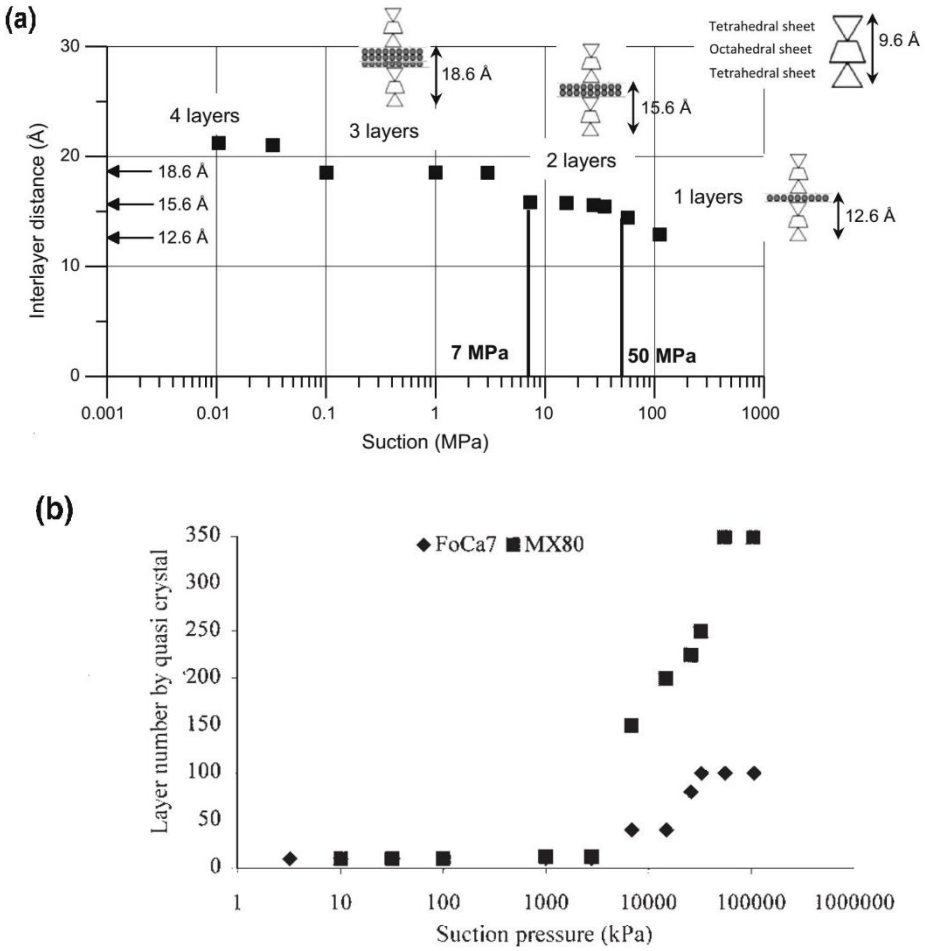

Fig. 1.17. The hydration of FoCa7 and MX80; (a) number of adsorption layers of water molecules (Menaceur et al., 2016); (b) number of layers per particle (Saiyouri et al., 2004)

moelcules and form the DDL, as shown in Fig.1.16. The negative charge leads to the increase of concentration of exchangeable cations in the region adjacent to the external surface of clay particle. Thus, water molecules approch to the clay particles. Double-layer swelling depends on the exchangeable cation type and the solution concentration. Bolt (1956) applied the theory of electronic double layers to investigate the compressibility of pure clays. Saiyouri et al. (2000) investigated the swelling of FoCa7 (Fourges-Cahaignes clay) and revealed that the inter-particle space can reach 150 Å.

For COx claystone, Menaceur et al. (2016) investigated the microstructure changes upon drying or wetting based on the MIP tests (Fig 1.18). According to the crystalline swelling theory proposed by Saiyouri et al. (2004), the initial state of COx claystone (suction: 34 MPa) corresponds to the adsorption of two layers of water molecules (2 W hydration) on the smectite surface. For the suction of 9 MPa, it does not have an evident influence on its microstructure without significant changes of mean pore diameter. Under drying path, the evolution of

adsorption layers of water molecules is similar to the step hydration of FoCa7 and MX80 in Saiyouri et al. (2000, 2004).

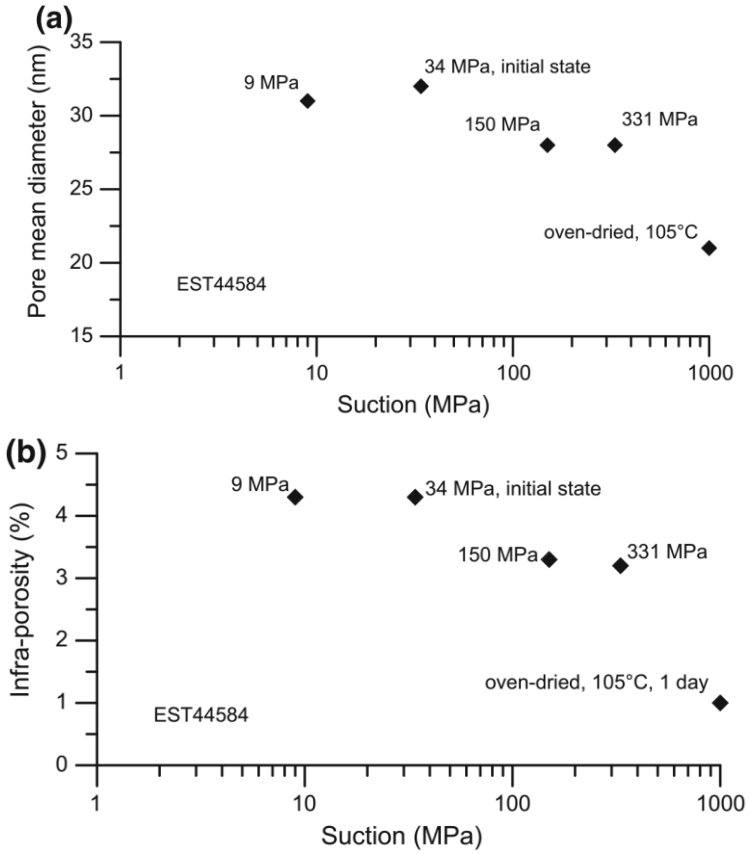

Fig. 1.18. (a) Changes in mean MIP diameter of COx with suction; (b) changes in infra-porosity with suction (Menaceur et al., 2016)

1.3.2 Water retention property

The water retention property plays a key role for the understanding of hydro-mechanical behaviours of soils (Montes Hernandez et al. 2004; Boulin et al., 2008; Ferrari et al. 2014). A lot of studies investigated the water retention properties of COx claystone (Zhang et al., 2013; Wan et al., 2013; Menaceur et al., 2016; Wei et al., 2017). The water retention curve (WRC) obtained from the suction-controlled method (vapour equilibrium method) show significant hysteresis (Fig. 1.19). The air entry value is around 10 MPa. The observation on the volume change behaviour show that irreversible volume changes occurred after a wetting/drying cycle from initial state. These irreversible volume changes are due to micro-cracks generated either by wetting or drying, as shown in other studies (Zhang et al., 2013; Menaceur et al., 2016; Wei et al., 2017).

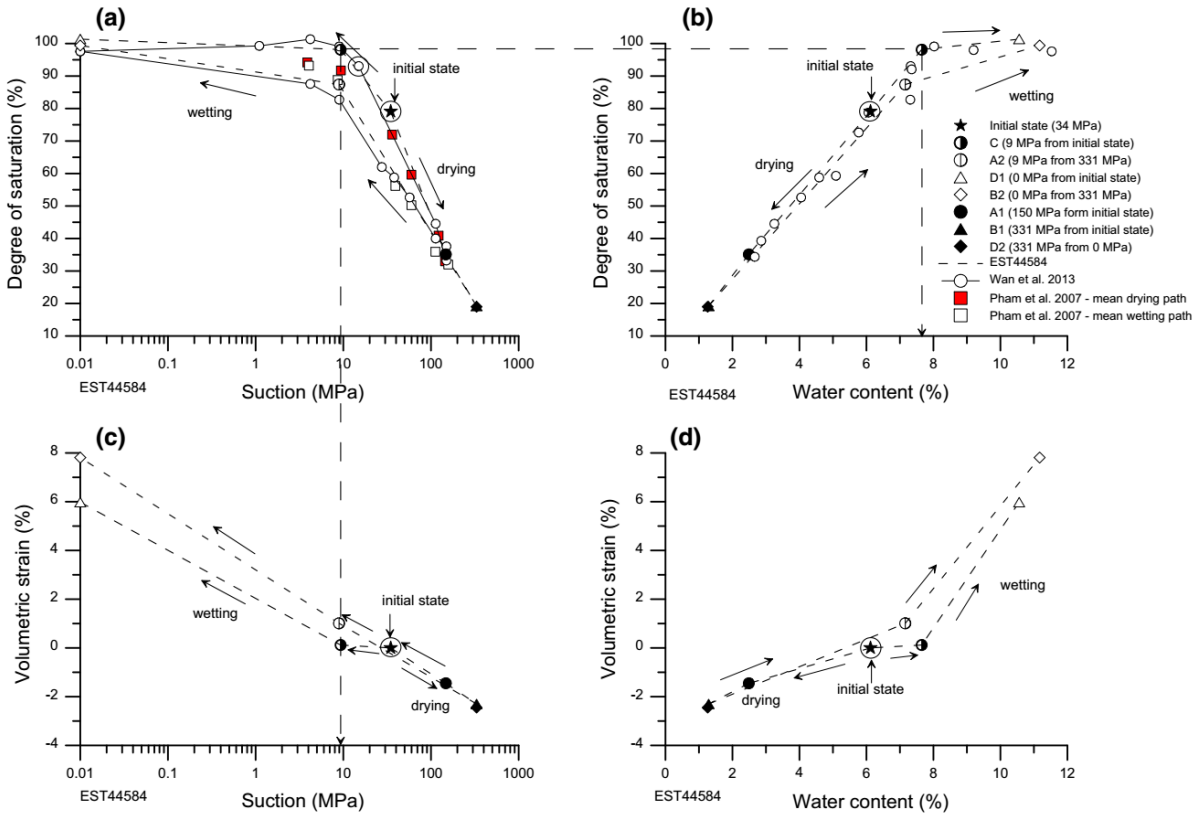

Fig. 1.19 Water retention properties of COx claystone (Menaceur, 2014)

1.3.3 Swelling/shrinkage behaviour

The swelling/shrinkage behaviour of COx claystone is characterised by the changes in swelling pressure, swelling strain and damage upon wetting/drying (Davy et al. 2007; Wang, 2012; Zhang et al., 2013; Menaceur et al., 2016; Wei et al., 2017; Zhang et al., 2020). Zhang et al. (2020) investigated the swelling pressure of COx claystone using different methods (Fig. 1.20) and found higher swelling pressure with the swell-consolidation method in Fig. 1.21. This phenomenon was also observed by Montes et al. (2004), Bornert et al. (2010) and Wang et al. (2014). In addition, Zhang et al. (2010) studied the differences in uniaxial (parallel to the bedding) swelling pressure of COx claystone with different clay contents uses the apparatus in Fig. 1.22, showing higher water adsorption potential at higher the clay content.

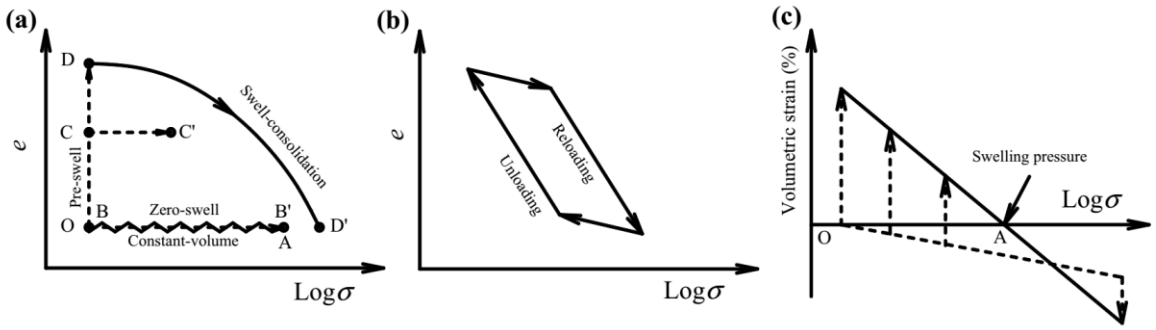

Fig. 1.20. Methods for the determination of swelling pressure: (a) swell-consolidation method, pre-swell method, zero-swell method and constant-volume method; (b) method proposed by Cui et al. (2013); (c) swell-under-load method (Zhang et al., 2020)

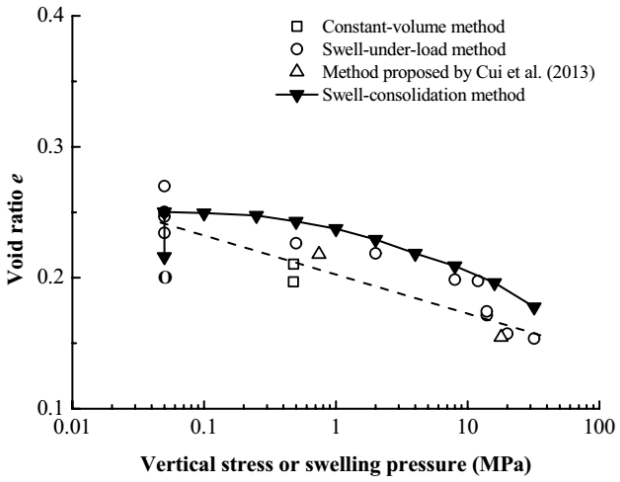

Fig. 1.21. The swelling pressures of COx with different methods (Zhang et al., 2020)

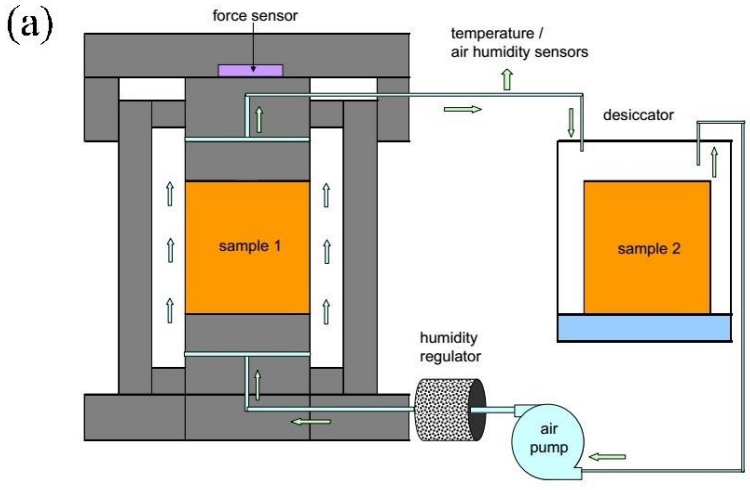

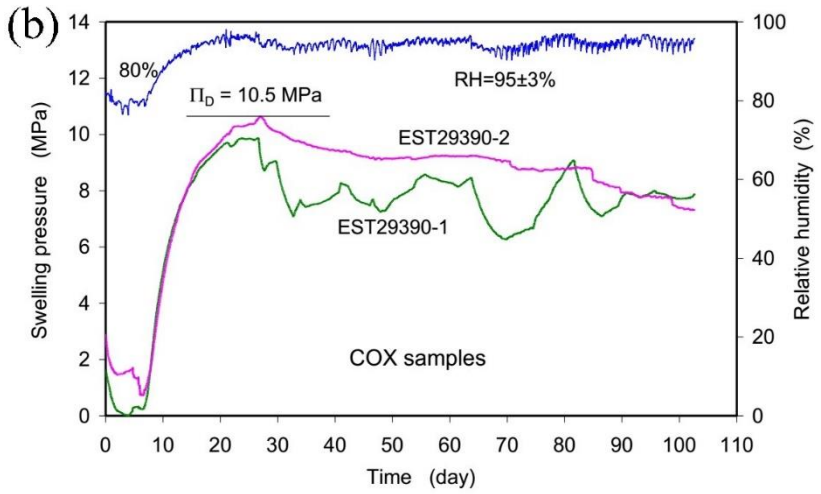

Fig. 1.22 (a) apparatus for uniaxial swelling pressure determination and (b) evolution of swelling pressures measured on COx claystone (Zhang et al., 2010)

Many experiments were carried out to study the volume change behaviour of COx claystone upon wetting/drying (Davy et al. 2007; Pham et al. 2007; Zhang and Rothfuchs, 2004, 2008; Delay et al. 2010; Zhang 2011, 2013; Wan et al. 2013; Menaceur et al. 2016). The swelling of COx claystone was mainly attributed to the osmotic swelling (due to the double layers swelling), while the contributions of microscopic swelling (due to the adsorption of water molecules) and the pure mechanical swelling (due to the reduction of negative pore pressure) were insignificant (Pimentel, 2015; Zhang et al., 2019). Also, Fig. 1.23 shows that wetting can induce some micro-cracks, which was reported in many studies (Montes et al. 2004; Bornert et al. 2010; Wang et al. 2014, 2015; Menaceur et al. 2016).

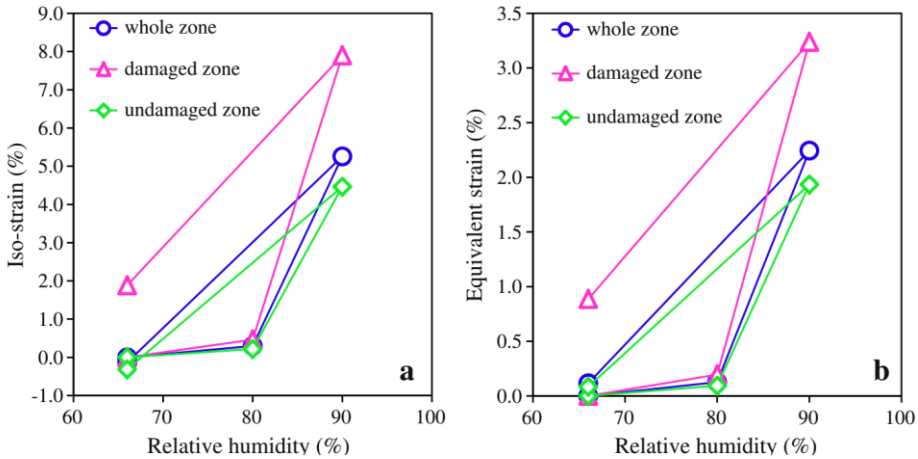

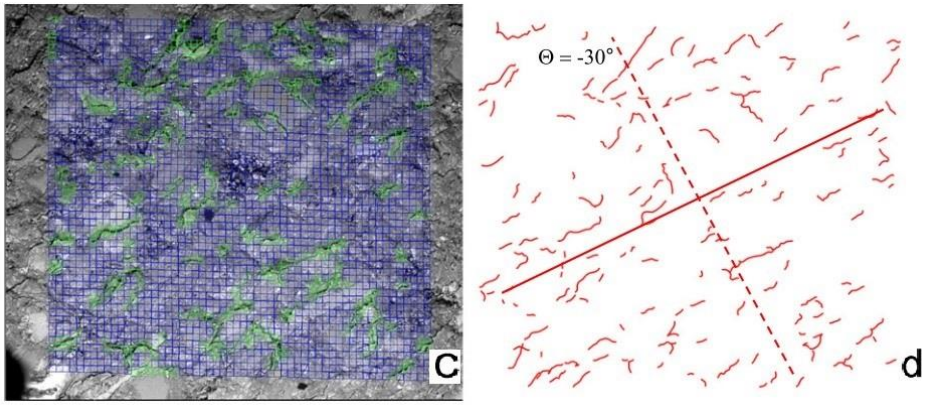

Fig. 1.23. (a) iso-strain; (b) equivalent strain; (c) damaged zone (green) and undamaged zone (blue); (d) orientation of micro-cracks due to wetting (Wang et al. 2014)

As mentioned before, there are some bonds between the clay matrix and calcite and carbonates grains, and the swelling and shrinking of clay minerals can change the pore space and further damage the bonds (Kowalski, 2003; Wang, 2012).

The micro-cracking phenomenon was also observed by Wei et al. (2017) with environmental scanning electron microscope (ESEM). The photographs in Fig. 1.24 indicate that under drying at 158 MPa suction, some microcracks occurred along the bedding plane with dense clay matrix. During the wetting process, numerous cracks also appeared along the bedding direction. For the wetting under low stress or free condition, clay minerals can significantly swell. However, the small pore space limits the free swelling, resulting in microscopic damage and cracks. Besides, the bonds can also prevent clay minerals to swell, intensifing the damage phenomenon, especially under wetting/drying cycles. Based on the MIP data in Fig. 1.15, a new pore family was identified between 7 µm and 100 µm under the zero suction, which was regarded as the contribution of cracks by wetting damage (Menaceur et al., 2016).

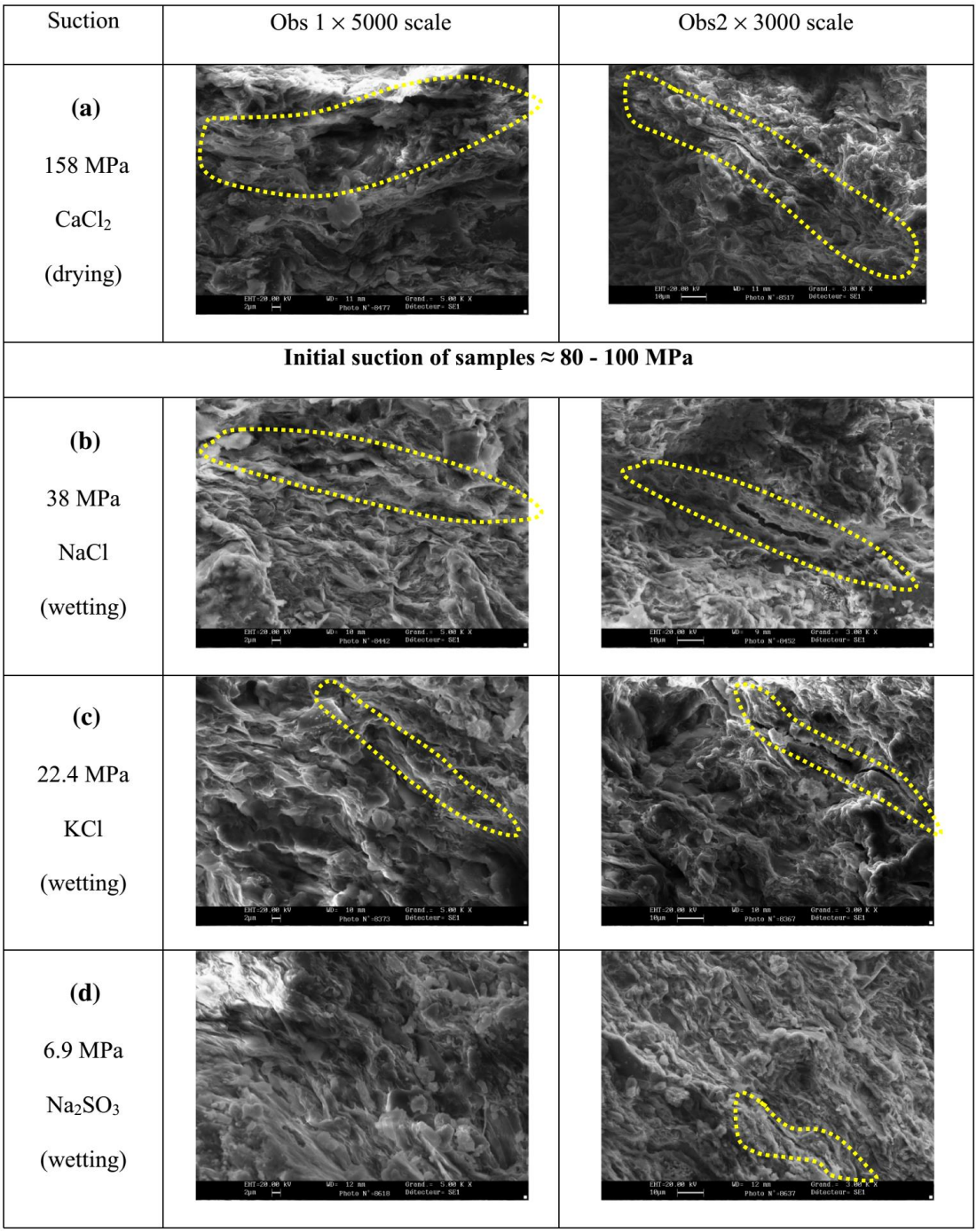

Fig. 1. 24. ESEM photographs of COx claystone at different suctions (perpendicular to bedding) (Wei et al., 2017)

1.3.4 Self-sealing property

As discussed before, COx claystone can be damaged due to stress release (unloading) and wetting/drying (Armand et al. 2013; Armand et al. 2014; Wang et al. 2014; Wei et al., 2017). On the other hand, many experimental studies in the laboratory (Davy et al. 2007) and in situ

(Meier et al., 2000; de La Vaissière et al., 2015) indicated that the cracks/fractures can be closed gradually with the increasing of confining pressure, especially under saturated state.

The closure of fracture under a given confining pressure can be modelled using a hyperbolic function (Goodman, 1976 and Bandis et al., 1983) or an exponential (Bock et al., 2010). An exponential model (Eq. 1-2) was adopted by Zhang et al. (2013) for the relationship between confining pressure and fracture closure:

$$\Delta b = b_m\left[1 - \exp(-\alpha\sigma_n^{\beta})\right] \tag{1-2}$$

where Δb is the aperture closure, b_m is the possible maximum aperture closure (equal to the initial aperture), σ_n is the normal stress (confining pressure), α and β are constants.

The relationship between the aperture closure Δb and the applied normal stress σ_n for both COx claystone and Opalinus clay were reported by Davy et al. (2007) and Zhang (2010, 2011, 2013). The relationship is highly non-linear and includes significant hysteresis under loading/unloading cycle. With the increase of normal stress, the fracture closure becomes more difficult due to the increasing of fracture stiffness, as shown in Fig.1.25.

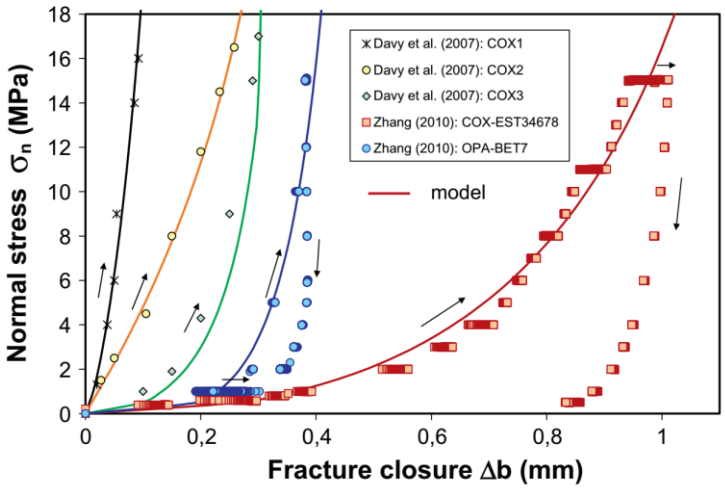

Fig. 1.25. Relationship of fracture closure with applied normal stress (Zhang, 2011)

On the other hand, for the fractured unsaturated claystone under water hydration, the swollen clay minerals can clog fractures with time. As a result, the hydraulic conductivity decreases, as shown in Fig.1.26. Also, with the increase of normal stress, the hydraulic conductivity decreased continuously, which is consistent with the variation of fracture size under normal stress. This demonstrates the strong interaction between water and clay minerals in COx claystone (Zhang, 2011, 2013).

The self-sealing of fractures due to swelling and clogging of clay minerals can be observed clearly in Fig. 1.27. Before water flowing, sharp wall edges of fractures are clearly visible. After that, the fractures on the surface become blurred, full of slaked and swollen clay particles. The disappearance of the fractures is a clear evidence of the self-healing and the degree of healing depends on the initial intensity of fractures, the content of clay minerals, the confining stress, the duration of consolidation, etc. (Tsang and Bernier, 2005; van Geet et al., 2008; Zhang, 2011; Zhang, 2013).

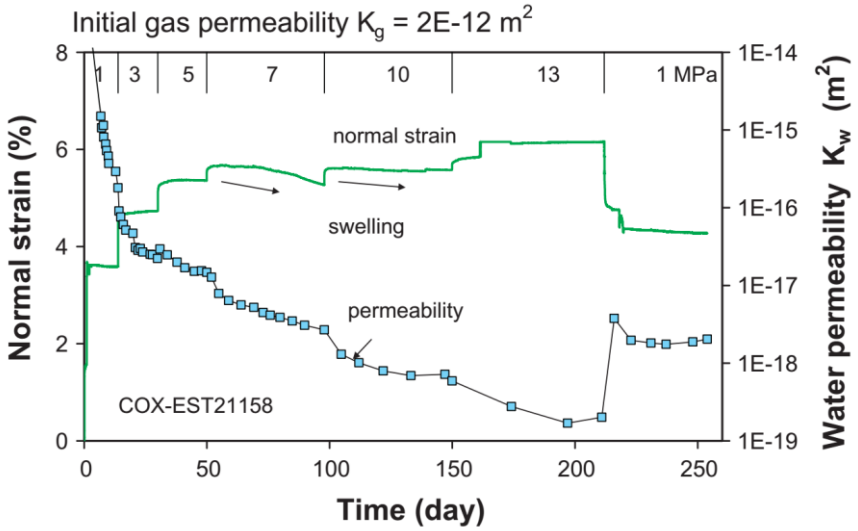

Fig. 1.26. Evolution of normal strain and water permeability with time (Zhang, 2013)

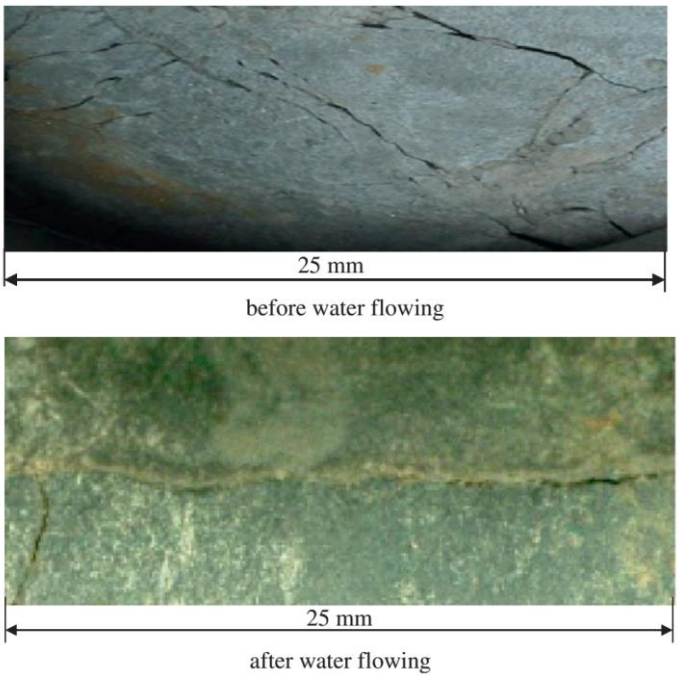

Fig. 1.27. Pictures of the fractures on the surface of COx claystone before and after water flowing (Zhang, 2011)

The self-sealing of COx claystone is mainly induced by the rearrangements of clay minerals and related to the void closure due to clay minerals swelling near fractures (Rothfuchs et al. 2007; van Geet et al. 2008; Zhang 2011; Zheng et al. 2014; de la Vaissière et al. 2015). In Fig. 1.28, the sealing phenomenon is further confirmed through 3D tomography used to monitor an artificial crack in COx claystone after water injecting. The sealing process is related to the swelling of clay minerals in three stages (see Fig. 1.29) (Komine and Ogata, 2003; Wang et al. 2015): (i) interlayer swelling of the smectitic phases (crystalline swelling); (ii) interparticle swelling by osmotic effect (osmotic swelling); (iii) crack obstruction by aggregation of particles (clogging). The self-sealing of fracture reduces water permeability effectively and slows down the diffusion velocity of radionuclides (Giot et al., 2019).

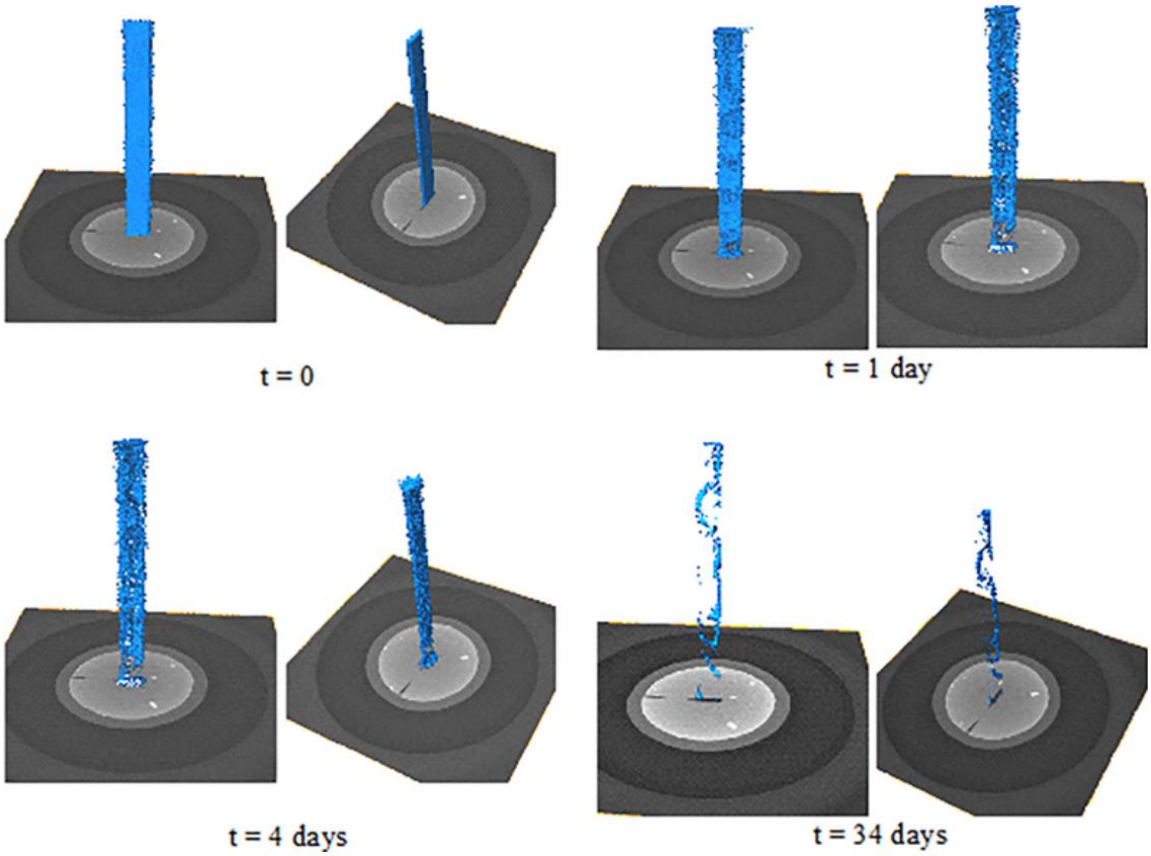

Fig. 1.28. The evolution of crack volume in COx claystone (UA sample) by 3D tomography (Giot et al., 2019)

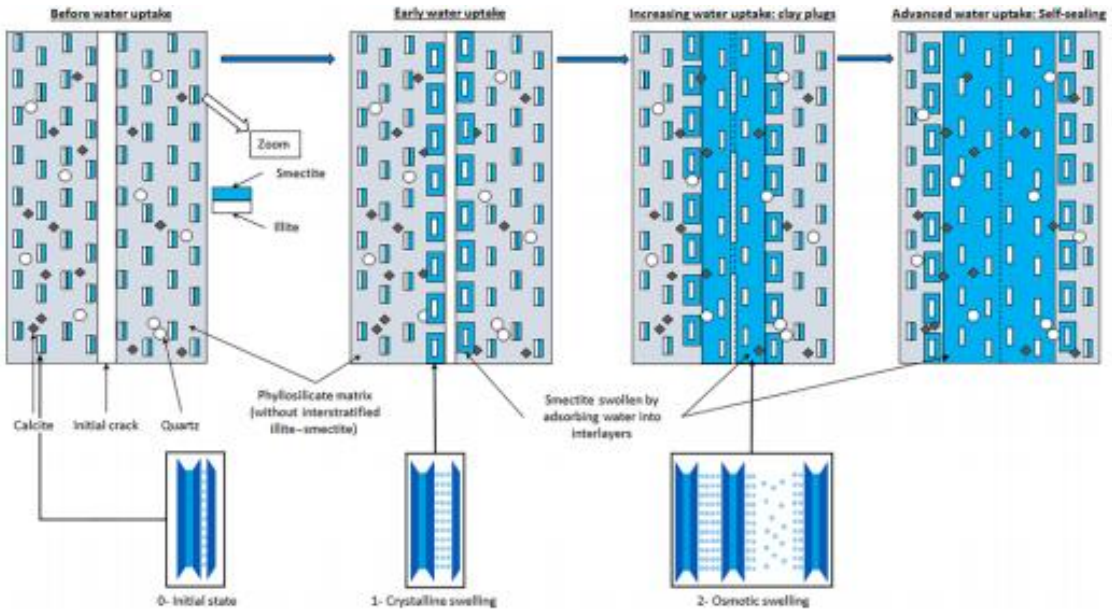

Fig. 1.29. Self-sealing process due to crystalline and osmotic swelling of clay minerals in COx claystone (Giot et al., 2019)

Besides, to better understand the physics of self-sealing phenomenon, Di Donna et al. (2019) conducted X-ray tomography tests on Argillite Unit (U.A.) and Transition Unit (U.T.) COx samples with different fracture thicknesses. For the U.A. sample, it has a higher clay content than U.T. An example of the closure process of fracture is presented in Fig. 1.30. Based on the observations, the self-sealing mechanism is divided into three phases: (i) the swelling of clay minerals near the fracture surface, including crystalline and osmotic swelling; (ii) further swelling of clay minerals farther from the fracture, which induced the disaggregation of smaller

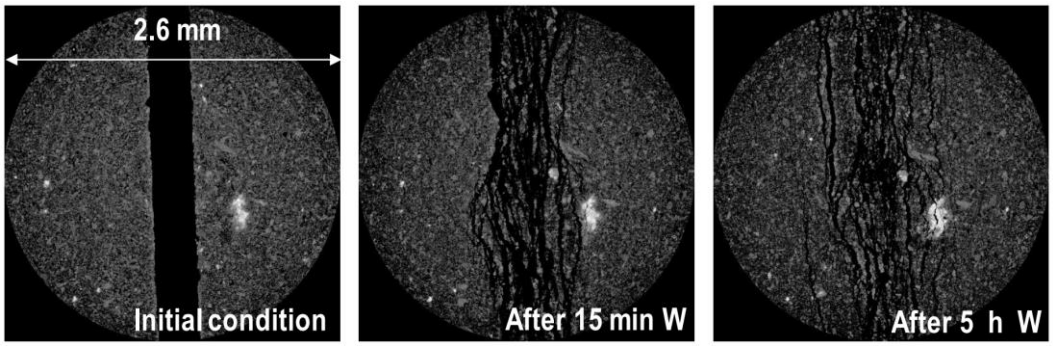

Fig. 1.30. X-ray images at different steps during test H2122 (U.A.), resolution 0.7 µm (bedding plane parallel to the slice) (Di Donna et al., 2019)

claystone grains, clogging the fracture; (iii) homogenization, which means the disaggregated small claystone grains will continue to swell and the macro pores between claystone grains will collapse under the confining pressure, during a long period.

1.4 Mechanical behaviour and the influencing factors

In the context of the disposal of radioactive waste, the stability of host formation is essential for the safety of the repository, especially under high geostress (up to 16 MPa for COx claystone in the major principal stress direction). Thus, the mechanical performance of COx claystone needs to be well understood and characterized. In addition, the consideration of different influencing factors such as temperature, humidity, etc. is also important, in particular with respect to the long-term performance of COx claystone. This section focuses on the mechanical behaviour of COx claystone with consideration of stress conditions and effects of temperature, humidity, anisotropy and time.

1.4.1 Volume change behaviour

The volume change behaviour of COx claystone was investigated by many researches (Chiarelli et al., 2003; Mohajerani, 2011; Menaceur, 2014, Belmokhtar et al., 2017; Zhang et al., 2015 and 2019). The results obtained by Mohajerani (2011) and Menaceur (2014) indicated that under saturated condition, the porosity after rebounding was larger than that at the initial state when the COx sample was loaded to a high stress then unloaded. It was interpreted by the more damage induced by high stress inside the sample, releasing more smectite minerals (Fig. 1.31a). On the other hand, the damage due to loading could result in that the volumetric elastic rebounding changes with respect to the history maximum stress $\sigma_{v,max}$. It can be demonstrated in terms of changes in rebounding slope at different unloading stresses in Fig. 1.31b.

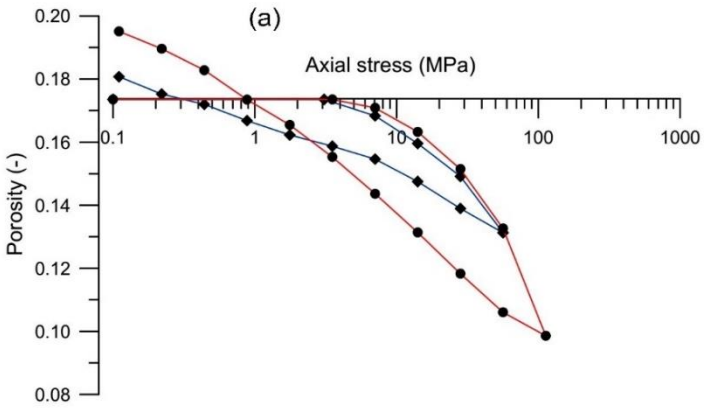

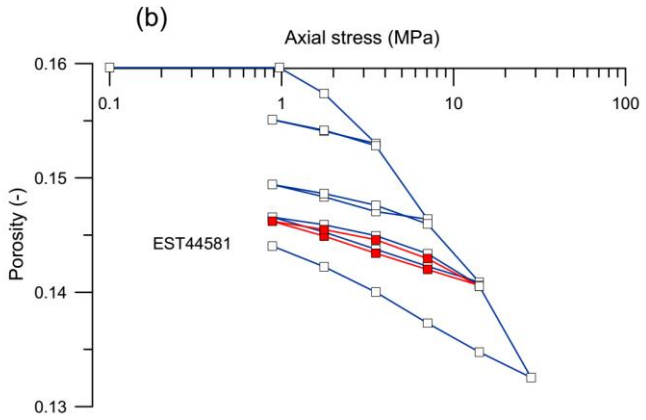

Fig. 1.31. Oedometric compression curves (Menaceur, 2014)

Moreover, Chiarelli et al. (2003) studied the isotropic compression behaviour at initial unsaturated state. There are two fundamental phenomena observed: (1) significant axial and lateral plastic residual strains were obtained after unloading, due to the pore collapse inside the sample; (2) the developments of axial and lateral strains with stress showed different evolution features due to the anisotropy of COx claystone. These observations are consistent with the triaxial isotropic compression results obtained by Zhang et al. (2015, 2019).

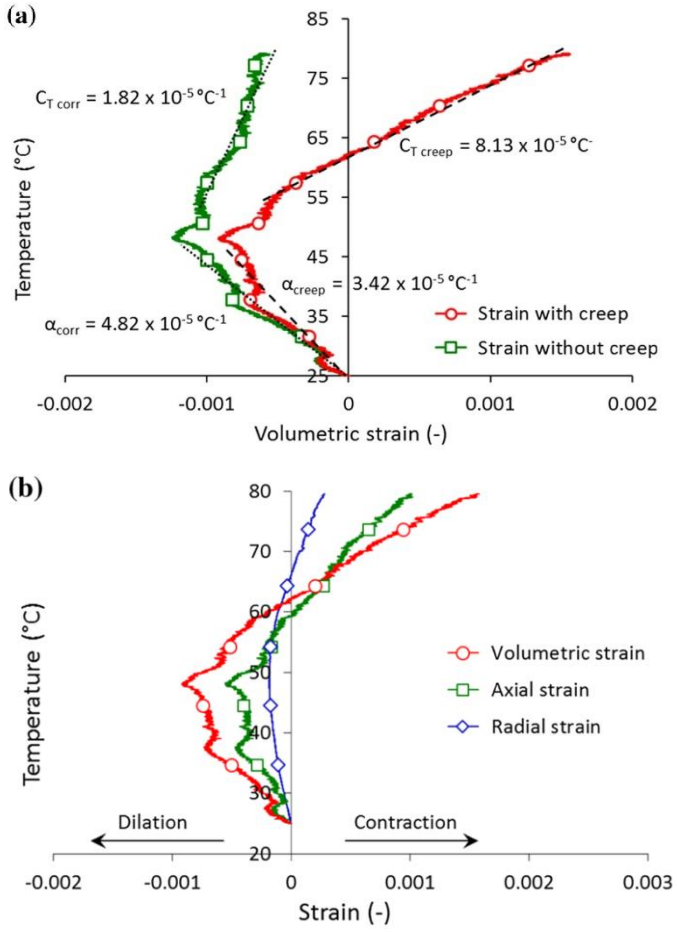

Fig. 1.32. Volume changes due to heating (Belmokhtar et al., 2017)

In addition, the thermal volume change behaviour was investigated by several authors (Mohajerani et al., 2011, 2013; Menaceur et al., 2016; Belmokhtar et al., 2018; Braun et al., 2019). Generally, thermoelastic expansion phenomenon was observed for overconsolidated clays, while thermoplastic contraction at normally consolidated state. For COx claystone, thermoplastic contraction was identified by Mohajerani et al. (2013) and Menaceur et al. (2016). In addition, the creep effect on thermal volume change can be observed in Fig. 1.32a. In Fig. 1.32b, the differences between axial strain and radial strain indicate the influence of anisotropy. In addition, Braun (2019) observed that the thermoplasticity of COx claystone mainly occured in the direction perpendicular to the bedding but not in the direction parallel to the bedding.

1.4.2 Shear behaviour

The shear behaviour of COx claystone was widely investigated under different test conditions and test methods, including uniaxial compression (Espitia and Caicedo 2014; Fabre and Pellet 2006; Gasc-Barbier et al. 2004; Yang et al. 2011, 2013), triaxial compression at constant confining pressure (Liu et al. 2015, 2017, 2018; Liu and Shao 2016; Sarout and Guéguen 2008; Sarout et al. 2007; Zhang et al. 2013), micro/nano-indentation (Auvray et al. 2015; Gratier et al. 2004; Hu et al. 2013; Zhang et al. 2012) and hollow cylinder triaxial cell etc.(Bemer et al. 2004; Huang et al. 2014; Mohajerani et al. 2011; Montes et al. 2004). The basic shear behaviour of COx claystone under different confining pressures are presented in Fig. 1.33 (saturated sample) and Fig. 1.34 (unsaturated sample at 90 % relative humidity). It is worth noting that triaxial compression tests under constant mean stress was conducted by Liu et al. (2019). Actually, this loading path is compatible with the change of stress state in a host formation around a tunnel before and after the excavation, as demonstrated by Liu et al. (2019). This case can be simply described in Fig. 1.35.

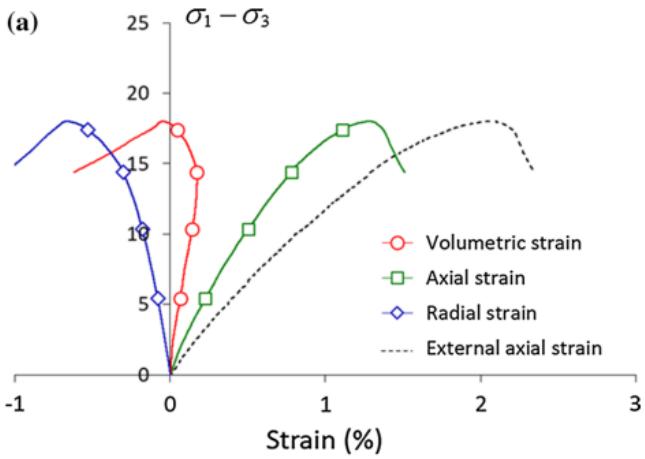

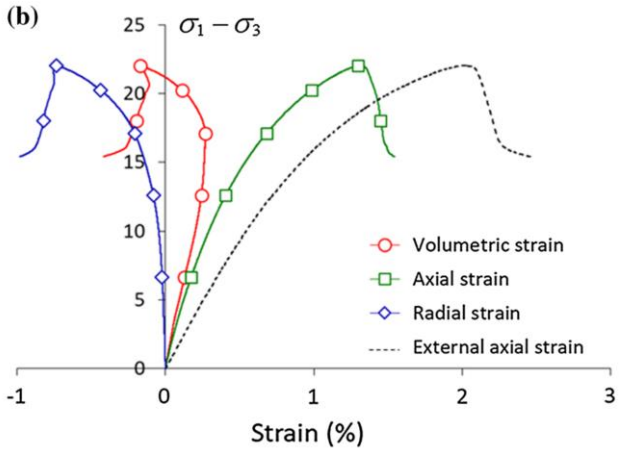

Fig. 1.33 Stress–strain curves of drained triaxial tests at different σ_3 values: (a) 8 MPa; (b) 12 MPa (Belmokhtar et al., 2018)

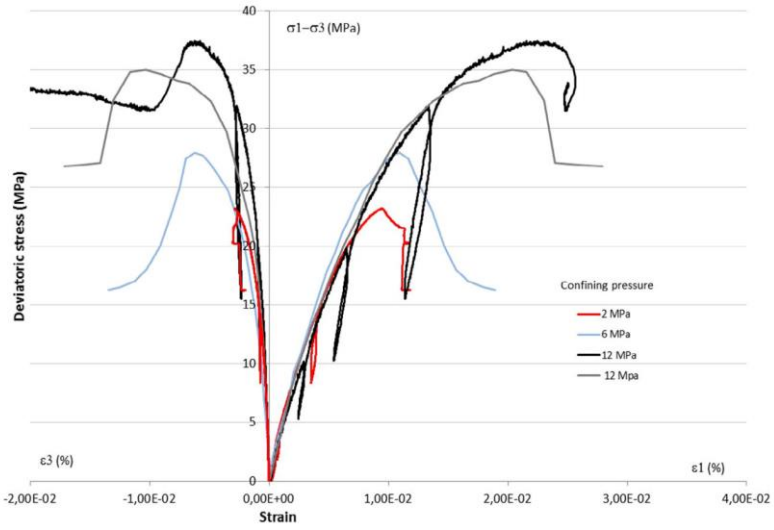

Fig. 1.34. Stress-strain curves of triaxial compression tests under different confining pressures on COx claystone (Armand et al., 2017)

On the other hand, the water content can significantly affect the mechanical behaviour of COx claystone in terms of elastic modulus, peak strength, dilitancy, etc., (Bornert et al., 2010; Chiarelli et al., 2003; Vales et al., 2004; Zhang et al., 2004). Liu and Shao (2016) conducted four trixial tests on COx claystone with different initial water contents, as shown in Fig. 1.36. The peak strength decreases with increasing water content, while the corresponding axial strain increases. It means the increase of water content can make the sample less resistant and more deformable. In addition, the dilitancy onset stress decreases similarly. This phenomenon can be observed in Fig. 1.36. It was explained by the fact that higher water content can result larger swelling of clay minerals and make the sample more ductile (Montes et al., 2004).

On the other hand, the increasing of temperature can intensify the interaction between clay minerals and water, making COx claystone more ductile. The increase of temperature can also result in the decrease of shear strength and the increase of the corresponding axial strain of the COx claystone (Liu et al., 2018), in agreement with other results in literatures (Delage, 2013; Menaceur et al., 2015, 2016; Mohajerani et al., 2013; Zhang, 2015; Zhang et al., 2017).

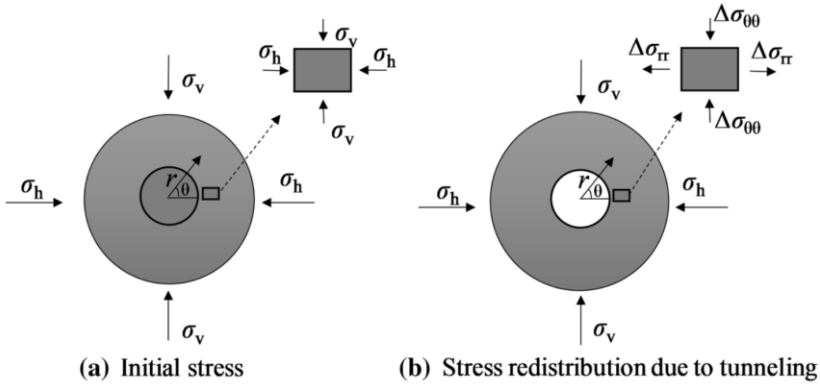

Fig. 1.35. Change of stress state around a tunnel after excavation (Liu et al., 2019)

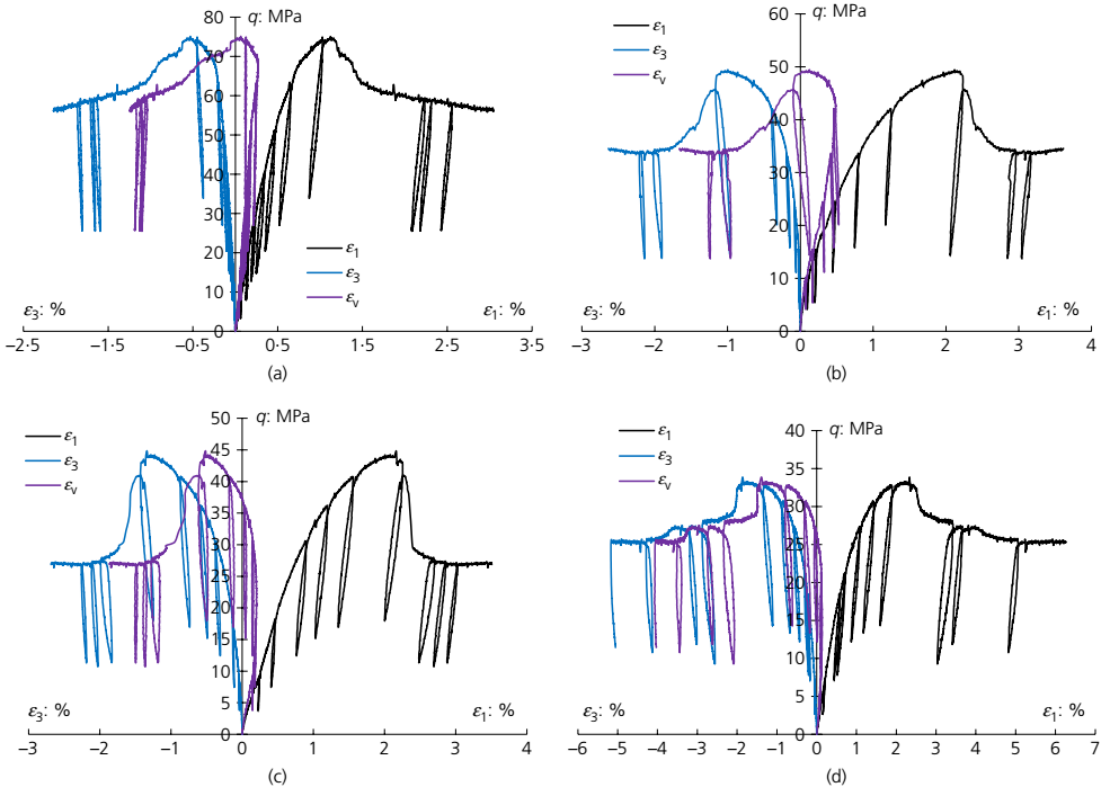

Fig. 1.36. Strain-stress curves of COx claystone at different relative humidity: (a) dried; (b) RH = 76%; (c) RH = 85%; and (d) RH = 98% (Liu and Shao, 2016)

Besides, few researchers focused on the rate-dependent effect on the shear behaviour. The triaxial experimental results obtained by Liu et al. (2018) show that the selected three strain rates do not affect the development of stress-strain curves significantly, as shown in Fig. 1.37.

Based on the data of shear strength from literatures (Hu et al., 2014; Menaceur et al., 2015; Belmokhtar et al., 2018), the failure envelops in p'-q plane are plotted in Fig 1.38. Generally, higher initial porosity will result in lower shear strength under the same mean stress. Moreover, the slope is almost the same for different porosities. The shear strength of COx claystone at higher initial water content and lower temperature is lower (Liu et al. 2018), as shown in Fig. 1.38b. Based on the shear data, the frictional angle and cohesive strength can be calculated, as summarized in Table 1.3. The average frictional angle and effective cohesion are 22.3° and 5.6 MPa, respectively.

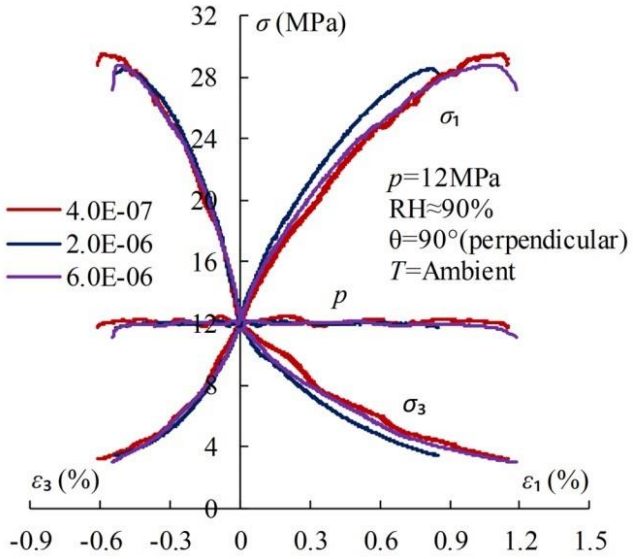

Fig. 1.37. Stress–strain curves from triaxial tests under constant mean stress with different axial strain rates (Liu et al., 2018)

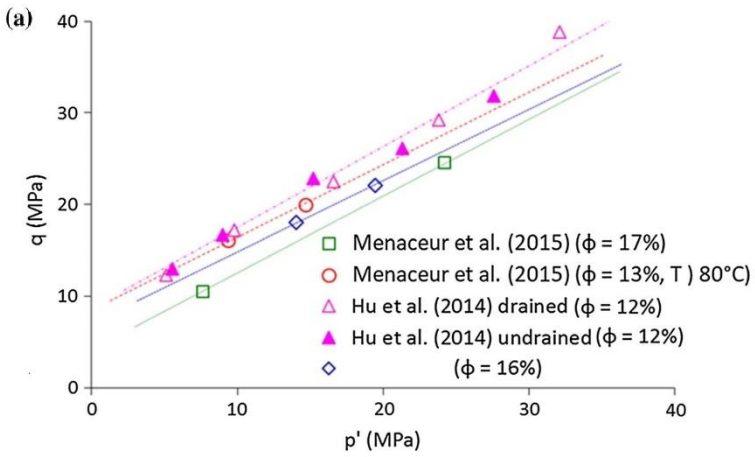

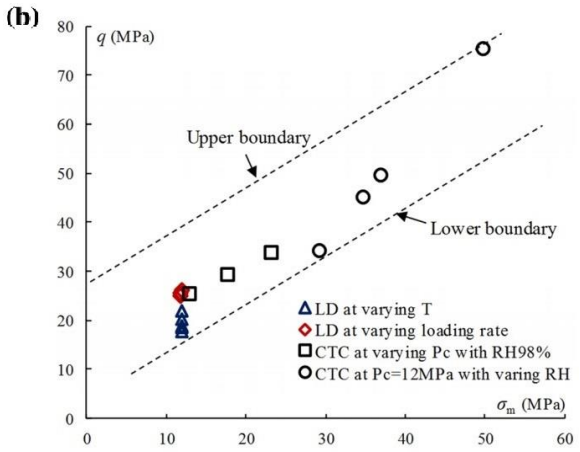

Fig. 1.38. Shear envelopes of COx claystone: (a) saturated samples (Belmokhtar et al., 2018); (b) unsaturated samples (Liu et al., 2018)

Table 1.3. The frictional angle and cohesion of COx claystone

Source	Frictional angle (°)	Cohesion (MPa)	Note
Wileveau and Bernier (2008)	25.0	7.0	-
Hu et al. (2014)	21.4	3.9	Drained
	19.6	3.8	Undrained
Zhang (2016)	24.0	6.5	-
Guayacán-Carrillo et al. (2017)	23.0	6.6	Perpendicular to bedding
		5.9	Parallel to bedding
		5.6	45° to bedding
Belmokhtar (2017)	21.0	-	-

1.4.3 Anisotropic behaviour

As a kind of sedimentary soft rock, COx claystone shows a typical transversely isotropic behaviour. To date, a lot of in-situ and laboratory tests were carried out to clarify the effect of anisotropy on mechanical responses of COx claystone (Zhang and Rothfuchs, 2004, David et al., 2007; Zhang et al., 2010; Yang et al., 2013; Zhang et al., 2012; Belmokhtar, 2017). The transversely isotropic elastic theory is usually adopted to analyse the mechanical behaviour of COx claystone. The elastic stress-strain relation is expressed as follows:

$$\begin{bmatrix} \varepsilon_x \\ \varepsilon_y \\ \varepsilon_z \\ \gamma_{xy} \\ \gamma_{yz} \\ \gamma_{zx} \end{bmatrix} = \begin{bmatrix} \frac{1}{E_1} & -\frac{\nu_1}{E_1} & -\frac{\nu_2}{E_2} & 0 & 0 & 0 \\ -\frac{\nu_1}{E_1} & \frac{1}{E_1} & -\frac{\nu_2}{E_2} & 0 & 0 & 0 \\ -\frac{\nu_2}{E_2} & -\frac{\nu_2}{E_2} & \frac{1}{E_2} & 0 & 0 & 0 \\ 0 & 0 & 0 & \frac{2(1+\nu_1)}{E_1} & 0 & 0 \\ 0 & 0 & 0 & 0 & \frac{1}{G_2} & 0 \\ 0 & 0 & 0 & 0 & 0 & \frac{1}{G_2} \end{bmatrix} \begin{bmatrix} \sigma_x \\ \sigma_y \\ \sigma_z \\ \tau_{xy} \\ \tau_{yz} \\ \tau_{zx} \end{bmatrix} \quad (1\text{-}3)$$

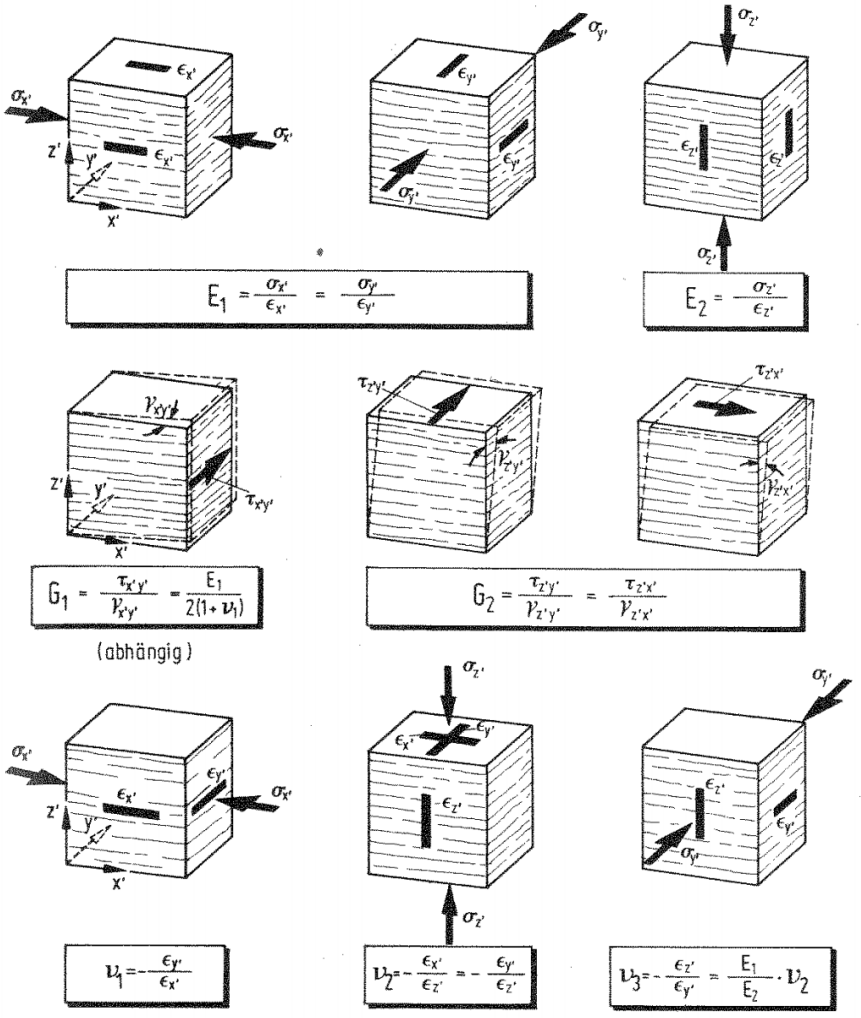

Fig. 1.39. Definition of the transversely isotropic elastic parameters with respect to bedding planes (after Wittke, 1984)

Normally, the Young's modulii determined from the unloading-reloading cycles at two main directions (perpendicular and parallel to bedding) increase at the beginning of loading (fissure

closure), then stablize before the peak stress. The axial strains at peak stress are dependent on the orientation of bedding plane. The short-term strength is dependent on loading path and direction with respect to the bedding. For a given loading condition, the peak strengths also depend on the angle with respect to bedding, reaching the minimum value at 45° for the compression test and at 30° for the extension tests (Zhang et al., 2015, 2019), as shown in Fig. 1.40. Liu et al. (2018) evaluated the anisotropy by adopting a new parameter M_{11}/M_{31} ($M_{11} = \Delta\sigma_1/\Delta\varepsilon_1$, $M_{11} = \Delta\sigma_1/\Delta\varepsilon_1$), which should be equal to -2 for isotropic materials (Liu et al., 2018). However, the experimental value is always lower than -2 (in Fig. 1.41), which confirmed the structural anisotropy of COx claystone.

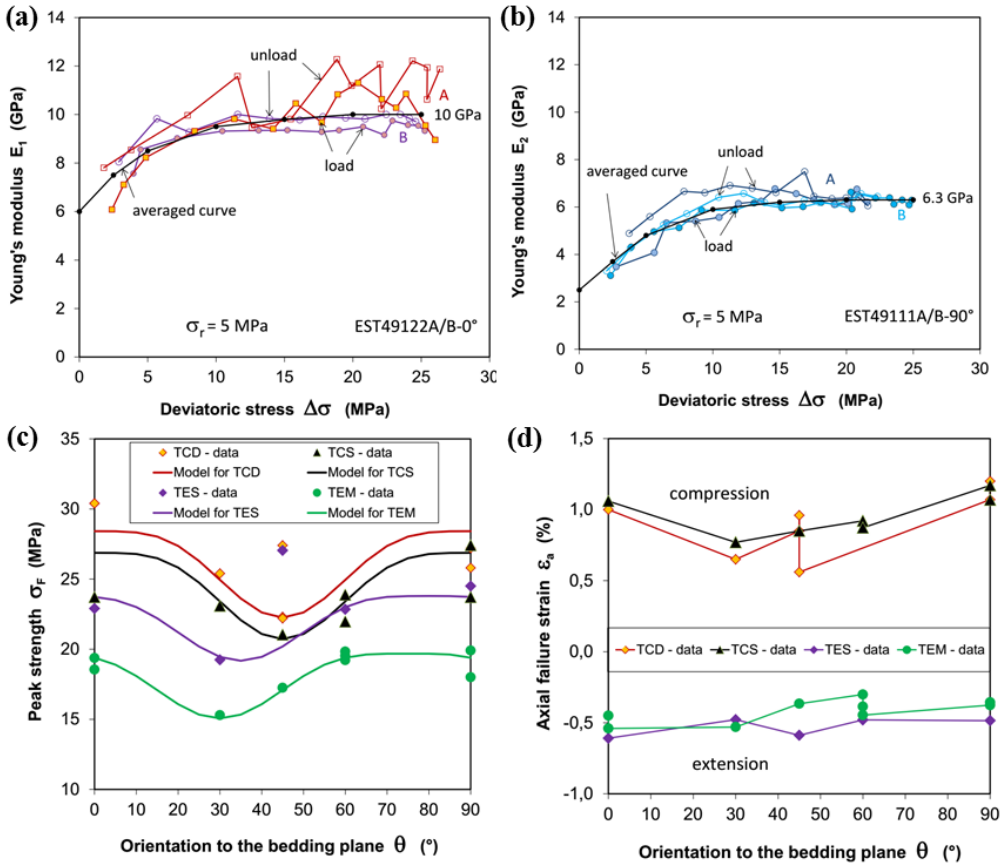

Fig. 1.40. Different parameters characterizing the anisotropy of COx claystone: (a) E_1 (perpendicular to bedding) versus deviator stress; (b) E_2 (parallel to bedding) versus deviator stress; (c) peak strength versus the orientation to bedding plane; (c) axial failure strain versus orientation to bedding plane (after Zhang et al., 2019)

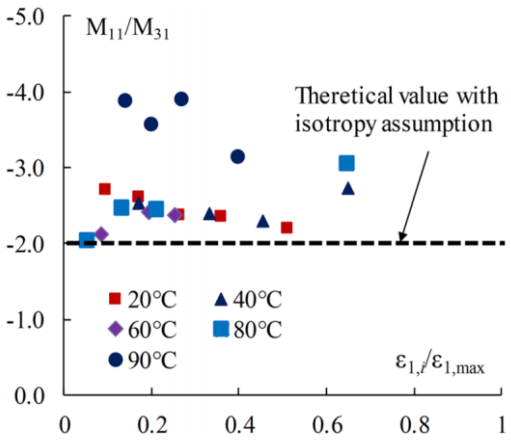

Fig. 1.41. Effect of temperature on shear modulus under constant mean stress (Liu et al., 2018)

1.4.4 Time-dependent behaviour

The creep behaviour of COx claystone was explored in many studies (Zhang et al., 2004; Zhang et al., 2010, 2013; Zhang et al., 2015; Zhang et al., 2019). The loading conditions considered include uniaxial creep loading, triaxial creep loading and multi-step creep loading. Generally, for the creep behaviour of geomaterials, there are two key points to be considered: (a) whether there is a threshold value for the visco-plastic deformation; (b) whether there is a steady-state creep rate under a given constant stress state (Ghoreychi, 1997, 1999). The results from creep and relaxation tests on COx claystone indicate that there is not a low creep stress threshold, while there is a steady-state creep stage. Moreover, the effects of sample size and anisotropy are not significant for the long-term behaviour. In terms of effect of temperature, it is significant under low stresses, while insignificant under high stresses, as shown in Fig. 1.42. The loading rate effect is also insignificant (Liu et al., 2018). It is worth noting that the experimental data is limited and only a few studies are focusing on the effect of moisture content (or suction) on the visco-plastic behaviour.

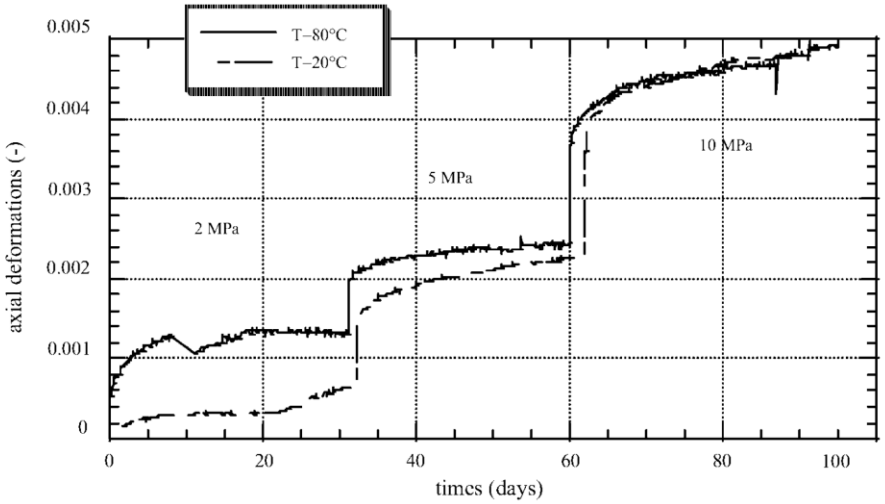

Fig. 1.42. Influence of temperature on creep strain (Gasc-Barbier et al., 2004)

1.4.5 Damage behaviour

During the mechanical loading process, the damage induced can be identified by evaluating the mechanical parameters, including Young's modulus, Poisson's ratio, plastic volume strain, etc. In addition, some researchers adopted photographic techniques, SEM and µ-tomography, to monitor the COx claystone cracking due to the mechanical damage (Bésuelle et al., 2006; Lenoir et al.,2007; Viggiani et al., 2013; Wang, 2012; Wang et al., 2014; Menaceur et al., 2016). As discussed in section 1.4.2, shearing of COx claystone can indeed result in damage. Menaceur et al. (2016) measured the hydraulic conductivity to characterize the evolution of damage during the shearing process, which was confirmed by observing the shear band and micro-cracks on the surface of sample after shearing. With 3D X-ray tomography, the evolution of damage inside COx sample was identified under uniaxial loading, as shown in Fig 1.43. The evolution of cracks during shearing was observed at different loading steps. Furthermore, some interesting phenomena were identified in Wang (2012). For the mineral inclusions (carbonate and quartz grains), the splitting, inter slipping of coarse grains were observed at a micro scale, based on the image analysis shown in Fig. 1.44. These phenomena were confirmed by the laboratory tests conducted by Wang (2012).

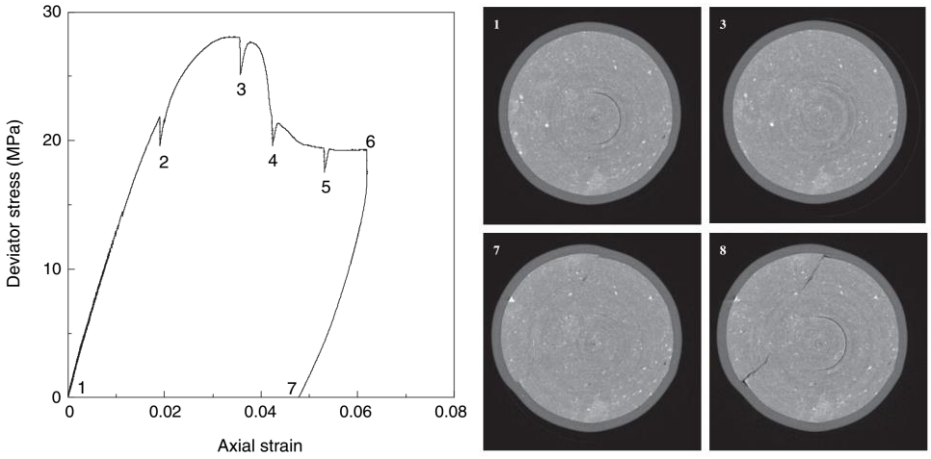

Fig 1.43. Stress strain curve (left) and the corresponding tomography image at a given section (test ESTSYN01) (right) (Lenoir et al.,2007)

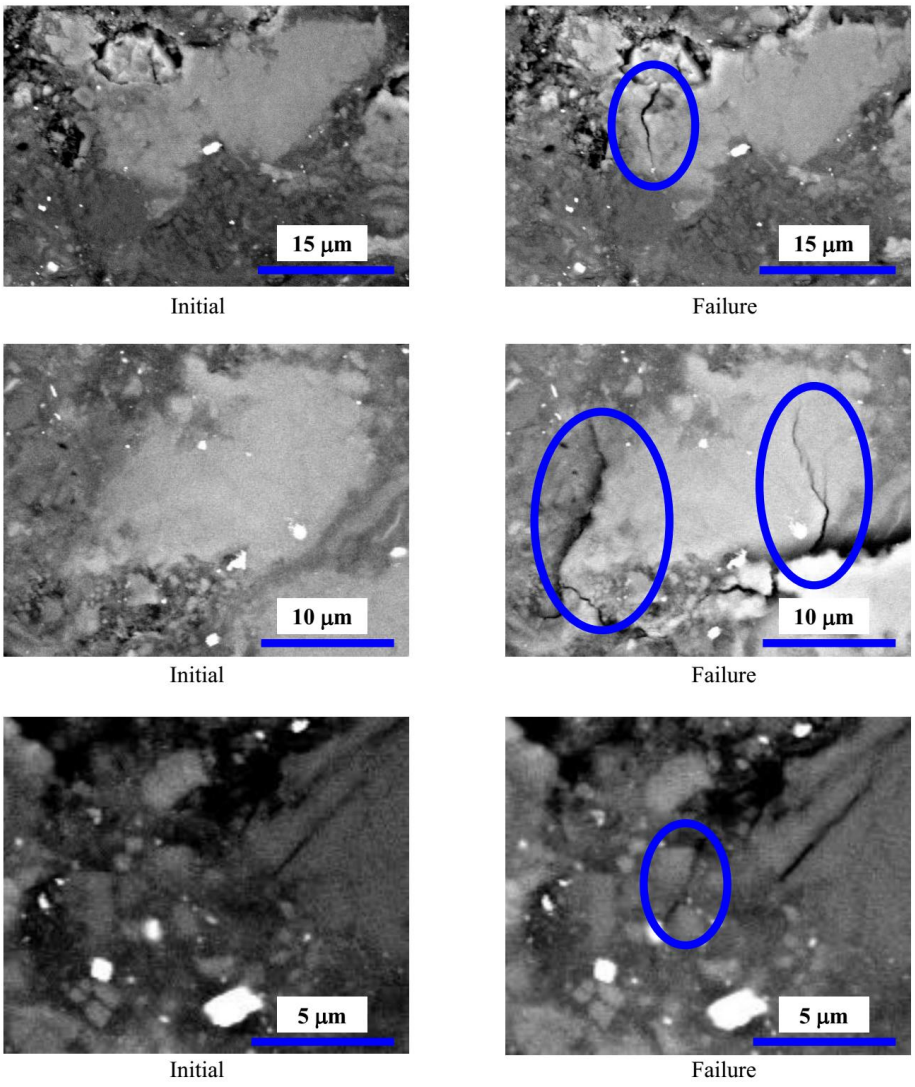

Fig. 1.44. Damage induced in uniaxial compression test at different locations (top, middle and bottom) (Wang, 2012)

1.5 Modelling the elasto-visco-plastic behaviour

Generally, the time-dependent behaviour of geomaterials include creep, stress relaxation and rate dependency. To model these behaviours, a large number of elasto-visco-plastic (EVP) constitutive models were built (Qu et al., 2010; Yin and Tong, 2011; De Gennaro and Pereira, 2013). There are three types of such models: empirical models, rheological models and general stress-strain-strain rate models (Liingaard et al., 2004). In this section, some typical models and relevant aspects are reviewed and discussed.

The empirical models are widely adopted for their simplicity (Karim and Gnanendran, 2014). The rheological models are also often used to describe the uniaxial conditions (Liingaard et al. 2004). The general stress-strain-strain rate models are built based on viscoplastic theory. There are a lot of time independent elastoplastic models for saturated soils (e.g. Adachi and Oka, 1982; Kutter and Sathialingam, 1992; Yin and Graham, 1999). However, only a few of EVP models are developed to describe the time-dependent behaviours of unsaturated soils (De Gennaro and Pereira, 2013; Mac et al., 2017). In addition, for stiff soils, the variations of stress state and hydraulic conditions can induce damage and further changing their mechanical behaviours, which is also studied by few researchers (Bui et al., 2016, 2017; Bian et al., 2017).

1.5.1 EVP models for saturated soils

In the constitutive EVP models for saturated soils (Qiao et al., 2016), the following variables are adopted, with the strain increment partitioned into an elastic part and a visco-plastic part:

$$p' = \frac{1}{3}\sigma'_{ii} \tag{1-4}$$

$$q = \sqrt{\frac{3}{2}s_{ij}s_{ij}} \tag{1-5}$$

$$\mathrm{d}\varepsilon = \mathrm{d}\varepsilon^{e} + \mathrm{d}\varepsilon^{vp} \tag{1-6}$$

where q and s_{ij} are the mean stress and deviatoric stress tensor, respectively.; $\mathrm{d}\varepsilon, \mathrm{d}\varepsilon^{e}$ and $\mathrm{d}\varepsilon^{vp}$ are the total, elastic and visco-plastic strain increments, respectively.

Generally, non-linear elastic theory is adopted (Hujeux, 1979; Hong, 2013; Qiao et al., 2016). The isotropic and deviatoric components of the elastic strain increments are calculated as:

$$\mathrm{d}\varepsilon_v^e = \frac{\mathrm{d}p\prime}{K} \tag{1-7}$$

$$\mathrm{d}\varepsilon_s^e = \frac{\mathrm{d}q}{3G} \tag{1-8}$$

where K and G are the bulk elastic modulus and the shear elastic modulus.

Over-stress in EVP theory

For the determination of visco-plastic strain, the overstress concept was introduced and developed, as reported in Perzyna (1963, 1966), Olszak and Perzyna (1966, 1970) and Sekiguchi (1985). In Perzyna's overstress concept, it is assumed that the viscous effect can be neglected in the conventional elastic region, which means that the traditional yield surface is time-independent. The corresponded visco-plastic strain can be determined by Eq. 1-9:

$$\mathrm{d}\varepsilon_{ij}^{vp} = \gamma\Phi(F)\frac{\partial g}{\sigma'_{ij}} \tag{1-9}$$

where γ is the fluidity parameter; Φ is the viscous nucleus; F is the overstress function; g is potential function; and σ'_{ij} is the effective stress tensor.

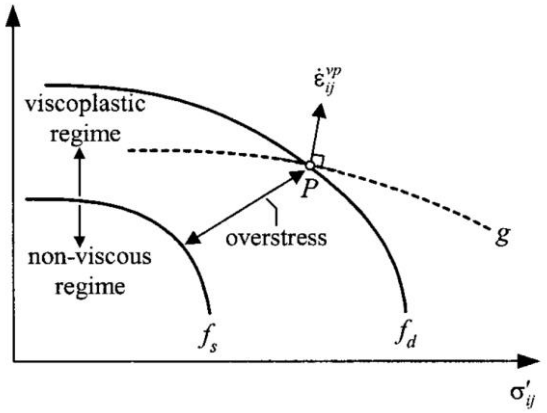

Fig. 1.45. The dynamic yield surface f_d and the static yield surface f_s (Perzyna, 1963).

As presented in Fig. 1.45, the function f_d describes the dynamic loading surface on which the current stress state P is located. The overstress theory differs from the general elasto-plasticity in the sense that the consistency rule is not used. This implies that the inelastic strains in the overstress model are not related to the stress history but to the current stress point only, while the inelastic strains are related to the stress rate in the elasto-plasticity. Furthermore, by assuming the invalidity of the consistency rule, the stress state is allowed to be on, within or outside the static yield surface. This is used in the definition of overstress F. F is defined as the distance in stress space between the current stress state and the static yield surface f_s. The viscous nucleus Φ is as follows:

$$\langle\Phi(F)\rangle = \begin{cases} 0 & \text{for } F \leq 0 \\ \Phi(F) & \text{for } F > 0 \end{cases} \tag{1-10}$$

The magnitude of $d\varepsilon_{ij}^{vp}$ is given by γ and the viscous nucleus $\langle\Phi(F)\rangle$. The determination of the viscous nucleus $\Phi(F)$ is based on experimental data (Phillips and Wu, 1973; Adachi and Okano 1974, 1982; Oka et al. 1987; di Prisco and Imposimato 1996). The overstress F is regarded as the distance between the static and dynamic yield surfaces. Wood (1990), Eisenberg and Yen (1981) and Hinchberger and Rowe (1998) claimed that the static yield surface was obtained by performing extremely slow tests.

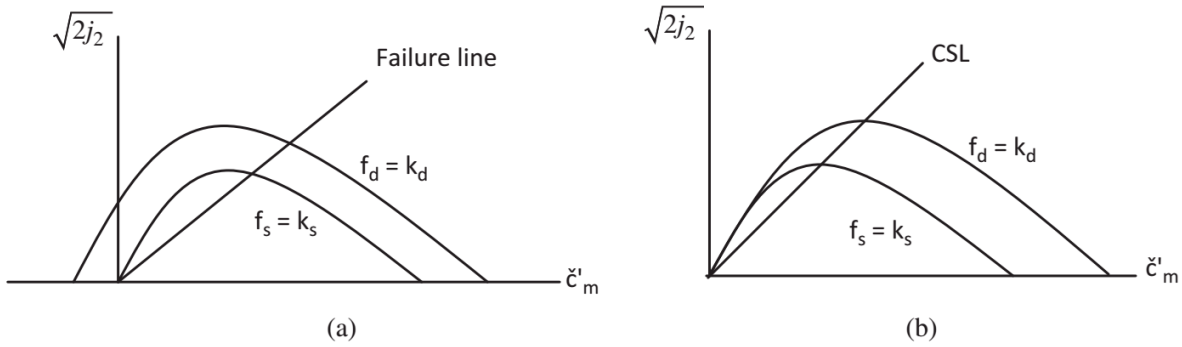

Fig. 1.46. Static and dynamic yield surfaces, (a) proposed by Adachi and Okano (1974) and (b) proposed by Adachi and Oka (1982). Note that the horizontal and vertical axes represent the mean stress and the deviator stress, respectively.

Non-stationary flow surface EVP theory

Based on the isotach concept (Fig. 1.47), the nonstationary flow surface theory (NSFS) concept was developed to model the visco-plastic behaviour of saturated soils in a general stress space with Eq. 1-11, as illustrated in Fig. 1.48. The yield surface flows with time, enabling the creep, relaxation and rate-dependent properties of saturated soils to be modelled (Liingaard et al., 2004; Qiao, et al., 2016). The stress–strain-strain rate relationship was modified and replaced by the stress–strain-visco-plastic strain rate to model the stress relaxation behaviour, which was validated by Laloui et al. (2008) and Kabbaj et al. (1986).

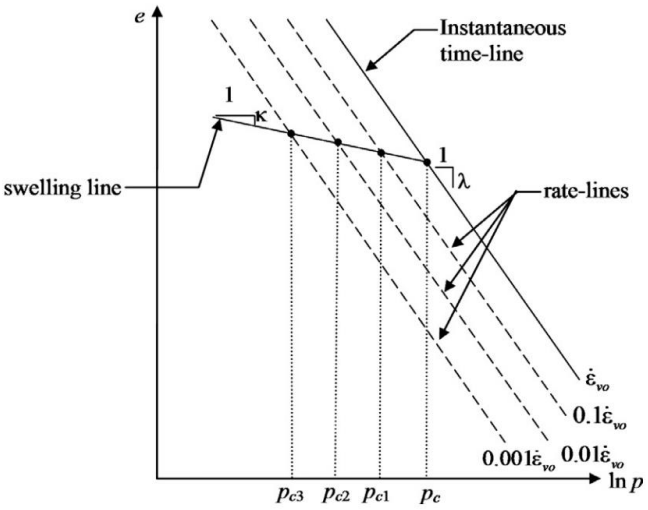

Fig. 1.47. The isotach concept (De Gennaro and Pereira, 2013)

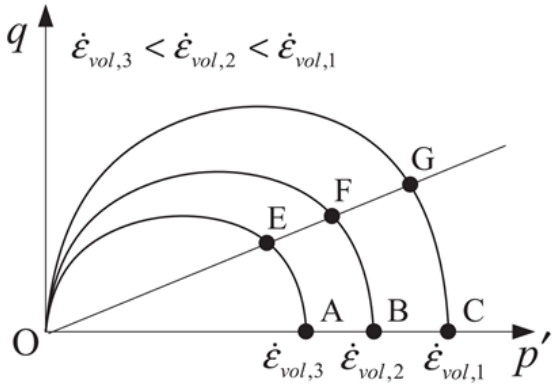

Fig. 1.48. Schematic illustration in p'-q plane (after Qiao, et al., 2016).

$$F = F\left(\boldsymbol{\sigma}, \alpha_m, \varepsilon_{ij}^{vp}, \dot{\varepsilon}_{ij}^{vp}\right) \tag{1-11}$$

where $\boldsymbol{\sigma}$ denotes the effective stress tensor; α_m is the vector of nonhardening parameters; ε_{ij}^{vp} and $\dot{\varepsilon}_{ij}^{vp}$ are the vector of time-dependent hardening parameters.

The corresponding viscoplastic strain can be calculated by Eq. 1-12:

$$\mathrm{d}\varepsilon_{ij}^{vp} = \lambda \frac{\partial g}{\sigma'_{ij}} \tag{1-12}$$

where λ is a non-negative viscoplastic multiplier and g is the viscoplastic potential. Experimental results have demonstrated that the visco-plastic strain evolves in an identical manner during both the creep process and the loading process, implying that the visco-plastic potential remains the same form regardless of loading (Sekiguch, 1985; Walker, 1985).

Incorporating the maximum strain rate concept, the loading criteria can be expressed as follows:

$$F_I(\boldsymbol{\sigma},\ \alpha_m, \varepsilon_v^{vp},\ \dot{\varepsilon}_v^{vp}) = 0 \quad \text{with} \quad \mathrm{d}F_I > 0 \qquad \text{Loading} \qquad (1\text{-}13a)$$

$$F_I(\boldsymbol{\sigma},\ \alpha_m, \varepsilon_v^{vp},\ \dot{\varepsilon}_v^{vp}) = 0 \quad \text{with} \quad \mathrm{d}F_I = 0 \qquad \text{Neutral loading} \qquad (1\text{-}13b)$$

$$F_I(\boldsymbol{\sigma},\ \alpha_m, \varepsilon_v^{vp},\ \dot{\varepsilon}_v^{vp}) = 0 \quad \text{with} \quad \mathrm{d}F_I < 0 \qquad \text{Unloading} \qquad (1\text{-}13c)$$

The flow yield surface varies with stress, visco-plastic volumetric strain and visco-plastic volumetric strain rate, indicating that the loading criterion is also related to these factors.

1.5.2 EVP model for unsaturated soils

To date, few EVP models have been developed to describe the time-dependent behaviour of unsaturated soils. Gennaro and Pereira (2013) proposed a visco-plastic constitutive model for unsaturated geomaterials by extending the isotach approach to partially saturated states. Mac et al. (2013) formulated a model within the framework of visco-plastic consistency and the bounding surface plasticity model. The model provides a continuous transition from rate-independent plasticity to rate-dependent visco-plasticity.

In Gennaro and Pereira's model, the Barcelona Basic Model (BBM) developed by Alonso et al., (1990) was employed and extended by using a relatively simple method to reflect the effects of time and suction. Two independent stress variables are adopted to describe the mechanical behaviour of unsaturated soils, net stress p_{net} and suction s. The following formula was adopted to model the relationship between the yield stress $p_y'$and the strain rate $\dot{\varepsilon}_v$ (Ladd, 1971; Leroueil, 2006):

$$\log p_y' = A + \alpha \log \dot{\varepsilon}_v \qquad (1\text{-}14)$$

$$\alpha = C_{\alpha e}/C_c \qquad (1\text{-}15)$$

where A and α are materials constants; $C_{\alpha e}$ and C_c are the secondary consolidation coefficient and the compressibility index, respectively.

Considering the effect of suction on yield stress p_y' and α, a linear dependence between α and suction s was formulated (Eq. 1-16), which can be identified based the experimental data presented in Fig. 1.49.

$$\alpha(s) = \alpha(0) - bs \qquad (1\text{-}16)$$

where $\alpha(0)$ is the slope of the linear yield stress–strain rate relationship for saturated soils in log–log space and b is a forth additional constitutive parameter describing the rate of change of α with suction.

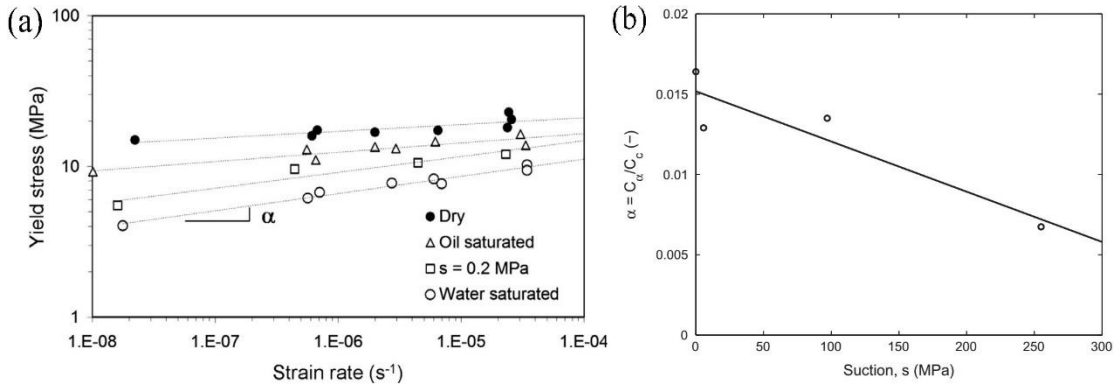

Fig. 1.49. Constant Rate of Strain (CRS) tests (Gennaro and Pereira, 2013): (a) evolution of yield stress with strain rate of Lixhe chalk (data from Priol et al., 2007); (b) evolution of α with suction for rockfill (data from Oldecop and Alonso, 2007).

By incorporating the hardening variable ε_v^{vp} and the volumetric strain rate $\dot{\varepsilon}_v^{vp}$, the expression of yield function and plastic potential G can be obtained, as in BBM:

$$F = q^2 + M^2(p + p_s)\left\{p - p_c\left[\frac{p_{r0}^{ref}}{p_c}\left(\frac{\dot{\varepsilon}_v}{\dot{\varepsilon}_v^{ref}}\right)^{\alpha(s)}\exp\left(\frac{v}{\lambda(0)-\kappa}\varepsilon_v^p\right)\right]^{\frac{\lambda(0)-\kappa}{\lambda(s)-\kappa}}\right\} \tag{1-17}$$

$$G = \alpha q^2 + M^2(p + p_s)\left\{p - p_c\left[\frac{p_{r0}^{ref}}{p_c}\left(\frac{\dot{\varepsilon}_v}{\dot{\varepsilon}_v^{ref}}\right)^{\alpha(s)}\exp\left(\frac{v}{\lambda(0)-\kappa}\varepsilon_v^p\right)\right]^{\frac{\lambda(0)-\kappa}{\lambda(s)-\kappa}}\right\} \tag{1-18}$$

The visco-plastic model developed by Mac et al. (2013) is based on the bounding surface plasticity, as reported by Khalili et al. (2005) and Russell and Khalili (2006). The rate-dependent bounding and loading surfaces are defined to establish a continuous transition from rate-independent plasticity to rate-dependent visco-plasticity. Unlike the overstress-based models, the model proposed can meet the consistency condition. The effective stress approach proposed by Khalili and Khabbaz (1998) and Khalili et al. (2004) for unsaturated soils was adopted in the model. The suction hardening effect was taken into account using the coupled influence approach where suction has a multiplicative effect on the visco-plastic volumetric hardening (Khalili et al., 2008).

The bounding surface and loading surface adopted in the formulation was described by Khalili et al. (2005), as follows:

$$F\left(\bar{p}', \bar{q}, \bar{p}'_c\right) = \left(\frac{\bar{q}}{M_{cs}\bar{p}'}\right)^N - \frac{\ln(\bar{p}'_c/\bar{p}')}{\ln R} \tag{1-19}$$

$$f\left(p', q, p'_c\right) = \left(\frac{q}{M_{cs}p'}\right)^N - \frac{\ln(p'_c/p')}{\ln R} \tag{1-20}$$

where the superimposed bar denotes the stress conditions on the bounding surface; parameter $\bar{p}'_c$ and p'_c control the size of *F* and *f*; the material constant *R* represents the ratio between $\bar{p}'_c$ and $\bar{p}'$ in the $p' - q$ plane; the material constant *N* controls the curvature of the surface.

The image point is defined using a mapping rule such as a straight line passing through the centre of homology and $\boldsymbol{\sigma}'$ intersects the bounding surface at $\bar{\boldsymbol{\sigma}}'$ having the same unit normal vector as $\boldsymbol{\sigma}'$ on the loading surface (Fig. 1.50). The unit normal vector at the image point defining the direction of loading is given by:

$$\mathbf{n} = \frac{\partial f/\partial \boldsymbol{\sigma}'}{\|\partial f/\partial \boldsymbol{\sigma}'\|} = \frac{\partial F/\partial \bar{\boldsymbol{\sigma}}'}{\|\partial F/\partial \bar{\boldsymbol{\sigma}}'\|} \tag{1-21}$$

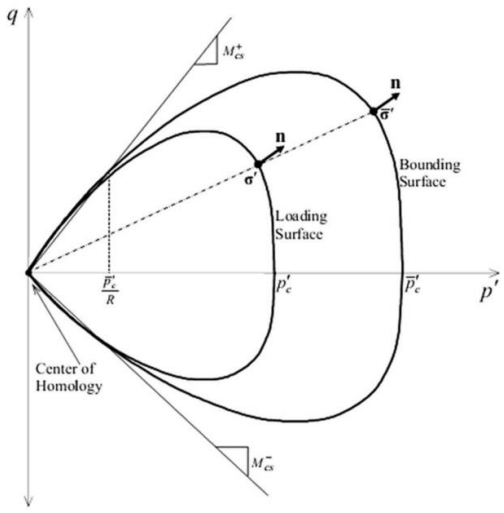

Fig. 1.50. Bounding surface, loading surface and image point (Mac et al., 2017).

The visco-plastic potential defines the direction of visco-plastic strain increments. A plastic potential is generally expressed using a plastic flow rule relating the plastic dilatancy *d* to the stress ratio $\eta = q/p'$. In the current formulation, the potential functions are given by:

$$g(p', q, p_0) = \bar{\bar{t}}\left[q + M_{cs}p' \ln\left(\frac{p'}{p_0}\right)\right] \text{ for } A = 1 \tag{1-22}$$

$$g(p', q, p_0) = \bar{\bar{t}}\left[q + \frac{AM_{cs}p'}{A-1}\left(\left(\frac{p'}{p_0}\right)^{A-1} - 1\right)\right] \text{ for } A \neq 1 \tag{1-23}$$

where *A* is a material parameter depending on the amount of energy dissipation; $\bar{\bar{t}}$ is a parameter describing the dilatancy.

1.5.3 Visco-plastic damage model for unsaturated soils

As discussed before, COx claystone can exhibit significant irreversible damage properties under the effects of stress and suction. Thus, it appears important to take the damage behaviour into account in the visco-plastic modelling.

For the unsaturated stiff soils/soft rocks, Bui et al. (2016, 2017) and Bian et al. (2017) proposed different constitutive models to reproduce the time-dependent behaviour. The model proposed by Bui et al. (2016, 2017) is based on the framework of mixture theory for multiphase porous media (Coussy, 2004), with consideration of continuum damage and Perzyna's visco-plasticity theory (Perzyna, 1966). In the hydro-mechanical modelling, the strain is often decomposed into two parts: an elastic and a plastic part (Collins and Houlsby, 1997). The total strain tensor $\boldsymbol{\varepsilon}$ and total porosity variation $\Delta\phi$ are decomposed into an elastic $\boldsymbol{\varepsilon}^{\boldsymbol{e}}$ and a viscoplastic part $\boldsymbol{\varepsilon}^{\boldsymbol{vp}}$:

$$\boldsymbol{\varepsilon} = \boldsymbol{\varepsilon}^{\boldsymbol{e}} + \boldsymbol{\varepsilon}^{\boldsymbol{vp}} \tag{1-24}$$

$$\Delta\phi = \phi - \phi_0 = \Delta\phi^e + \Delta\phi^{vp} \tag{1-25}$$

where ϕ and ϕ_0 stand for the current and initial total porosities, respectively.

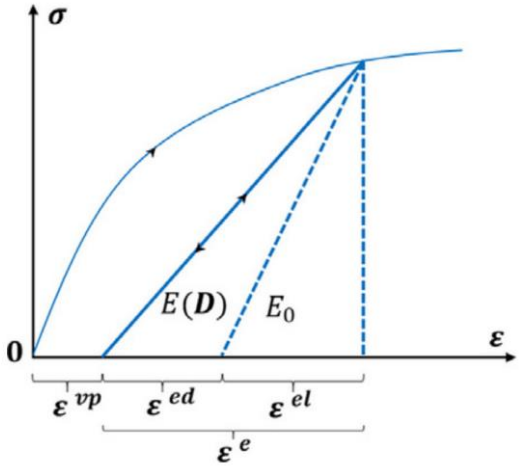

Fig. 1.51. Strain decomposition (Bui et al., 2017)

To consider the damage effect on the elastic properties presented in Fig. 1.51, $K(D)$ and $G(D)$ need to be determined. The bulk and shear moduli of damaged media are assumed to hold the following simplified expressions:

$$K(D) = K_0(1-D); G(D) = G_0(1-D) \tag{1-26}$$

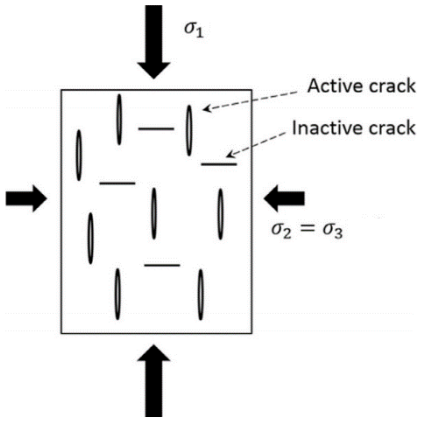

Fig. 1.52. Representation of the damage state under triaxial conditions (after Bui et al., 2017).

To consider the elastic damage in the model, the damage behaviour needs to be specified. Inspired by Lemaitre's model (Lemaitre, 1994), the damage behaviour is described as follows:

$$\dot{D} = \frac{1}{K_d}\left\langle\frac{F_d(\boldsymbol{\sigma'})}{\sigma_r}\right\rangle^{k_1}(1-D)^{-k_2} \tag{1-27}$$

where $F_d(\boldsymbol{\sigma'})$ is a damage-criterion function representing the effect of stress state on the damage evolution and delimits the domain where damage is deactivated; K_d, k_1 and k_2 are material parameters.

In the unsaturated case, apart from the above parameters, water retention parameters are needed to compute the equivalent pressure. For instance, the widespread van Genuchten's (VG) model (van Genuchten, 1980) can be employed:

$$S_r = \left(\frac{1}{1+(\alpha s)^n}\right)^m \tag{1-28}$$

where a ($a > 1$) is a material parameter, and α, n and m are model parameters.

Then, combining the following yield function, the visco-plastic strain rate can be determined as follows:

$$F_{vp}(\boldsymbol{\sigma'}) = q + \eta_{vp}\sigma' \tag{1-29}$$

$$\mathrm{d}\varepsilon^{vp} = \frac{1}{K}\left\langle\frac{q+\eta_{vp}\sigma'}{\sigma_r}\right\rangle^N \frac{\gamma_{vp}^{-M}}{1-D}\left(\frac{3\boldsymbol{s}}{2q} + \frac{1}{3}\eta_{vp}\delta\right) \tag{1-30}$$

where η_{vp} is a model parameter quantifying the pressure-sensitivity of the creep behaviour; K, M and N are model's parameters.

The above model emphasized the validity of the effective stress concept in plasticity (more details in Zhou et al., 2008), from partially saturated to fully saturated media, based on the

thermodynamic condition. Furthermore, the continuous transition between saturated and unsaturated states represents a major advantage for the visco-plastic modelling.

Similarly, Bian et al. (2017) developed a coupled elastoplastic and visco-plastic damage model for describing the delayed behaviour of hard clay during the underground gallery excavation process. However, it is worth noting that, unlike in Bui et al. (2016), the total strain is divided into three parts:

$$\mathrm{d}\varepsilon = \mathrm{d}\varepsilon^{e} + \mathrm{d}\varepsilon^{p} + \mathrm{d}\varepsilon^{vp} \tag{1-31}$$

where $\mathrm{d}\varepsilon^{p}$ and $\mathrm{d}\varepsilon^{v}$ are the plastic and visco-plastic strain increments, respectively.

The unsaturated behaviour is described using the extended Biot's theory (Biot, 1955, 1973; Bishop & Blight, 1963; Coussy, 2004; Jia et al., 2007). Unlike the models using two independent variables (Fredlund and Rahardjo, 1993 and Alonso et al., 1990), this model uses the equivalent pore pressure to represent the effect of liquid pressure and its dependency on water saturation degree. The equivalent pore pressure is expressed in Eq. 1-32. The function represents the isothermal water retention curve (Jia et al., 2007; Zhou et al., 2007; Bian et al., 2017).

$$\mathrm{d}\pi = \mathrm{d}p_{gz} - S_{lq}(p_{cp})\,\mathrm{d}p_{cp} \tag{1-32}$$

where π is pore pressure; $S_{lq}(p_{cp})$ represents the isothermal water retention curve; p_{gz} is pore air pressure; p_{cp} is the capillary pressure.

For the modelling of damage behaviour, a coupled damage equation is adopted:

$$\mathrm{d}\underline{\underline{\sigma}} = \underline{\underline{\underline{\underline{c}}}}(\omega) : (\mathrm{d}\underline{\underline{\varepsilon}} - \mathrm{d}\underline{\underline{\varepsilon}}^{p} - b d\pi \underline{\underline{\delta}}) \tag{1-33}$$

where b is Biot coefficient; $\underline{\underline{\delta}}$ represents the second order unit tensor; the fourth order tensor $\underline{\underline{\underline{\underline{c}}}}(\omega)$ represents the damaged elastic matrix. The isotropic damage characterized by a scalar variable ω is adopted in the model.

Due to the different failure modes, the damage variable is decomposed into two parts: ω_c for the compressive damage and ω_t for the tensile one. From the damage model proposed by Mazars (1984), the evolutions of tensile damage and compressive damage are determined, respectively. The global damage variable is defined as:

$$\omega = (1 - \alpha_t)\omega_c + \alpha_t \omega_t;\ \alpha_t = \frac{\left\|\underline{\underline{\sigma^{+}}}\right\|}{\left\|\underline{\underline{\sigma}}\right\|} \tag{1-34}$$

$$f_\omega^t = \omega_t - \left(1 - \frac{1}{\exp(B_t Y_\omega^t)}\right) = 0 \tag{1-35}$$

$$f_\omega^c = \omega_c - \left(1 - \frac{1}{\exp(B_c Y_\omega^c)}\right) = 0 \tag{1-36}$$

where the coefficient α_t controls the contribution of tensile and compressive damage to total damage; $\underline{\sigma}^+$ is the positive part of stress tensor; Y_ω^t and Y_ω^c are two different driving forces, respectively; parameter B_c and B_t control the kinetic of compressive and tensile damage and can be determined using uniaxial compression test.

On the other hand, accounting for the damage effect, the plastic and visco-plastic yield surfaces are shown in Fig. 1.53. Based on the plastic and visco-plastic characterizations, the plastic yield function, plastic flow rule, visco-plastic yield function and visco-plastic flow rule used are as follows.

$$F_p = q - g(\theta)\alpha(\gamma^p)\left(-c_1 + \sqrt{c_1^2 + 4c_2\left(c_3 - \frac{p}{f_c(\omega)}\right)}\right)\frac{f_c(\omega)}{2c_2} = 0 \tag{1-37}$$

$$Q_p = q - \eta g(\theta)\alpha(\gamma^p)\left(-p + c_3 f_c(\omega)\right)\ln\left(\frac{-p + c_3 f_c(\omega)}{I_0}\right) = 0 \tag{1-38}$$

$$F_{vp} = q - g(\theta)\alpha_{vp}(\gamma^p)\left(-c_1 + \sqrt{c_1^2 + 4c_2\left(c_3 - \frac{p}{f_c(\omega)}\right)}\right)\frac{f_c(\omega)}{2c_2} = 0 \tag{1-39}$$

$$Q_{vp} = q - \eta g(\theta)\alpha(\gamma^p)\left(-p + c_3 f_c(\omega)\right)\ln\left(\frac{-p + c_3 f_c(\omega)}{I_0}\right) = 0 \tag{1-40}$$

where the three constants c_1, c_2 and c_3 define the curvature of yield surface; the variable I_0 geometrically defines the intersection of the plastic potential; the variable $g(\theta)$ as a function of Lode's angle is integrated for taking the influence of loading path into account; $f_c(\omega)$ represents the uniaxial compression strength.

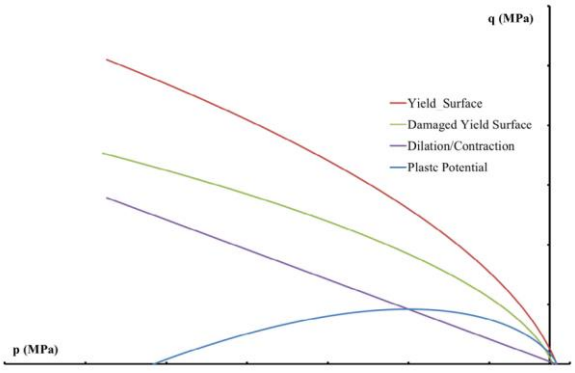

Fig. 1.53. Illustration of the yield surface, the damaged yield surface and the plastic potential (Bian et al., 2017).

This model can describe the main features of the hard clay/soft rock observed in laboratory and in-situ experimental investigation, including the plastic deformation, the visco-plastic deformation and the damage under unsaturated stress state.

1.6 Conclusions

In this chapter, the Meuse\Haute-Marne site and the main hydro-mechanical behaviour of COx claystone observed essentially from the laboratory tests on sample were described, and the visco-plastic modelling of soils was reviewed, with consideration of the effects of unsaturation and damage. The following conclusions can be drawn:

The basic information about the Meuse\Haute-Marne site was presented, including the location of the site, excavation of MHM URL and fractures induced. The in situ investigations and measurements on fracture networks in the fractured zone show that there are different shapes of the fractured zone around drifts along the major and minor horizontal stress directions. In addition, there are two types of fractures: extensional and shear fractures. The measurement on hydraulic conductivity around the drift demonstrated that the damage in the fractured zone induced significant change of hydraulic behaviour.

The mineral composition and microstructure can significantly affect the hydro-mechanical behaviours of COx claystone. The swelling of COx claystone can change its microstructure and the swelling potential is dependent on the content of clay minerals. The swelling/shrinkage of COx claystone due to wetting/drying resulted in damage characterized by cracking. The cracks can be closed under loading, especially at saturated state.

Mechanical loading can also result in the damage of COx claystone. The increasing of water content and temperature can make COx claystone more ductile, presenting thus a more deformable property. The anisotropic properties of COx claystone were characterized in terms of Young's modulus, Poisson ratio and peak strength. There is an orientation to bedding, at which the peak strength reaches the minimum. The plastic deformation due to mechanical loading can induce the crack of coarse grains inside COx claystone at a microscale, thus further results in the macro damage.

To date, there are mainly two kinds of visco-plastic theories, over-stress and non-stationary flow surface. Based on these theories, a large number of EVP constitutive models were developed for saturated soils. By contrast, the modelling of the visco-plastic behaviour of unsaturated soils is relatively limited. It is more difficult to model their time-dependent behaviour due to the difficulty of the selection of stress variables and the complexity of suction

effect on mechanical parameters. Further, considering the effect of damage in unsaturated EVP modelling, the damage evolution law used is usually built based on mathematics and cannot give a clear physical meaning in terms of crack/fracture inside the damaged media. These aspects will be considered in the modelling of time-dependent behaviour of unsaturated COx claystone with consideration of damaged effect.

Chapter 2. Materials and experimental techniques

In this chapter, the basic properties of COx claystone and the chemical composition of synthetic water used are first presented. Then, the experimental devices adopted for investigating the damage, compression, swelling, microstructure and rate-dependent behaviours are depicted. Afterwards, the techniques of microstructure observation using mercury intrusion porosimetry and µ-tomography as well as the techniques used for suction measurement and suction control are presented. Finally, the test programs for triaxial and oedometer tests are described. In triaxial cell, only intact samples are involved. The main objective of triaxial tests is to develop a relevant method for damaged sample preparation. In oedometer, intact, artificially fractured and damaged samples are tested. Moreover, suction controlled compression and constant rate compression are depicted.

2.1 Materials tested

As indicated in chapter 1, Callovo-Oxfordien (COx) claystone cores were drilled from the underground research laboratory. The COx claystone cores used in this study were extracted by bore drilling from the depth around 490 m. The cores were covered by membrane and conserved in a fully confined cell (T1) with axial steel spring and radial mortar filling, preventing water loss and soil rebounding, as shown in Fig 2.1. The axial stress applied by the steel spring can reach 0.6 MPa (Conil et al., 2018).

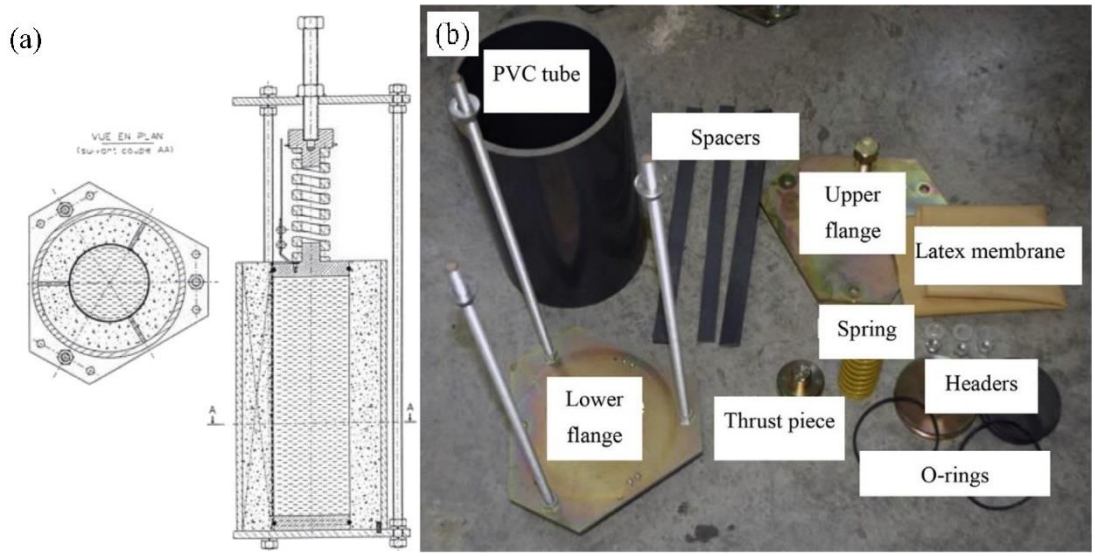

Fig. 2.1. T1 cell used for COx claystone: (a) Schematic representation; (b) The components (Conil et al., 2018)

In this study, all cores in T1 cells have each a diameter of 80 mm or 120mm and a length of 300 mm. The basic information of the studied cores is shown in Table 2.1. The sampling locations of all cores are also given in detail. In the laboratory, the T1 cells were opened with wrench and cutting equipment. As an example, core ID: EST58107 is shown in Fig. 2.2.

When the core was drilled in the MHM URL, the direction of bedding plane was marked, as shown in Figs. 2.2b and c. As indicated in section 1.4.3, anisotropy plays an important role in the mechanical behaviour of COx claystone. It is thus important to pay particular attention to the bedding plane while preparing the soil samples.

Table 2.1 COx claystone cores used in this study

Core ID	Date of sampling	Date of opening	Diameter (mm)	Length (mm)	Location
EST57180	17/10/2017	04/02/2018	80	300	OHZ1601 17.90 m-18.20 m
EST57178	17/10/2017	26/03/2018	80	300	OHZ1601 17.20 m-17.50 m
EST57914	10/04/2018	23/05/2018	120	300	OHZ3006 17.39 m-17.69 m
EST57911	10/04/2018	25/09/2018	120	300	OHZ3006 16.56 m-16.86 m
EST58107	10/06/2018	18/03/2019	80	300	OHZ3107 9.05 m-9.35 m

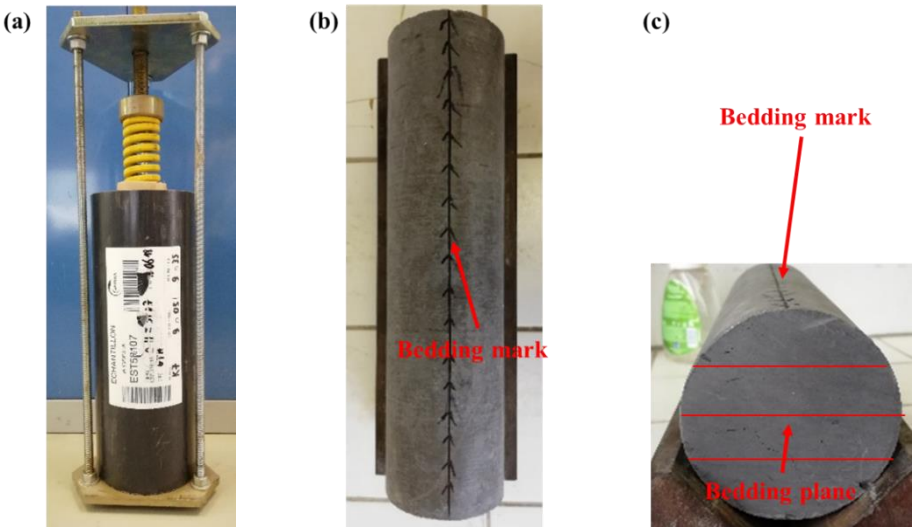

Fig. 2.2. The opening process of COx claystone: (a) T1 cell before opening; (b) the core after opening; (c) the end section of the core

A simple method is adopted to verify the bedding plane direction. After the T1 cell was opened, a small piece of COx disk was taken using a sawing machine (Fig. 2.3) and then soaked into water for one hour. According to the direction of cracks, the bedding plane was identified. When the cracking direction is parallel to the bedding mark, the initial bedding mark is judged to be good. Otherwise, the cracking direction is regarded as the real bedding plane. This determination method is described in Fig. 2.4. Results show that the initial bedding marks of all the cores used in this study correctly represent the real bedding direction.

Fig. 2.3. The sawing machine with a core installed: far view (left) and near view (right)

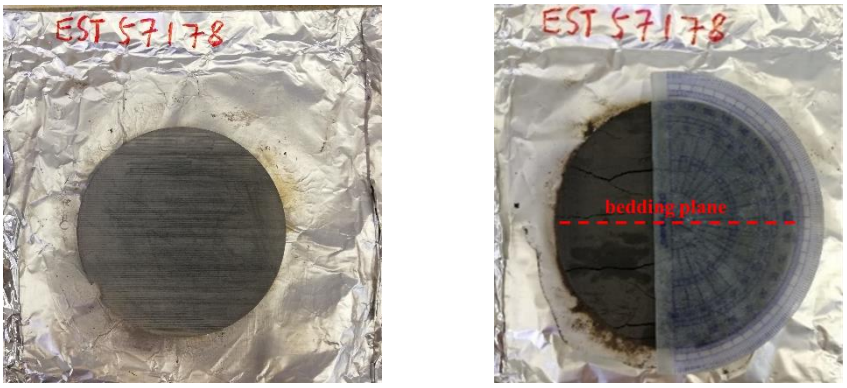

Fig. 2.4. Determination of bedding plane: before soaking (left) and after soaking (right).

COx claystone has a specific gravity of 2.7 (Wang et al., 2012; Zhang et al,.2015). Its mineralogy is mainly composed of clay minerals, carbonate and quartz, as indicated in section 1.2. The clay content varies over depths and locations. After the T1 cell was opened, the basic physical parameters of COx claystone cores were measured immediately, minimizing the effect

of dehydration. The physical properties of COx claystone were determined in the laboratory and are shown in Table 2.2.

Table 2.2 Physical properties of COx claystone cores

Core ID	Density (g/cm^3)	Dry density (g/cm^3)	Porosity (%)	Water content (%)	Suction (MPa)	Saturation degree (%)
EST57178	2.39	2.22	17.7	7.86	16.37	98.6
EST57180	2.40	2.22	17.8	7.83	19.98	97.7
EST57914	2.43	2.27	15.7	6.76	18.87	98.2
EST57911	2.43	2.28	15.4	6.56	24.23	97.6
EST58107	2.40	2.21	17.9	8.06	20.33	99.3
Zhang et al. (2019)	2.40-2.45	2.22-2.28	15.2-17.8	6.50-7.50	-	-

The initial suction was measured by the dew point PotentialMeter (WP4) described in section 2.2. In addition, to investigate the swelling behaviour, synthetic water was adopted, which has the same chemical composition as the site water (Table 2.3).

Table 2.3 Chemical composition of the synthetic water from ANDRA

Components	NaCl	$NaHCO_3$	KCl	$CaSO_4 \cdot 2H_2O$	$MgSO_4 \cdot 7H_2O$	$CaCl_2 \cdot 2H_2O$	Na_2SO_4
Mass (g/L)	0.130	2.216	1.950	0.035	1.082	1.356	0.053

2.2 Experimental techniques

2.2.1 High pressure oedometer

The high pressure oedometer employed has a dual level loading system (in Fig. 2.5), allowing a maximum vertical stress up to 113 MPa (Menaceur, 2014) for a sample with a diameter of 38 mm. It was initially manufactured for investigating the volume change behaviour of engineered barriers materials under dozens of MPa (Marcial et al., 2002). The vertical

displacement is measured by a transducer with an accuracy of 1 μm. The detailed description of the oedometer cell is presented in Fig. 2.6. There are three parts: piston, cell wall and base. There are two valves on the base to control the injecting and discharge of water or vapor.

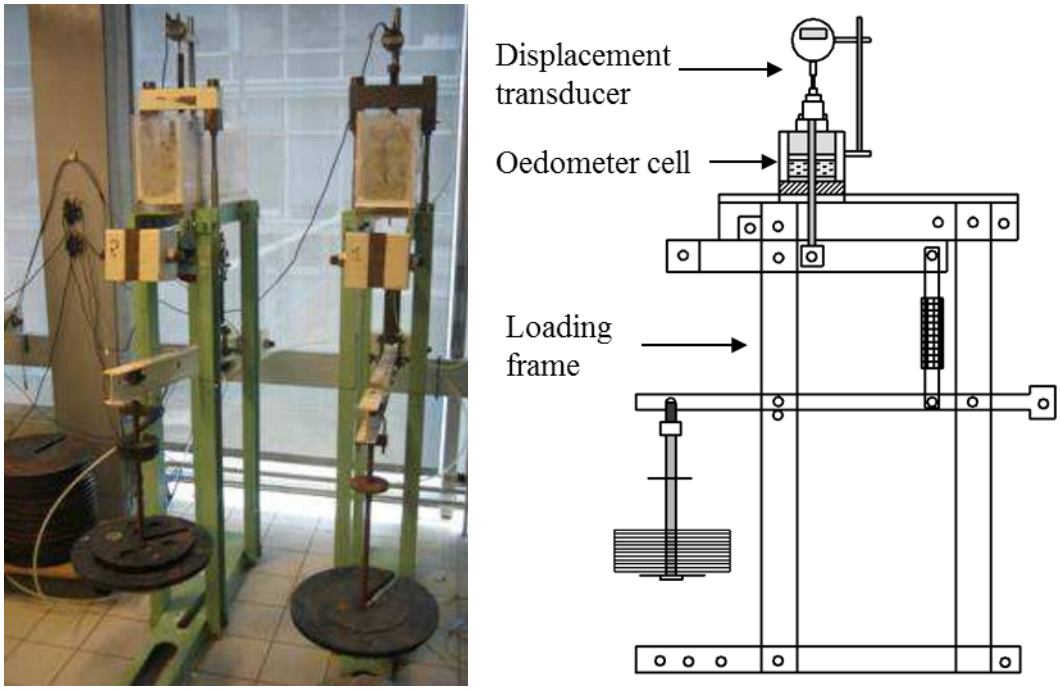

Fig. 2.5. High pressure oedometer: photography (left); schematic (right)

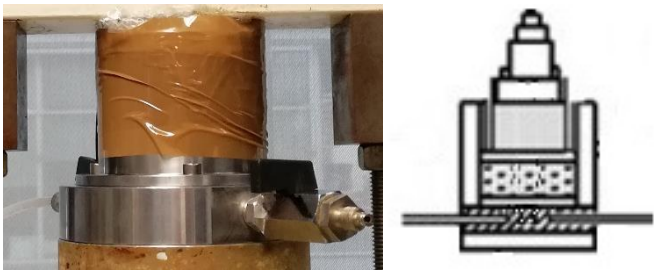

Fig. 2.6. Oedometer cell: photography (left); schematic (right)

In this study, high pressure oedometer tests were carried out on fractured and damaged samples for investigating the swelling and compression behaviours of COx claystone. It was also adopted to study the swelling and compressibility of intact COx claystone by Mohajerani (2011) and Menaceur (2014).

For running a test, the sample was first placed in the cell with two metallic porous disks at the top and bottom. Prior to sample installation, some grease was applied on the inner wall of the oedometer ring to reduce the friction between the wall and the sample. Then, an initial small vertical stress was applied to keep a good contact between the sample and the piston. Both the swelling step and the compression step were followed.

- Firstly, the synthetic water (in case of saturated condition) or vapor with a given relative humidity (in case of suction controlled condition) was injected from the bottom until the vertical displacement stabilized based on a stabilisation criterion.
- Then, the vertical stress was loaded in steps. Each stress is the double of the previous one.

Besides, under saturated condition, the hydraulic conductivity under each stress level was measured using a pressure-volume controller shown in Fig.2.7. After the vertical deformation stabilizes under each stress, a pressure is applied using the pressure-volume controller (CPV) to inject the synthetic water from the bottom. To avoid corrosion of the CPV by the synthetic water, a solution converter is used, as shown in Fig 2.8. The inlet and outlet are connected to the CPV and the oedometer cell, respectively. The hydraulic conductivity (k_{test}) is calculated based on the Darcy's law using the following formula Eq. (2.1):

$$k_{test} = \frac{\Delta V}{S\Delta t} / \frac{P_{GDS}}{\rho_w g H} \tag{2.1}$$

where ΔV is the volume change recorded by CPV at the time interval Δt. S and H are the sectional area and height of oedometer sample, respectivly. P_{GDS} is the water pressure applied by CPV. ρ_w and g are the density of pure water and the acceleration of gravity, respectively.

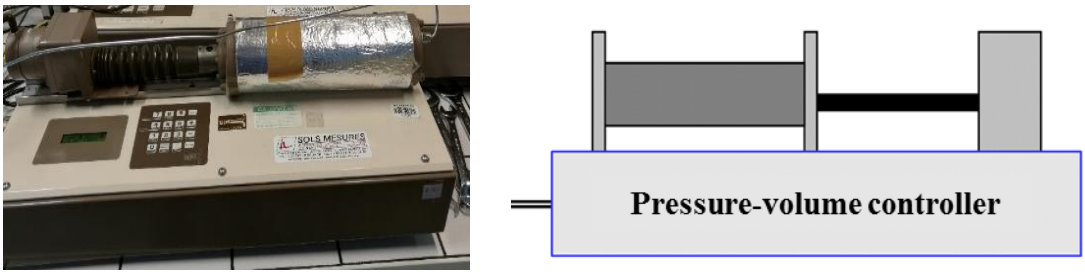

Fig. 2.7. Pressure-volume controller: photography (left); schematic (right)

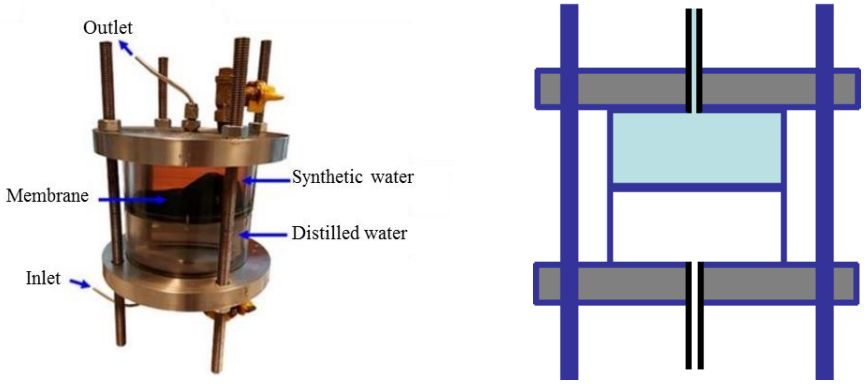

Fig. 2.8. Solution converter: photography (left); schematic (right)

2.2.2 Triaxial device

To obtain the damaged COx claystone in the laboratory for further testing in oedometer, the shear damage properties need to be investigated with traixial tests. The loading device and the triaxial cell used in this study are displayed in Fig. 2.9. The self-compensating cell has three parts: cap, side wall and base. The deviator stress is applied by a press. The axial stress can be measured by the two sensors inside and outside of the cell. The press used has a capacity of 100 kN, corresponding to a maximum stress of 88.2 MPa on a sample of 38 mm diameter. Inside the triaxial cell, temperature is recorded by a thermal sensor. Note that the cell can be heated using a heating belt to investigate the soil behaviour under varying temperatures. The pore pressure and confining pressure are applied by CPVs with the maximum stresses of 4 MPa and 64 MPa, respectively. More details about the triaxial cell can be found in Le (2008), Nguyen (2013) and Dao (2015). The axial and radial displacements are measured locally using LVDT type displacement sensors (Fig. 2.10). Four radial LVDTs and axial 2 LVDTs are used for this purpose. The accuracy of LVDT is 0.001 μm.

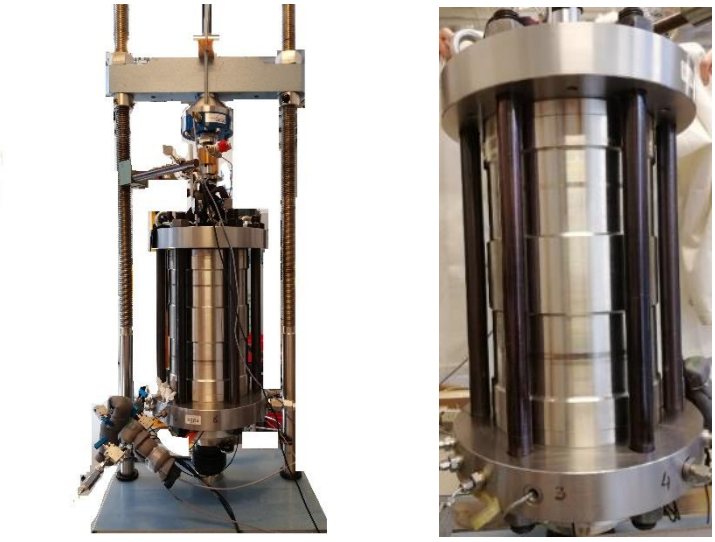

Fig. 2.9. Triaxial test device (left) and triaxial cell (right)

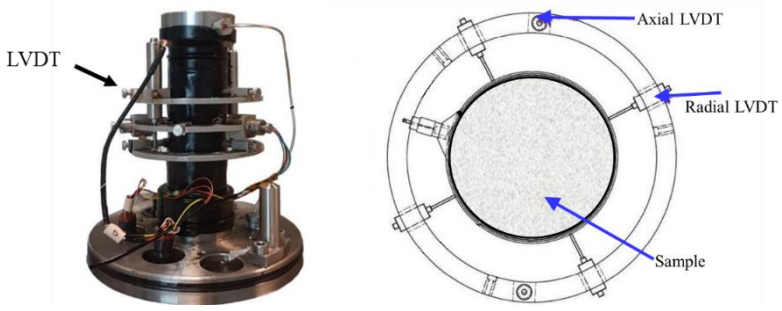

Fig. 2.10. Measurement system of local deformation: photography (left); schematic (right)

The damage behaviour of the COx claystone was investigated by triaxial test under different loading paths. Firstly, the sample was isotopically loaded to a target value of 14 MPa, which is close to the average in situ stress as reported by Armand et al. (2013, 2014) and Belmokhtar (2017). For the shear process, the related stress path is illustrated in Fig. 2.11a. The detailed loading conditions are illustrated in Fig.2.11b and Fig.2.11c:

- Path a– triaxial compression by increasing the axial stress σ_1 at constant radial stress σ_3;
- Path b– triaxial compression by keeping the mean stress $p = (\sigma_1+2\sigma_3)/3$ constant through increasing axial stress σ_1 and decreasing radial stress σ_3 simultaneously.

Several unloading-reloading cycles were applied to evaluate the elastic parameters during unloading. The loading direction is perpendicular to the bedding plane. Actually, stress path b is similar to the damage mode experienced by COx in the field during gallery excavation, as demonstrated by Liu et al. (2018).

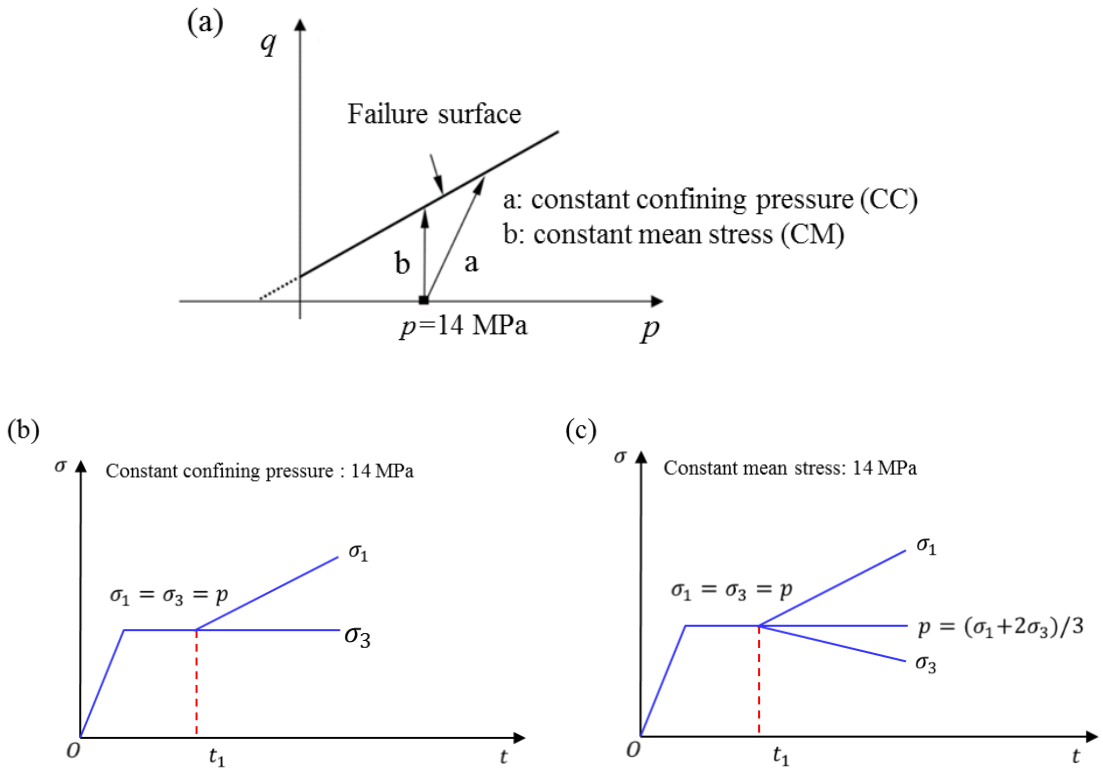

Fig.2.11. (a) stress path in p-q plane; (b) stress path under constant confining pressure stress; (c) stress path under constant mean stress

2.2.3 Microstructure observations

The microstructure investigation on COx claystone aims at analyzing the pore size distributions (PSD) after hydraulic and mechanical loadings, and further quantifying the micro cracks induced by damage. Two experimental techniques, μ-computed Tomography and mercury intrusion porosimeter (MIP), are adopted for this purpose.

Mercury Intrusion Porosimetry

Mercury intrusion porosimeter is based on the measurement of the volume of mercury penetrated into the pores of a material under a mercury intrusion pressure. With the increasing mercury intrusion pressure, mercury can fill the pores of decreasing diameter. For each pressure level, a suitable time interval is used for pores filling.

For the MIP test, a small amount of soil is taken and put into liquid nitrogen which was vacuum-cooled before (below -196 °C). Afterwards, the soil is lyophilized using the freezing dry device shown in Fig. 2.12, as suggested by Delage and Pellerin (1984). The soil is then introduced into the penetrometer which includes a sample cup bonded to a metal-clad, precision-bore, glass capillary stem (Fig. 2.13).

Fig. 2.12. The freezing-dry device

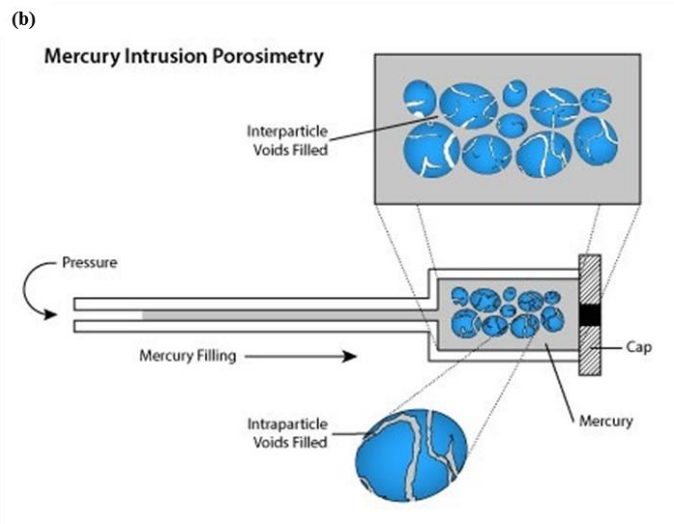

Fig. 2.13. The penetrometer: (a) photography; (b) schematic (https://www.particletechlabs.com/about/ptl-press?start=10)

An Autopore IV 9500 mercury intrusion porosimeter was used in this study, as shown in Fig. 2.14. There are two intrusion systems: one low-pressure (33,000 psia maximum pressure) and one high-pressure analysis ports, which can provide the intrusion pressures from 0.0035 MPa to 227.5 MPa.

Fig. 2.14. Mercury intrusion porosimetry device

With the adopted porosimeter, the detectable pore diameters are between 360 μm and 0.006 μm based on Laplace's law:

$$p = \frac{4\sigma \cos\theta}{d} \tag{2.2}$$

where d is the coresponding pore diameter, σ is the surface tension of mercury (0.485 N/m), θ is the contact angle (130°), p is the mercury pressure.

The volume of intruded mercury can be recorded under the corresponding pressure. Then, by summing up the volume step by step, the cumulative curve can be acquired. Similarly, the pore size distribution density function can be determined. Generally, to plot the cumulative curve and pore size distribution density curve, the logarithm of the corresponding pore diameter is adopted.

The main limitations of MIP tests are as follows:

- Enclosed pores: the isolated pores are surrounded by the aggregated solid particles. They cannot be intruded by mercury (Romero and Simms 2008).
- Constricted pores: the pores can be accessed through the smaller ones. Thus, they cannot be intruded at the corresponding intruded mercury pressure but the pressure corresponding to the smaller pores.
- Non-intruded pores: the pores with the diameter smaller than that corresponding to the maximum intruded mercury pressure cannot be intruded because of the limited intruded pressure (Delage, 2007).
- Non-detected pores: the smectite platelets (thickness of 9.6 Å) with 1 layer of water molecule have an interlayer distance of about 12 Å (Saiyouri et al. 1998). The minimum pore detected has the diameter around 6 nm in MIP test. Thus, the intra-particle pores with the order of nanometres cannot be accessed by mercury.

The analysis of intrusion and extrusion cycles indicated that some mercury remained in the sample due to the 'throat effect'. Thereby, Romero et al. (2012) proposed that the second cycle coincides with the non-constricted or free-porosity because this part of pores without the 'throat effect' can be obtained through the second intrusion. Generally, the cylindrical pore mathematical model is adopted in MIP analysis, even though the real shapes of pores can be significantly irregular.

μ-computed Tomography

μ-computed Tomography (CT) is adopted to observe the fractures in the damaged samples. There are three main components: X-Ray source, sample with wood support and detector. Through the CT technique, the 3D images of COx claystone can be obtained. The samples are placed between the X-Ray source and the detector. Eq. (2.3) is used to describe the relation between the incident intensity I_0 and the transmitted intensity $I(x)$:

$$I(x) = I_0 \exp(-\mu x) \tag{2.3}$$

where x is the length of this material and μ is the linear attenuation coefficient of the material.

Here, the attenuation coefficient μ is related to the incident ray energy, which depends on the number of atoms in the element. Abdallah (2019) gave the chemical composition of the element in the material and their relative proportions. X-Ray attenuation is related to the grey levels which are used for reconstructing the image. It indicates the physical volume proportion of absorbed and scattered X-Rays through the material in terms of voxel.

In this study, the CT scanned samples have a diameter of 38 mm, a height of 10 mm for oedometer sample and 65 mm for triaxial sample. The CT test device, namely UltraTom microtomograph (RX-Solutions, Chavanod, France), is presented Fig. 2.15, with a voxel resolution of 24 µm for all the scanning in this study. This device is equipped with a 230KV Microfocus Hamamatsu L10801 X-Ray source and a PaxScan 2520V flat panel detector for the full resolution (Varian, Palo Alto, USA). A complete scan can be obtained by rotating the middle wood support. The sample is covered by wax during the whole scanning process, avoiding water loss by evaporation.

In addition, for scanning large samples, a copper filter with a thickness of 0.5 mm is put on the beryllium window of the source. To obtain the images with good quality, the X-ray voltage of 100 kV and a proper electron beam intensity were selected as the main parameters of source. The stack method by rotating the sample is adopted to obtain the best resolution of an image of the full sample. The source and the detector can be transformed along the vertical direction in steps. In each CT test, the top of the sample is first scanned. Thus, the source is at the face of it in the beginning. During each scanning, both the source and detector go down when a 360° rotation of the CT sample is finished. For the next scanning, the same procedure is repeated. At the end of each test, thousands of projections are obtained. To decrease the random noise of the images, the radiographies at the corresponding angle are averaged. The horizontal section images can be reconstructed by adopting the X-Act software (RX-Solutions, Chavanod, France), with the voxel size of 24 µm and the standard filtered back projection algorithm for conical projection as proposed by Feldkamp et al. (1984). The test duration depends on the size of the sample and the resolution used. In this study, the test last 8 to 28 h for different oedometer and triaxial samples.

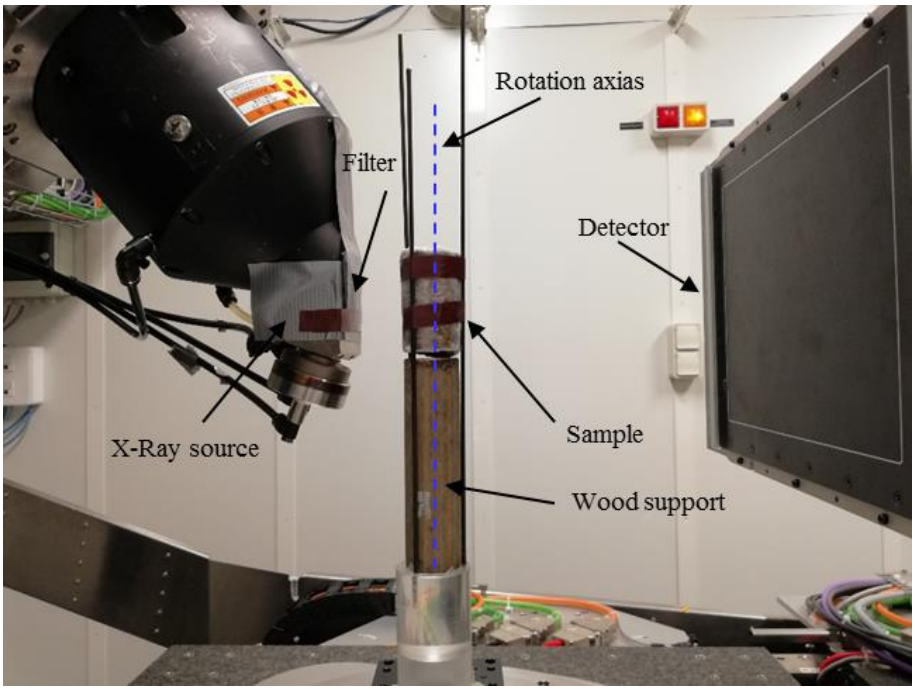

Fig. 2.15. Test equipment of μ-computed Tomography

Finally, the images are stacked with the software Fiji (https://imagej.net/Fiji), which can be used to construct the 3D image. By adjusting the images with different threshold values of grey level, the structures (e.g. pores and cracks) and mineral composition (e.g. sand grains) can be displayed. Then, by comparing the CT results before and after oedometer or triaxial tests, the crack volume can be quantified.

2.2.4 Measurement and control of suction

2.2.4.1 WP4 hygrometer technique

In this study, total suctions are measured using the dew point PotentialMeter (WP4) shown in Fig. 2.16. The WP4 consists of four parts: a dew point sensor, a fan, a sealed chamber and an infrared thermometer/temperature sensor. The fan allows acceleration of the equilibrium between vapor and soil sample. At equilibrium, the relative humidity (RH) defined in Eq. 2.4 is recorded:

$$RH = p/p_0 \tag{2.4}$$

where p is the vapour pressure of air and p_0 is the saturation vapour pressure at sample temperature.

The total suction (Ψ) can be determined based on the Kelvin's equation:

$$\Psi = \frac{RT}{M} \ln RH \tag{2.5}$$

where R is the gas constant (8.31 J/mol K), T is the Kelvin temperature of the sample, M is the molecular mass of water (M = 18 g/mol).

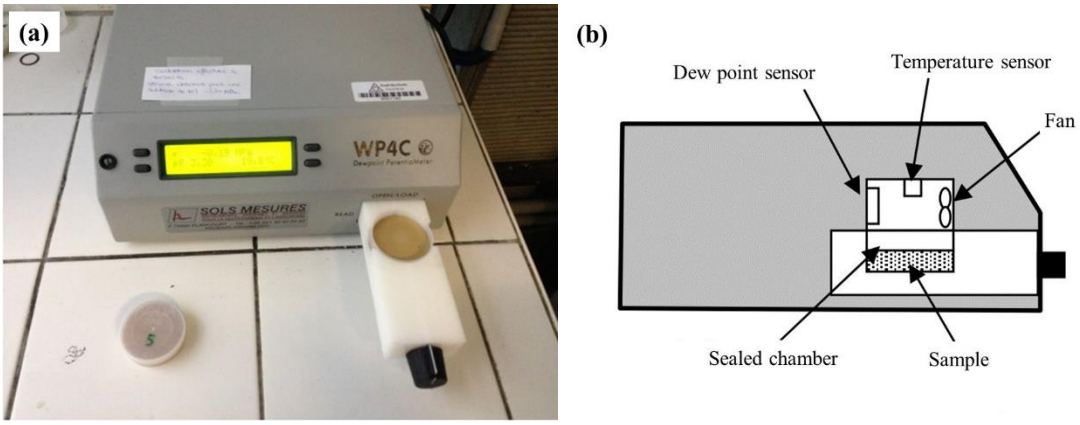

Fig. 2.16. WP4 hygrometer used in suction measurement: (a) photography (Wang, 2016); schematic (Samingan, 2005)

While running a measurement, the sample is placed in the sealed chamber. Once the vapor equilibrium is reached, the air begins to be cooled down by the chilled mirror until the temperature of dew point which is detected by the dew point sensor. At the same time, the dew point temperature and the temperature of the sample are recorded by the temperature sensor and the infrared thermometer, respectively. Based on that, p and p_0 can be determined respectively, giving the HR value.

2.2.4.2 Vapor Equilibrium Technique

The vapor equilibrium technique (VET) is adopted to control the suction of unsaturated soils in high suction range (in the order of MPa). VET has been widely used to impose suction on soils for determining the water retention curve (WRC) (Agus et al., 2001; Blatz et al.,2002; Schanz et al., 2004; Wang, 2012; Wan et al., 2013). The principle is the same as that of WP4 hygrometer technique. When the water vapor pressure reaches the target equilibrium state, the potential of water in the soil sample equals the imposed suction. VET can be adopted to control the range of total suction from several MPa to hundreds of MPa. For the lower suctions (e.g. less 4.2 MPa), the accuracy of VET is not enough, because it is more sensitive to temperature change (Agus and Schanz, 2003). It is also because of the logarithmic relationship between suction and relative humidity. The isothermal condition is important for the relative vapor pressure between

the salt solution and the air above the solution (Delage et al., 1998; Cuisinier and Masrouri, 2004). Thus, it is necessary to keep the temperature constant in the test.

In this study, two experimental setups are adopted. The first one is the desiccator shown in Fig. 2.17, which includes the saturated solutions on the bottom, a porous plate and a glass container for soil sample. The volume and mass of the sample can be measured regularly to judge whether the sample reaches the suction equilibrium. The second one is the setup shown in Fig. 2.18, which is usually adopted in oedometer test and constant-volume swelling pressure test with controlled suctions. There are four components: plastic tube for the circulation of vapor, pump for vapor circulation, a first bottle for the storage of salt solution and the second bottle for the caption of condensed water. The commonly used salt solutions and corresponding suctions are summarized in Table 2.4.

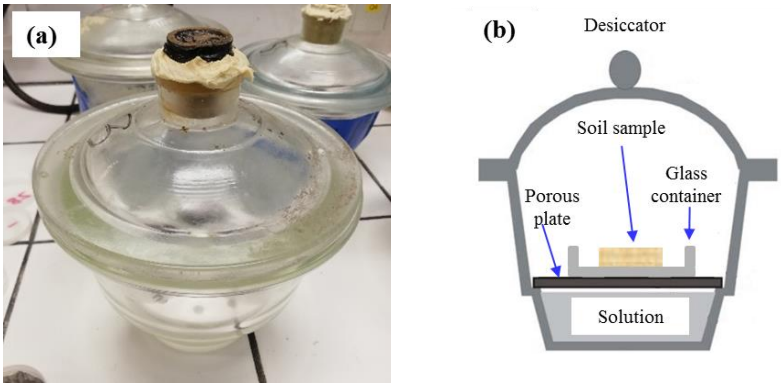

Fig. 2.17. The desiccator test setup: (a) photography; (b) schematic

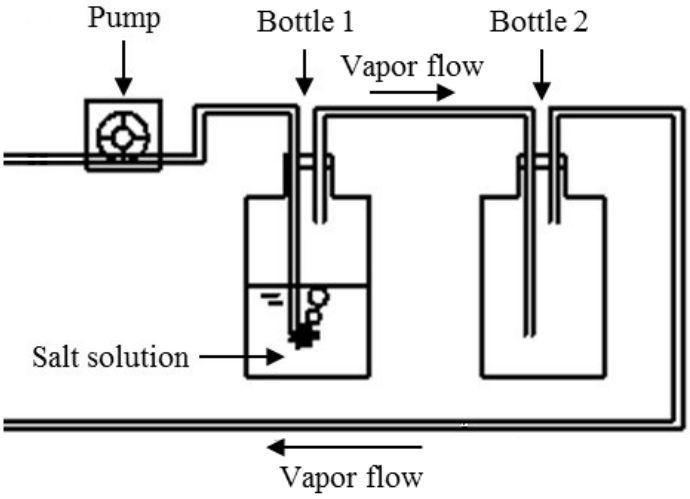

Fig. 2.18. Vapor circulation system

Table 2.4 Saturated saline solution and corresponding suctions at 20 ℃ (data from Delage et al., 1998; Wan et al., 2013; Menaceur, 2014; Guerra, 2018; Debure, 2019)

Saturated saline solution	Relative humidity (%)	Suctions (MPa)
K_2SO_4	97.0	4.2
$CuSO_4 \cdot 5H_2O$	95.7	6.1
KH_2PO_4	95.5	6.3
$Na_2HPO_4 \cdot 12H_2O$	93.7	9.0
KNO_3	93.7	9.0
$ZnSO_4 \cdot 7H_2O$	91.3	12.6
$Na_2SO_3 \cdot 7H_2O$	90.9	13.1
$(NH_4)_2SO_4$	83.5	24.9
NaCl	76.0	37.8
NH_4NO_3	67.0	59
$Mg(NO_3)_2$	55.0	82.4
K_2CO_3	64.7	113.2
$MgCl_2$	33.0	150.0
LiCl	15.0	261.5
KOH	9.0	331.0

2.2.5 Compression test at constant strain rate

The compression test at constant rate of strain (CRS) is usually conducted in oedometer. Compared to the conventional oedometer test, CRS test can obtain the mechanical parameters related to the consolidation characteristics of soils more rapidly. Besides, CRS test can also provide a continuous compression curve, allowing easier determination of mechanical parameters (Sheahan and Watters, 1997). For the selection of strain rate, it is of paramount importance to avoid excess pore water pressure (ASTM, D. 4186). In case of generation of pore water pressure, the secondary compression and consolidation properties can be also analysed by recording the variation of excess pore water pressure with time. Generally, the Casagrande's method is adopted to determine the yield stress (Casagrande, 1936). The slopes of the compression curve before and after yield stress are defined as the rebound index C_s and compression index C_c.

The rate-dependent behaviour of saturated soils has been investigated by many researchers through CRS test (Leroueil et al., 1985; Leroueil, 1996; Tatsuoka et al., 2002; Kim and Leroueil, 2001). Nevertheless, only few researchers focused on unsaturated soils (Gennaro et al., 2003; Qin et al., 2015). In this study, CRS tests with different controlled suctions were performed for the investigation of the rate-dependent compression characteristics of damaged COx claystone. The isotache approach was applied to analyse the effects of suction and strain rate on the compression indexes. The CRS testing device consists of the loading frame, a force sensor, a displacement transducer and an oedometer cell, as shown in Fig. 2.19. The force sensor has a capacity of 50 kN. The axial loading displacement rate can vary between 10^{-4} and 9 mm/min by imputting the target value through the control panel. The test includes two steps: the suction-equilibrium step and the compression step. For the unsaturated sample, the target suction was imposed through VET method (Delage et al., 1998). The saturated sample was obtained by injecting water into the sample under a small vertical stress. It will be described in section 2.3.

In addition, calibration tests were performed on the empty oedometer cell of 38 mm diameter, aiming at eliminating the effect of deformation of the cell and the loading frame on the measurement of displacement. Because the strain rate effect is investigated in the present work, two loading displacement rates were considered in the calibration tests. Fig. 2.20 shows the correlations between the displacement and the vertical stress under different loading rates. The coinciding calibration curves indicate the negligible effect of loading rate on instrument deformation.

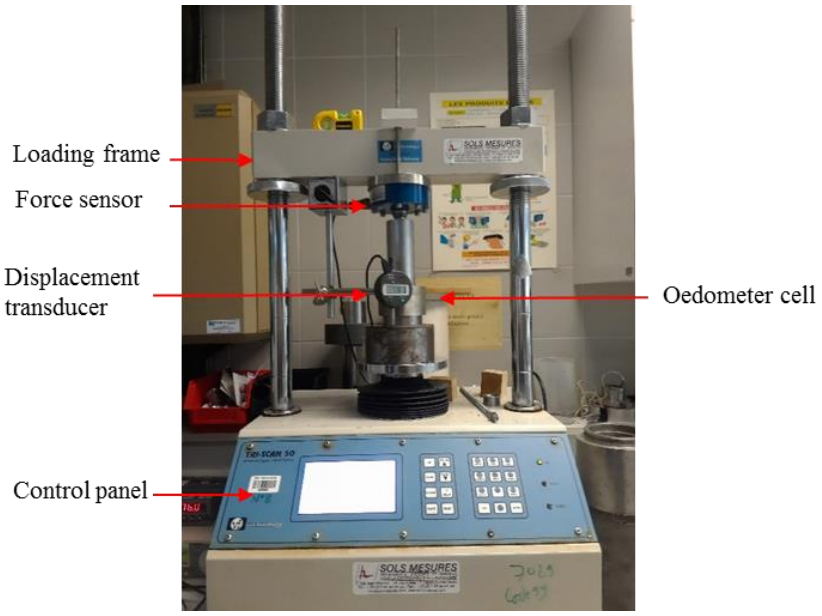

Fig. 2.19. The CRS test

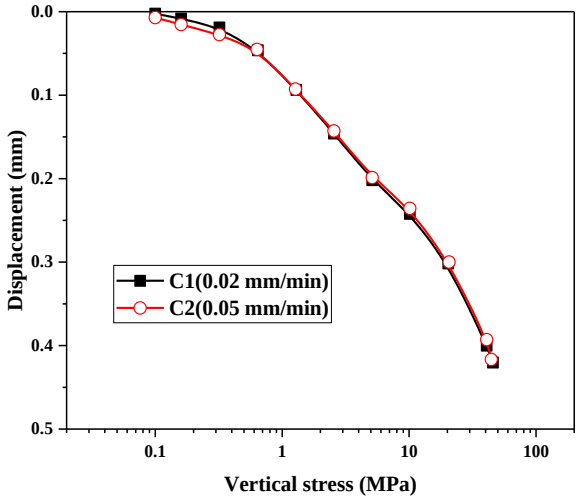

Fig. 2.20. Calibration curves of oedometr cell and loading frame at different loading rates

2.3 Test programs

2.3.1 High pressure step-loading oedometer test on fractured samples

The oedometer samples were obtained from the COx core (EST57180). The artificial fractured samples were made by using the cutting and sawing machines. The sample preparation method is detailed in chapter 3. The average width of the horizontal facture depends on the roughness of the surface between two disks, and is equal to the difference between the total height of the stacked two disks and the sum of the height of two separate disks. If needed, the surface can be polished by using a sand paper to control its roughness. The average width of vertical facture equals the difference between the diameter perpendicular to the direction of vertical fracture and the diameter of oedometer cell. In this study, the values of 0.1 mm and 0.3 mm were adopted as the widths of horizontal and vertical fractures, respectively. These values allowed the samples with different fractured directions to have the same initial global void ratio, and ensured that the fractures can be closed by the swelling of clay minerals based on the experimental evidence from Giot et al. (2018) and Di Donna et al. (2019).

As illustrated in Table 2.5, two test conditions were adopted: Case 1 - the sample was wrapped with filter paper between the sample and cell wall at the radial direction; Case 2 - without filter paper. Filter papers were used in tests TH-1 and TV-1 to simulate the in situ condition with underground water directly flowing into the fractures. Tests TH-2 and TV-2 without filter paper simulate the in situ condition with underground water infiltrating into fracture through COx claystone. For the latter, the vertical hydraulic conductivity was measured with CPV (Fig. 2.8). By contrast, test TI was performed on intact sample.

The test procedure includes two stages, the swelling stage and the compression stage, as described in section 2.2.1. An initial vertical stress 0.05 MPa was applied in the swelling process to ensure a good contact. The synthetic water (Table 2.3) was used to saturate the sample. The maximum vertical stress applied was 64 MPa in the compression process.

Table 2.5 The test program of fractured oedometer samples

Test No.	Initial suction (MPa)	Fractured direction	Thickness of fracture (mm)	Filter paper	Hydraulic conductivity
TH-1	22.2	Horizontal	0.1	√	-
TV-1	22.6	Vertical	0.3	√	-
TH-2	23.7	Horizontal	0.1	-	√
TV-2	23.3	Vertical	0.3	-	√
TI	22.9	/	/	-	√

2.3.2 Triaxial test

The damage behaviour of COx claystone was investigated through triaxial test. The preparation process of triaxial sample is presented detailedly in chapter 3. The loading process includes two stages. Firstly, the sample was isotopically loaded at a loading rate of 100 kPa/min (Belmokhtar, 2017) up to 14 MPa. which corresponds to the in situ stress. Then, the sample was sheared at an axial strain rate of 6×10^{-6} /s^{-1}, as recommended by Zhang et al. (2015, 2019) and Liu et al. (2018). Two loading paths were followed: constant confining pressure and constant mean stress, as described in section 2.2.2. Although the triaxial sample was initially slightly unsaturated, the saturation process was not imposed to avoid the possible hydration damage on COx claystone in the re-saturation process (Wang, 2012).

There are nine triaxial tests in total (Table 2.6). The triaxial samples in tests CM-4, CM-5, CM-6, CM-7 and CM-8 were loaded, not till failure, but till a deviator stress corresponding to a defined damage criterion. The aim is to prepare the damaged COx claystone used in the follow-up experiments. The damage criterion is proposed based on the analysis on the triaxial test results of COx claystone, including CC, CM-1, CM-2, CM-3 and those in literatures, which is depicted in chapter 3. Besides, the triaxial sample in test CM-4 was scanned with μ-computed Tomography before and after testing to characterize the damage due to shearing.

Table 2.6 Triaxial test program

Test No.	Porosity (%)	Water content (%)	Initial suction (MPa)	Diameter (mm)	Height (mm)	Core ID	Loading-unloading
CC	15.4	6.6	20.2	38	65	EST57911	√
CM-1	17.8	7.8	20.0	38	65	EST57180	-
CM-2	15.7	6.7	18.9	38	65	EST57914	-
CM-3	15.7	6.7	18.9	38	65	EST57914	√
CM-4	17.9	8.06	20.5	38	65	EST58107	-
CM-5	17.9	8.06	20.5	38	65	EST58107	-
CM-6	17.9	8.06	20.5	38	65	EST58107	-
CM-7	17.9	8.06	20.5	38	65	EST58107	-
CM-8	17.9	8.06	20.5	38	65	EST58107	-

2.3.3 High pressure oedometer test on damaged samples

The high pressure oedometer tests were conducted on the damaged COx samples under different controlled suctions. The damaged oedometer samples were obtained by cutting the triaxial sample in test CM-4 after shearing. The detailed description is presented in chapter 3.

The test procedure was the same as described in section 2.2.1, including suction equilibration and step loading. In this study, the zero suction was imposed by injecting synthetic water to flood the sample, while other suctions were imposed with the VET system (Fig. 2.18). Due to unloading effect during extraction and water loss during the storage, the samples had an initial suction around 27 MPa. The strain rate 0.025%/day used by Romero et al. (2003) was adopted for the suction equilibration. The vertical strain was considered as stabilized under each load when it was lower than 5×10^{-4}/8h (AFNOR, 2005). In addition, each sample was scanned with μ-computed Tomography (CT) before and after the test to explore the variation of fissure volume inside the sample due to compression. Table 2.7 presents the test program in detail:

Table 2.7 Test program for unsaturated damaged oedometer samples

Test No.	Initial suction (MPa)	Target suction (MPa)	Solution	Hydration method	Sample ID	CT
TD-0	25.8	0	Synthetic water	Flooding	EST58107-D1	√
TD-4	25.8	4.2	K_2SO_4	VET	EST58107-D2	√
TD-9	27.4	9	KNO_3	VET	EST58107-D3	√
TD-24	27.4	24.9	$(NH_4)_2SO_4$	VET	EST58107-D4	√

2.3.4 CRS test on damaged samples

To study the time-dependent behaviour of unsaturated damaged COx claystone, CRS tests were conducted. The oedometer damaged samples are obtained from the damaged triaxial sample after shearing, including tests CM-5, CM-6, CM-7 and CM-8. For the initial suction imposition, the damaged oedometer sample was placed into a desiccator with a saturated saline solution or distilled water, to equilibrate to the target suction, as shown in Fig. 2.17. When the mass of the samples in the desiccator stabilized (checked by weighing the samples periodically), the target suction was regarded as achieved. Then, a small piece was taken and measured by using the Decagon WP4 dew point tensiometer to check the imposed suction. After suction equilibration, the volume of the sample was measured using a caliper to determine the soil density. Then, the sample was placed in the oedometer cell and compressed with the loading frame shown in Fig. 2.19. During the compression process, the suction controlled system in Fig. 2.18 was used for the tests at suctions 4.2 MPa, 9 MPa and 24.9 MPa. In addition, for the tests at zero suction, the sample was first put in the cell, then synthetic water was injected from the bottom of cell. A pore pressure transducer was installed on the bottom of cell to measure the possible excess pore pressure.

The strain rate applied in the CRS test should be low enough to guarantee the constant suction condition (Qin et al., 2015). A loading rate 3.3×10^{-3} MPa/s was adopted in the isotropic compression test on an unsaturated chalk by Gennaro et al. (2003), corresponding roughly to a strain rate of 10^{-5}/s. Qin et al. (2015) also adopted 10^{-5}/s as the maximum strain rate in the CRS test on highly compacted GMZ bentonite. Results indicate that this strain rate is enough to ensure the suction constant during the compression process. The same maximum strain rate

was adopted in this study. In addition, the single-stage was adopted, as recommended by Leroueil et al. (1985) and Qin et al. (2015).

The test program is shown in Table 2.8. The four suctions selected are the same as those used in the step-loading high pressure oedometer tests on damaged claystone.

Table 2.8 CRS test program

Test No.	Initial suction (MPa)	Target suction (MPa)	Solution	Hydration method	Strain rate (s^{-1})	Sample ID
T0S5	25.3				1×10^{-5}	X1
T0S6	25.3	0	Synthetic water	Flooding	1×10^{-6}	X2
T0S7	25.3				1×10^{-7}	X3
T4S5	26.1				1×10^{-5}	X4
T4S6	26.1	4.2	K_2SO_4	VET	1×10^{-6}	X5
T4S7	26.1				1×10^{-7}	X6
T9S5	27.2				1×10^{-5}	X7
T9S6	27.2	9	KNO_3	VET	1×10^{-6}	X8
T9S7	27.2				1×10^{-7}	X9
T24S5	24.6				1×10^{-5}	X10
T24S6	24.6	24.9	$(NH_4)_2SO_4$	VET	1×10^{-6}	X11
T24S7	24.6				1×10^{-7}	X12

2.4 Conclusions

This chapter presents the materials studied, the experimental techniques employed and the test programs followed.

The studied COx claystone was extracted from the MHM URL at the depth -490 m. The synthetic water used has the same chemical composition as the in situ underground water. Besides, a simple method was used to redetermine the bedding plane direction, validating the bedding marks on COx cores.

High pressure oedometer tests on fractured claystone were designed to investigate the effect of fracture on the swelling and compression behaviours. The evolution of hydraulic conductivity with vertical stress was also explored. Triaxial tests were adopted to study the damage properties of claystone, and the aim is to further define a suitable damage criterion for the preparation of damaged samples in the laboratory. High pressure oedometer tests were performed on the damaged samples under controlled suction condition to study the compression behaviour and the creep behaviour. The VET technique was adopted for the suction control. WP4 hygrometer was used to measure the suctions of COx core and the unsaturated samples prepared for mechanical testing. μ-computed tomography was adopted to characterize the fissures inside the samples before and after mechanical testing. Mercury Intrusion Porosimetry (MIP) technique was also used to observe the microstructure of claystone. CRS tests on damaged samples were performed to explore the effects of strain rate and suction on the damaged COx claystone.

Chapter 3. Development of the methods for preparing fractured and damaged samples

In this chapter, the preparation of fractured and damaged samples in the laboratory is described in detail. Triaxial and intact oedometer samples are first prepared. The fractured samples were prepared from the intact oedometer samples. For the damaged samples, a new preparation method was proposed based on the analysis and discussion on the evolution of mechanical parameters due to damage in triaxial tests. A new parameter was defined and selected as the damage index. The damaged oedometer samples used in this study were prepared based on the proposed method.

3.1 Triaxial and intact oedometer samples

As described in chapter 2, the basic physical parameters of COx core were first measured when the T1 cell was opened. Then, the core was drilled with a drilling machine along the direction perpendicular to the bedding plane, as shown in Fig.3.1. There are four parts: joystick, plastic box, auger and fixing device. The auger with diameter 38 mm was used to drill the COx core. It is worth noting that a very low drilling speed (2 mm/min) was adopted to avoid damaging the COx sample. Then, a COx claystone cylinder was obtained with a diameter of 38 mm. Following that, with the sawing machine described in chapter 2, the cylinders were cut with different heights. For triaxial tests, the height 65 mm was selected due to the limited diameter (80 mm) of COx core. Note that the ratio between height and diameter is around 1.7, slightly lower than the standard value 1.85-2.25 (XP CEN ISO/TS 17892-8, 2005).

The intact oedometer sample of COx claystone can also be obtained by sawing the COx cylinder into the disk with a height 10 mm. The detailed sample preparation process is represented in Fig. 3.2. Besides, during the drilling and sawing processes, it is essential to wrap the sample with plastic film to avoid water loss from the COx core.

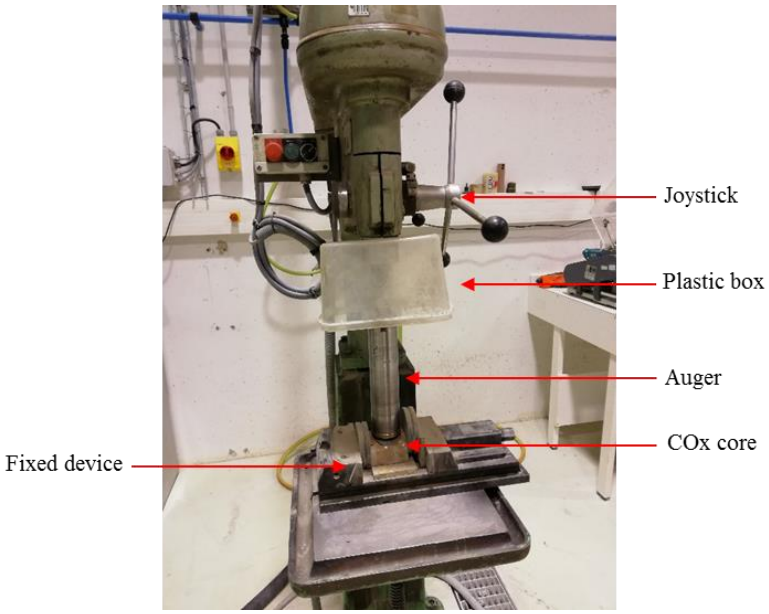

Fig. 3.1. The machine for drilling

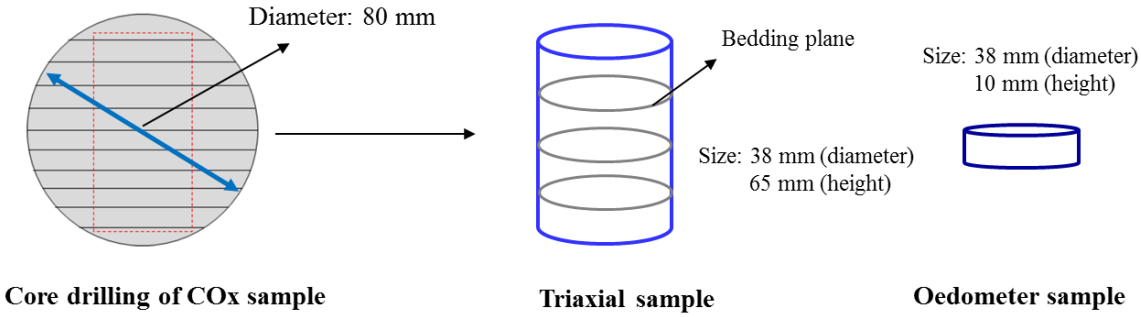

Fig. 3.2. The sampling process of COx claystone

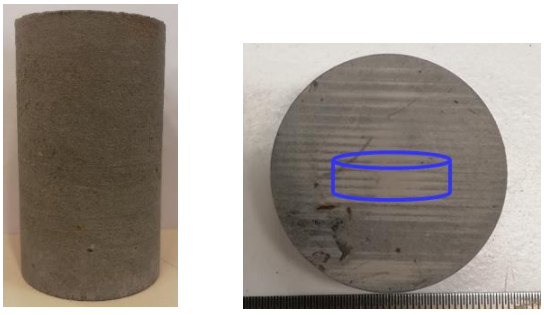

Fig. 3.3. The photos of triaxial sample (left) and oedometer sample (right)

3.2 Fractured sample

To obtain the fractured oedometer sample, the intact COx oedometer sample was sawed into thinner disk in the direction of cross section or semicircle shape in the direction of diameter. Correspondingly, the horizontally and vertically fractured oedometer samples were obtained, respectively, as shown in Fig. 3.4. The average width of the horizontal facture is related to the

roughness of the surface between two disks, while the vertical one depends on the difference between the diameter perpendicular to the direction of vertical fracture and the diameter of oedometer cell. By polishing the contact surfaces of the two parts of each sample, the target thickness of fracture was obtained.

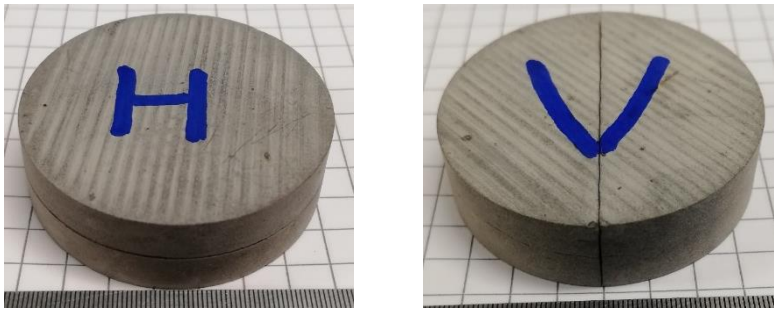

Fig. 3.4. Fractured Oedometer samples: horizontal fracture (left) and vertical fracture (right)

3.3 Damaged sample

For the preparation of damaged oedometer samples, the damage behaviours of COx claystone are first investigated in order to develop a relevant damage criterion. For that, high pressure triaxial test on COx claystone was carried out. The damage criterion was developed by analyzing the mechanical behaviour and the distribution of fissures.

3.3.1 Triaxial test

3.3.1.1 Calibration test

In the triaxial test, the deformation of membrane should be calibrated, as pointed out by Belmokhtar et al. (2017). For the calibration, a steel cylinder was used to replace soil sample. The elastic parameters of steel are E = 200 GPa and υ = 0.22 and it is regarded as an isotropic material. It has a diameter of 38 mm and a height of 76 mm. In Fig. 3.5, the cylinder represents the triaxial sample, the black line represents the membrane, the arrow represents the radial LVDT stem in contact with the membrane directly.

The deformation of steel cylinder under different confining pressure can be calculated. The axial strain of steel cylinder is equal to the radial strain under isotropic loading. Combining the measurement of LVDT, the relationship between confining pressure and membrane deformation (ΔD_m) can be obtained. It is almost linear, as shown in Fig. 3.6. In the following tests, this relationship is used to calibrate the radial deformation of claystone sample.

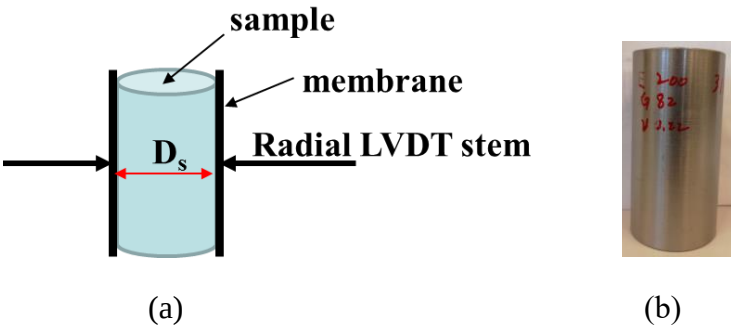

(a) (b)

Fig. 3.5. (a) schematic of calibration test; (b) streel cylinder used in the calibration test

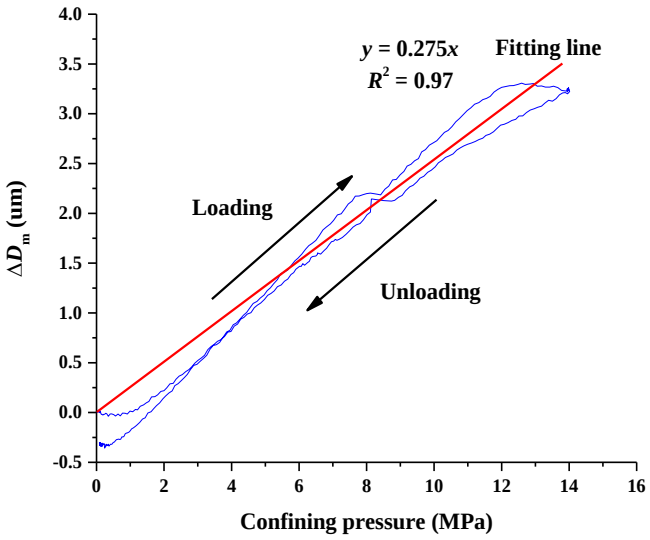

Fig. 3.6. Change in membrane thickness with confining pressure

3.3.1.2 Isotropic loading

Fig. 3.7a shows the evolutions of different strains during isotropic loading. The maximum pressure 14 MPa is applied, aiming at closing up the possible microcracks in the triaxial samples due to the possible damage induced in the drilling and sawing processes (Mohajerani et al., 2011; Zhang et al., 2019). In Fig. 3.7a, at the beginning of loading, the axial strains of tests CM-1 and CM-2 increase more quickly than those of tests CM-3 and CC, indicating that some microcracks may exist in the corresponding triaxial samples. The similar phenomena were observed on other rocks (Niandou et al., 1997; Chiarelli et al., 2003). It is worth noting that the results obtained in this study are comparable with those obtained by Zhang et al. (2015) shown in Fig. 3.7b. Fig. 3.8 schematically shows the closure of microcracks induced by loading.

The isotropic loading leads to non-linear stress-strain relationship in the axial direction. Moreover, the strain ε_1 in the direction perpendicular to bedding is significantly larger than ε_3 in the direction parallel to bedding. This is because: (1) the claystone is an anisotropic material;

(2) the bedding direction is the major opening direction of microcracks (Zhang et al., 2015).

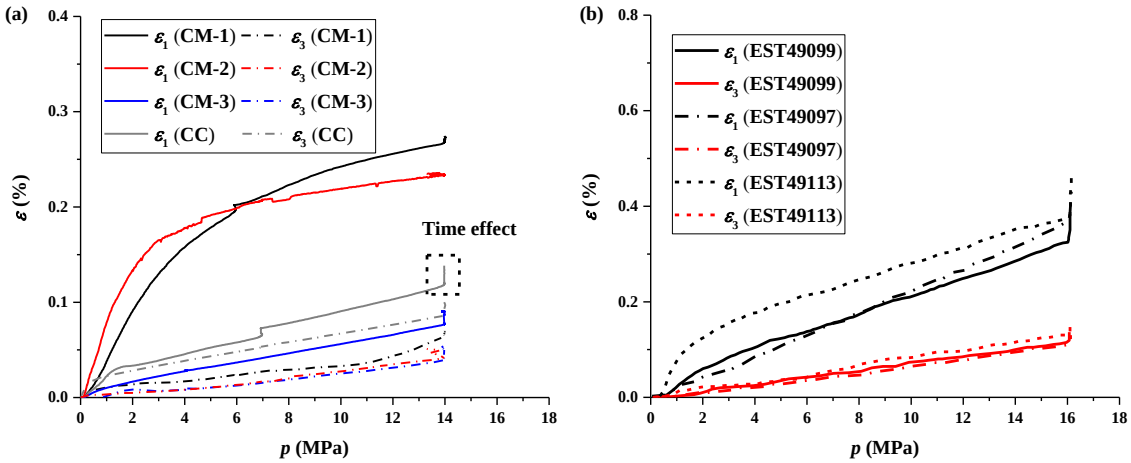

Fig. 3.7. Strains measured in axial and radial directions: (a) this study; (b) data from Zhang et al. (2015)

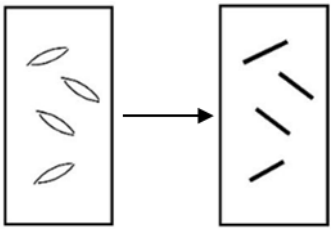

Fig. 3.8. Schematic diagram of microcrack closure during isotropic loading

3.3.1.3 Shear loading

Fig. 3.9a shows the stress-strain curves under constant mean stress. For test CM-3, 4 loading-unloading cycles are applied to analyse the damage through changes of Young's modulus. The stress-strain curve is almost linear at the beginning of loading, suggesting lack of microcracks. It becomes progressively non-linear, indicating the coupling effects of plasticity and damage (Le Pense et al., 2016; Bian et al., 2017). Note that these results are comparable to those obtained by Liu et al. (2018). For test CM-3, the peak stress q_{max} (23.7 MPa) is larger than 22.1 MPa (see Fig. 3.9b) due to the higher mean stress. Fig. 3.10 presents the variations of axial stress, lateral stress and mean stress with respect to axial strain and lateral strain in test CM-3. With the increase of axial stress, lateral stress correspondingly decreased. The changes of axial stress were around two times that of lateral stress. It appears that during the shearing process, the mean stress was kept constant well before the peak stress. This observation is consistent with the stress path for CM test described in chapter 2.

On the other hand, test CC was conducted under constant confining pressure (14 MPa). The

results are shown in Fig. 3.11a. Also, 4 unloading-loading cycles were applied. The corresponding peak stress obtained is 34.3 MPa. By contrast, the peak stresses under constant confining pressure 12 MPa obtained by Armand et al. (2017) and Liu et al. (2018) are 34.9 MPa, 37.5 MPa and 34.9 MPa, respectively, as shown in Fig. 3.11b. It is found that with a lower confining pressure, slightly higher peak stresses were determined under 12 MPa. It is reported that the triaxial samples used by Armand et al. (2017) and Liu et al. (2018) had lower initial water contents around 6 %, while the triaxial sample used in test CC has a higher initial water content 6.6 %. Liu and Shao (2016) reported that the peak for COx claystone decreased with the increase of water content. This can explain why a lower peak stress was obtained under a higher confining pressure.

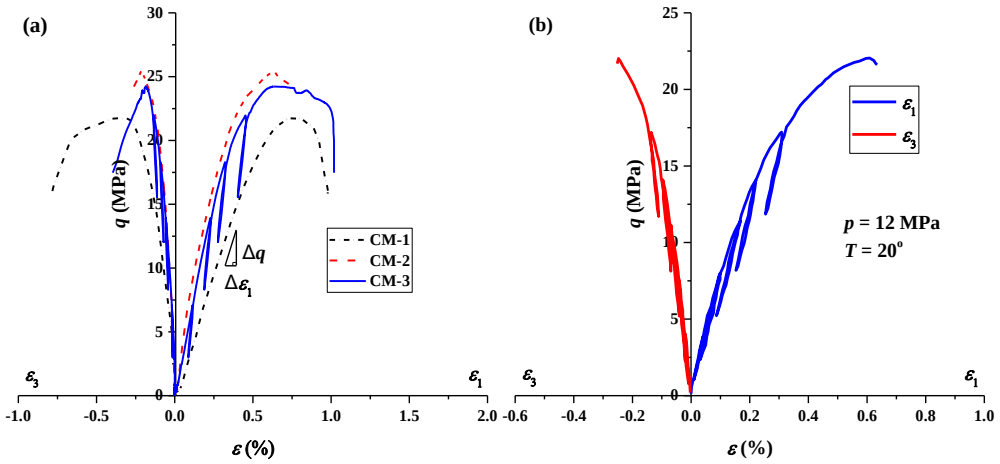

Fig. 3.9. Strain-stress curves under constant mean stress: (a) p = 14 MPa (this study); (b) p = 12 MPa (data from Liu et al., 2018)

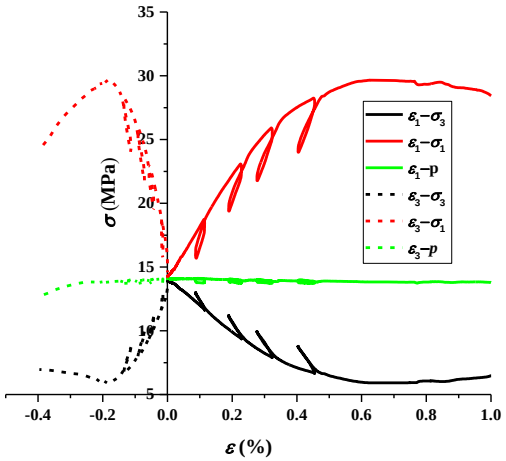

Fig. 3.10. Strain-stress curve under constant mean stress (Test CM-3)

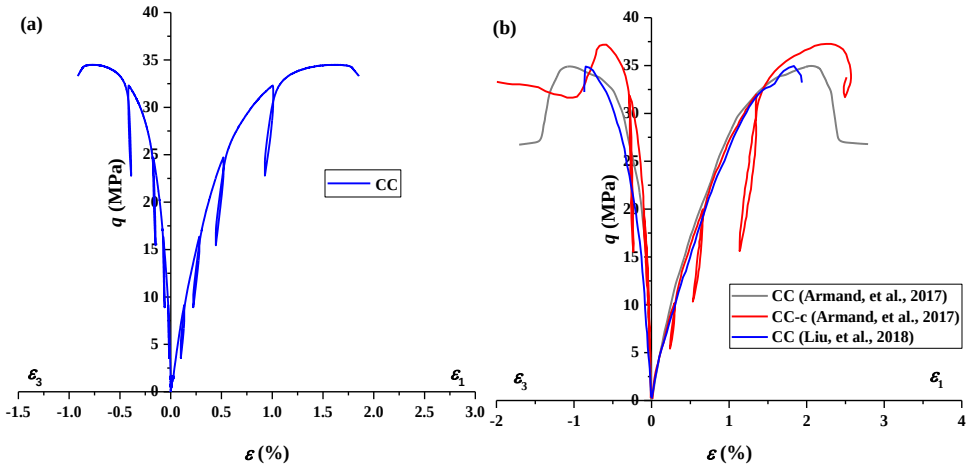

Fig. 3.11. Strain-stress curves under constant confining pressure: (a) σ_3 = 14 MPa (test CC in this study); (b) σ_3 = 12 MPa (data from Armand et al., 2017 and Liu et al., 2018)

3.3.1.4 Evaluation of mechanical parameters

Based on the triaxial test results, the damage behaviour of COx claystone is analysed and discussed in terms of variations of mechanical parameters with deviator stress. The stress state in triaxial test is shown in Fig. 3.12. For COx claystone, according to the isotropic loading results, it has obvious transversely isotropic properties. Therefore, in the analysis, transversely anisotropic elasticity assumption is made. For comparison, the case of isotropic elasticity assumption is also considered. The elastic stress-strain relationship is given by Hook's law Eq. 1-3, as recommended by Wittke (1984). According to the isotropic and transversely anisotropic elastic assumption (Zhang et al., 2015), the elastic parameters are determined, respectively. The determination method is shown in Table 3.1.

Table 3.1 Determination of elastic parameters under different loading paths

Loading path	Isotropic assumption	Transversely isotropic assumption
Constant confining pressure ($\sigma_3 = constant$)	$E = \frac{\Delta q}{\Delta \varepsilon_1}$ $\nu = -\frac{\Delta \varepsilon_3}{\Delta \varepsilon_1}$	$E_1 = \frac{\Delta q}{\Delta \varepsilon_1}$ $\nu_1 = -\frac{\Delta \varepsilon_3}{\Delta \varepsilon_1}$
Constant mean stress ($\sigma_1 + 2\sigma_3 = constant$)	$G = \frac{E}{2(1+\nu)} = \frac{\Delta q}{3\Delta \varepsilon_1}$	$E_1 = 2(1+\nu_1)\frac{\Delta q}{3\Delta \varepsilon_1}$

Note: $\Delta q = \Delta\sigma_1 - \Delta\sigma_3$, where E_1 is the young's modulus parallel to the axial direction, ν_1 is the corresponding Poisson's ratio.

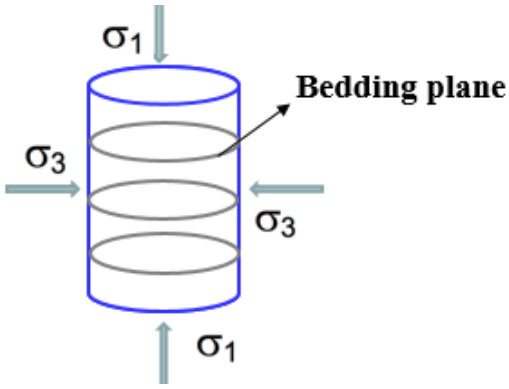

Fig. 3.12. The stress state in triaxial test

Based on the unloading-reloading cycles, the shear and Young's moduli (G and E) are calculated based on the isotropic assumption firstly, as presented in Fig. 3.13. G and E both slightly decrease with the increase of axial strain, which demonstrates that shear loading indeed induces damage of the sample (Liu et al., 2016). Comparison with that obtained by Liu et al. (2018) shows that with higher mean stress, G and E are larger, indicating the dependency on mean stress. Fig. 3.14 compares the obtained peak stresses with those from Armand et al. (2017). A reasonable linear relationship is obtained based on the triaxial results under different loading paths.

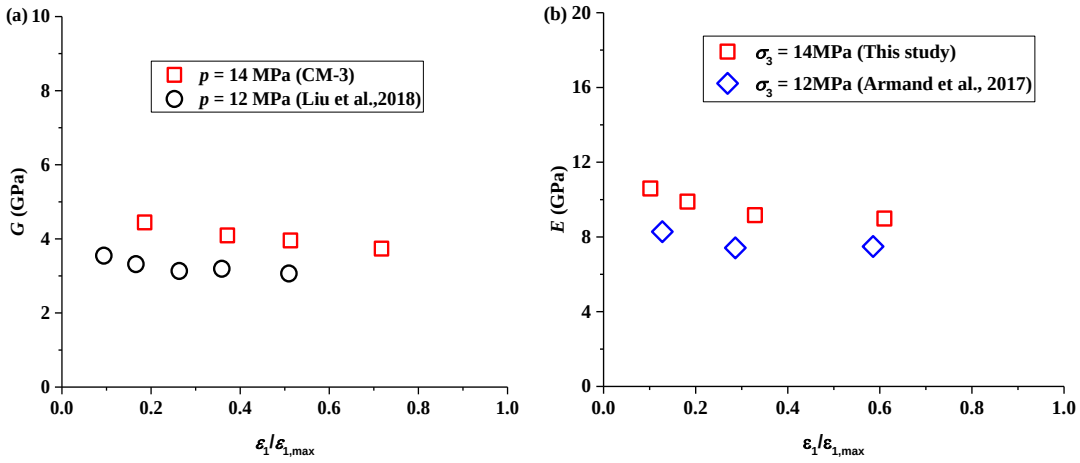

Fig. 3.13. Variations of shear modulus and Young's modulus with axial strain (isotropic assumption): (a) under constant mean stress; (b) under constant confining pressure

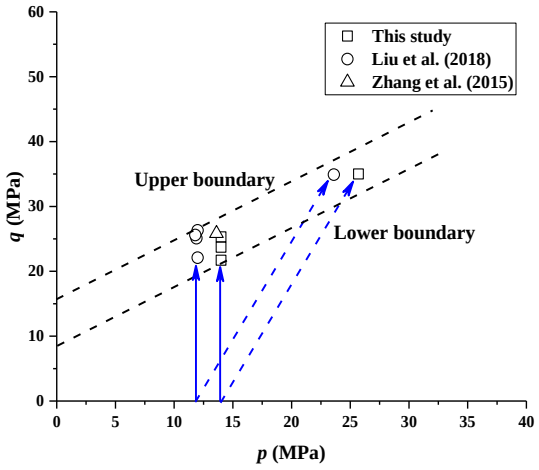

Fig. 3.14. Comparison of the shear strengths in this study and that obtained by Zhang et al. (2015) and Liu et al. (2018). Note: all the samples are as open state, loaded at around 20°C and the loading direction is perpendicular to bedding plane. "as open state" means the state that COx claystone core was just opened from T1 cell.

According to the variations of elastic parameters (G and E), damage during the loading process can be analyzed. However, in order to obtain damaged sample, the sample cannot be loaded up to peak stress (i.e. failure state), it is important to consider other parameters in the development of the damage criterion. The tangent elastic parameters (G_T, E_T and υ_T) along the axial direction are determined for this purpose. They were determined from the shear stress-strain curves using the moving point regression technique, as recommended by Eberhardt et al. (1998) and Espitia et al. (2017). A fixed strain interval is adopted in this method to fit a straight line, aiming at obtaining the corresponding tangent slope of stress-strain with less errors and subjectivity. The strain interval $\Delta\varepsilon_1 = 0.02$ % was adopted in this study. Besides, G_I and E_I in this study represents the average tangent shear and Young's moduli at the initial loading stage. To some extent, they are equivalent to the real initial shear and Young's moduli of triaxial samples. Qi et al. (2020) reported that Young's modulus can be identified based on the ratio of q to ε_1 at the initial loading stage (i.e. ε_1 = 1%). In this study, the q and ε_1 strain at $\varepsilon_1 = 0.1$ % was selected.

Fig. 3.15 shows that the normalized tangent shear modulus G_T/G_I for test CM-3 decreases with the increase of q and ε_1 during the loading process. Before the first unloading-reloading cycle, G_T/G_I changed little, while after that it decreased quickly. Besides, the corresponding q (21.3 MPa) at the fourth unloading is around 0.9 time the peak shear stress (q_{max} = 23.7 MPa). G_I is 5.4 GPa and $\varepsilon_{1,max}$ corresponding to peak stress is 0.62 %, respectively. Comparing the two curves in Fig. 3.15, it is found that the decreasing tendencies of G_T/G_I in terms of normalised q and ε_1 are different.

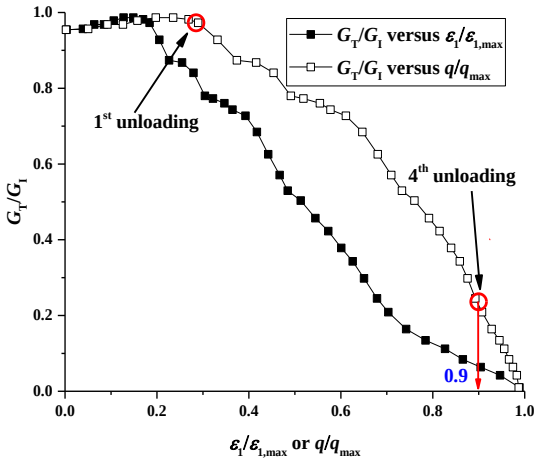

Fig. 3.15. Variations of normalised G_T/G_I with normalised q and ε_1 under isotropic assumption in test CM-3.

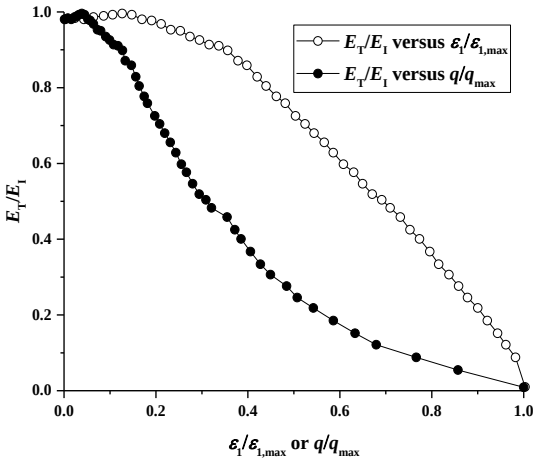

Fig. 3.16. Variations of normalised E_T/E_I with normalised q and ε_1 under isotropic assumption in test CC. Note: E_I and $\varepsilon_{1,max}$ are 10.5 GPa and 1.41 %, respectively.

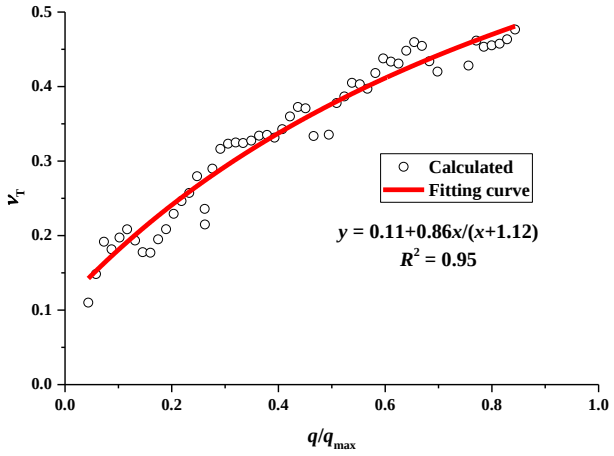

Fig. 3.17. Variations of tangent Poisson's ratio υ_T with q and ε_1 under isotropic assumption in test CC

Moreover, the normalized tangent modulus and Poisson's ratio υ_T in test CC are calculated, as shown in Fig. 3.16 and Fig. 3.17, respectively. It is observed that E_T/E_I decreases with the increase of deviator stress as in Fig. 3.15, while υ_T increases as reported by Zhang et al. (2015, 2019).

As presented in Eq. 1-3 and Table 3.1, E_1 and E_T cannot be calculated directly using the results from the constant mean stress test. Zhang et al. (2015, 2019) reported that Poisson's ratio changed little. Thereby, a constant Poisson's ratio 0.2 was recommended by Zhang et al. (2015, 2019) and Zeng et al. (2019). By taking a constant Poisson's ratio equal to 0.2, E_1 and E_T under constant mean stress can be calculated from the test result under constant mean stress. Fig. 3.18 shows the variation of normalised E_T/E_I (E_I = 10.9 GPa) in test CM-3, showing a decreasing trend as for G_T/G_1 in Fig 3.15 with an isotropic assumption. In addition, E_1 was calculated from the unloading-reloading cycle. It is observed that it decreases a little, indicating the damage inside due to loading. Through X-ray CT observations, Viggiani et al. (2013) observed that microcracks emerged and propagated gradually during triaxial loading even after the peak stress. This is consistent with the decrease of axial Young's moduli E_T and E_1. The evolution of microcracks is depicted schematically in Fig 3.19. With the increase of deviator stress, microcracks were generated progressively, then propagated, finally formed a connection fracture.

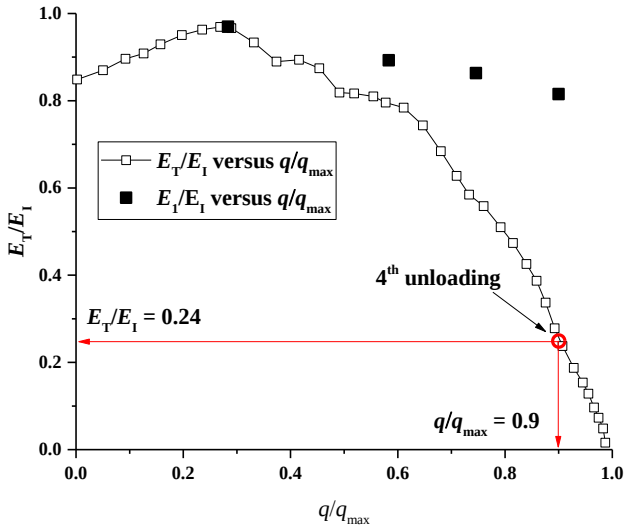

Fig. 3.18. Variations of normalised E_T with normalised q under transversely isotropic assumption in test CM-3.

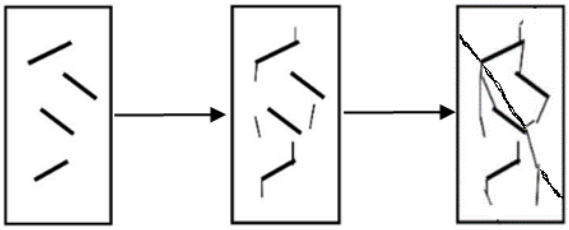

Fig. 3.19. Schematic diagram of microcrack evolution during loading.

To further analyze the variations of tangent modulus E_T with deviator stress q, the triaxial results from this study and other literatures are compiled. $E_{T,0.9}$ and E_I obtained from the collected triaxial results are summarized in Table 3.2. Interestingly, the ratio between $E_{T,0.9}$ and E_I varies in a small range from 0.18 to 0.26, whatever the samples and the test conditions. The average value is 0.22. This indicates that the normalized tangent modulus E_T/E_I can be taken as an indicator of damage degree for COx claystone. In addition, the ratios of E_T/E_I at different q/q_{max} values are plotted in Fig. 3.20. Results indicate that the evolutions of E_T/E_I with respect to q/q_{max} from different works present significant similarities. A quantitative relationship can be obtained by best fitting.

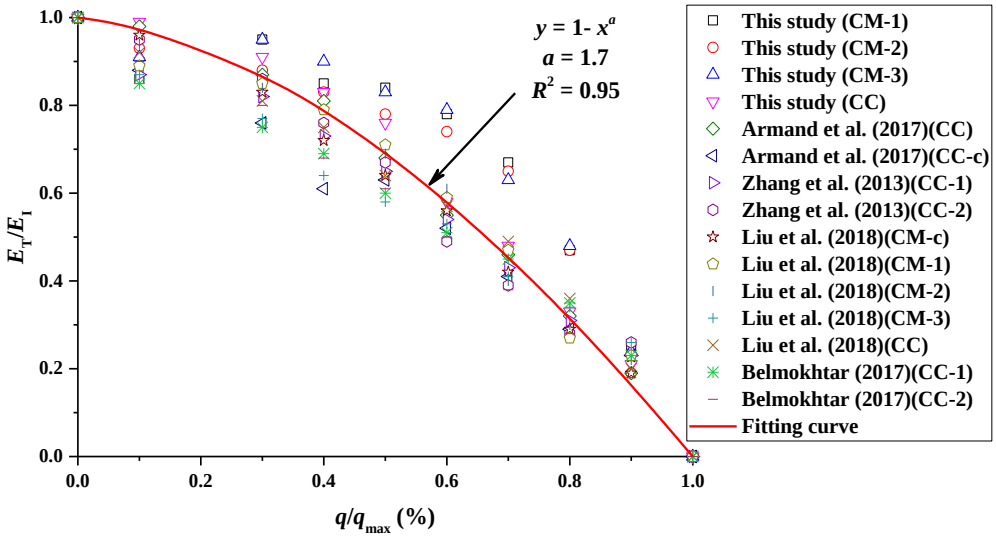

Fig. 3.20. Variations of normalised tangent modulus E_T/E_I with q/q_{max}

Table 3.2 Comparison of $E_{T,0.9}$ and E_I from different studies

Source	Test No.	Initial saturated condition	Confining pressure or mean stress (MPa)	Peak stress (MPa)	0.9 time peak stress (MPa)	E_I (GPa)	$E_{T,0.9}$ (GPa)	$E_{T,0.9}/E_I$
This study	CM-1	as-open state	14	21.7	19.53	7.2	1.8	0.25
	CM-2	as-open state	14	25.3	22.77	9.9	1.9	0.19
	CM-3	as-open state	14	23.7	21.33	10.9	2.6	0.24
	CC	as-open state	14	34.3	30.87	10.5	2.2	0.21
Armand et al. (2017)	CC	RH 90%	12	34.8	31.32	6.3	1.2	0.19
	CC-c	RH 90%	12	37.3	33.57	6.1	1.4	0.23
Zhang et al. (2013)	CC-1	as-open state	10	33.1	29.8	5.1	1.2	0.23
	CC-2	as-open state	12	34.8	31.3	6.2	1.6	0.26
Liu et al. (2018)	CM-c	as-open state	12	22.1	19.89	8.48	1.6	0.19
	CM-1	as-open state	12	26.2	23.58	4.83	1.1	0.23
	CM-2	as-open state	12	25.6	23.04	4.65	1.0	0.22
	CM-3	as-open state	12	24.9	22.41	4.75	1.2	0.26
	CC	as-open state	12	35.1	31.59	5.1	1.0	0.20
Belmokhtar et al. (2017)	CC-1	saturated	8	18.0	16.2	2.92	0.67	0.23
	CC-2	Saturated	12	21.8	19.6	4.19	0.75	0.18

Note: CM (constant mean stress); CC (constant confining pressure); c (with unloading-reloading cycle); as-open state (same saturation as that from the corresponded T1 cell); RH (relative humidity); loading direction parallel to bedding plane for that in Zhang et al. (2013).

3.3.2 X-ray tomography and MIP analysis

To further verify the effectiveness of E_T/E_I as a damage indicator, another triaxial test CM-4 was conducted. The triaxial sample was loaded to a ratio E_T/E_I 0.22 and then unloaded. The triaxial sample was scanned through X-ray tomography to observe the distribution of microcracks before and after tests. Fig. 3.21 shows the loading-unloading curve. As discussed before, E_T/E_I decreases with the increase of deviator stress. The triaxial sample was scanned for twice: the first is before triaxial test and the second one is when the sample was unloaded from the triaxial cell. The corresponding tangent Young's modulus at the beginning of loading stage and the unloading point are 8.1 GPa and 1.8 GPa, respectively.

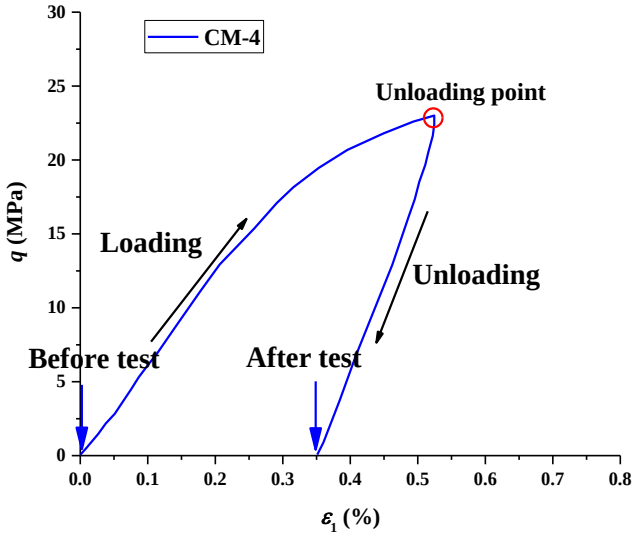

Fig. 3.21. Stress-strain curve of test CM-4

The images from CT test were analysed and compared at three selected sections, as shown in Fig. 3.22. Fig. 3.23 presents the CT images before and after test. Clear clay matrix and granular inclusions (calcite, quartz, etc.) can be identified on all images, which is consistent with the observations by Robinet (2008) and Robinet et al. (2012). There is no evident microcracks before triaxial test. On the contrary, the microcracks emerged after test, even though the distribution of microcracks does not seem uniform.

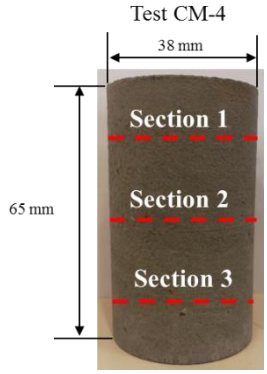

Fig. 3.22. The selected sections of CT results

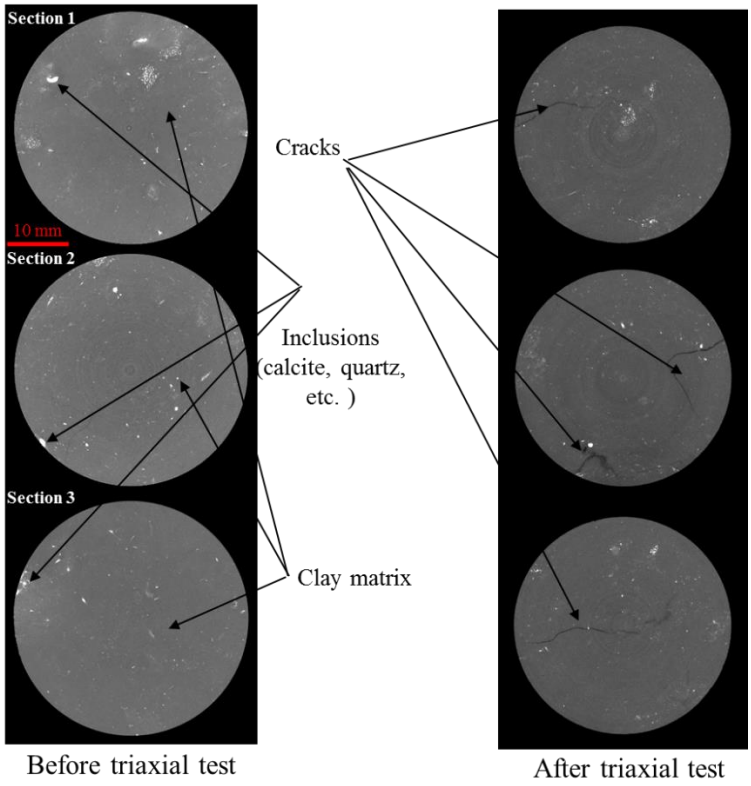

Fig. 3.23. 2D X-ray tomography images

The voxel of CT images has a dimension 24 μm. To quantify the damage degree due to loading, the microcrack volume inside the traxial sample was estimated. First, each CT image was transformed into 8 bit with the grey level ranging from 0 to 255 (i.e. $2^8 - 1$) using the software ImageJ (Ferreira and Wayne, 2012), as shown in Fig. 3.24. For the image analysis, three locations (Fig. 3.24) are selected to characterize the grey levels of microcrack and claystone. Fig. 3.25 presents the evolution of grey level with the distance along the selected lines. To quantify the proportion of microcracks in the image, the microcrack zone and intact claystone zone need to be distinguished. A threshold grey level value 75 was first taken, as shown in Fig. 3.25. Then, the grey level of voxels above and below the threshold value are replaced by the

maximum 255 and minimum grey value 0, respectively. Thus, the image is binarized with black and white colours. Fig. 3.26 shows the two zones divided. After that, according to the average grey value obtained through ImageJ, the proportion of cracking area in the image was identified. For section 1 (S1), the mean grey value is 254.523 and the proportion of cracking area is 1.87 %. Following this procedure, the proportion of cracking area of each image can be calculated. By stacking all the images together, the proportion of total cracking volume in the whole triaxial sample was determined. They are 0.02 % and 1.72 % before and after test, respectively. Besides, based on the image analysis, results indicate that the widths of microcracks are in the range from 24 μm to 576 μm. The determination method for microcrack width is shown in Fig. 3.25a. Armand et al. (2014) reported that through the in situ borehole analysis, the microcracks with the dimension between 0.1 and 0.4 mm dominated in the fractured zone around the excavated drifts. In this sense, the sizes of microcracks in the damaged claystone obtained through triaxial test are comparable with the in situ ones.

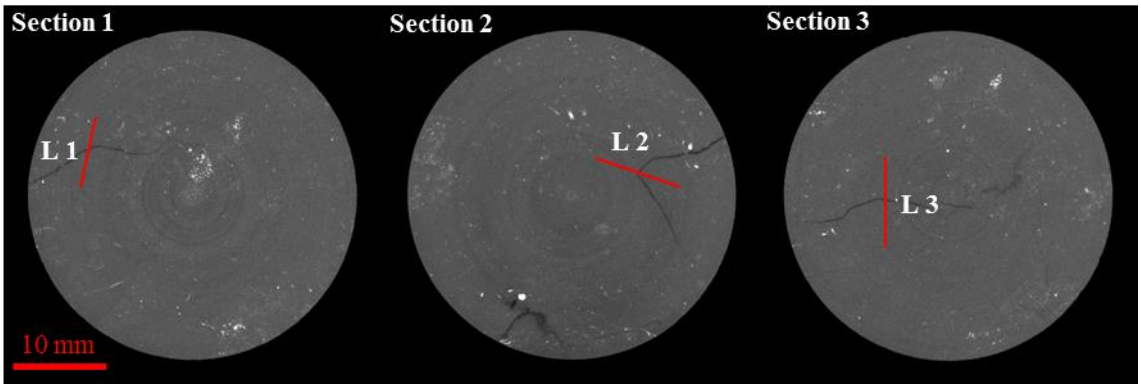

Fig. 3.24. The selected lines with cracks and intact part inside the sample

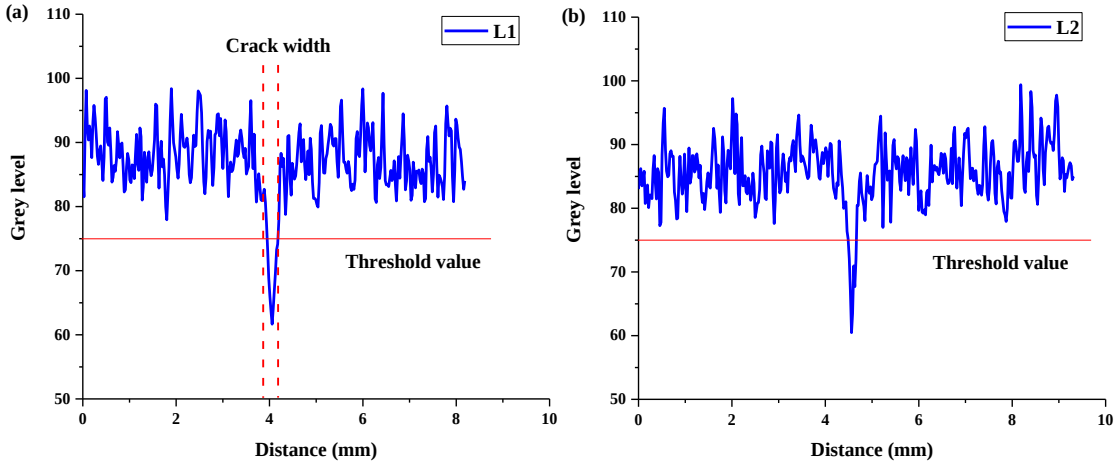

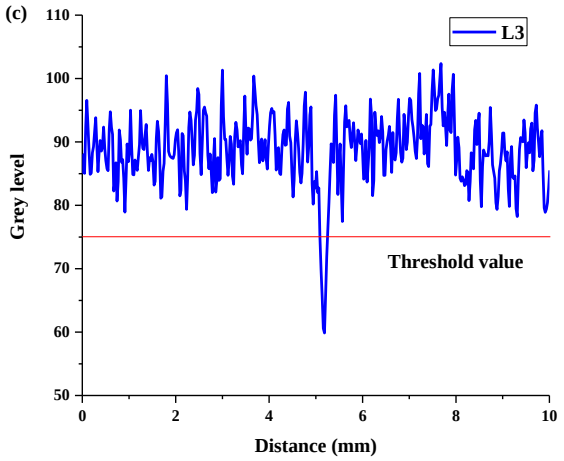

Fig. 3.25. Evolution of grey level with the distance from the selected lines

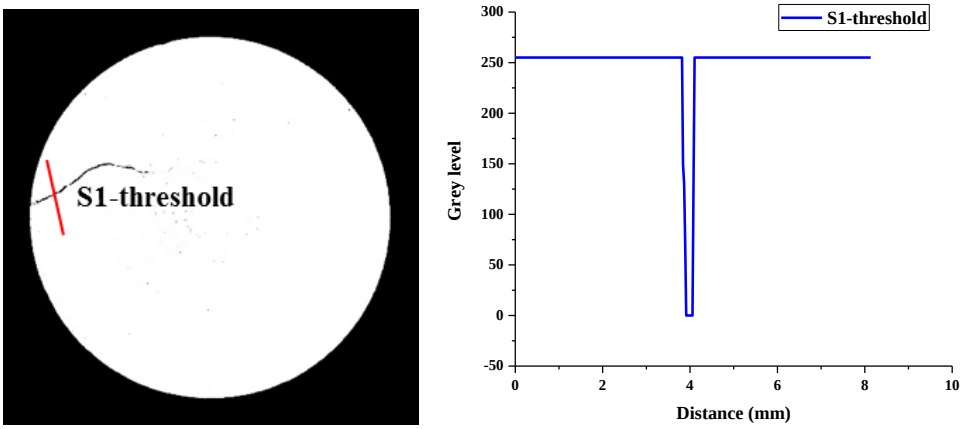

Fig. 3.26. The transformation of grey level in section S1: (a) 2D image; (b) evolution of grey level

With the method above, the microcracks detected can also be presented in three-dimensional way (3D). Fig. 3.27 shows the 3D distributions of microcracks inside the sample before and after test. It is found that there is almost no microcracks before test, while some significant microcracks were observed after test, most of them being located in the zone far from the sample ends. In addition, a hardly visible shear band was observed because of the strain localization. This is consistent with the observations by Lenoir et al. (2007) and Viggiani et al. (2013) using 3D Digital Image Correlation technique.

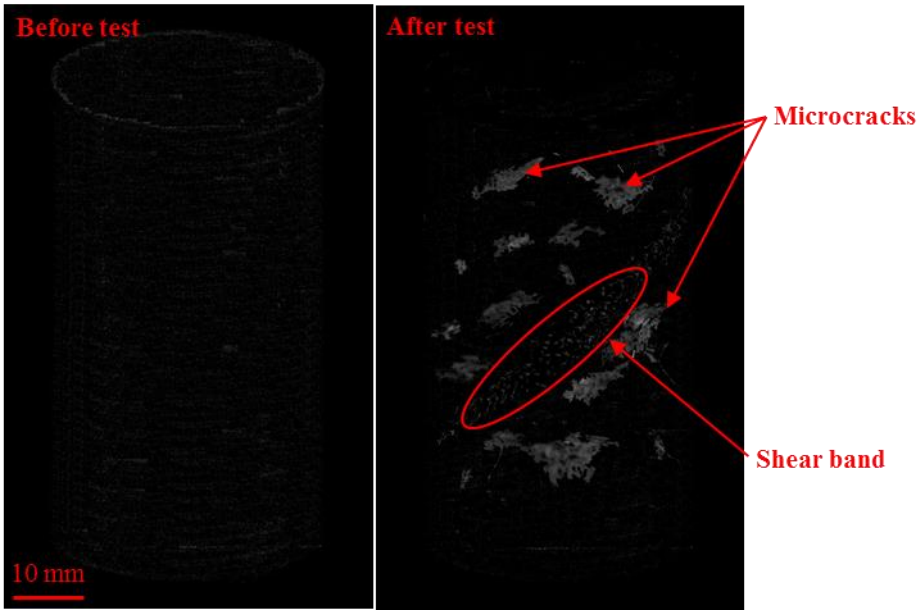

Fig. 3.27. 3D distributions of microcracks before and after test

To further quantify the damage level inside the sample, the damage coefficient defined by Dao et al. (2015) and Mokni et al. (2020) was adopted, as follows:

$$D = \frac{\phi_{crack}}{\phi} \tag{3-1}$$

where ϕ is the total porosity and ϕ_{crack} is the cracking porosity (i.e. the ratio between cracking volume and the whole volume).

The void ratios of the triaxial sample are respectively 0.218 and 0.214 before and after test, indicating an insignificant volume change. Based on the CT test, the corresponding damage coefficients determined are 0.001 (D_B) before test and 0.096 (D_A) after test, indicating the negligible microcracks at initial state and the evident microcracks due to shearing.

After CT scanning, two small samples were taken from the triaxial sample to conduct MIP tests. The void ratios of the two samples are 0.221 and 0.224, respectively. The locations of MIP samples are presented in Fig. 3.28. Fig. 3.29 presents the pore size distribution curves. By referring to Dao et al. (2015), Menaceur et al. (2016) and Mokni et al. (2020), the size of 1 μm was defined as the threshold diameter for microcracks. It is found that the detected void ratios after test are slightly larger than the initial ones. This dilatancy was contributed by the microcracks generated by shearing. In this study, the E_T/E_I value 0.22 corresponds to 0.9 time q_{max}. Zhang et al. (2013) reported that the average crack initiation stress ratio and dilatant stress ratio are 0.6 and 0.83, respectively. Note that crack initiation stress ratio and dilatant stress ratio represent the ratios between deviator stresses and peak stress, which correspond to cracks and

dilatancy appearances, respectively. The value of 0.9 is obviously larger than the two ratios, indicating the appearance of microcracks and volume dilatancy. The sizes of most microcracks are larger than 24 μm. The average proportion of cracking volume in the two MIP samples is 1.68 % after test. The damage coefficients are 0.015 (D_B) before test and 0.094 (D_A) after test, respectively. Comparison between CT and MIP results highlights that before test, D_B determined from MIP test is slightly larger than that from CT, due to the minimum size 24 μm of microcracks detected in CT test. Thus, the microcracks with the size between 1 and 24 μm cannot be considered in CT test. After test, D_B determined from CT and MIP results show the slightly different values. This is because microcracks larger than 24 μm due to shearing dominate in the microcrack network and the proportion of microcracks less than 24 μm are negligible. This also indicates that it is acceptable to use CT scanning to characterize the microcracks. Besides, the difference of damage coefficients between two methods may also result from the MIP sampling locations and the uneven distributions of microcracks. This can be evidenced by the 3D uneven distribution of microcracks in Fig. 3.24. By comparing the dimensions of microcracks due to shearing with those due to hydration obtained by Menaceur et al. (2016), it is found that mechanical loading creates larger microcracks than wetting, larger than 50 μm against 3 to 50 μm. This is consistent with the observation by Wang (2012).

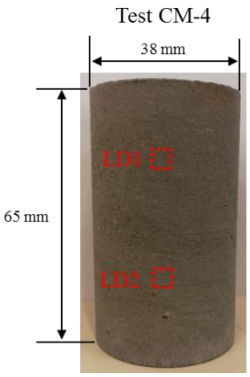

Fig. 3.28. The selected locations of MIP samples

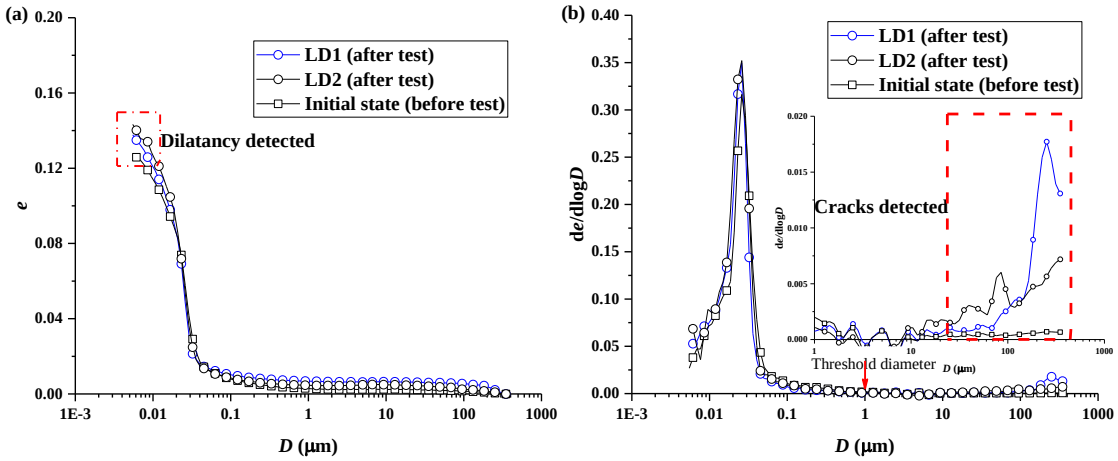

Fig. 3.29. Comparison of pore size distributions between the initial state and the one after test at the selected points

3.3.3 Preparation of damaged sample

3.3.3.1 Selection of damage criterion

As discussed in sections 3.3.1 and 3.3.2, the normalized tangent Young's modulus E_T/E_I is a relevant indicator to characterize the evolution of damage properties of COx claystone with changes of deviator stress. By analyzing the distribution of microcracks in test CM-4, it is found that significant damage was produced at the unloading point (Fig. 3.21), which corresponds to E_T/E_I 0.22. As summarized in Table 3.2, the ratio 0.22 corresponds to 0.9 time q_{max}. The ratio 0.9 is larger than the average crack initiation stress ratio 0.6 and the average dilatant stress ratio 0.83 identified by Zhang et al. (2013). In general, microcracks occur and the volume of rock begins to expand when the deviator stress exceeds the dilatant stress, as reported by Eberhardt et al. (1998) and Nicksiar et al. (2012). Besides, the decrease of G and E at the 4th unloading (corresponding to 0.9 time q_{max} in test CM-3) in Fig. 3.13 confirms that damage was indeed produced due to shearing. However, it is more complicated to use G or E as indicators to produce damaged claystone, because the sample needs to be loaded and unloaded many times in that case to calculate G or E.

Finally, based on the new indicator E_T/E_I proposed in this study, a damage criterion (E_T/E_I = 0.22) was selected to prepare all the damaged claystone samples used in this study. It ensures that damage can be generated inside the sample before the failure stress. It is worth noting that the constant mean stress loading path is adopted to prepare damaged claystone. This is consistent with the change of stress state in tunnel excavation, as reported by Liu et al. (2018).

3.3.3.2 Procedure of sample preparation

In this study, the damaged claystone is used in two types of test: oedometer test with controlled suction and CRS test with controlled suction. The procedure of sample preparation includes two steps: (1) an intact triaxial sample is loaded to the ratio E_T/E_I 0.22 in the high pressure triaxial cell, then unloaded; (2) the sample is sawed with the sawing machine to the target dimensions.

For the oedometer test with controlled suction, the triaxial sample from CM-4 was sawed into four samples with the dimensions 10 mm height and 38 mm diameter. Because the aim of this test is to investigate the effect of suction on hydro-mechanical behaviour of damaged claystone, the oedometer samples used for the four suctions selected were obtained from the same damaged triaxial sample to reduce the effects of triaxial sample differences. The sawing process is presented in Fig. 3.30a. On the other hand, for the CRS test with controlled suction, the main purpose is to explore the strain rate effect. Thus, each triaxial sample was cut into three samples with the dimensions 10 mm height and 38 mm diameter (Fig. 3.30b), corresponding to the three strain rates selected. In total, there are four suctions used in the CRS tests. Thus, four triaxial tests were performed to prepare the damaged samples. The stress-strain curves of the four triaxial tests are shown in Fig. 3.31. There are some differences for the stress-strain curves of four triaxial tests, but not significant. Considering different mechanical properties to be investigated in oedometer test with controlled suction and in CRS test, different preparation methods were adopted for damaged samples. The detailed information of sample preparation for the four tests are displayed in Table 3.3. Note that "sample ID" is the code name of the CRS samples, corresponding to the test program shown in chapter 2.

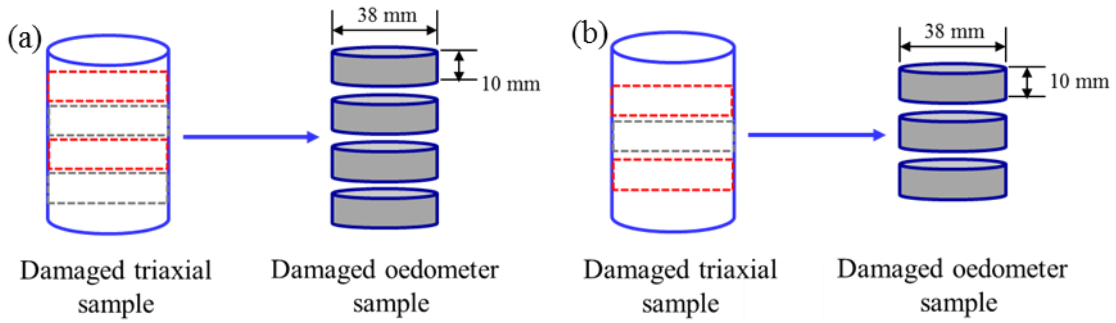

Fig. 3.30. The process of sample preparation: (a) oedometer test with controlled suction; (b) CRS test with controlled suction

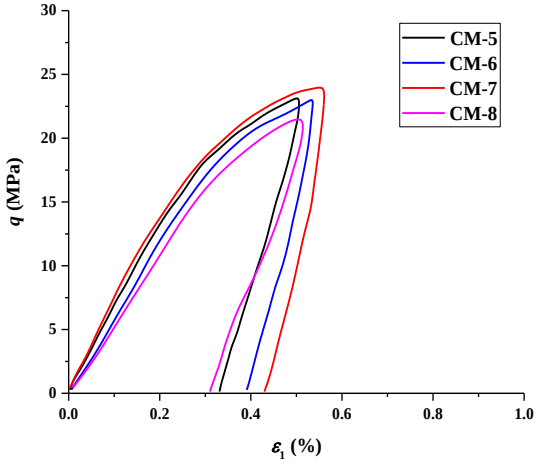

Fig. 3.31. Stress-strain curves of tests CM-5, CM-6, CM-7 and CM-8

Table 3.3 Damaged samples for CRS tests

Test No.	E_I (GPa)	E_T at unloading point (GPa)	Sample ID
			X1
CM-5	8.3	1.83	X2
			X3
			X4
CM-6	7.9	1.74	X5
			X6
			X7
CM-7	8.6	1.89	X8
			X9
			X10
CM-8	7.6	1.67	X11
			X12

3.4 Conclusions

This chapter is devoted to the development of the preparation methods of the samples used for triaxial and oedometer tests, involving intact, fractured and damaged samples. For the preparation of damaged samples, a new criterion was proposed based on the ratio of moduli E_T/E_I. The main conclusions are summarized as follows:

In the laboratory, COx claystone cylinder was first drilled from the COx core with the drilling machine. Then, by sawing the claystone cylinder, triaxial and intact oedometer samples were obtained with the target dimensions.

For the preparation of fractured claystone, intact oedometer samples were sawed into two parts, either in thinner disks or in semicircles. The thickness of the corresponding fracture depends on the roughness of contact surfaces between the two parts, which can be controlled by polishing the surfaces with a sand paper.

For the preparation of damaged samples, triaxial tests were first performed. The shear modulus G and Young's modulus E were determined and then used to analyze the damage properties. It was observed that both the shear modulus and Young's modulus decreased slightly with the increase of deviator stress. The degradation of mechanical parameters indicates that the damage was indeed generated inside the triaxial sample. For a practical reason, the tangent Young's modulus E_T was used to analyze the evolution of damage during shearing. Based on the analysis and discussion on E_T obtained in this study and other works, it is found that the average ratio $E_{T,0.9}/E_I$ 0.22 is a good criterion to characterise the sample damage corresponding to 0.9 q_{max}. This criterion was further validated by analysing the proportion of microcrack volume through X-ray tomography and MIP tests. Indeed, when the triaxial sample was loaded to the ratio E_T/E_I 0.22, significant microcracks were generated. Based on this criterion, an experimental procedure was proposed to prepare damaged samples used in oedometer tests and in CSR tests with suction control.

Chapter 4. Hydro-mechanical behaviour of intact and fractured COx claystone

In the first part of this chapter, the grain breakage phenomenon and its effect on the compressibility of COx claystone and other natural soils are reviewed and validated. Based on the mineral composition and compression behaviour, oedometer tests on artificial sand-clay mixture is designed to further analyse the effect of grain breakage on the compressibility of soils with granular inclusions. This part aims et clarifying a fundamental question about possible grain breakage effect on COx claystone volume change behaviour. In the second part of this chapter, the hydro-mechanical behaviour of fractured COx claystone is investigated and compared with that of intact one. Both horizontal and vertical fracture directions were considered.

4.1 Effect of grain breakage on compression behaviour of COx claystone

4.1.1 Introduction

Some previous studies showed that the compressibility of COx claystone increased in high stress range (Mohajerani, et al., 2011 and Menaceur, 2014). It is worth noting that this phenomenon is different from the observations on common clays, as described in Mesri and Godlewski, 1977. Wang (2012) observed that the calcite and quartz grains in COx claystone can be crushed under uniaxial compression. Considering the mineral composition of COx claystone (around 50% calcite and quartz grains), it is suspected that the increase of compressibility under high stress is related to the grain breakage.

The compression behaviour of granular materials (e.g. sand and rockfill) were widely investigated (Lee and Farhoomand, 1967; Nakata et al., 2001; Mesri and Vardhanabhuti, 2009; Mun and McCartney, 2017). It was found that under low stress the volume change of such materials is mainly attributed to grain rearrangement, rotation and inter-grain slip, while under high stress, the volume change can be greatly affected by grain breakage - the compression index was found to increase with stress, whatever the initial void ratio, mineralogy, grain size distribution and angularity (Nakata et al., 2001; Mesri and Vardhanabhuti, 2009).

Nevertheless, for clayey soils, the volume change behaviour is mainly controlled by the collapse of voids, as illustrated by Delage (2010) through observation at mercury intrusion porosimetry (MIP). For natural soils, this pore volume decreasing process is characterised by a compression

index which first increases to a maximum value with increasing stress, then decreases to a small value (Mesri and Godlewski, 1977). The former corresponds to the collapse of large pores, while the latter corresponds to the compression of small pores.

There are some natural fine-grained soils which contain a significant fraction of granular elements or grains such as quartz and calcite. To some extent, such soils can be regarded as composite materials with fines and granular grains. It has been well documented that the granular inclusions can significantly affect the global mechanical behaviour of soils (Revil et al., 2002; Monkul and Ozden, 2007; Zuo and Baudet, 2015; Crisci et al., 2019). Typically, for natural stiff clays, the texture is generally defined by clay, silt and sand (including quartz, calcite etc.). The granular inclusions are usually formed by mineral deposition and precipitations (Bauer Plaindoux et al., 1998; Klinkenberg et al., 2009; Debure et al., 2018). For such soils, both pore collapse and grain breakage may occur, depending on the stress level and the fine or grain fraction. In other words, the volume change behaviour may be greatly dependent on the stress level and fine or grain fraction.

In this section, the volume change behaviour of two natural clayey soils (COx claystone and Opalinus shale) reported in the literature was firstly explored in terms of compression index and mineral composition, allowing the grain breakage effect to be evidenced. Then, oedometer tests were performed on natural Teguline clay to verify this effect. Finally, artificial sand-clay mixtures were prepared with different clay fractions and tested in oedometer, allowing clarification of the role of fine fraction in the grain breakage phenomenon.

4.1.2 Analysis of the compression behaviours of COx and Opalinus claystones

The oedometer compression data of COx claystone and Opalinus clay are collected from literature (Mohajerani et al., 2011; Menaceur, 2014; Favero et al., 2016; Crisci et al., 2019). The mineral compositions of the two materials are shown in Table 4.1 and Table 4.2, respectively. It is found that for COx claystone, the quartz and carbonate parts almost occupy half of the mineral composition, as shown in Table 4.1. Similarly, for Opalinus clay, it also contains a large amount granular part (calcite and quartz) ranging from 34% to 54%, as shown in Table 4.2. To some extent, they can be regarded as mixtures of clay minerals with quartz and carbonate granular grains.

The compression curves of COx claystone are shown in Fig. 4.1. Tests T1 to T4 were performed by Menaceur (2014), while tests T5 and T6 were performed by Mohajerani et al. (2011). The COx claystone samples were saturated at constant volume, and then loaded in steps to 56 MPa

or 113 MPa, in the direction perpendicular to the bedding plane. A non-linear compression behaviour is observed without obvious straight line section. Thereby, it is difficult to define a unique compression index for characterizing the compressibility of COx claystone. Thus, a step compression index C_c* under each vertical stress was employed, as shown in Fig. 4.1. The similar method was adopted in Deng et al., (2012). Fig. 4.2 presents the computed C_c* for tests T1 to T6. With the increase of vertical stress, C_c* exhibits a slow increasing tendency, then increased rapidly after a critical stress. For all the six tests, the critical stresses are similar, ranging from 14 MPa to 28 MPa, as shown in Fig. 4.2. The difference can be attributed to the variability in mineral composition and initial void ratio.

Similarly, Fig. 4.3 presents the oedometer compression curves of Opalinus clay from tests TS and TD by Favero et al. (2016) and from tests T3V and T8V by Crisci et al. (2019). The tested Opalinus samples were extracted at different depths and had different initial void ratios. They were saturated at a constant vertical stress of 0.1 MPa and then loaded up to 100 MPa in steps. On the whole, the similar compression tendency was observed as for COx claystone. There is also a two-stage phenomenon similar to COx claystone in terms of C_c* variations, as shown in Fig. 4.4. However, C_c* of Opalinus clay is smaller than that of COx claystone, indicating a lower compressibility. A certain variability of critical stress is also identified – the values range from 9 MPa to 12 MPa.

Table 4.1. Mineralogy composition of COx claystone

Source	Clay (%)	Carbonates (calcite) (%)	Quartz (%)	Others (%)
Bauer Plaindoux et al. (1998)	40-50	20-30	25-30	＜10
Ghoreychi (1999)	30-60	20-40	-	＜5
Wright (2001)	40-45	30	25	0-5
Guéry et al. (2008)	45	28	23	4

Table 4.2. Mineralogy composition of Opalinus clay

Test No.	Source	Carbonates (calcite) (%)	Quartz (%)	Clay (%)	Others (%)
TS	Favero et al. (2016)	13	13	66	8
TD	Favero et al. (2016)	14.5	30	47	8.5
T3V	Crisci et al. (2019)	7.6	22	61	9.4
T8V	Crisci et al. (2019)	11.2	33	46	9.8

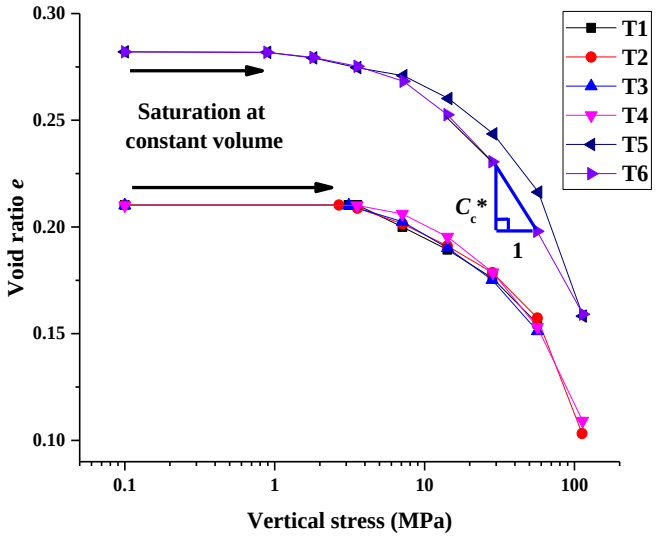

Fig. 4.1. Compression curves of COx claystone

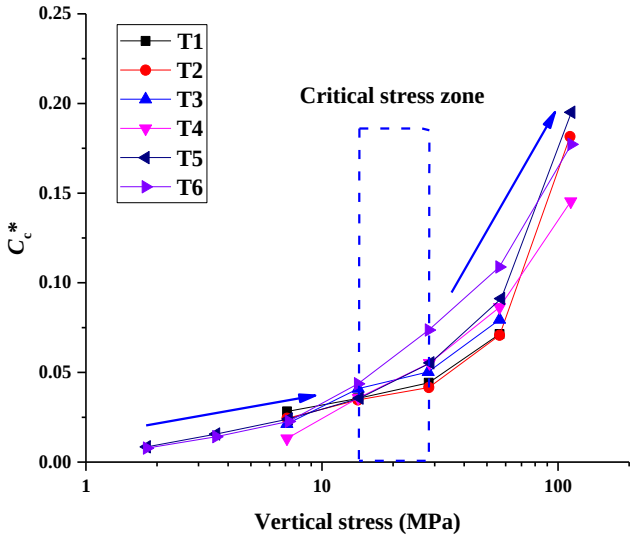

Fig. 4.2. C_c* versus vertical stress for COx claystone

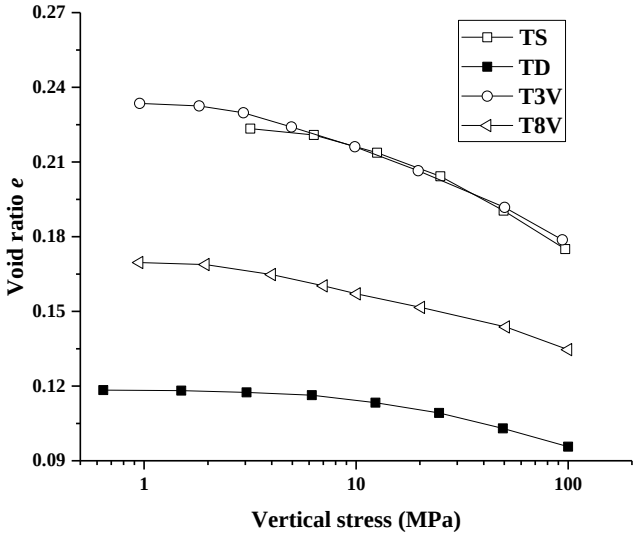

Fig. 4.3. Compression curves of Opalinus clay

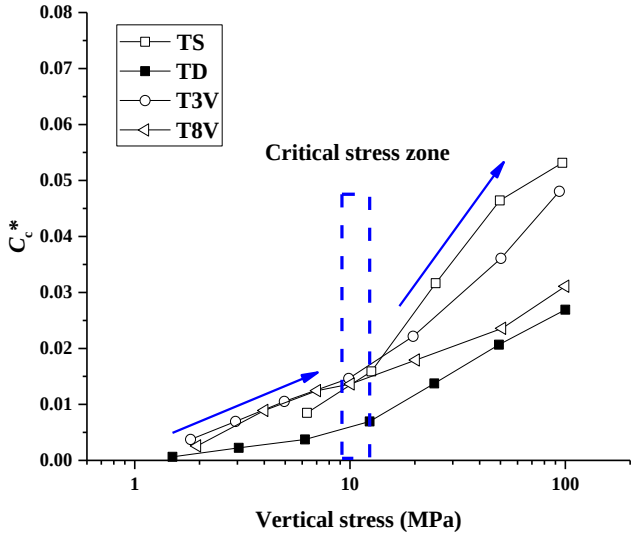

Fig. 4.4. C_c* versus vertical stress for Opalinus clay

The observed two-stage variation C_c* appears quite uncommon. Indeed, for remoulded clayey soils, C_c* firstly increases quickly, then keeps almost constant (Mesri and Godlewski, 1977). For sands and structured clayey soils, it decreases after reaching a maximum value (Nakata et al., 2001; Mesri and Vardhanabhuti, 2009). In addition, through the analysis of mineral grain distribution with BSE (backscattered electron) pictures for COx claystone (Klinkenberg et al., 2009) and Opalinus clay (Houben et al., 2014), it was observed that the granular inclusions, including quartz and carbonate grains, are unevenly distributed and locally aggregated in the clay matrix. Using the environmental scanning electron microscopy (ESEM) technique, Wang (2012) observed that some coarse grains in COx claystone were broken under uniaxial

compression. It can be thus suspected that the uncommon two-stage change of C_c* was related to the grain breakage phenomenon - with grain breakage, C_c* increased, showing a higher compressibility.

4.1.3 Compression behaviour of Teguline clay

4.1.3.1 Material and methods

To verify the uncommon compression phenomenon observed on Opalinus clay and COx claystone, high pressure oedometer tests were carried out on natural stiff Teguline clay. Two Teguline clay cores were taken by bore drilling in Aube, France. Oedometer samples of diameter 50 mm and height 20 mm were prepared in the laboratory by trimming. The specific gravity of this soil is 2.71. The mineralogy composition was determined by Debure et al. (2018) and Lerouge et al. (2018), and shown in Table 4.3. The basic physical characteristics of the two cores are presented in Table 4.4.

Table 4.3. Mineralogy composition of Teguline clay

Source	Carbonates (calcite) (%)	Quartz-feldspar (%)	Clay (%)	Others (%)
Debure et al. (2018)	9.4-16.5	26.1-31.7	56-57.4	-
Lerouge et al. (2018)	9	36	51	＜5

Table 4.4. Initial geotechnical properties of Teguline clays

Core	Depth (m)	Water content (%)	Dry density (g/cm^3)	Void ratio
AUB220	19.07-19.43	9.79	2.18	0.24
	28.08-28.40	9.79	1.94	0.40
AUB230	8.83-9.15	17.51	1.81	0.50
	13.70-14.02	11.76	2.05	0.32
	26.00-26.32	15.93	1.91	0.42

Oedometer tests were performed. In each test, after installing the sample into the cell, a saturation process was applied under a vertical stress corresponding to the in-situ stress, aiming

at avoiding soil swelling or change of microstructure (Zhang et al., 2018, 2019). The corresponding in-situ effective vertical stress σ'_{v0} was estimated based on Eq. 4-1 by assuming the underground water table to be at the ground surface:

$$\sigma'_{v0} = \sigma_{v0} - u_0 = \gamma_{sat} h - \gamma_w h \quad (4\text{-}1)$$

where γ_{sat} and γ_w are the soil average unit weight and the water unit weight, respectively; h is the depth; u_0 is the pore water pressure.

After the saturation, loading was applied by increasing the vertical stress in steps till 16 or 32 MPa, in the direction perpendicular to the bedding plane. The vertical strain was considered as stabilized, when it was lower than 5×10^{-4}/8h (AFNOR, 2005). The test programme is shown in Table 4.5.

Table 4.5. Test programme for Teguline clay

Test No.	Core	Depth (m)	In-situ stress (MPa)	Maximum stress (MPa)
T2-19	AUB220	19.07-19.43	0.22	32
T2-28		28.08-28.40	0.33	32
T3-8	AUB230	8.83-9.15	0.10	16
T3-13		13.70-14.02	0.16	32
T3-26		26.00-26.32	0.30	32

4.1.3.2 Results

Fig. 4.5 shows the compression curves of Teguline clay from two boreholes and five depths. The initial void ratios have some difference, indicating a certain variability. Fig. 4.6 shows that C_c* of tests T3-8 and T3-26 has a rapid increase after 8 MPa, which can be regarded as the values of critical stress. For tests T2-19, T2-28 and T3-13, although a relatively steady C_c* increasing trend is obtained, a critical stress can be determined at 16 MPa where a more significant C_c* increase is noted. Further examination shows that the effect of initial void ratio has insignificant effect on the critical stress because the samples from the same core at different depths (thus different initial void ratios) have the same critical stress value. The difference

between the two cores may be attributed to the effect of mineralogy variability.

The existence of a critical stress for Teguline clay can be also explained by the grain breakage. Indeed, it appears from Table 4.3 that the mineralogy of Teguline clay is defined by almost half of clay minerals and half of other minerals such as quartz, feldspar and carbonates or calcite (Debure et al., 2018; Lerouge et al., 2018). Thereby, this soil can be also regarded as a composite material, including clay matrix and granular inclusions. Lerouge et al. (2018) reported that these granular inclusions have different size, shapes and strength. In addition, their distributions are uneven. Under a certain stress, these grains can be broken, giving rise to an increase of C_c*.

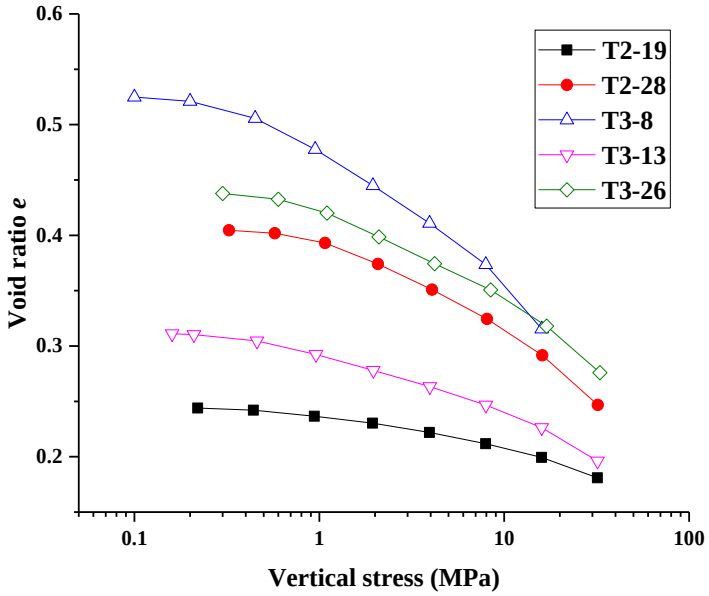

Fig. 4.5. Compression curves of Teguline clay

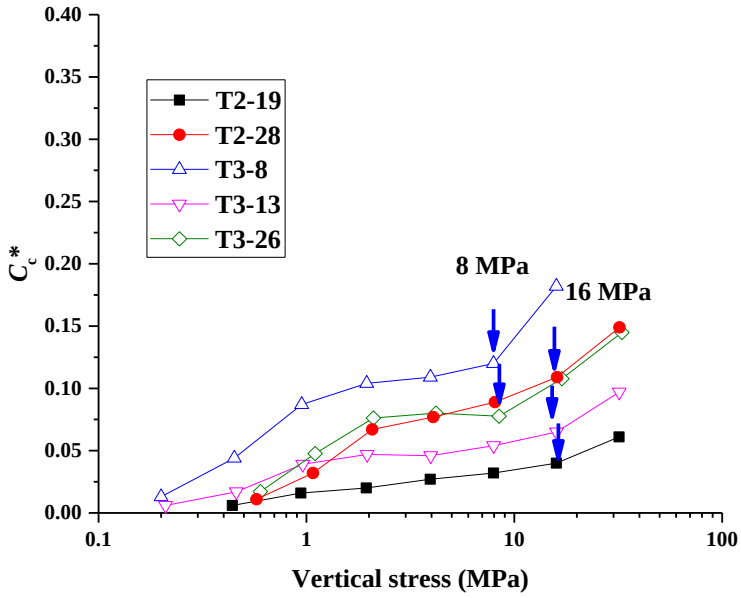

Fig. 4.6. C_c* versus vertical stress for Teguline clay

4.1.4 Compression behaviour of sand/kaolinite mixtures

4.1.4.1 Material and methods

To further clarify the effect of grain breakage on soil compressibility, oedometer tests were carried out on artificial Hostun sand/Speswhite kaolinite mixtures. Hostun sand (HN31) is a uniform and sub-angular silica material with a diameter at 50% passing D_{50} of 0.32 mm, a uniformity coefficient C_u of 1.3 and a specific gravity G_s of 2.65 (Feia et al., 2014). The Speswhite kaolinite has a water content of 0.9 % and G_s of 2.64 (Muhammed et al., 2018). The grain-size distribution curves of Hostun sand and kaolin clay were obtained by sieving and hygrometer methods, respectively. The results are shown in Fig. 3.30. Seven clay contents (20, 30, 40, 60, 80, 90, 100) were considered (Table 4.6). These samples were prepared by compaction in oedometer cell. The dimensions of the samples were 38 mm diameter and 15 mm height, defining a dry density of 1.65 Mg/m^3. In addition, the pure sand sample (S100K0) with the same dimension was prepared by taping in oedometer cell, avoiding significant grain breakage prior to testing. The aim of test S100K0 is to characterize the grain breakage behaviour of pure sand. Oedometer tests were performed with loading in steps till 100 MPa. Vertical strain was considered as stabilized when the rate was below 1 μm/10min, as recommended by Shiptona and Coop (2012).

Table 4.6. Test programme for sand-clay mixture

Test No.	Clay fraction by dry mass (%)	Initial sand fraction by volume (%)	Note
S100K0	0	52.6	/
S80K20-C	20	50.1	Compacted
S70K30-C	30	43.8	Compacted
S60K40-C	40	38.5	Compacted
S40K60-C	60	27.7	Compacted
S20K80-C	80	12.9	Compacted
S10K90-C	90	6.3	Compacted
S0K100-C	100	0	Compacted

4.1.4.2 Results

The compression curves of sand-clay mixtures with different clay fractions are presented in Fig. 4.7. For test S100K0 with pure sand, yield occurs at around 6 MPa. Before 6 MPa, the slope is small, corresponding mainly to the rearrangement of sand grains. By contrast, beyond 6 MPa, the slope becomes much larger, which must correspond to the grain breakage, as reported by Mesri and Vardhanabhuti (2009), Mun and McCartney (2017). For other samples with different clay fractions, the compression curves exhibit a more gradual yielding process. At the same initial void ratio, the tests with medium clay contents (S40K60-C and S60K40-C) exhibit relatively lower void ratios under the same vertical stress, suggesting a higher compressibility. By contrast, the tests with lower and higher clay contents (e.g. S80K20-C and S10K90-C) show larger void ratio, suggesting a lower compressibility.

Fig. 4.8 shows that C_c* increases with the increase of vertical stress. As before, the critical stresses are identified at the points where C_c* increases significantly, as shown in Fig. 4.1. For each test, the critical stress divides the vertical stress values into two zones: low stress zone and high stress zone. In addition, C_c* of pure sand (S100K0) is significantly higher than those of other mixtures in the high stress range. C_c* increases slowly in the low stress zone, but quickly in the high stress zone even under 100 MPa stress. This is consistent with the observations on natural soils such as COx claystone, Opalinus clay and Teguline clay.

Fig. 4.9 shows the comparison of grain size distributions (GSD) of soils S100K0, S60K40-C, S40K60-C and S0K100-C before and after testing. For S100K0, significant grain breakage was identified with production of a large amount of smaller grains. On the contrary, for S0K100-C, no grain breakage was identified. This suggests that the grain breakage phenomenon is strongly dependent on the grain size. At a size as small as the kaolinite particle one, grain breakage cannot occur. This is consistent with the observation by Shipton and Coop (2012). For the mixtures S40K60-C and S60K40-C, it is observed that grain breakage also occurs. Moreover, at a higher sand fraction (S60K40-C), the grain breakage phenomenon is more significant.

Fig. 4.10 shows that the evolution of critical stress with sand fraction, either in mass (Fig. 4.10a) or in volume (Fig. 4.10b). The critical stress exhibits a nearly linear decreasing tendency in low and high sand fraction ranges, while a transitional change is observed in the middle range. Using a bilinear method, a characteristic sand fraction in mass (f_{mc}) and a characteristic sand fraction in volume (f_{vc}) can be determined, as for other soil mixtures by Revil et al. (2002), Shipton and Coop (2012), Wang et al. (2018) and Qi et al. (2020).

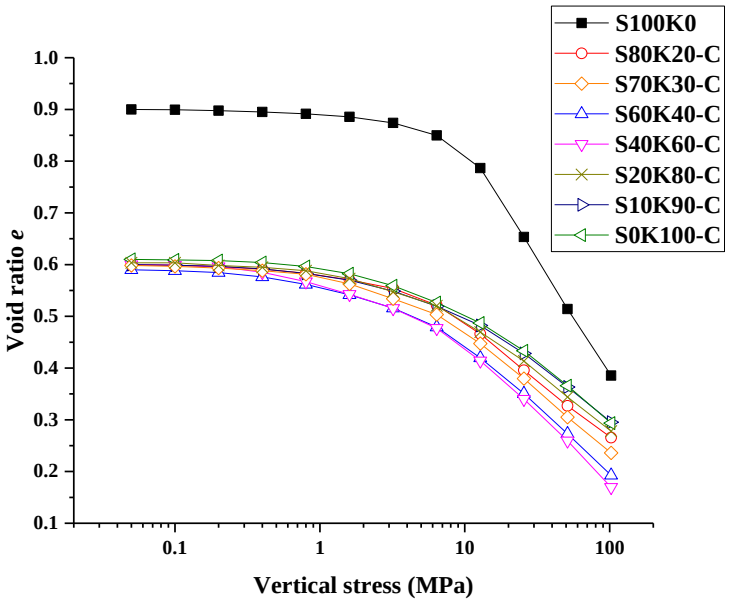

Fig. 4.7. Compression curves of sand-clay mixtures

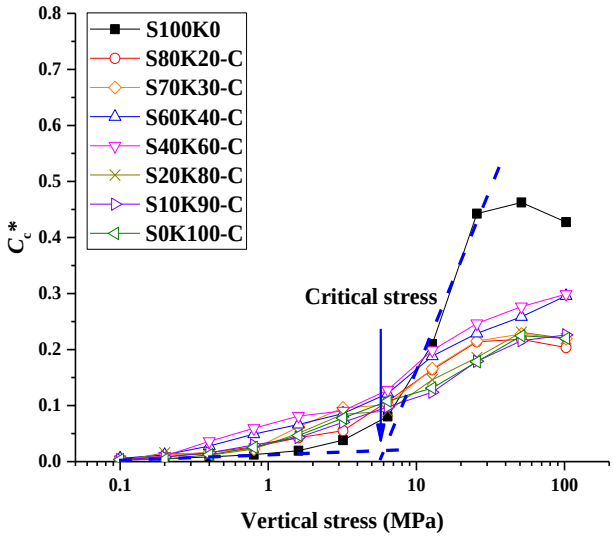

Fig. 4.8. C_c* versus vertical stress for sand-clay mixtures

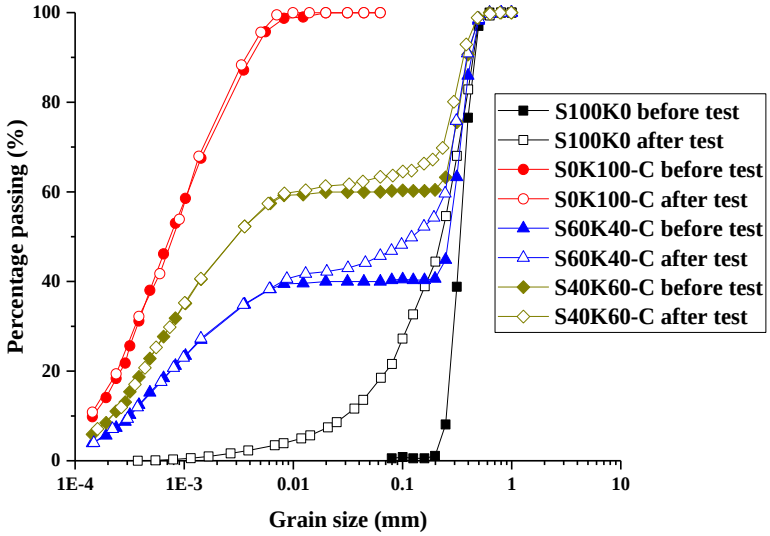

Fig. 4.9. Grain size distributions before and after tests

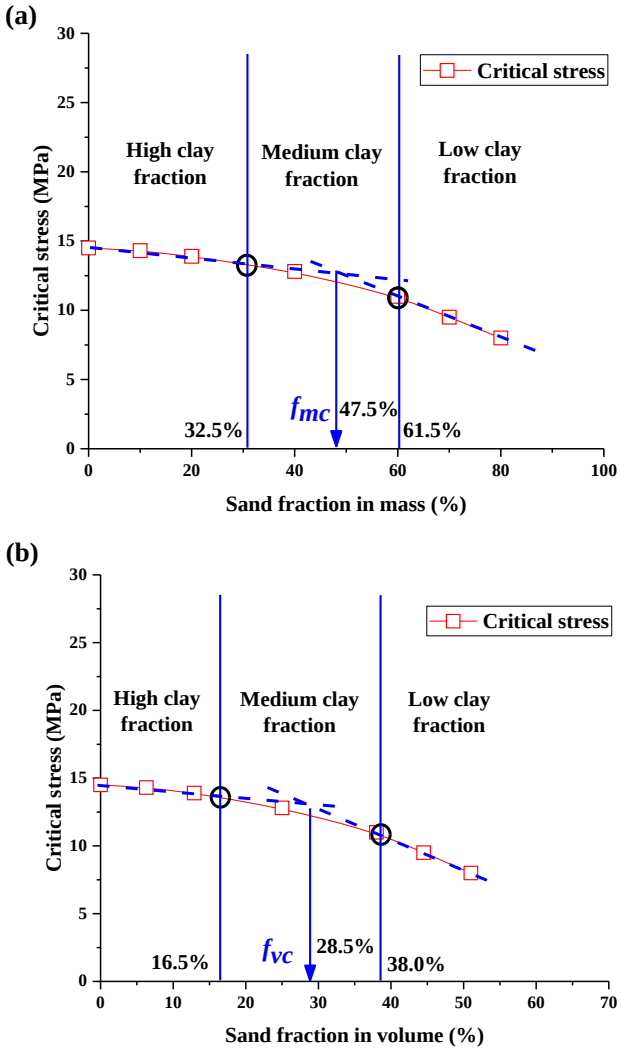

Fig. 4.10. Variation of critical stress with sand fraction: (a) in mass; (b) in volume

4.1.5 Interpretation and discussion

The proportion of fine or coarse grains in soil mixture defines its structure and thus its compression behaviour (Shipton and Coop, 2012; Zuo and Baudet, 2015; Qi et al., 2020). Generally, there is a threshold coarse grain content, which divides the soil structure into two types: fine grain and coarse grain dominated structures. The transitional fine content is found to be between 20% and 50%, depending on the mineralogy, size and shape of coarse grains (Zuo and Baudet, 2015).

For sand/clay mixtures, Monkul and Ozden (2007) found that the soil structure is dominated by sand grains when the clay content is below 20%. Moreover, Shipton and Coop (2015) found that with a transitional clay content, the mechanical behaviour of sand/clay mixture changes significantly with clay content. Thus, it appears more appropriate to divide the structure of soil mixture into three zones. By adopting the deviation point (black circle) between the straight line part and the curving part in Fig. 4.10, three zones can be indeed well defined: low clay fraction zone (LC), medium clay fraction zone (MC, i.e. transition zone) and high clay fraction zone (HC).

Mun and McCartney (2017) summarized a large amount of experimental studies on the compression behaviours of granular materials, indicating that grain breakage plays a major role in the shearing and compression processes under high stress. The breakage of coarse grains can enable poorly graded soils to shift to a better graded state, inducing void closure. This is confirmed by the comparison of the grain size distribution curves before and after test S100K0. In the LC case (see Fig. 4.11), sand skeleton is formed and sand grains are in contact with each other. Thus, the volume change behaviour is governed by the rearrangement of sand grains under low stress, and by the grain breakage in high stress range. The lower the clay fraction, the more the sand grain contacts and the more significant the grain breakage characterised by a lower critical stress as shown in Fig. 4.10. On the contrary, in the HC case, all sand grains are dispersing in a clay matrix (Fig. 4.11). As the volume change is mainly induced by the collapse of pores in clay matrix (Delage, 2010), the critical stress changes little, suggesting that there is no occurrence of breakage phenomenon. In the MC case, the distribution of sand grains is complex in the mixture. A part of sand grains is initially in contact with each other, defining local clay matrices and local sand skeletons (Fig. 4.11). With the increase of vertical stress, more sand grains are in contact, increasing the size of sand skeletons. When the vertical stress exceeds a certain value, sand grain breakage occurs, resulting in a higher compressibility of

mixture. This explains why for tests S40K60-C and S60K40C in Fig. 4.8, C_c* displays more continuous increasing tendency under high stress. Summarising, the compression process in the MC case can be divided into two stages: (i) low stress stage where the volume change is mainly induced by the compression of clay matrix as in the HC case without sand grain breakage; (ii) high stress stage where sand grain breakage occurs after large sand skeletons are formed as in the LC case, leading to a higher compressibility of mixture. As a conclusion, the compression behaviour of sand-clay mixture is governed by both sand grain breakage and collapse of pores in the clay matrix, depending on the sand-clay ratios and stress levels.

As indicated before, based on the analysis of mineral compositions, COx claystone, Opalinus clay and Teguline clay can all be regarded as soil mixtures with clay matrix and granular grains (carbonate and quartz, etc.). The same compression phenomenon (rapid and continuous increasing of C_c*) were observed on these natural soils and the artificial sand clay mixtures. It can thus be deduced that the compression behaviour of natural soils is also jointly governed by breakage of granular grains and collapse of pores in clay matrix. In particular, when a natural soil contains of clay fraction in the medium range, relatively high stress is needed to form large granular grain skeleton and thus grain breakage. This may result in a continuous increasing C_c* as observed in Fig. 4.6.

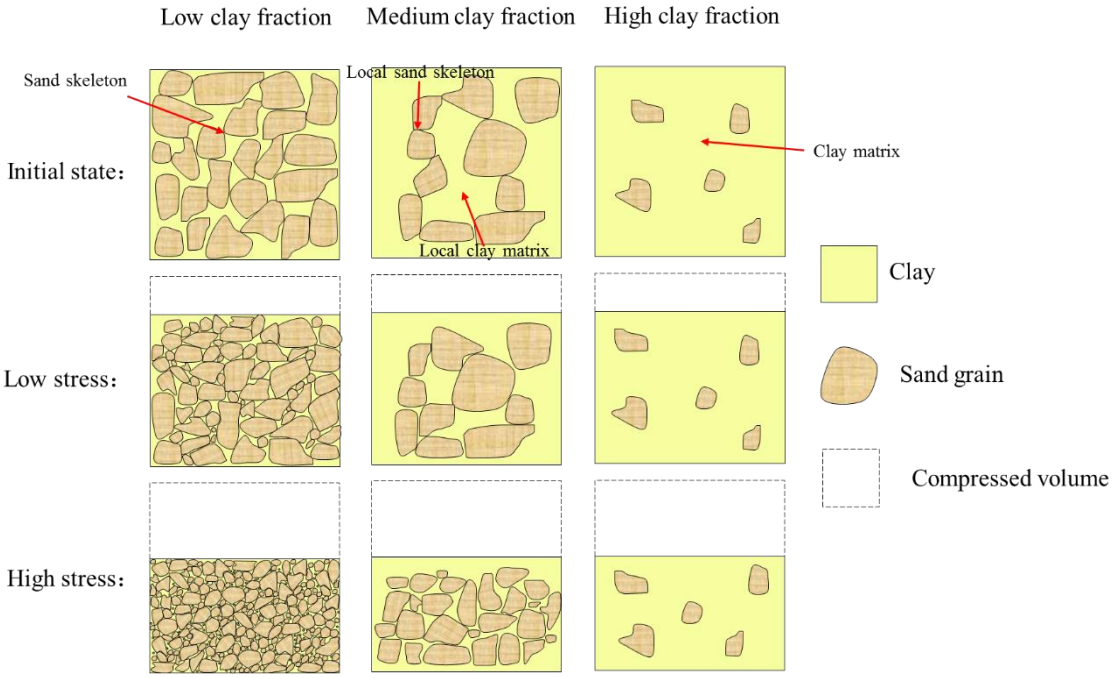

Fig. 4.11. Representation of soil structure changes during the compression process for different clay fractions

It is worth noting that in addition to the granular grain content, other factors such as grain size

and shape can affect the grain breakage phenomenon. Indeed, Klinkenberg et al. (2009) reported that compared to COx claystone, Opalinus clay has carbonate and quartz grains of larger size and in more irregular shapes. It is thus expected that Opalinus clay is more breakable than COx claystone. Indeed, Nakata et al. (2001) and Mesri and Vardhanabhuti (2009) reported that, for the grains of larger size, the grain breakage is more significant, which is characterised by a lower critical stress. This explains why Opalinus clay has a lower critical stress (9-12 MPa) than COx claystone (14-28 MPa).

4.2 Effect of fracture on swelling and compression behaviour of COx claystone

4.2.1 Swelling behaviour

As described in chapter 2, two test cases were set to simulate the different in situ conditions with underground water infiltrating into fracture through COx claystone: Case 1 - the sample was wrapped with filter paper between the sample and cell wall at the radial direction to simulate the underground water directly flowing into the fractures; Case 2 - without filter paper to simulate the underground water infiltrating into fracture through COx claystone. Filter papers were used in tests TH-1 and TV-1 to simulate the in situ condition with underground water directly flowing into the fractures. Tests TH-2 and TV-2 without filter paper simulate the in situ condition with underground water infiltrating into fracture through COx claystone. By contrast, test TI was performed on intact sample without filter paper.

For the saturation process in the two cases, sample began to swell under the initial stress after synthetic water was injected. Fig. 4.12 shows the evolution of vertical swelling strains with time in the two cases. Based on the development of vertical swelling strain, three significant stages are divided: initial swell, primary swell and secondary swell, as recommended by Rao et al. (2006) and ASTM, D4546 (2014). The vertical swelling strain increased slowly with time at the beginning, then increased quickly, finally increased steadily. At the end of the swelling process, test TH-1 exhibited a higher vertical strain than test TV-1 (3.49 % against 3.06 %) in Case 1, while the vertical strains of tests with fractures (TH-2: 3.19 % and TV-2: 3.38 %) are closer in Case 2. The vertical strains in both cases are smaller than that of test TI (3.54 %).

Fig. 4.13 shows the evolution of the vertical swelling strain rate with time, which is defined by the difference of swelling strain at time interval in log scale. It is found that the vertical swelling strain rates of all tests increased with time at the beginning, then reached the maximum, finally decreased steadily. As presented in Fig. 4.13a, the vertical swelling strain rate of test TH-1 in

the initial swell and secondary swell stages were slightly lower than that of test TV-1, while much larger in the primary swell stage. However, without the effect of filter paper (Case 2), tests TH-2, TV-2 and TI revealed the similar vertical swelling strain rate in the primary swell stage (Fig. 4.13b). In initial swell stage, TV-2 has a larger swelling rate than TH-2 and TI. Nevertheless, test TI has a larger swelling rate than tests TH-2 and TV-2 in the secondary swell stage.

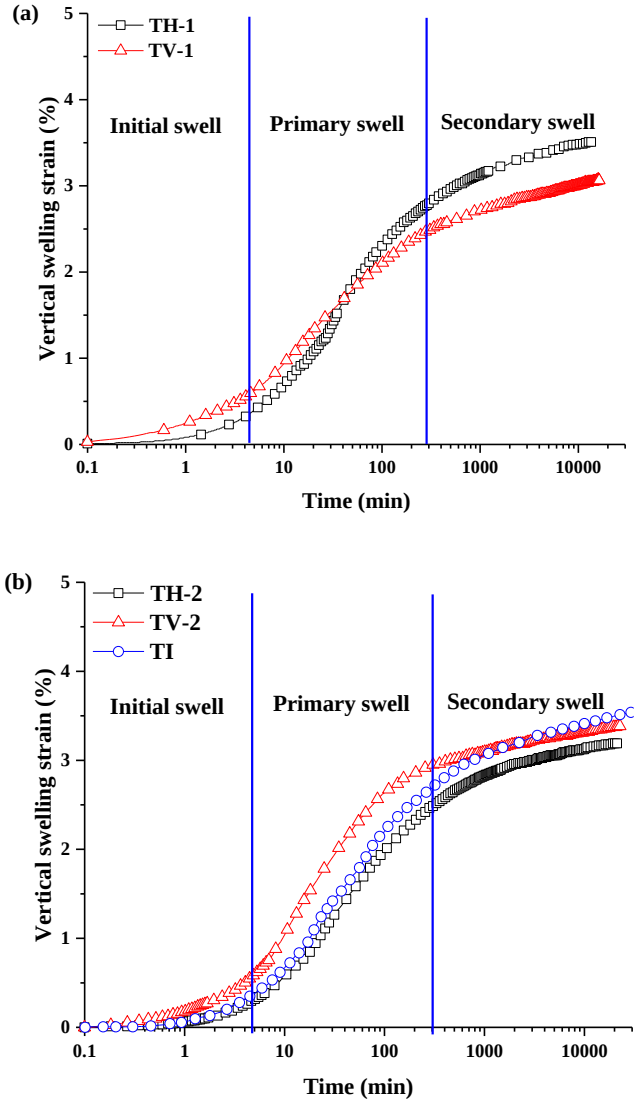

Fig. 4.12. Vertical swelling strain versus time; (a) Case 1; (b) Case 2 and test TI

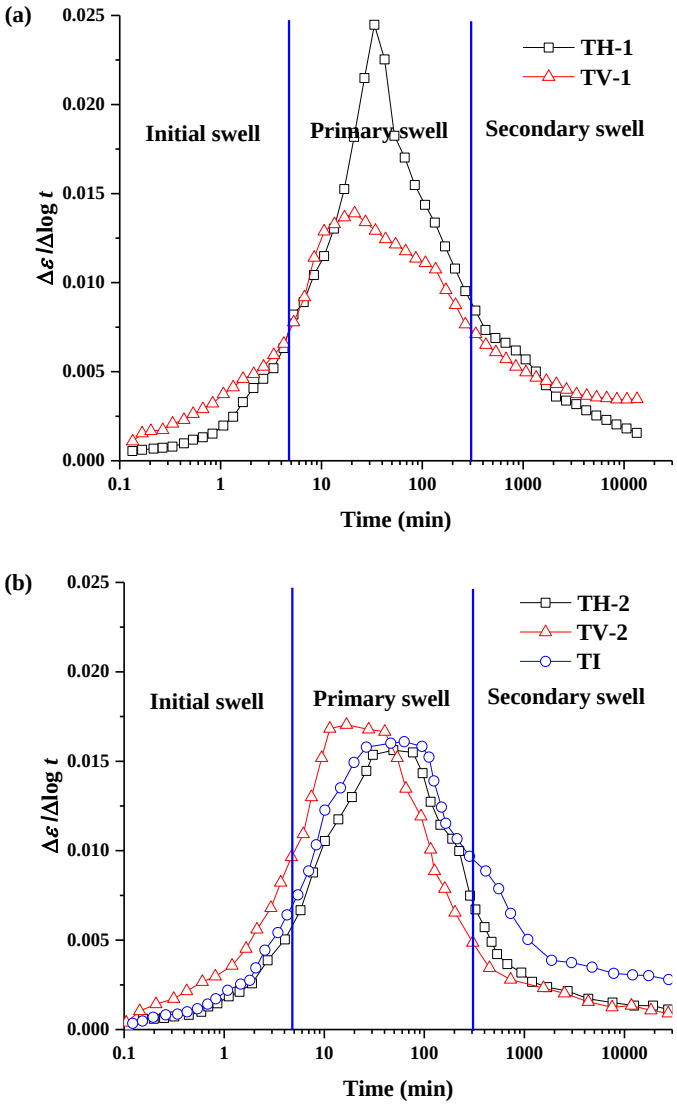

Fig. 4.13.Vertical swelling strain rate ($\Delta\varepsilon/\Delta\log t$) versus time: (a) Case 1; (b) Case 2 and test TI

Fig. 4.14 shows the swelling processes of fractured and intact claystone, corresponding to two cases mentioned (i.e. different in situ conditions). Due to the vertical water injection direction, synthetic water went into the vertical fracture more easily in spite of the effect of filter. Thus, the samples with vertical fracture swelled more quickly at the initial swell stage, demonstrated by the higher vertical strain (Fig. 4.12) and strain rate (Fig. 4.13). In Case 1, after water entered the horizontal fracture via the filter paper, the hydration rate of test TH-1 speeded up because of the shorter infiltration path compared to test TV-1. Thus, it results in a higher vertical swelling strain rate in the primary swell stage (Fig. 4.13a). In addition, at the end of the tests, the higher final swelling strain and lower strain rate of test TH-1 lead to a swelling strain closer to that of test TV-1. This can be explained by their similar global initial void ratios or dry densities. By contrast, in Case 2, tests TH-2 and TI have the same infiltration path, showing the similar

vertical swelling strains (Fig. 4.12b) and strain rates (Fig. 4.13b) in the initial and primary swelling stages. The results indicate that the swelling of fractured claystone depends on the infiltration path and the direction of initial fracture.

The initial swell and primary swell of all tests can be supposed to be induced by the crystalline swelling in clay minerals, while the osmotic swelling mainly contributed to the further increase of vertical strain in the secondary swell stage (Rao et al., 2006; Di Donna et al., 2019). Due to the effect of swelling, the factures can be closed gradually, which corresponds to the self-sealing property as reported by Zhang (2011, 2013). The self-sealing in COx claystone is mainly induced by the swollen clay minerals, as demonstrated through 3D tomography results conducted by Giot et al. (2018) and Di Donna et al. (2019). During this self-sealing process, the hydraulic conductivity decreases gradually, as observed by Giot et al. (2018). The existing experimental results (van Geet et al., 2008; Zhang, 2011; de la Vaissière et al., 2015) show that the self-sealing process can be divided into three stages: (i) closure - the swelling of claystone near the fracture surface induces fracture closure with the expansion of clay minerals; (ii) clogging - the claystone grains disaggregate and clog the fracture zone; (iii) homogenization - the macro-pores between the disaggregated claystone grains collapse by the further swelling of claystone farther from the fracture zone.

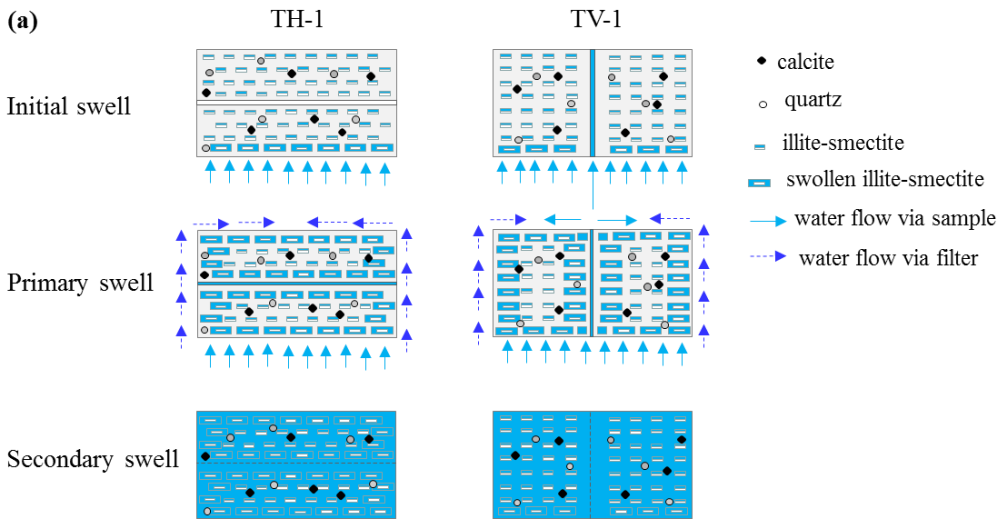

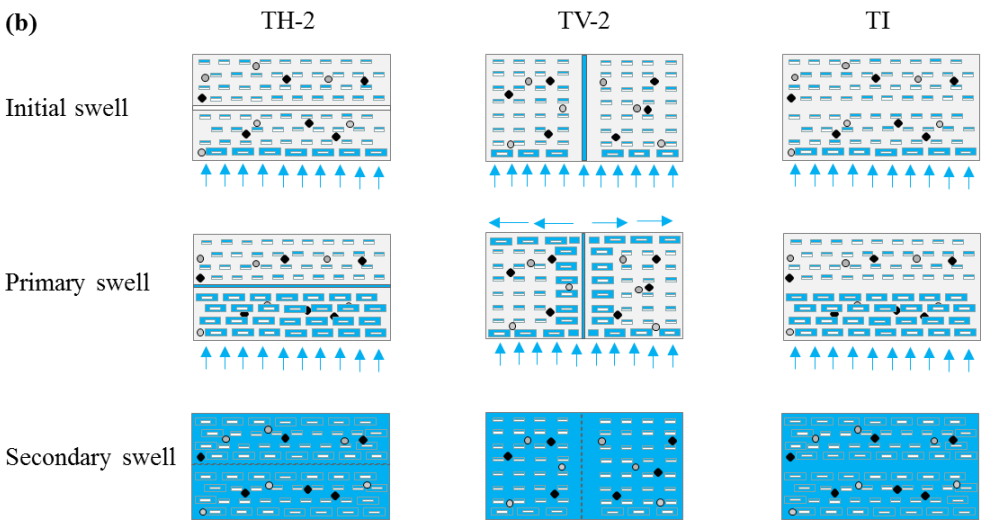

Fig. 4.14. Schematic view of the swelling process: (a) Case 1; (b) Case 2 and test TI

4.2.2 Compression, hydraulic conductivity and creep

All compression curves are reported in Fig. 4.15 and Fig. 4.16a for Case 1 and Case 2 respectively, in terms of global void ratio (including the filled fracture). Fig. 4.15 shows that with increasing vertical stress, the void ratios of test TH-1 become smaller than that of test TV-1, indicating that the compressibility of sample with horizontal fracture is higher than that with vertical fracture. This confirms the dependency of the compression behaviour on the fracture orientation. The similar phenomenon is observed in Fig. 4.16a. The yield stress (0.45 MPa) of test TH-1 is smaller than that of test TV-1 (0.65 MPa). The similar phenomenon is observed while comparing TH-2 and HV-2: the yield stress of test TH-2 (0.48 MPa) is smaller than that of TV-2 (0.71 MPa). These results show that after swelling, the compression behaviour of the sample with fractures is not significantly different. By contrast, test TI exhibits a significantly higher yield stress (1.08 MPa). Besides, the curve of test TI becomes closer to that of test TH-2 in the high stress range, as shown in Fig. 4.16a. It appears from these results that: (i) the filled fracture zone due to swelling is a weak zone, resulting in a higher compressibility of the fractured sample; (ii) the increase of stress can induce collapse of the macro-pores in the filled fracture zone, enabling the compression curve to gradually approach the intact one. Note that this macro-pore collapse effect was also reported by Zhang (2011, 2013). In addition, a significant change of slope is observed after 16 MPa with respect to the compression curves (Fig. 4.15 and Fig. 4.16a), indicating the increase of compressibility. This is due to the grain breakage, as analysed before.

The vertical hydraulic conductivities (k) were measured. Comparing the measured k (Fig. 4.16b)

to the compression curve (Fig. 4.16a), it is found that the *k* of test TV-2 slightly decreases with loading before the yield stress, then decreases significantly. This is closely related to the volume change of the sample. The similar phenomenon was observed by Zhang (2011, 2013). Blackwell et al. (1990) highlighted that the permeability of clayey soils is significantly related to the macro-porosity. In this sense, it can be inferred that the measured *k* of test TV-2 is controlled by the large pores in the filled fracture zone. For test TH-2, the measured *k* in test TH-2 is governed by the small pores in the intact part, which can be deduced from the comparison between tests TH-2 and TI in Fig. 4.16b. This is correlated to the relationship between the direction of the measured *k* (vertical) and that of fracture zone (horizontal or vertical). Note that intact part means the zone without fracture inside the sample before test. The stress 0.25 MPa (Fig. 4.16b) can be regarded as the yield point of intact part in test TV-2. Interestingly, this corresponding stress corresponds to the yield stress identified in Fig. 4.16a. After around 16 MPa, the *k* of TV-2 decreases steadily and is comparable with that of test TI, indicating that the hydraulic conductivity of the fractured sample "recovers" the intact one (Fig. 4.16b). By contrast, due to the steady decreasing of the porosity of intact part, test TH-2 displays a gradual decrease of *k*, as test TI.

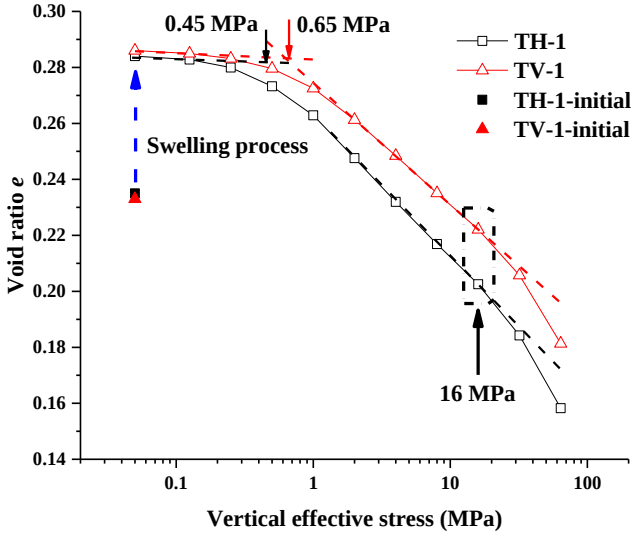

Fig. 4.15. Compression curves of tests TH-1 and TV-1

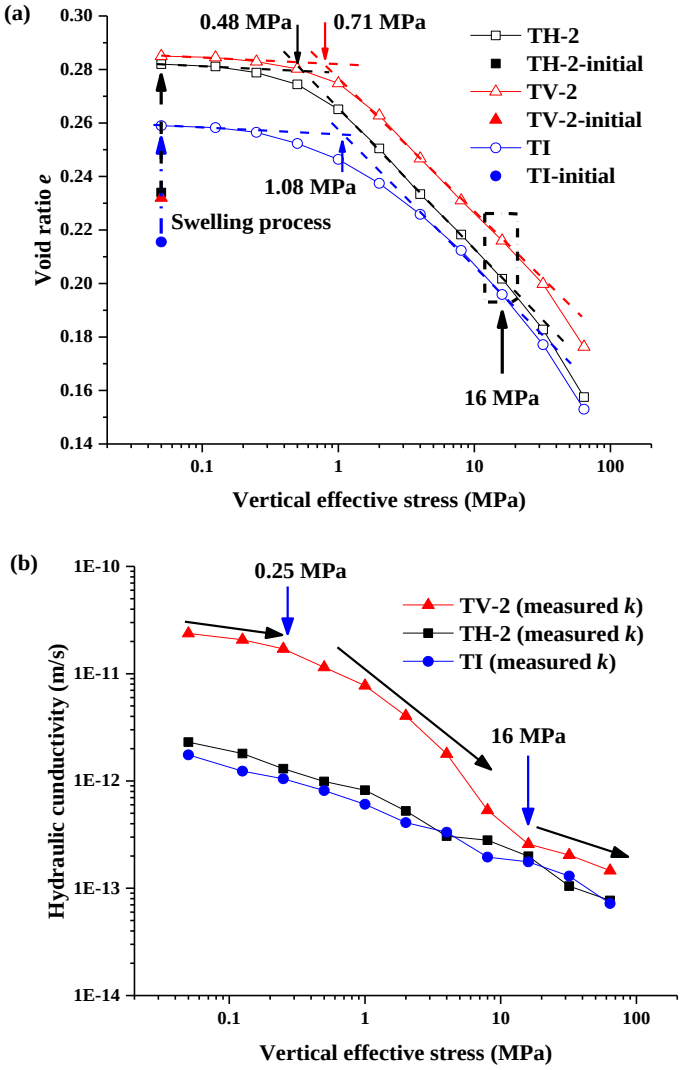

Fig. 4.16. Tests TH-2, TV-2 and TI: (a) compression curves; (b) hydraulic conductivity curves. Note: the measured k was determined by using pressure-volume controller

To further estimate the hydraulic conductivity of COx claystone, the hydraulic conductivities are calculated by back-analyzing the oedometric test results based on the consolidation theory (Biot, 1941; ASTM-2435, 1996). The simplified one-dimensional consolidation equation is adopted, as shown in Eq. 4-2 (Biot, 1941; Crisci, et al., 2019):

$$c_v \frac{\partial^2 u_e}{\partial z^2} = \frac{\partial u_e}{\partial t} - C \frac{\partial \sigma_z}{\partial t} \tag{4-2}$$

where u_e is the excess pore water pressure, σ_z is the total vertical stress, t is the time, c_v is the consolidation coefficient and C is the ratio between the increment of u_e and the increment of σ_z under undrained condition. c_v can be calculated with Eq. 4-3:

$$c_v = \frac{k(1+e)}{\gamma_w a} \tag{4-3}$$

where k is the hydraulic conductivity, a is the compression coefficient, e is the void ratio under each stress and γ_w is the water unit weight. The compression coefficient a is the ratio between the decrement of e and the increment of σ_z, as follows:

$$a = \frac{-\Delta e}{\Delta \sigma_z} \tag{4-4}$$

In addition, based on the time-deformation curve under each vertical stress in oedometer test, the consolidation coefficient c_v can be determined by Eq. 4-5 (ASTM-2435, 1996). In this study, c_v is determined based on the curve with logarithm of time.

$$c_v = \frac{T_{50} H_{D_{50}}^2}{t_{50}} \tag{4-5}$$

where $T_{50} = 0.197$, t_{50} is the time corresponding to 50 % of the primary consolidation, H_{D50} is the length of the drainage path at 50 % of primary consolidation.

Thus, the global vertical hydraulic conductivity can be calculated by combining Eq. 4-3 to Eq. 4-5 and compared with that measured from the test.

All hydraulic conductivities obtained are summarized with respect to vertical effective stress and void ratio in Fig. 4.17. With the increase of vertical effective stress, all hydraulic conductivities display a similar decreasing tendency (Fig. 4.17a). Fig. 4.17b shows that small changes of void ratio can lead to a significant reduction of hydraulic conductivity, indicating the strong dependencies on void ratio. The measured hydraulic conductivity of test TV-2 is significantly higher than the others, indicating that the large pores in the filled fracture zone indeed intensifies the water permeability. Favero et al. (2016) and Crisci et al. (2019) made the similar observations on Opalinus clay shale, pointing out that the hydraulic conductivity is significantly affected by the larger pores and can be enhanced by the presence of fractures.

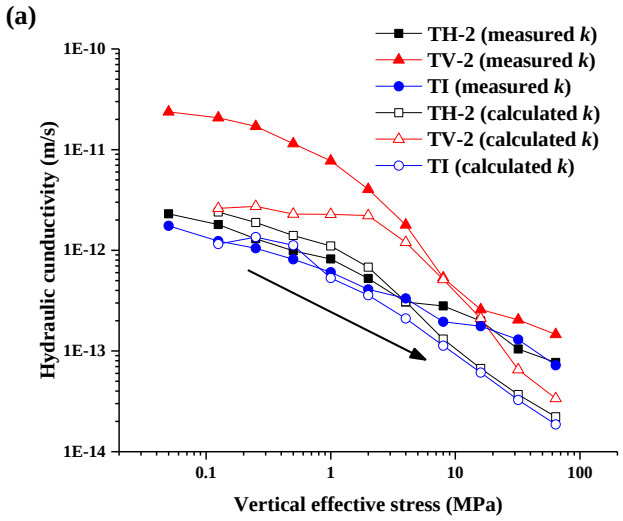

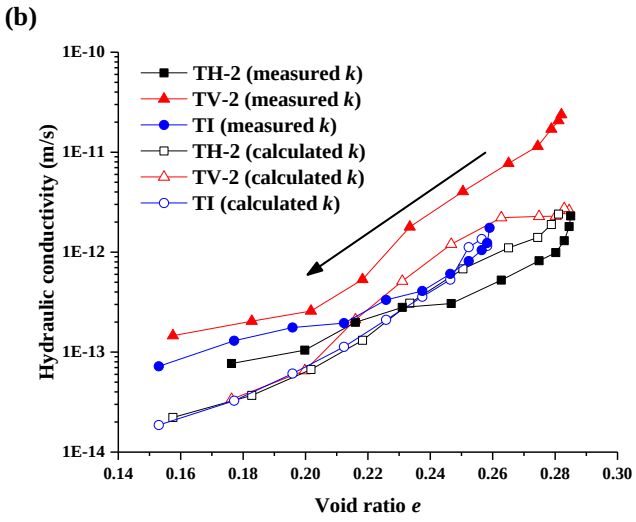

Fig. 4.17. Tests TH-2, TV-2 and TI: (a) hydraulic conductivity versus vertical effective stress; (b) hydraulic conductivity versus void ratio. Note: the calculated k was obtained from the consolidation theory.

Fig. 4.18 depicts evolutions of the compression coefficient a and the consolidation coefficient c_v, which are determined by Eq. 4-4 and Eq. 4-5, respectively. a and c_v both decrease rapidly in low stress range with the increase of vertical stress for tests TH-2, TV-2 and TI. After 16 MPa, the compression coefficients a (Fig. 4.18a) of three tests change little and exhibit the same decreasing tendency. This further confirms that the fracture effect on compressibility is negligible. Besides, the values of consolidation coefficient c_v (Fig. 4.18b) also tend to stabilize. Because the void ratios change little (Δe less than 0.1) in Fig. 4.16a, while the hydraulic conductivities change by several orders of magnitude in Fig. 4.17b, it can be inferred that c_v is rather governed by the variation of hydraulic conductivity. Thus, the higher c_v of test TV-2 as compared to those of tests TH-2 and TI (Fig. 4.18b) also verifies the observations from Fig. 4.17. Compared to test TI, test TV-2 has a hydraulic conductivity indeed intensified by the macro-pores in the filled fracture zone, while TH-2 shows negligible effect of the filled fracture zone. This indicates the dependency of hydraulic conductivity on the orientation of fractures.

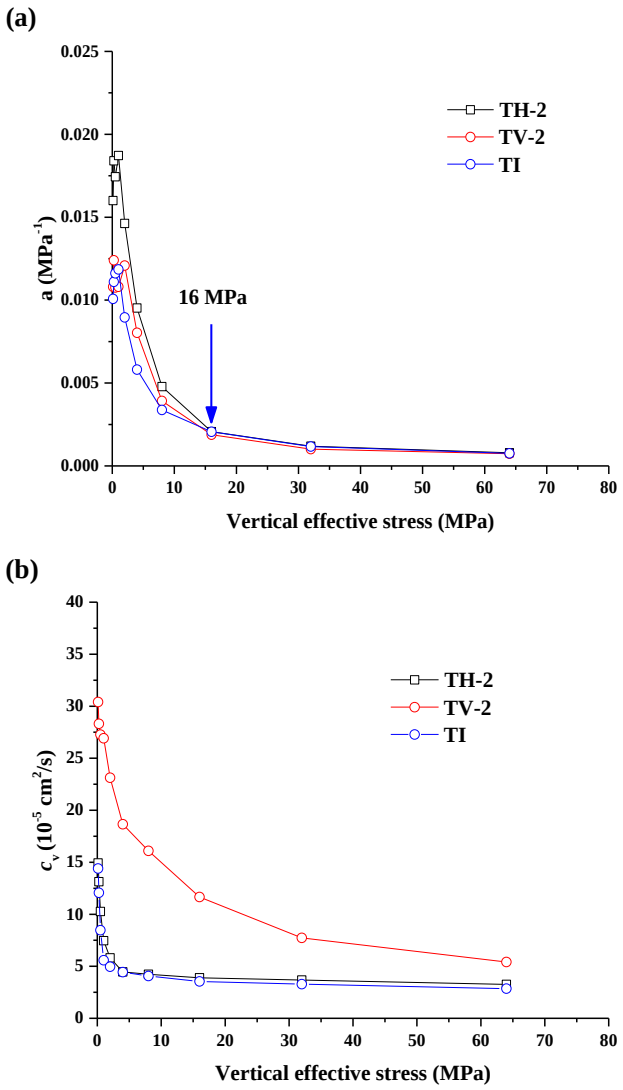

Fig. 4.18. Tests TH-2, TV-2 and TI: (a) compression coefficient versus vertical effective stress; (b) consolidation coefficient versus vertical effective stress

Considering the gradual yielding of COx claystone with stress, the step compression index C_c* is determined to study the variation of compressibility with stress, as recommended by Deng et al., (2012). Based on the time-void curve, the secondary consolidation coefficient C_α is determined to analyze the creep behaviour (ASTM-2435, 1996). The calculation method is shown in Fig. 4.19. Fig. 4.20 shows that with the increase of stress in Case 1, both C_c* and C_α increase first, then change little, finally increase significantly. C_α and C_c* of test TH-1 are slightly higher than those of test TV-1 due to the effect of fracture orientation. This also suggests that although the fracture was healed up by swelling, the filled fracture zone is still a weak zone, characterised by a higher compressibility and a larger creep. The C_c* and C_α in Fig. 4.20 are replotted with respect to the fracture orientation in Fig. 4.21. It is observed that both C_α and C_c* show a three-stage relationship. C_α and C_c* almost increase linearly with stress in the lower

(zone I) and higher stress (zone III) ranges, but change little in the mid-range (zone II). The stress (1 MPa) for TH-1 corresponding to the dividing point between zone I and zone II is lower than that (4 MPa) for TV-1. The stresses (around 16 MPa) corresponding to the dividing point between zone II and zone III are almost the same, which is consistent with the observations made on the compression curves in Fig. 4.15 and Fig. 4.16a.

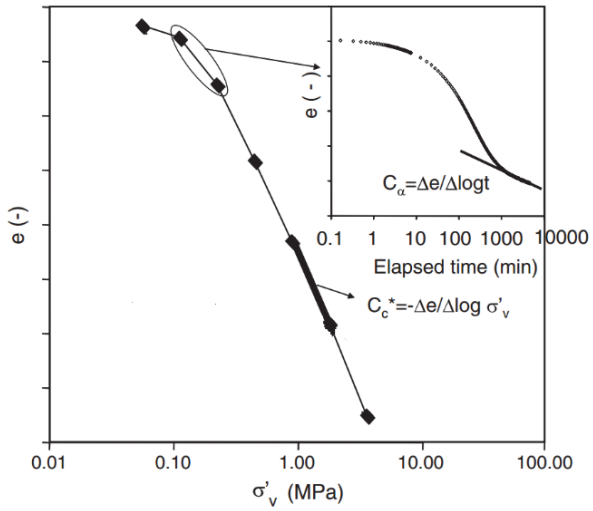

Fig. 4.19. Determination of parameters C_c* and C_α (after Deng et al., 2012)

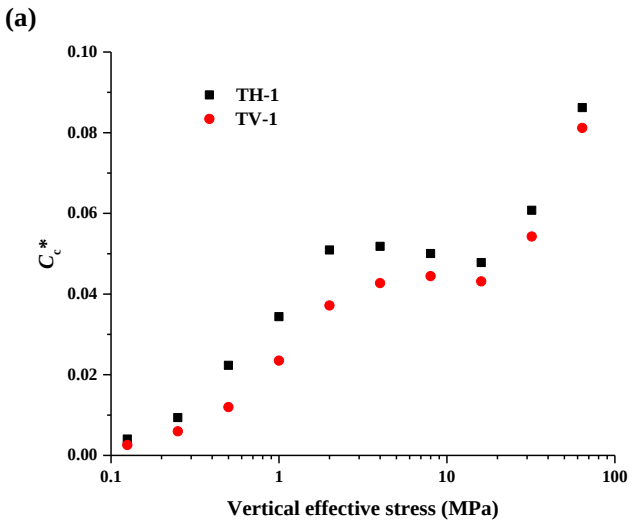

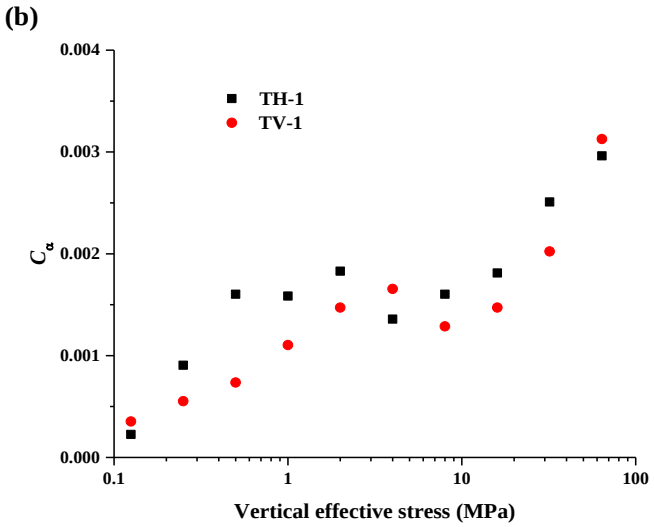

Fig. 4.20. Tests TH-1 and TV-1: (a) C_c* versus vertical effective stress; (b) C_α versus vertical effective stress

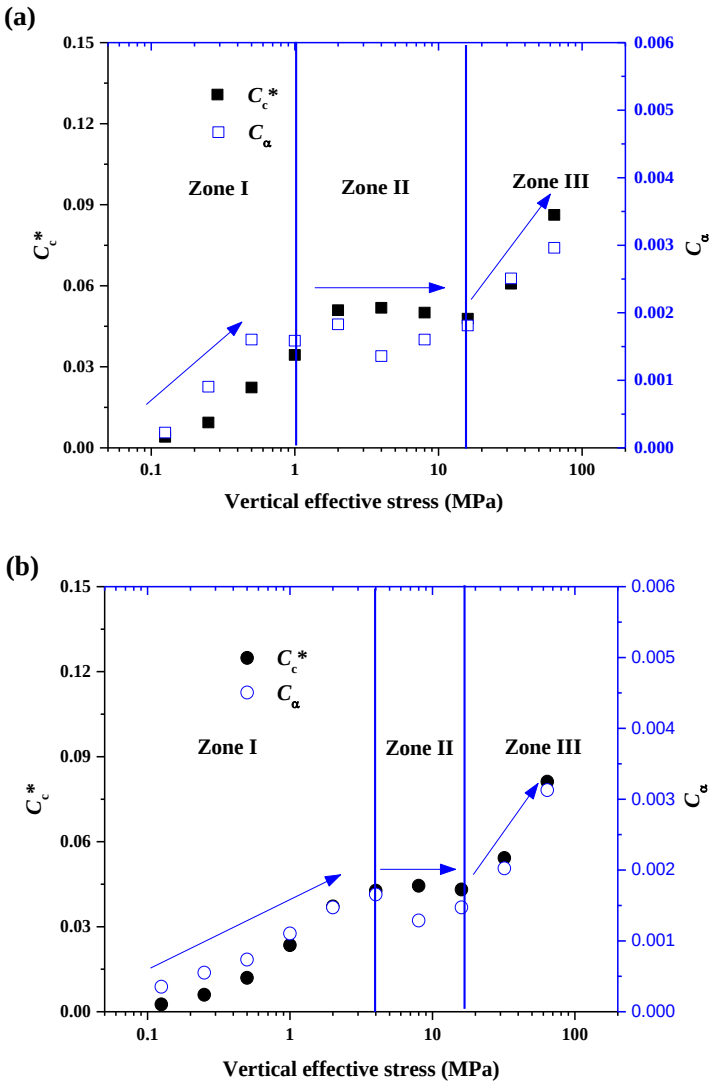

Fig. 4.21. C_α and C_c* versus vertical effective stress: (a) TH-1; (b) TV-1

In Fig. 4.22, the evolutions of C_c* and C_α of tests TH-2 and TV-2 in Case 2 are described. A negligible effect of infiltration paths is observed. It is worth noting that before 16 MPa, C_α and C_c* of tests TH-2 and TV-2 are significantly higher than those of test TI, showing a higher compressibility and a higher creep. This is consistent with the compression curves shown in Fig. 4.16a. Besides, for test TI with intact sample, C_c* and C_α display a continuously increasing tendency, suggesting that the compressibility and creep of COx claystone are stress-dependent. This phenomenon is quite uncommon because C_c* and C_α increase generally with the increase of stress in the low stress range, while keep almost constant in the high stress range (Mesri and Godlewski, 1977; Lambe and Whitman, 1979; Favero et al., 2016). In addition, it was reported that high stress compression on shales can break down the bonds, producing discontinuities (Aversa, et al., 1993; Carter et al., 2010; Mohajerani, et al., 2011). This can lead to further increase of compressibility under high stress.

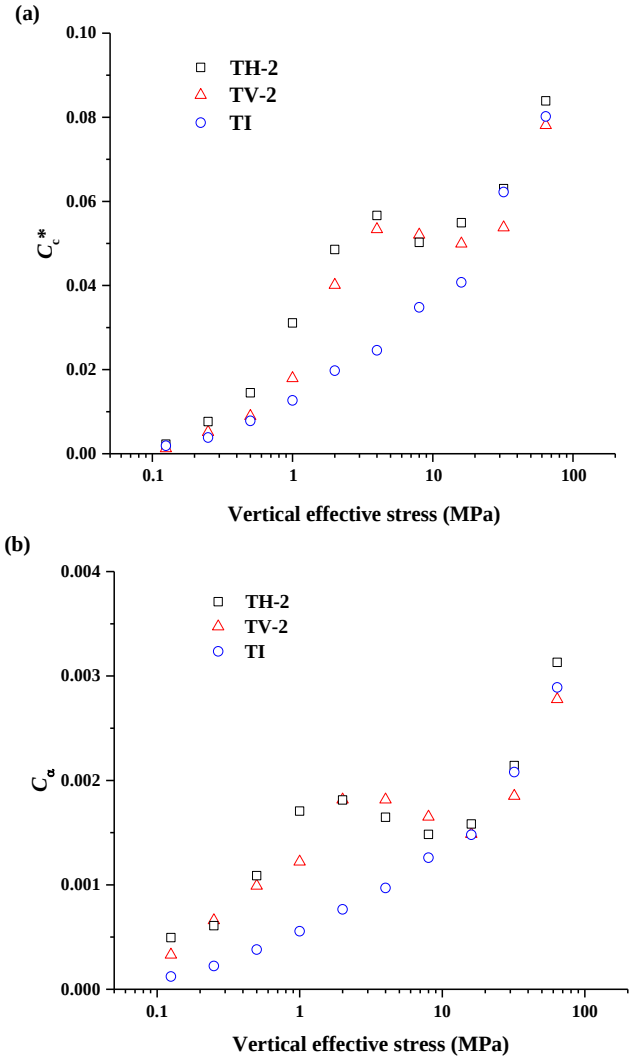

Fig. 4.22. Tests TH-2, TV-2 and TI: (a) C_c* versus vertical effective stress; (b) C_α versus vertical effective stress

A conceptual model is proposed in Fig. 4.23 to describe the evolutions of C_c* and C_α with stress. Two key points, transitional and threshold points, are defined. Before the transitional point, ΔC_c* and ΔC_α increase with increasing stress, then reach the maximum values, suggesting that the contribution of weak fracture zone to the compressibility and creep reach the maximum. The corresponding transitional stress depends on the fracture orientation, as observed in Fig. 4.21. After the transitional point, ΔC_c* and ΔC_α decrease with increasing stress. At the threshold point (around 16 MPa), ΔC_c* and ΔC_α are close to zero, suggesting that the influence of fracture can be neglected. After that, the fractured and intact samples exhibit the similar C_c* and C_α, suggesting that the compression and creep properties of fractured claystone are almost recovered. Note that the threshold stress 16 MPa is close to the in situ stresses: σ_H = 16.1 MPa, σ_h = 12.4 MPa and σ_v = 12.7 MPa (Seyedi et al., 2017). Beyond this stress, it is inferred that the stable structure formed by the grain inclusions (quartz and calcite, etc.) in the in situ stress state is significantly disturbed, inducing the drastical change of the compressibility of COx claystone. This indicats the effect of stress history on the compression behaviour of COx claystone.

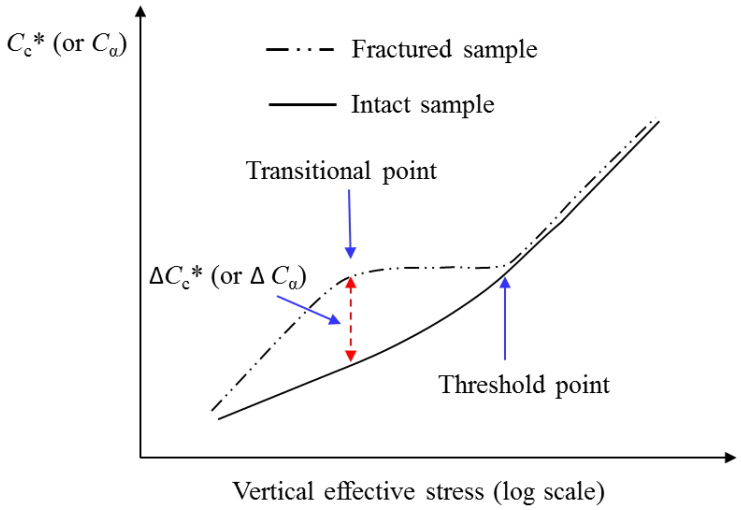

Fig. 4.23. The conceptual representation of the evolutions of C_c* and C_α with vertical effective stress

Fig. 4.24 shows that the relationships between C_α and C_c* for all the tests. It is almost linear for the intact claystone with a slope 0.0358. This is consistent with the observations (C_α/ C_c* = 0.03 ± 0.01) on shale and mudstone (Mitchell and Soga, 2005; Deng et al., 2012). Interestingly, for the fractured claystone, C_α is significantly larger than that predicted by a linear relationship before C_c* = 0.045 which corresponds to a stress of 16 MPa (threshold point) in Fig. 4.22. After that, the fractured and intact samples show similar C_α/C_c* values, indicating a negligible effect

of fracture in the high stress range. Mesri et al. (1994) reported that softer soils have larger C_α/C_c^* value. It can be thus inferred that the larger C_α indeed results from the weaker mechanical property of the filled fracture zone.

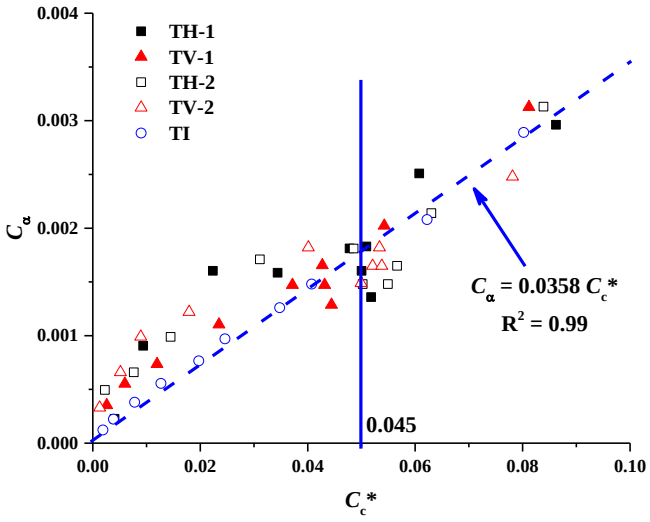

Fig. 4.24. C_c^* versus C_α

4.3 Microstructure observations

MIP tests were carried out to characterize the microstructures before and after the oedometer tests. Fig. 4.25 shows that for tests TH-1 and TV-1 (Case 1), the factures have healed up after hydration and compression, no visible fissures being observed. For each fractured sample, two locations were selected for MIP test after the oedomter test: intact part (disk) and intact part with fracture (disk with fracture). By contrast, only one location was selected for MIP test on intact sample in test TI, as shown in Fig. 4.26.

The results of test TH-1 are presented in Fig. 4.27. The pore size distribution shows a unimodal characteristic, indicating the presence of one major population of micro-pores. However, the peak of micro-pores decreased after compression. There are some macro-pores in the range from 15 µm to 40 µm for the disk with fracture in test TH-1, but significantly smaller than the original average fracture size 0.1 mm, showing the self-sealing properties of COx claystone under the coupling hydrometrical effect. In addition, the comparisons of cumulative curves indicate that due to compression, the intruded void ratio of disk in test TH-1 is significantly lower than the initial one, and also smaller than that of the disk with fracture in test TH-1 owing to the contribution of macrospores in the closed fracture.

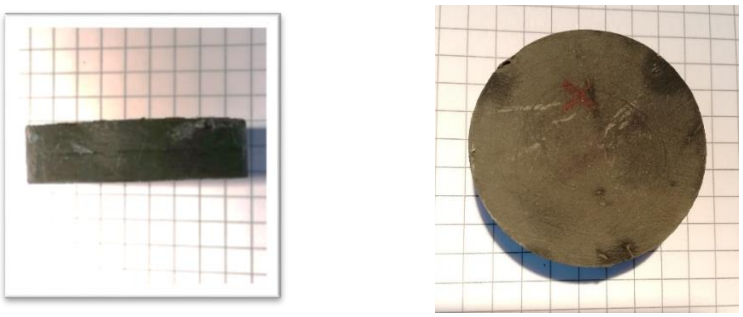

Fig. 4.25. Photographs of oedometer samples after tests: TH-1 (left); TV-1 (right)

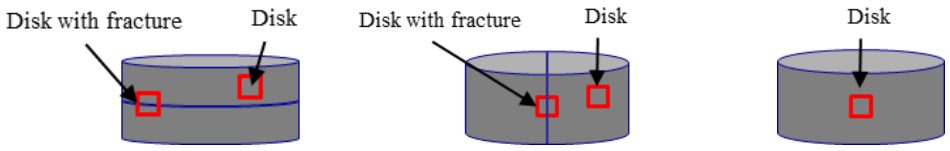

Fig. 4.26. Locations in fractured and intact samples selected for MIP observation

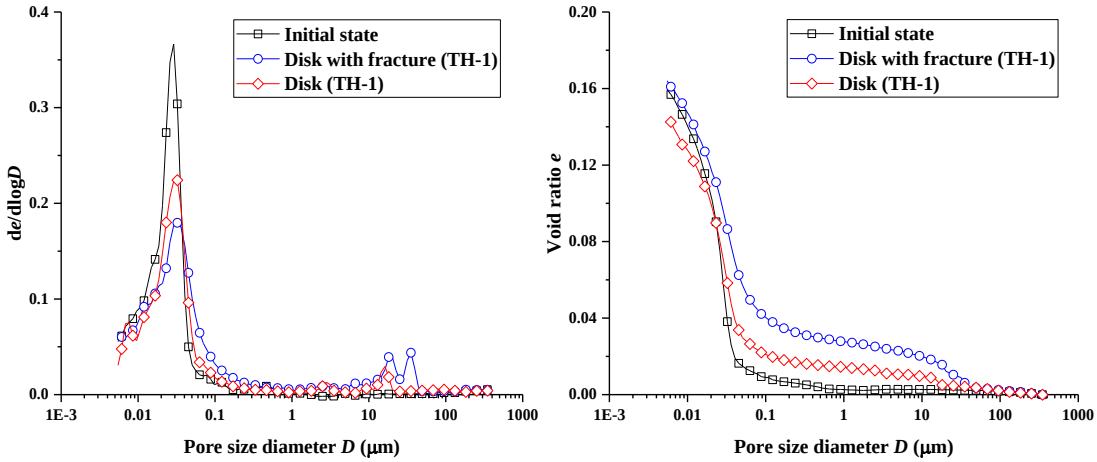

Fig. 4.27. Pore size distributions and cumulative intrusion curves for test TH-1

Fig. 4.28 displays the results of test TV-1. The pore size distribution also shows a unimodal characteristic, with one major population of micro-pores and the peak of micro-pores decreases after compression. The dimensions of macro-pores range from 100 μm to 200 μm for the disk with fracture in test TH-1, larger than that in TH-1 due to the larger initial average fracture size 0.3 mm. Besides, it may also be related to the fracture orientation. As discussed before, the horizontal fracture is easier to be closed under compression in oedometer.

Fig. 4.29 and Fig. 4.30 present the MIP results for tests TH-2 and TV-2 (Case 2). The pore size distribution curves also exhibit a unimodal characteristic as for tests TH-1 and TV-1. Significant macro-pores (larger than 100 μm) are observed in test TH-2. It may be induced by the opening of sealed fracture upon the oedometer sample was unloaded. For test TV-2, the size of macro-pores is around 100 μm, similar to that of test TV-2. The comparisons between Case 1 and Case

2 confirm that the initial hydration path scarcely affects the closure of fracture after compression.

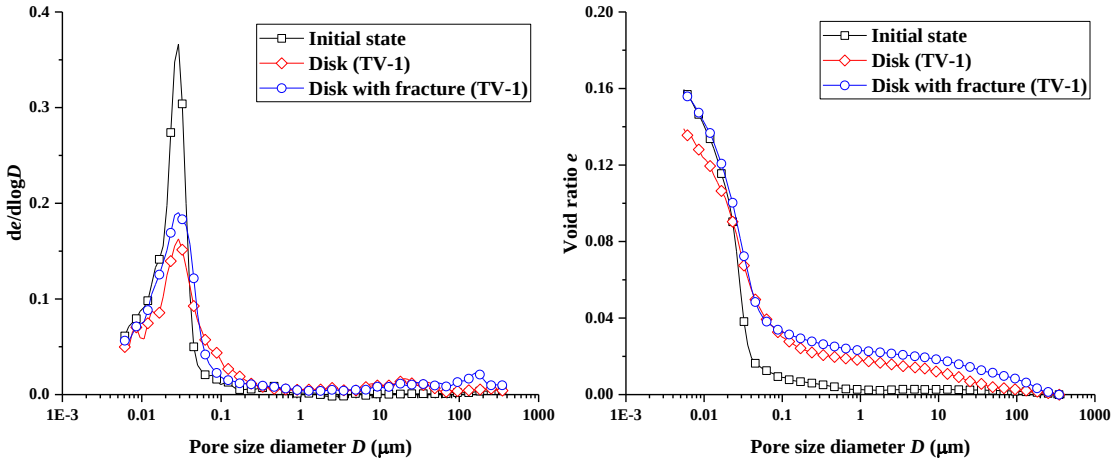

Fig. 4.28. Pore size distributions and cumulative intrusion curves for test TV-1

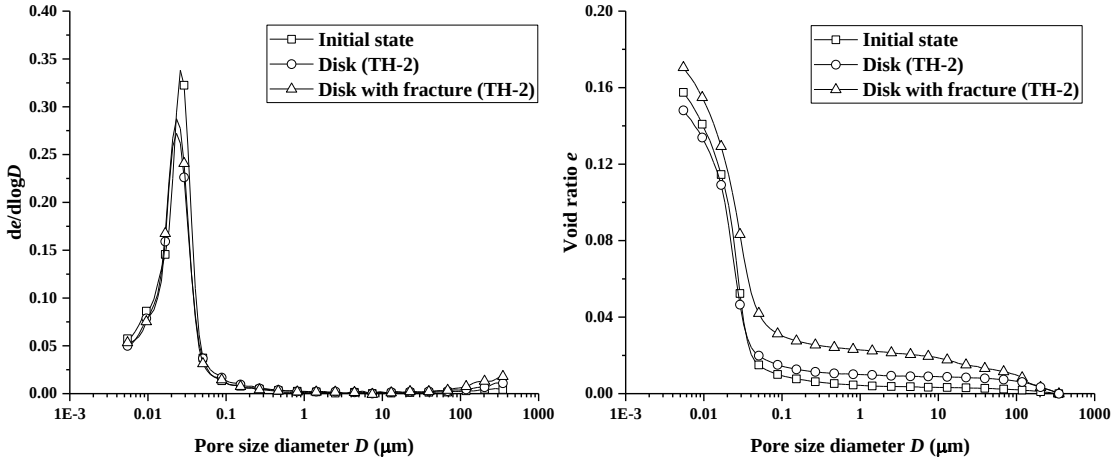

Fig. 4.29. Pore size distributions and cumulative intrusion curves for test TH-2

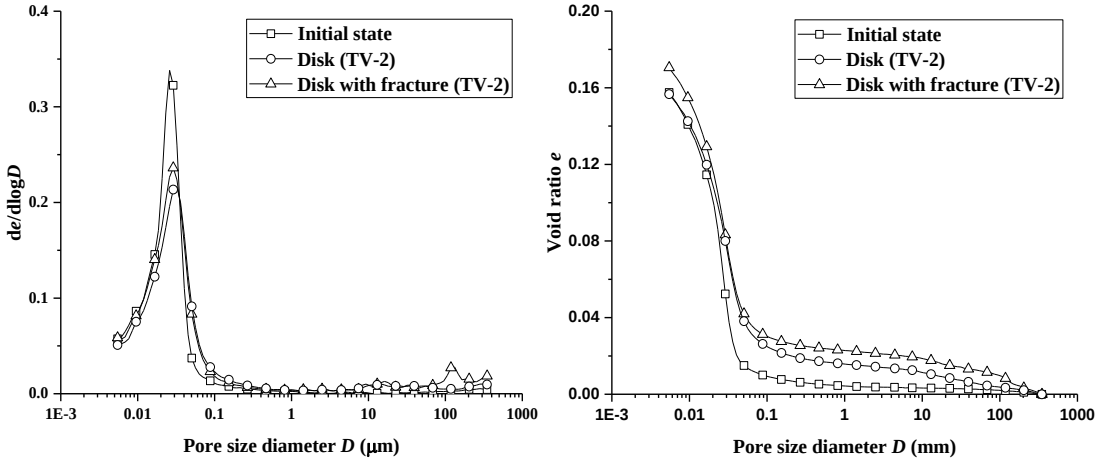

Fig. 4.30. Pore size distributions and cumulative intrusion curves for test TV-2

The results of test TI are shown in Fig. 4.31. There are almost no macro-pores (larger than 1 μm) observed. Comparisons between intact and fractured claystone confirm that the pre-existing

fracture is closed completely, even under the combined effects of hydration and compression.

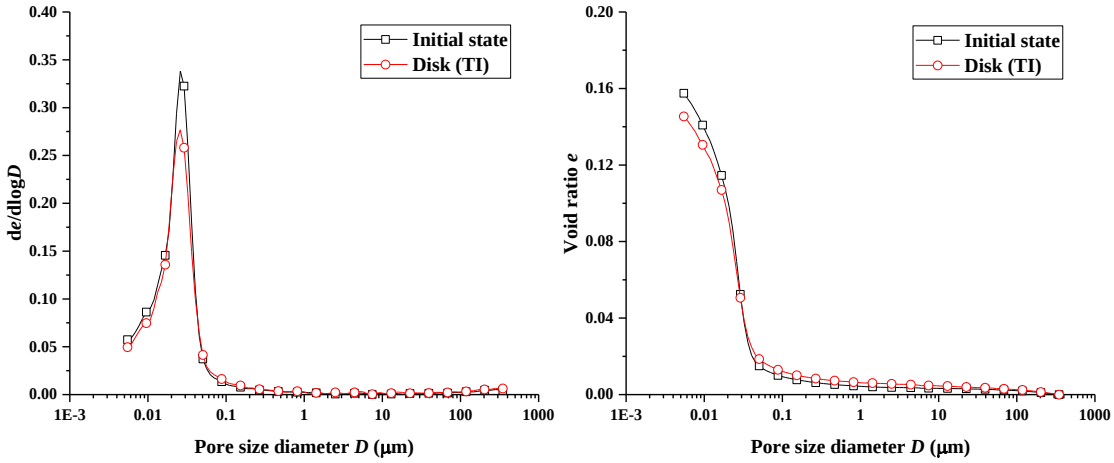

Fig. 4.31. Pore size distributions and cumulative intrusion curves for test TI

4.4 Conclusions

In this chapter, the volume change behaviours of COx claystone and Opalinus clay reported in the literature were explored to evidence the grain breakage effect. Natural Teguline clay was further tested for the purpose of confirmation. To better understand the role of fine fractions in the grain breakage phenomenon, oedometer tests were conducted on artificial sand-clay mixtures with different clay fractions. Moreover, oedometer tests were conducted on fractured and intact COx claystone, aiming at investigating the effects of fracture on the hydro-mechanical behaviour. The results of swelling, compression, hydraulic conductivity and creep were presented, allowing the following conclusions to be drawn:

For natural COx claystone, Opalinus and Teguline clays, all can be regarded as mixtures of clay minerals and granular grains. The variation of C_c* exhibits an uncommon two-stage phenomenon: with the increase of vertical stress, C_c^* first increases slightly and then rapidly after a critical stress. This two-stage change of C_c^* can be attributed to the grain breakage phenomenon which was also evidenced by several authors before (Klinkenberg et al., 2009; Wang, 2012) through image analysis.

The results obtained on the artificial sand-clay mixtures including pure sand and pure clay not only confirm the effect of grain breakage but also evidence the influence of clay fractions. The compression behaviour of these soils can be roughly distinguished into three zones according to the fine fractions. At low fine fractions, the compression behaviour is governed by grain breakage. At high fine fractions, the pore collapse of fines becomes dominating. At medium fine fractions, both pore collapse and grain breakage occur: pore collapses first, allowing grains

to be well in contact either directly (grain-grain contacts) or indirectly (grain-fine-grain contacts) to activate the grain breakage phenomenon upon further loading. Thus, the compression behaviour of sand-clay mixtures is governed by both sand grain breakage and collapse of pore in the clay matrix, depending on the sand-clay ratios and stress levels. This is consistent with the identified compression behaviour of natural fine-grained soils.

The existence of facture decreases the swelling strain of claystone and this phenomenon depends on the infiltration path and the orientation of fracture. The infiltration path affects the global swelling rate of fractured claystone. The self-sealing of fracture is mainly attributed to the swelling and clogging of COx claystone grains in the fracture zone.

Due to the weaker mechanical properties of the filled fracture zone, lower compression coefficient a, higher lower compression index C_c* and higher secondary consolidation coefficient C_α are observed for the fractured claystone, defining a higher compressibility and creep than the intact one. The compression and creep behaviours depend on the orientation of fracture and the stress level. Comparison of hydraulic conductivities between fractured and intact claystone indicates that the hydraulic conductivity can be partially recovered due to the collapse of macro-pores in the filled fracture zone. This is also confirmed by analysing the evolution of consolidation coefficients c_v with stress.

All samples present a uni-modal pore size distribution mode as the initial state. The dimension of macro-pores in the closed fracture depends on the fracture orientation (i.e. different initial fracture size). The results also confirm that the initial hydration path scarcely affect the closure of fracture after compression, and the pre-existing fracture cannot be closed completely even under the combined effects of hydration and high stress compression.

These findings clearly show the effect of fracture on the swelling, compression, permeability and creep of COx claystone. It is worth noting that the stress 16 MPa represents an important stress level. Beyond this stress level, the fracture effect can be neglected, but the compressibility increases further due to grain breakage.

Chapter 5. Hydro-mechanical behaviour of damaged COx claystone

In this chapter, the hydro-mechanical behaviour of damaged COx claystone was investigated. Suction controlled oedometer tests were performed to investigate the swelling, compression and creep behaviour of damaged COx claystone. The microcracks inside the damaged oedometer samples before and after the tests were analyzed through CT and MIP tests. The effect of strain rate on the compression behaviour of damaged COx claystone was investigated by conducting a series of CRS tests at different suctions. Based on the results obtained, several hydro-mechanical parameters (compression index λ and viscous parameter C_A, etc.) were determined and analyzed, helping characterize the time dependent properties of damaged COx claystone.

5.1 Suction effect on swelling and compression behaviour

5.1.1 Swelling behaviour

Four oedometer tests with controlled-suction were conducted - TD0, TD4, TD9 and TD24 with four corresponding suctions: 0 MPa, 4.2 MPa, 9 MPa and 24.9 MPa, respectively. The experimental procedure consists of two steps: suction equilibrium and step-loading. The samples were firstly equilibrated at the suctions 0 MPa, 4.2 MPa, 9 MPa and 24.9 MPa, respectively. During the suction application, an initial vertical stress of 0.05 MPa was applied to make a good contact between the piston and sample. In test TD0, the damaged claystone sample was hydrated by injecting synthetic water from the bottom of oedometer cell to impose zero suction. It is worth noting that the synthetic water used in this study has a quite low electrical conductivity (6.3 µS/cm), close to the value of 4 µS/cm for deionized water reported (Rao and Shivananda, 2005). The corresponding osmic suction estimated is 0.1 MPa based on the method proposed by Mata et al. (2002). Thus, this low osmotic suction in the present work is neglected. For the other three tests, the target suctions were applied by vapour equilibrium technique. Suction equilibrium is considered as reached when the vertical strain rate is below 0.025%/day, as recommended by Romero et al. (2003).

Fig. 5.1 presents the evolution of vertical strain with time in the suction equilibrium process for the four tests. It is observed that the test at higher suction shows a lower vertical swelling strain rate and needs less time for suction equilibrium. The final strains obtained for suctions of 0

MPa, 4.2 MPa, 9 MPa, and 24.9 MPa are 2.01% (e = 0.278), 0.61% (e = 0.247), 0.33% (e = 0.248) and 0.03% (e = 0.247), respectively. This is consistent with the observations on other unsaturated soils (Wang et al., 2013; Guerra et al., 2019).

Fig. 5.2 compares the vertical strains obtained in this study with those from other works. The data is plotted in a semi-logarithmic plane, showing a relative linear relationship between strain and suction for both the damaged claystone in this study and the intact claystone by Menaceur et al. (2016). In Fig. 5.2, the damaged claystone presents lower strain than the intact claystone. The difference is attributed to the effect of microcracks inside the damaged claystone. Due to the filling of swollen clay minerals in the microcracks, the swelling potential decreases. This is similar to the fracture effect on COx claystone (Zhang et al. 2020). In addition, for the intact claystone (Menaceur et al. 2016), the sample was hydrated under free swelling, while an initial vertical stress 0.05 MPa was applied in the oedometer swelling condition.

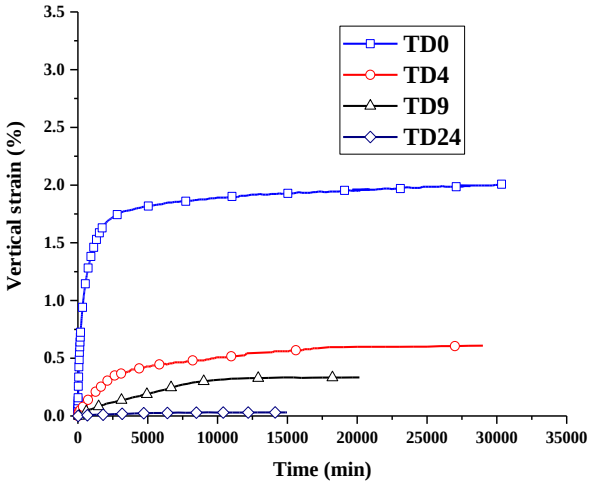

Fig. 5.1 Evolution of vertical strain with time during suction equilibration

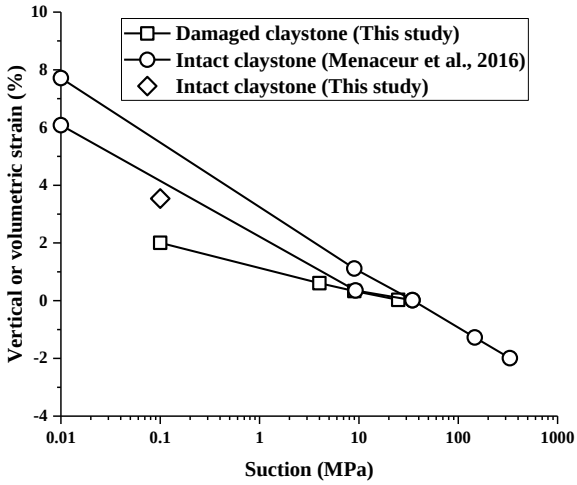

Fig. 5.2. Vertical or volumetric strain versus suction after suction equilibration

Note: the data for intact sample is from the oedometer test TI described in chapter 4

5.1.2 Compression and creep behaviours

After the applied suctions were equilibrated, the claystone samples were loaded in steps at constant suctions. Fig. 5.3 presents the compression curves at different suctions in terms of void ratio *e* with respect to vertical net stress. Note that the initial void ratios before swelling were slightly different due to the soil variability. It appears that the sample at a higher suction displays a lower compressibility. In general, each compression curve can be divided into two parts: an elastic part with low compressibility before yield stress and a plastic part with high compressibility after yield stress in a standard fashion. Interestingly, for test TD0, the compression curve deviates from the linear relation after 16 MPa, generating a third part with a higher compressibility. This phenomenon was attributed to the grain breakage effect in chapter 4.

The yield stress at each suction was identified using the method shown in Fig. 5.3. Fig. 5.4 shows that the changes in yield stress with respect to suction. It is observed that for the damaged claystone, yield stress increases with the increase of suction due to the suction hardening effect. This observation is in agreement with that on other unsaturated soils (Alonso et al., 1990).

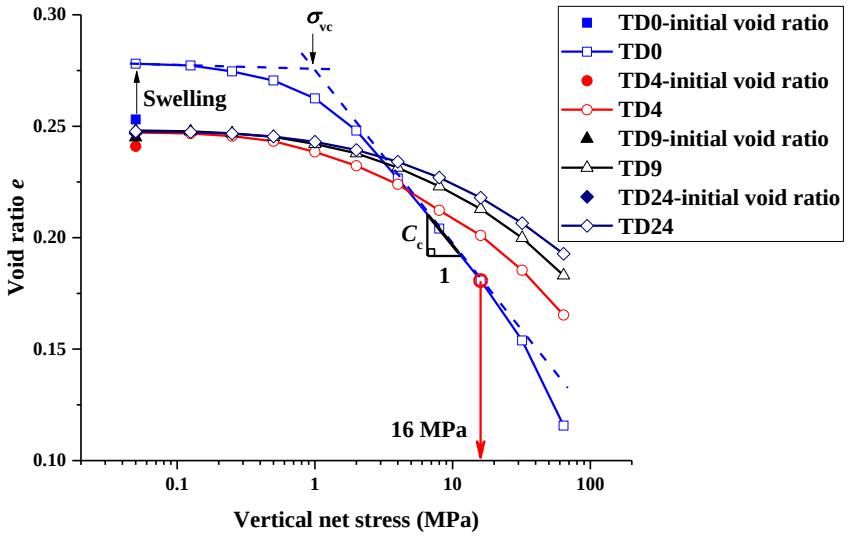

Fig. 5.3. Compression curves at different suctions

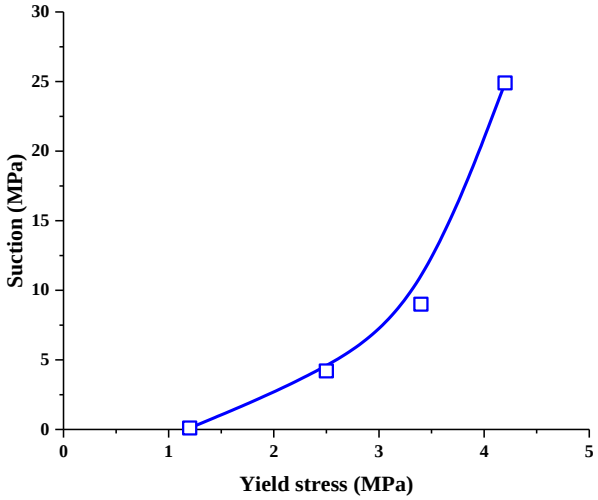

Fig. 5.4. Relationship between yield stress and suction.

The determination of the compression coefficient C_c is also depicted in Fig. 5.3. In a similar manner, the rebound coefficient C_s is identified based on the slope of initial linear part. Fig. 5.5 displays the evolution of C_c and C_s with respect to suction. As observed, C_c and C_s both decrease almost linearly with the increase of suction. Besides, the C_s of intact claystone at zero suction is very close to that of damaged claystone. Comparison of C_c at zero suction shows that the damaged claystone has a significantly larger C_c than the intact claystone, indicating that the preexisting microcracks inside the sample increase the compressibility in the second plastic part.

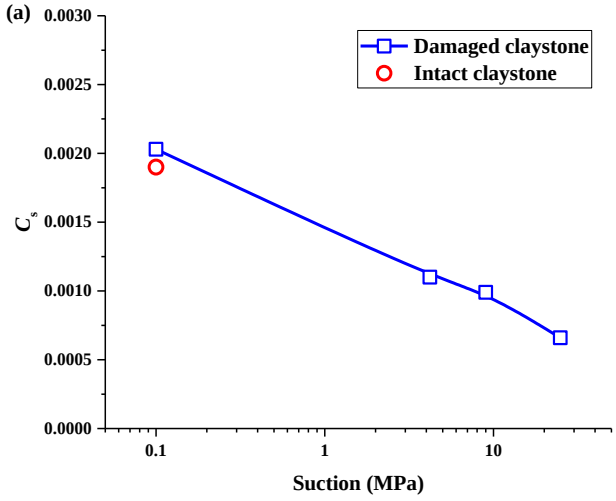

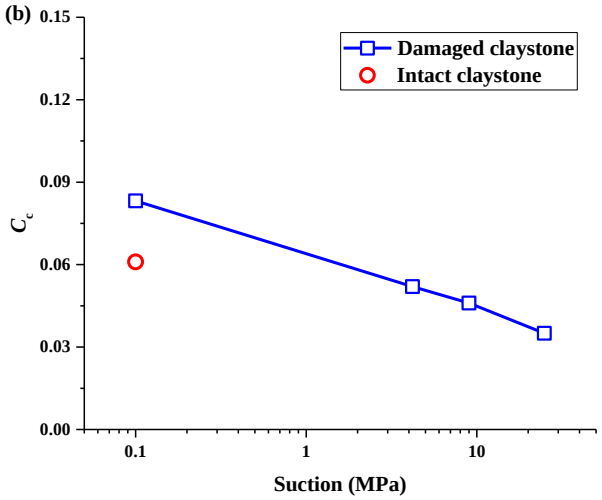

Fig. 5.5. Changes in C_s and C_c with suction.

Note: the data for intact sample is obtained from the oedometer test TI described in chapter 4

Fig. 5.6 presents the evolutions of the compression coefficient a and the consolidation coefficient c_v with vertical effective stress in test TD0. Their determination methods were detailed in chapter 4. It is found that a and c_v both decrease rapidly in the low stress range with the increase of vertical stress, while after 16 MPa, they change little and tend to stabilize, as for intact and fractured claystone depicted in chapter 4. For a, the final value 1.19×10^{-3} MPa^{-1} for the damaged claystone at 64 MPa is larger than the value 0.75×10^{-3} MPa^{-1} for the intact claystone, further confirming the higher compressibility of damaged claystone in high stress stage. Similarly, for c_v, the final values for damaged and intact claystone are 4.40×10^{-5} and 2.85×10^{-5} cm^2/s, respectively. As discussed in chapter 4, the change of c_v is mainly controlled by the hydraulic conductivity. This will be further analyzed.

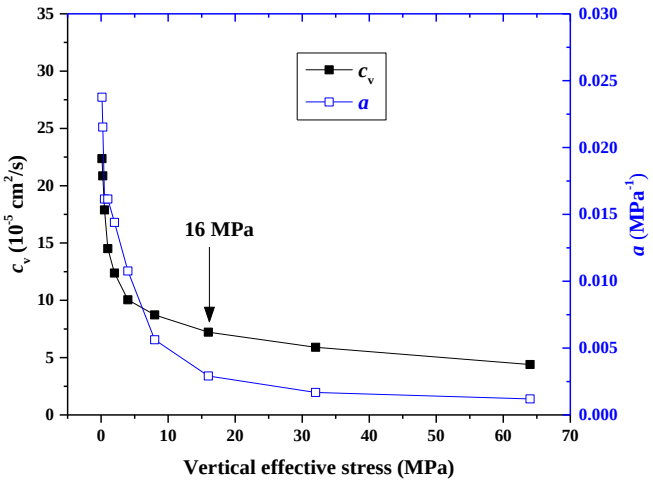

Fig. 5.6. c_v and a versus suction

Fig. 5.7 presents the hydraulic conductivities *k* obtained from test TD0, including the measured and calculated ones. For the damaged claystone, *k* determined by measurement and calculation are in good agreement, in terms of vertical effective stress or void ratio. *k* decreases with the increase of stress and the decrease of void ratio. From Fig. 5.7a a linear relationship between *k* and vertical effective stress is observed. The data was linearly fitted with Eq. 5-1, as recommended by Crisci et al. (2019). The reduction of *k* with the decrease of void ratio is more pronounced in the low stress range when void ratio is relatively larger, as shown in Fig. 5.7b. It is because in the initial loading phase, even though the preexisting microcracks inside the damaged claystone was closed due to the swelling of clay minerals, the zones of existing miscrocracks were still the weak zones mechanically with large micro-pores, as shown in chapter 4. These weak zones have a higher compressibility a larger hydraulic conductivity. The larger pores collapsed under relatively low stress, resulting in significant decrease of hydraulic conductivity. Equation Eq. 5-2 is proposed in this study to quantify the relationship between *k* and *e* by referring to the methods proposed by Samarasinghe et al. (1982) and Ren et al., (2016).

$$k = a(\sigma'_v)^b \tag{5-1}$$

$$\log k = ae^b - c \tag{5-2}$$

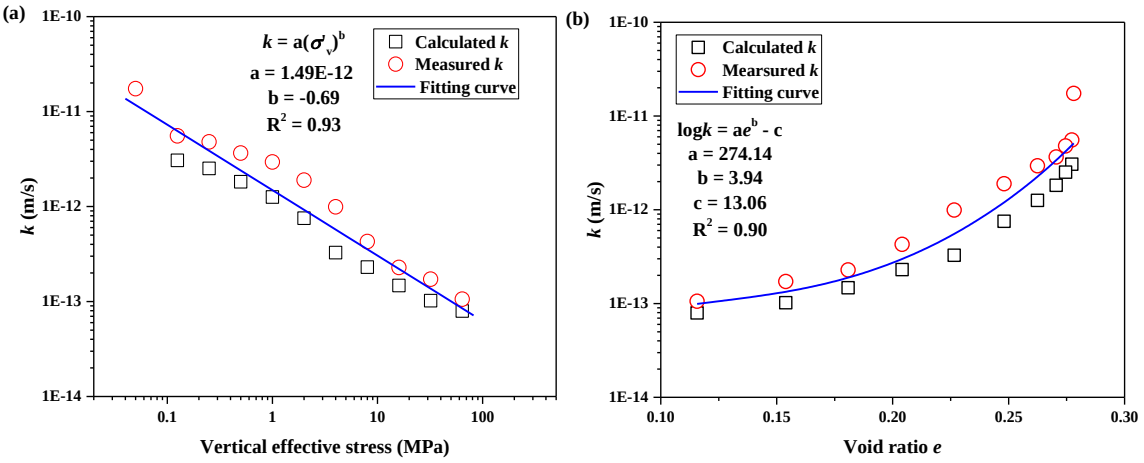

Fig. 5.7. (a) *k* versus vertical effective stress; (b) *k* versus void ratio.

Note: the measured *k* was determined using pressure-volume controller and the calculated one was obtained from the consolidation theory

The damaged claystone at 64 MPa has a larger *k* (7.94×10^{-14} m/s) than the intact claystone (1.86×10^{-14} m/s). By linking *k* to c_v, the larger c_v of damaged claystone compared to the intact claystone can be explained. On the whole, the hydraulic conductivity of the damaged claystone varies from 2.21×10^{-11} m/s to 7.94×10^{-14} m/s. Armand et al. (2014) reported that according to

the in situ investigation, the hydraulic conductivity of claystone with shear fractures in the fractured zone varies from 6×10^{-12} to 2×10^{-13} m/s. Thereby, the hydraulic conductivity obtained from the in situ and the laboratory investigations are consistent.

To further investigate the suction effect on the compression behaviour of damaged claystone, the relationships between step compression index C_c* and vertical net stress at different suctions are determined as shown in Fig. 5.8. Similarly, Fig. 5.9 displays the changes in secondary consolidation coefficient C_α with vertical net stress for the damaged claystone to characterize the creep properties. The two parameters can be identified from the compression curve in steps and the consolidation curve under each loading. The determination methods for the two parameters are the same as in Deng et al. (2012).

From Fig. 5.8, it is found that with the increase of vertical net stress, C_c* always shows a continuously increasing tendency at suctions 4.2 MPa, 9 MPa and 24.9 MPa. However, at suction zero, C_c* increases first, then changes little with vertical stress, finally significantly increases after 16 MPa. This indicates that the damaged claystone shows a similar compression behaviour as the fractured claystone, reflecting the effect of preexisting microcracks. This has been interpreted in terms of contributions of microcracks to the compressibility of damaged claystone in chapter 4. In a standard fashion, larger C_c* was observed for lower suction at the same stress, in agreement with the observations by Oldecop and Alonso (2007), Ye et al. (2014) and Rezania et al. (2020). The observations in this study exhibit the dependency of damaged claystone on suction and stress, as for the intact and fractured claystone depicted in chapter 4.

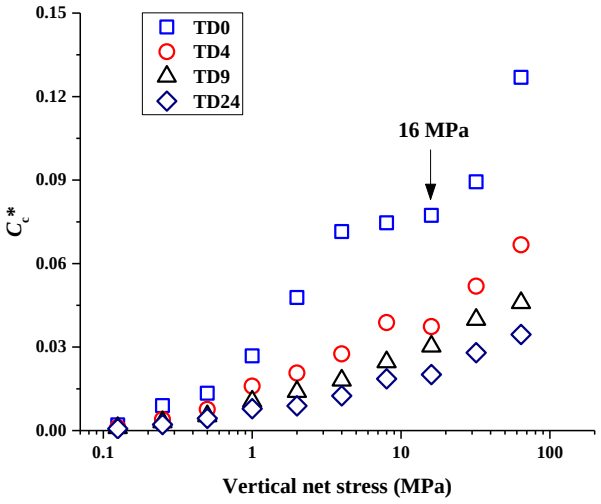

Fig. 5.8. C_c* versus s

With the changes of suction and stress, C_α presents an evolution similar to that of C_c*, as shown in Fig. 5.9. Rezania et al. (2020) reported that with the increase of suction, the generation of

water menisci at the inter-particle contacts produced a tensile pressure to the soil grains, resulting in the reduction of particles' freedom for the rearrangement at a given stress. Thus, C_α decreased with the increase of suction. In addition, many studies pointed out that for common clays C_c* and C_α both increased with the increase of stress before the yield stress, decreased or kept constant after the yield stress (Mesri and Godlewski, 1977; Graham et al., 1983; Anagnostopoulos and Grammatikopoulos, 2009; Rezania et al., 2020). This phenomenon was not observed in the present study. In fact, the variations of C_c and C_α of damaged COx claystone are fairly similar to those of natural stiff Boom clay as reported by Deng et al. (2012).

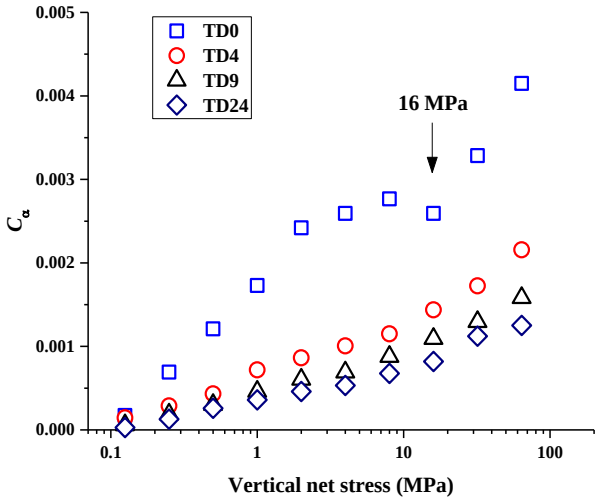

Fig. 5.9. C_α versus vertical stress at different suctions

To characterize the coupled effects of suction and stress, the changes in C_c* with C_α are shown in Fig. 5.10. In general, the relationship between C_c* with C_α is linear, as reported by Oldecop and Alonso (2007), Priol et al. (2007), Gennaro and Pereira (2013), Ye et al. (2014) and Qin et al. (2015). For tests TD4, TD9 and TD 24, the results obtained indeed show almost linear relationship. By contrast, for test TD0, C_c^* has a threshold value 0.073, corresponding to the vertical net stress 16 MPa, as presented in Fig. 5.10. Before that, C_α is larger than the linearly defined one, while after that, C_α /C_c* exhibits a good linear relationship. This is consistent with the results of intact claystone shown in chapter 4.

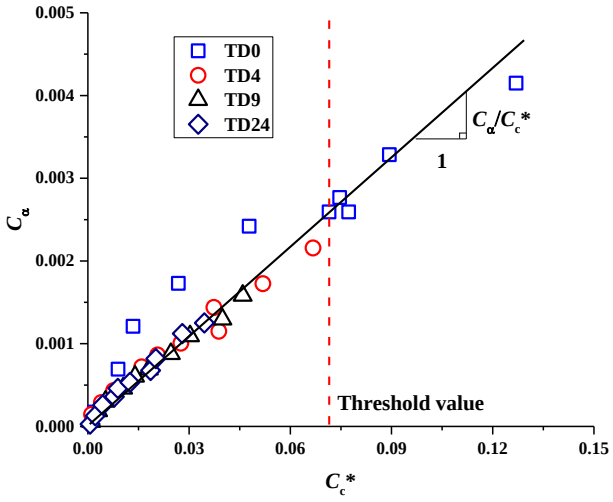

Fig. 5.10. C_α / C_c* relationship

The average slope of C_α/C_c^* at different suctions are calculated and plotted with respect to suction s in Fig. 5.11. With the increase of suction, the average slope C_α/C_c* decreased slightly. Menaceur et al. (2016) reported that the increase of suction reduces the water film thickness around the claystone platelets. In this sense, the stiffness of claystone particles increases and the slippage displacements between particles decrease in the long term. Therefore, the higher suction, the smaller the C_c* and C_α. Apparently, the effect of suction on C_c* is less significant than that on C_α, resulting in the decrease of C_α/C_c*. The relationship between suction s and C_α/C_c* is estimated by adopting Eq. 5-3, as recommended by Qin et al. (2015):

$$\frac{C_\alpha}{C_c^*} = a - b \times \ln(s + p_{at}) \tag{5-3}$$

where a represents the C_α/C_c* value at zero suction, b is a model parameter and p_{at} is the atmospheric pressure, equivalent to 0.1 MPa.

The ranges of C_α/C_c for different soils are presented in Fig. 5.12. It is found that the C_α/C_c* values obtained in Fig. 5.11 are consistent with the value 0.03±0.01 for shale and mud stone. From peat to rockfill, the stiffer the soil, the larger the C_α/C_c, indicating a positive correlation between the soil stiffness and C_α/C_c value. This is consistent with that in Fig. 5.11: the higher the suction, the larger stiffness, thus the lower the C_α/C_c. Similarly, as indicated before, for the saturated damaged claystone in test TD0, the swollen clay minerals filled the preexisting microcracks. As the zones filled by clay minerals have a larger compressibility, before the threshold value, C_α/C_c presented a higher ratio (i.e. larger slope) that the average one. After threshold value, the mechanical properties of the damaged claystone almost recovered to the intact one, leading to a linear C_α/C_c relationship.

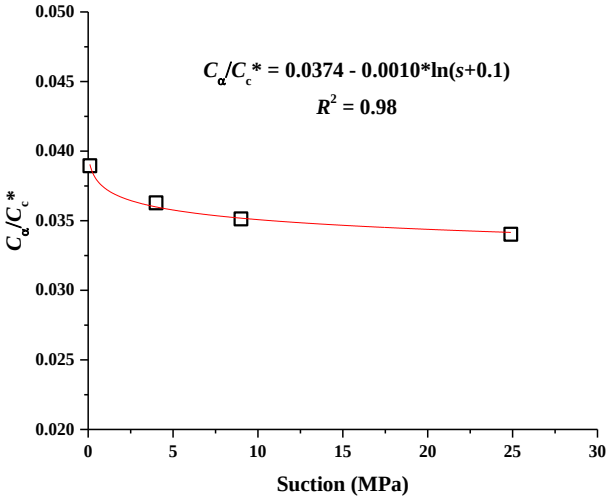

Fig. 5.11. C_α / C_c* versus s

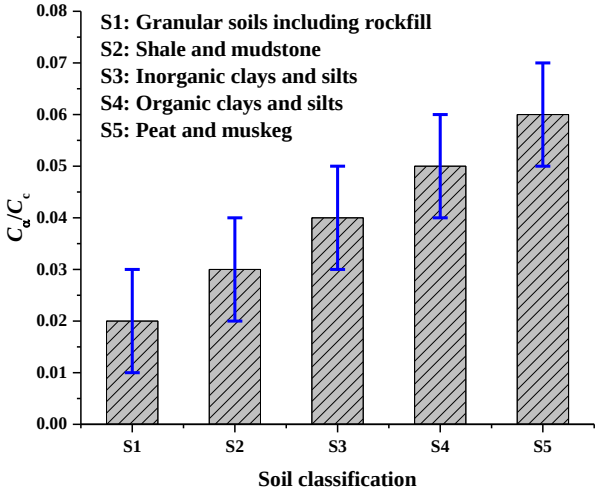

Fig. 5.12. C_α /C_c of different soils (data from Mesri et al., 1994)

5.1.3 Microstructure observations

In this section, microstructure observations were presented for the damaged samples before and after oedometer tests with controlled-suction. The aim is to investigate the evolutions of damages inside the samples under hydro-mechanical loadings. Two kinds of experimental methods were adopted, including μ-CT test and MIP test. Results are analyzed and discussed with respect to microstructure changes.

To observe the distributions of microcracks inside the sample, μ-CT tests were first performed, allowing overall observations on the samples. For the CT scanning, the image at the central cross section of each sample was selected as a section of interest, as shown in Fig. 5.13. The pixel size is 24 μm. Fig. 5.14 presents the CT images at the selected locations for four oedometer tests before loading. The grey level of each pixel in the 2D image depends on the mineral

composition and density. The high density regions correspond to the lighter grey levels, while the lower density to the darker grey levels (Guerra et al., 2017). In this sense, the black regions represent voids, and the black lines in the grey regions represent microcraks. The white regions represent the inclusions, including calcite and quartz (Robinet, 2008; Robinet et al., 2012). Based on the preliminary analysis on the 2D images, microcracks before oedometer test are identified, validating the preparation method of damaged sample described in chapter 3.

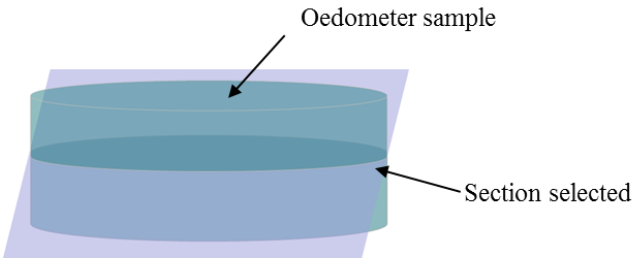

Fig. 5.13. Schematic diagram of the selected section for 2D image analysis

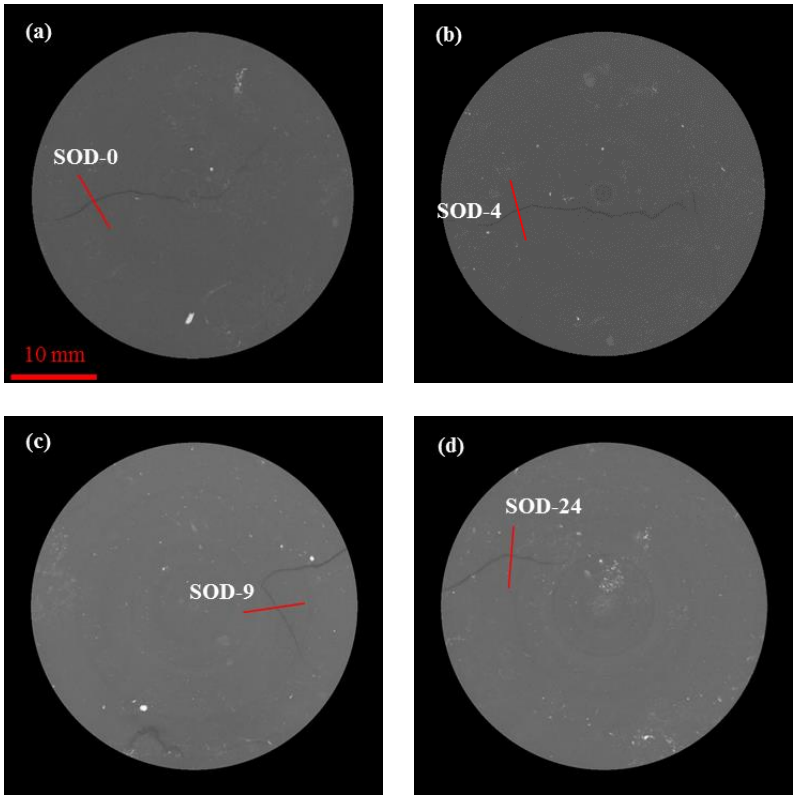

Fig. 5.14. The 2D image before oedometer tests: (a) test TD0; (b) test TD9; (c) test TD9 and (d) test TD24.

To further analyze the correlations between grey level and microcracks, four lines were selected in Fig. 5.14. Fig. 5.15 displays the distributions of grey levels for the selected lines. It is found that there are valleys for all the grey level curves and the lowest points with the lowest grey

values correspond to the locations of microcracks in Fig. 5.14. It is also found that the grey levels corresponding to the intact part change in a narrow range (from 85 to 95). This is consistent with the observations by Guerra et al. (2017). In addition, a unified threshold value 85 for the four oedometer samples can be determined from the grey level distribution curves to distinguish the cracking zone and intact zone. By binarizing the CT images in black and withe, the proportion of cracking area can be identified allowing the cracking degree to be quantified, as detailed in chapter 3.

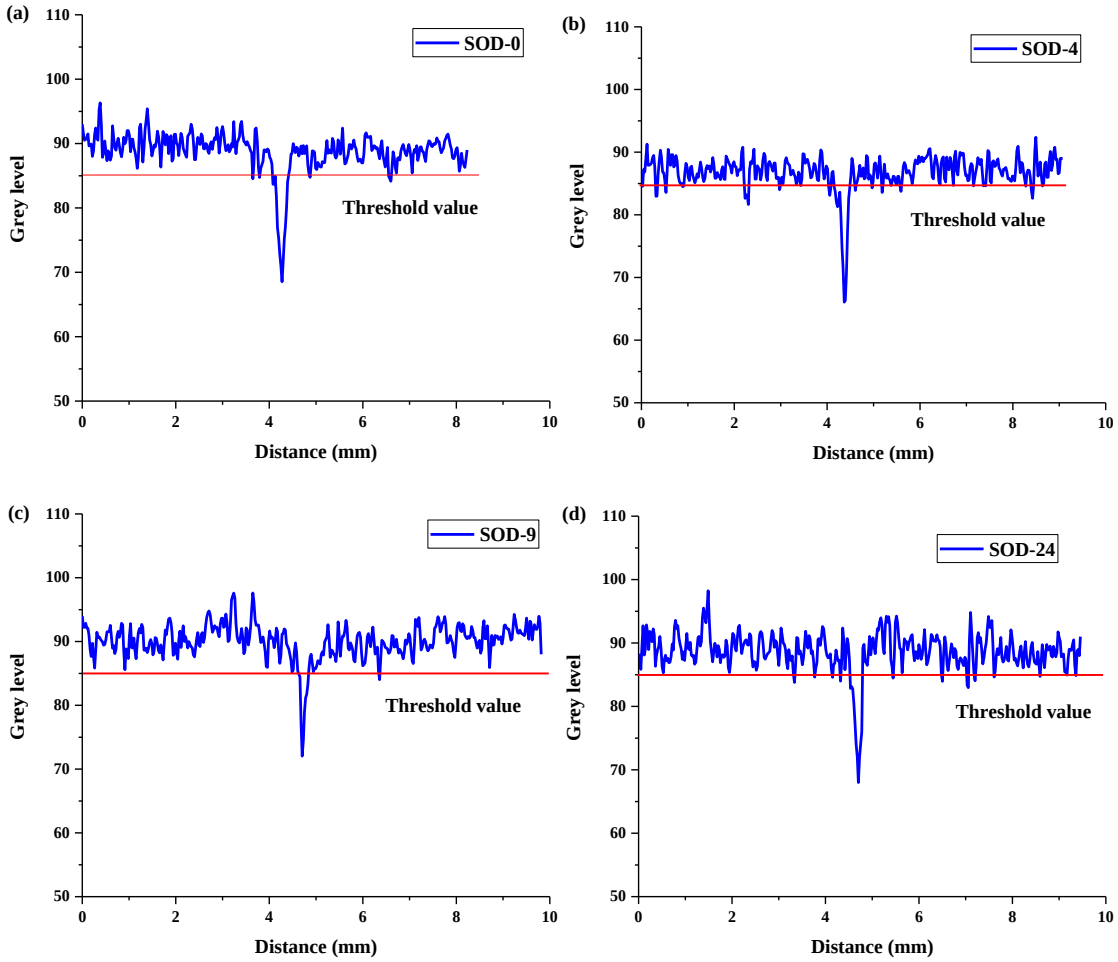

Fig. 5.15. Grey level distribution curves of the selected lines

According to the method described above, all the 2D images scanned were binarized. Then, the processed 2D images were stacked to reconstruct a 3D image. With the same method, the 3D images with respect to the distributions of microcracks were obtained. Fig. 5.16 presents the 3D distributions of cracking networks obtained from CT tests before and after oedometer tests. As before, the voxel size is equal to 24 μm. Before test, there are obvious cracks observed inside all the damaged samples. For test TD0, microcracks inside the sample are not significant after test. This can be interpreted with the closure of microcracks due to the mechanical compression.

In the test, the sample was loaded up to 64 MPa, which is significantly larger than the yield stress. Thus, significant volumetric strain was caused, leading to closure of microcracks. The similar phenomenon was observed in test TD4. However, for tests TD9 and TD24, obvious microcracks are observed inside the samples after oedometer tests. These results indicate that with the increase of suction, the microcracks inside the samples are more significant after oedometer tests. This is because the lower suction results in a higher water content in claystone. Thus, the clay minerals were hydrated more completely. In this case, claystone grains have lower stiffness and higher compressibility, allowing microcracks to be closed more easily. In conclusion, the closure of microcracks is suction-dependent.

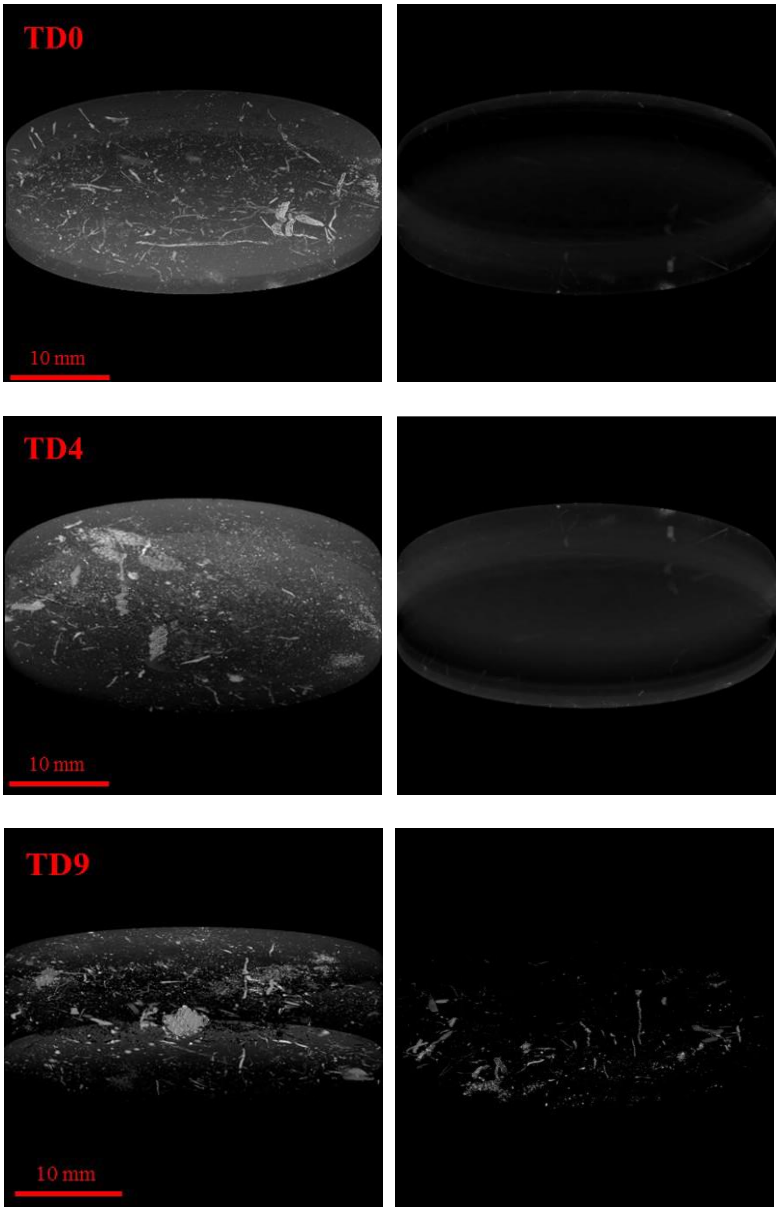

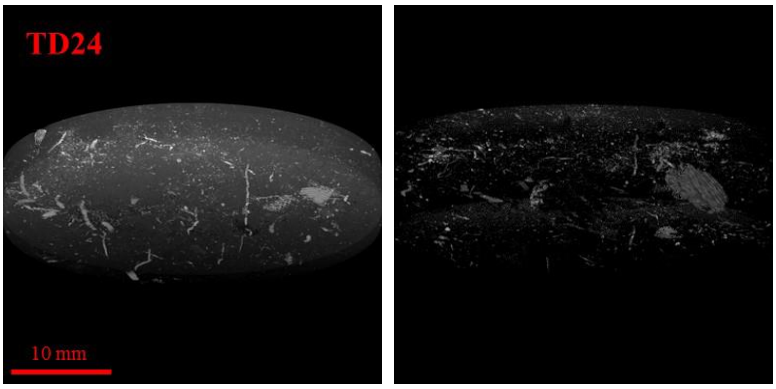

Fig. 5.16. 3D distributions of cracking networks obtained from CT tests: before oedometer test (left) and after oedometer test (right)

Several small pieces of claystone were taken from the centre of samples after unloading, and MIP tests were conducted to further investigate the microstructure changes. Fig. 5.17 presents the pore size distribution curves for tests TD0, TD4, TD9 and TD24 after oedometer tests, including the cumulative one and the density one. It is found that at suctions 0 MPa, 4.2 MPa, 9 MPa and 24.9 MPa, the intruded void ratios are 0.136, 0.138, 0,140 and 0.161, respectively, showing an increasing tendency. The corresponding total void ratios are 0.181, 0.184, 0,187 and 0.215, respectively. These observations indicate that the intruded void ratios are around 0.75 time the total ones, which is consistent with the observations by Yven et al. (2007), Boulin et al. (2008), Delage et al. (2014) and Menaceur et al. (2016). A delimiting diameter 1 μm can be selected to distinguish micro-pores and macro-pores. According to Wang (2012) and Menaceur et al. (2016), the macro pores were mainly induced by damage, by either hydraulic or mechanical loadings. Thus, this delimiting diameter can be also considered to distinguish the original pore population and the one induced by damage. The similar method was adopted by Dao et al. (2015) and Mokni et al. (2020). It appears that there are more large-pores at higher suctions. Moreover, all the density function curves in Fig. 5.17 present a monomodal shape with one inflection point. The delimiting diameter divides the density function curve into two comparable parts. Compared to the peak density value of the main pore population, the one of macro-pores for each test is significant lower. According to the brick model proposed by Menaceur et al. (2016), the pore diameter corresponding to the peak density value represents the mean pore diameter d_{MD} inside the COx claystone.

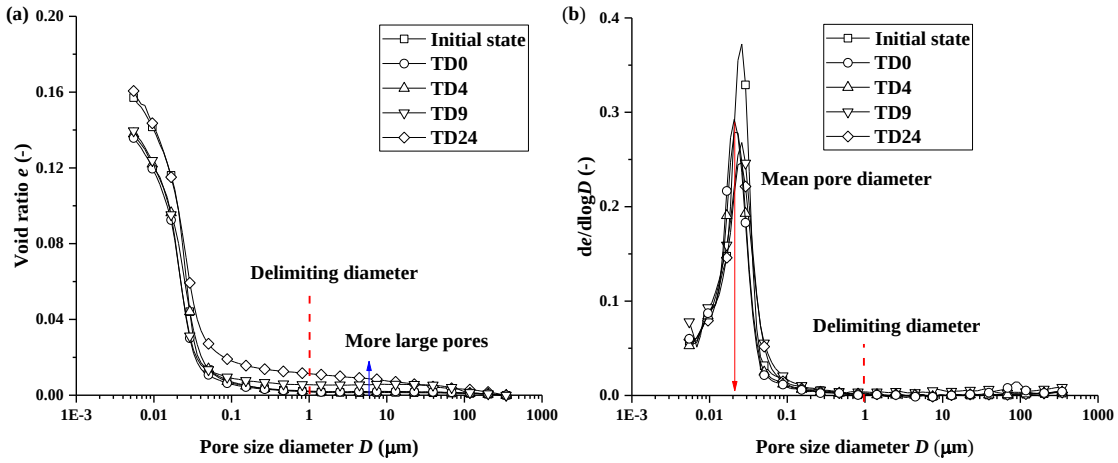

Fig. 5.17. Pore size distribution curves: (a) cumulative curve; (b) density function.

Note: 'initial state' means that the COx core was just taken from the T1 cell

In Fig. 5.18, the changes in mean pore diameter with respect to suction are presented, indicating that the mean diameter d_{MD} decreases with the decrease the suction. This is opposed to the results obtained by Menaceur et al. (2016): lower suction results in higher d_{MD}. It is worth noting that the tests were conducted under free swelling condition by Menaceur et al. (2016). Under such condition, with the decrease of suction, more water molecules were absorbed in the COx claystone platelets, resulting in an increase of mean pore diameter. In this study, the oedometer samples were loaded to 64 MPa, then immediately unloaded. Higher compressibility and lower void ratio were observed under lower suction, as shown in Fig. 5.3. This volume change caused more significant reduction of mean pore diameter under lower suctions.

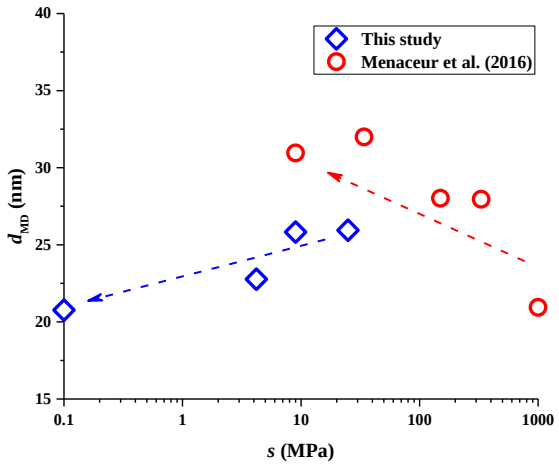

Fig. 5.18. Changes in mean MIP diameter with suction

In order to make a quantitative analysis of the damage of claystone, the damage coefficient adopted by Dao et al. (2015) and Mokni et al. (2020) was adopted. The coefficient D was defined as the ratio of the porosity of microcracks to the total one, as described in chapter 3. As

mentioned before, the proportion of cracking volume in each sample can be identified based on the 2D and 3D CT image analysis. Thus, a corresponding damage coefficient D_c can be calculated. Similarly, according to the delimiting diameter selected in MIP tests, the void ratio of microcracks can be obtained, also allowing a damage coefficient D_m to be calculated.

Fig. 5.19 presents the correlations between suction and damage coefficients obtained through CT and MIP tests. The damaged coefficients before oedometer tests in Fig. 5.19a were obtained from CT results, showing similar values, which suggests that the initial damage states of oedometer samples were comparable. After oedometer tests, D obtained through CT and MIP tests both increase with the increase of suction, as presented in Fig. 5.19b. This is consistent with the qualitative observations in Fig. 5.16. Further comparison shows that D_m is slightly larger than D_c at a given suction. For MIP results, the delimiting diameter 1 μm was adopted to distinguish microcracks inside the sample. However, for CT results, the voxel size is 24 μm, which means that the dimension of microcracks less than 24 μm are not included. Thus, the microcracks with the dimensions between 1 to 24 μm were ignored in the CT results. This explains the difference of D obtained by the two methods.

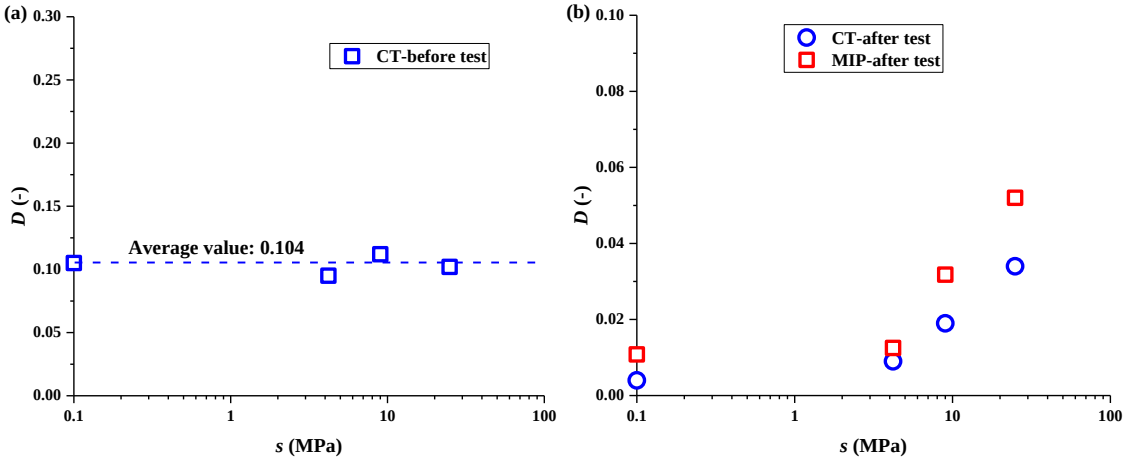

Fig. 5.19. Damage coefficient D determined from CT and MIP tests: (a) before oedometer test; (b) after oedometer test

5.2 Strain rate effect on compression behaviour

CRS tests were performed on damaged claystone at different suctions. Four suctions were first imposed on the damaged samples through VET method. Then, these samples at suction equilibrium state were compressed in oedometer cell under constant suction and strain rate. Based on that, the water retention properties were first analysed and discussed. According to

the compression results, the related mechanical parameters (compression index λ and viscous parameter C_A) were identified.

5.2.1 Water retention behaviour

For the suction equilibrium, the damaged samples with 38 mm in diameter and 10 mm in height were first placed into desiccators containing different saturated saline solutions. There are four solutions adopted: distilled water, K_2SO_4, KNO_3 and $(NH_4)_2SO_4$, which correspond to zero suction, 4.2 MPa, 9 MPa and 24.9 MPa (Delage et al., 1998; Wan et al., 2013; Menaceur et al., 2016; Guerra, 2018; Dardé, 2019). In order to record the changes of sample mass accurately, the total mass of sample in each desiccator was measured every two days. Then, the average water content at each suction was determined. Fig. 5.20 presents the evolutions of average water contents with time at four suctions during the suction equilibration process. It appears that the equilibrium state was reached when water content stabilized, which was also confirmed by the measurement of suction using WP4, as reported by Wan et al. (2013) and Menaceur et al. (2016). After suction equilibration, the final mass of each sample was taken and the corresponding water content was determined. In addition, the volume of each sample was measured before and after suction imposition with a caliper. Based on the variations of water content and volume, the corresponding void ratios and degrees of saturation can be determined. The results obtained are summarized in Table 5.1.

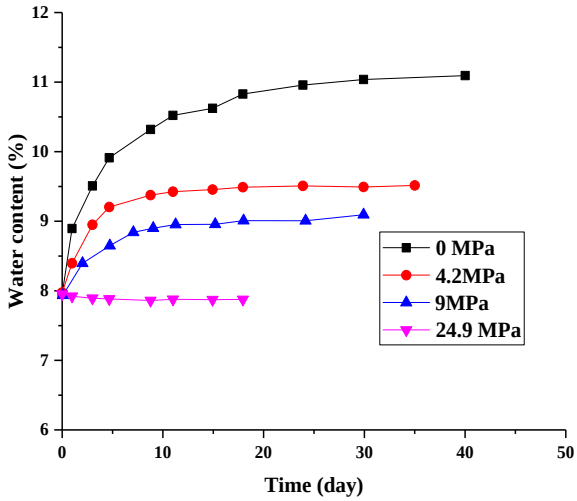

Fig. 5.20. Evolutions of average water content with time at different suctions

Table 5.1 Characteristics of damaged claystone samples before and after suction imposition

Sample ID	Target suction (MPa)	Initial state			Suction equilibrium state		
		Water content (%)	Void ratio (-)	Degree of saturation (%)	Water content (%)	Void ratio (-)	Degree of saturation (%)
X1	0	8.01	0.249	86.8	11.12	0.311	96.5
X2		7.99	0.253	85.3	11.01	0.309	96.2
X3		7.97	0.251	85.7	11.05	0.307	96.9
X4	4.2	8.03	0.255	85.0	9.52	0.276	93.1
X5		7.87	0.244	87.1	9.50	0.272	94.3
X6		7.94	0.247	86.8	9.58	0.271	95.4
X7	9	7.98	0.251	85.8	9.12	0.261	94.3
X8		7.82	0.248	85.1	9.03	0.258	94.5
X9		7.96	0.252	85.3	9.07	0.257	95.3
X10	24.9	7.86	0.246	86.3	7.91	0.247	86.5
X11		7.84	0.249	85.0	7.87	0.249	85.3
X12		7.93	0.247	86.7	7.85	0.246	86.1

Fig. 5.21. compares the water content and degree of saturation at different suctions between damaged claystone in this study and intact claystone obtained by Menaceur et al. (2016). It is found that compared to the intact claystone, the damaged claystone has a relatively higher water content, a larger void ratio and a similar degree of saturation at a given suction. For example, the average water content, void ratio and degree of saturation for the damaged sample at 9 MPa are 9.07 %, 0.259 and 94.7 %, respectively, while those for the intact claystone are 7.65 %, 0.210 and 98.1 %. It is thus inferred that the higher water content of damaged claystone is due to the higher clay content. Indeed, it was reported that the water retention capacity depends on the percentage of smectite contained in clay minerals (Yven et al., 2007; Wan et al., 2013). In addition, the existence of initial microcracks inside the damaged claystone increases the initial void ratio, which correspondingly results in a larger void ratio after suction equilibration. Consequently, the damaged and intact claystones have the similar degree of saturations at the same suction.

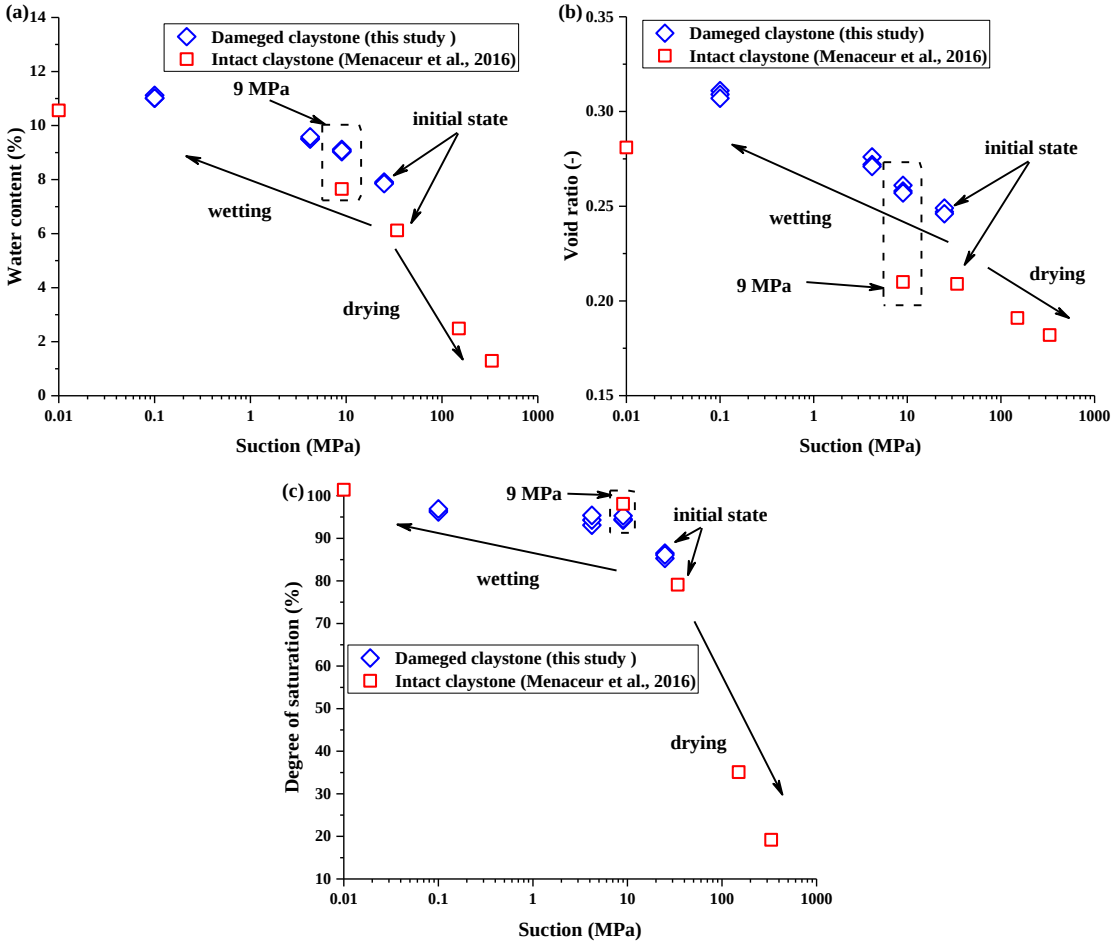

Fig. 5.21. Water retention properties: (a) water content versus suction; (b) degree of saturation versus suction

5.2.2 Compression behaviour

Once suction equilibrated, the samples were installed into oedometer cell and loaded under constant suction and strain rate. For the tests at saturated state, synthetic water was injected into the bottom of cell to keep zero suction, and a pore pressure sensor was installed at the bottom of cell to monitor the excess pore pressure due to loading. Thus, the corresponding vertical effective stress can be obtained. For the tests at unsaturated state, vertical net stress is used to describe the correlation between stress and strain (Coleman, 1962; Fredlund and Morgenstern, 1977; Gens, 1996; Wang et al., 2013).

Fig. 5.22 presents the vertical stress–strain curves at suctions 0 MPa, 4.2 MPa, 9MPa and 24.9 MPa under the strain rates 1×10^{-5} s^{-1}, 1×10^{-6} s^{-1} and 1×10^{-7} s^{-1}. It is found that for the tests at the same suction, the compression curves are almost parallel to each other in the virgin compression stage regardless of the strain rates. This implies that the compression curves have the similar slopes, thus the similar compression index. With the increase of strain rate, the vertical stain at

the same vertical stress is smaller and the yield stress is higher. Comparison of the compression curves at different suctions shows that a higher suction results in a lower compression strain at the same vertical stress, indicating the suction dependency of the compression behaviour. These observations are consistent with those on other unsaturated soils (Gennaro and Pereira, 2013; Qin et al., 2015; Rezania et al., 2020).

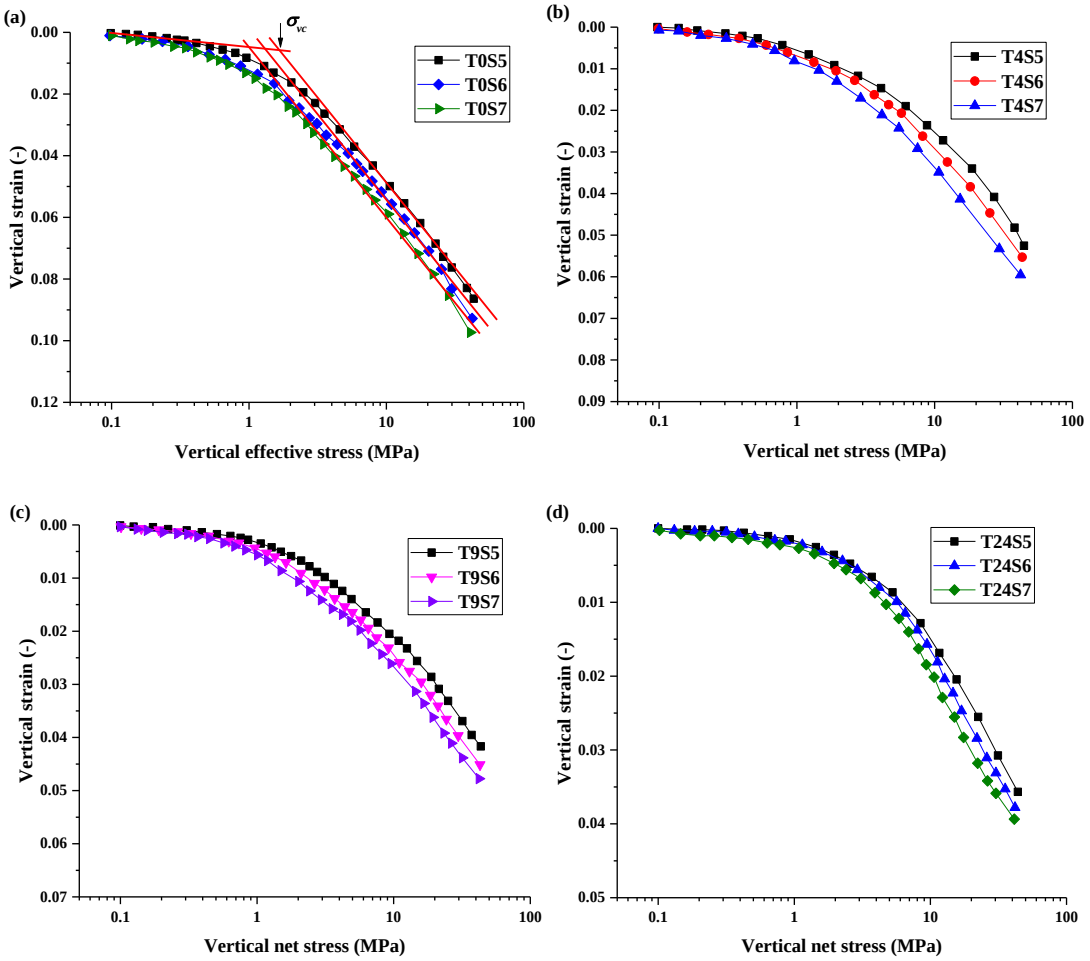

Fig. 5.22. Vertical stress-strain curves under different suctions and strain rates: (a) 0 MPa; (b) 4.2 MPa; (c) 9 MPa and (d) 24.9 MPa

In Fig. 5.22, the slope of stress-strain curve reflects the compressibility of soils. It appears that the compression index is independent of suction:

$$C_c = -\Delta e / \Delta \log \sigma_v \tag{5-4}$$

Fig. 5.23 presents the changes in C_c with respect to suction in a semi-logarithmic plane. With the increase of suction, C_c decreases, showing an almost linear correlation. This is also consistent with the observations on rockfill (Oldecop and Alonso, 2001), GMZ bentonite (Qin et al., 2015) and London Clay (Rezania et al., 2020).

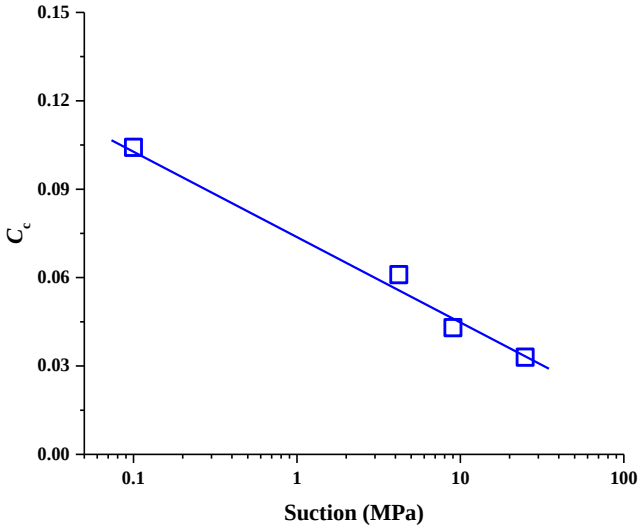

Fig. 5.23. Changes in C_c with respect to suction

As a compression parameter, yield stress is also used to describe the compression behaviour of soils. The method for its determination is presented in Fig. 5.22. Fig. 5.24 presents the relationships between the yield stress and suction at different strain rates. The yield stress increases with the increase of suction. The loading-collapse curves (LC) was proposed by Alonso and Gens (1990) to describe this relationship. The LC curve obtained presents a shape similar to those of other soils (Alonso and Gens, 1990; Cui and Delage, 1996; Rampino et al., 2000; Ye et al., 2014). Besides, with the increase of strain rate, the yield stress becomes larger. Leroueil et al. (1985) attributed this phenomenon to the more viscous behaviour at higher strain rate. Thus, the clay becomes more stiff, resulting in a higher yield stress. The similar observations were made on other saturated and unsaturated soils (Leroueil et al., 1985; Leroueil and Marques,1996; Gennaro and Pereira, 2013; Qin et al., 2015; Rezania et al., 2020).

To further analyze the effect of strain rate on yield stress, the yield stress is replotted versus strain rate in a logarithmic plane in Fig. 5.25. At each suction, the yield stress increases with the increase of strain rate, showing a linear correlation. This confirms the observation from Fig. 5.24. Interestingly, the slope of each line decreases with the increase of suction. To determine the slope, Eq. 5-5 is adopted, as recommended by Leroueil (1996), Gennaro and Pereira (2013) and Qin et al. (2015):

$$\log \sigma_{vc} = A + C_A \log \dot{\varepsilon}_v \tag{5-5}$$

where σ_{vc} is the yield stress, A are the soil parameters, and $\dot{\varepsilon}_v$ is the vertical strain rate. C_A is the parameter representing the viscosity, which is used to describe the rate-dependency of compression behaviour of soils. Leroueil (2006) and Gennaro and Pereira (2013) pointed out

that C_A is equivalent to the ratio between C_α and C_c, which correlates rate-dependency with creep.

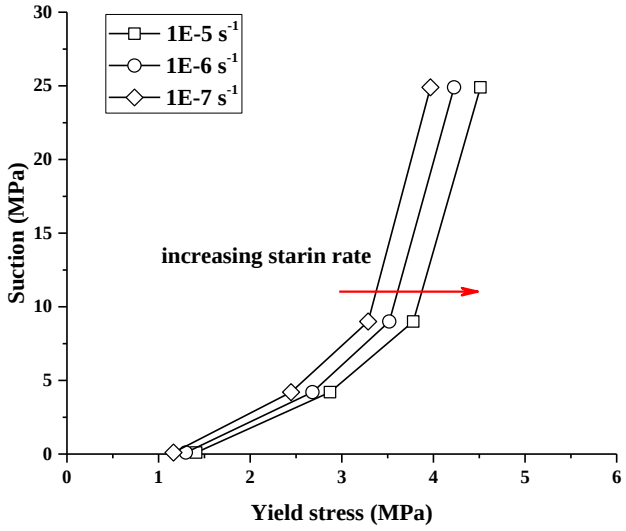

Fig. 5.24. Yield stress versus *s* at different strain rates

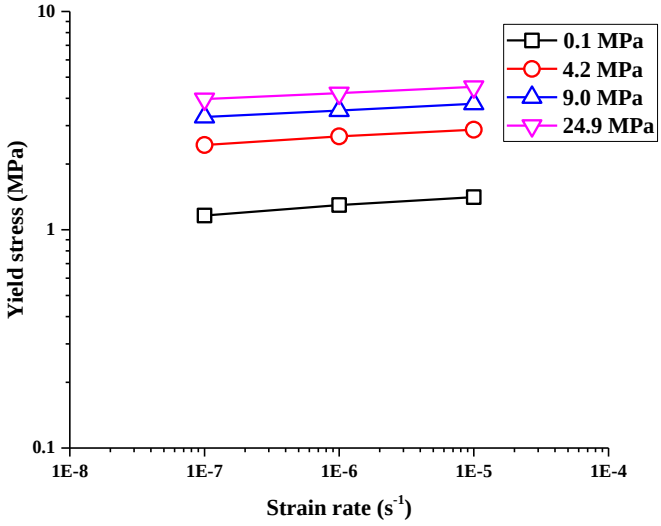

Fig. 5.25. Evolutions of yield stress with respect to strain rate

Fig. 5.26 presents the evolution of C_A with suction. It appears that C_A decreases with the increases of suction. Eq. 5-3 is modified by replacing C_α/C_c and a with $C_A(\mathrm{s})$ and $C_A(0)$, as shown in Eq. 5-6. The correlation between C_A and suction is thus identified, as shown in Fig. 5.26.

$$C_A(s) = C_A(0) - b \times \ln(s + p_{at}) \tag{5-6}$$

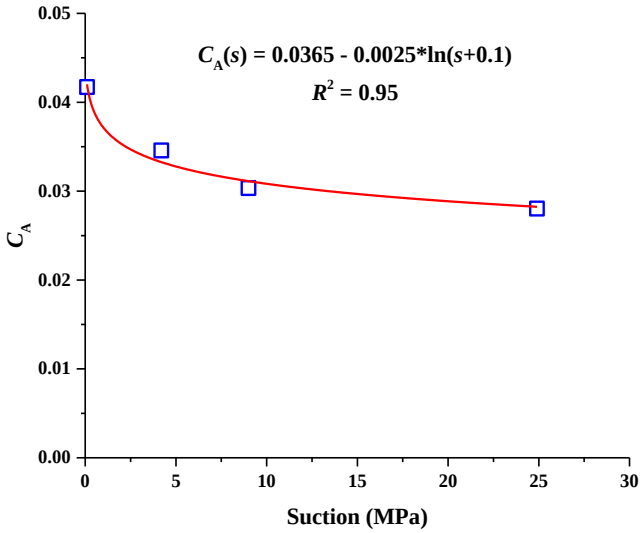

Fig. 5.26. C_A versus suction

5.3 Analysis of hydro-mechanical parameters

As indicated in sections 5.1.2 and 5.2.2, the related hydro-mechanical parameters for damaged claystone can be determined from the experimental results. In this section, the compression and viscous parameters obtained from oedometer (OED) and CRS tests were compared and discussed. Then, the LC curves were modelled with the identified parameters.

In order to model the compression behaviour, it is necessary to identify the slope of the compression line λ (Wood, 1990). Besides, for unsaturated soils, the stiffness increases with the increase of suction. Thus, the line slope λ also changes (Alonso and Gens, 1990). Alonso and Gens (1990) reported that the correlation between λ and suction can be described with Eq. 5-7, which has been widely adopted in the modelling of unsaturated soils (Alonso and Gens, 1990; Cui and Delage, 1996; Alonso et al., 1999; Sánchez et al., 2005; Yao et al., 2014).

Based on the analysis on the compression behaviour of unsaturated damaged claystone, the relationship between the compression index C_c and suction was built. In this regard, Eq. 5-8 is adopted to describe the correlation between C_c and λ, which is recommended by Wood (1990), Yin and Tong (2011) and Qin et al. (2015). According to that, λ was calculated based on C_c obtained from OED and CRS tests. Fig. 5.27 shows the changes in λ with respect to suction with the model parameters related to Eq. 5-7. The difference of λ determined with the two methods is quite small. This indirectly validates the suction control in CRS tests, indicating that the strain rate adopted can ensure constant suction during the compression process. It is worth noting that in general, λ is identified from the compression line from isotropic compression tests.

Wood (1990) and Lloret et al. (2003) pointed out that oedometer results can be used to determine the mechanical parameters of soils for the sake of simplicity.

$$\lambda(s) = \lambda(0)[(1-r)\exp(-\beta s) + r] \tag{5-7}$$

$$\lambda = C_c / \ln 10 \tag{5-8}$$

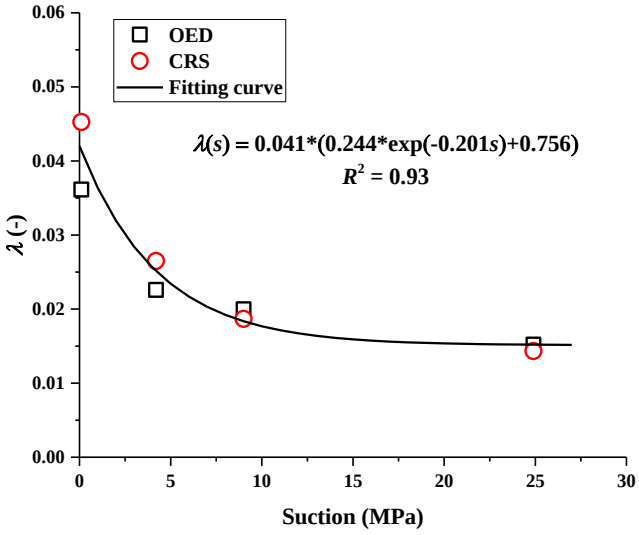

Fig. 5.27. λ versus s for damaged COx claystone

Parameter C_A plays a key role in the strain rate effect. As indicated before, C_A can be determined from the slope of C_α-C_c curve obtained from OED test or from the slope of strain rate-yield stress curve obtained from CRS test. C_A obtained from the two methods is summarized and presented in Fig. 5.28. There is little difference between the values from the two methods. With Eq. 5-6, the evolution of C_A with suction for the damaged claystone is determined based on the results from OED and CRS tests.

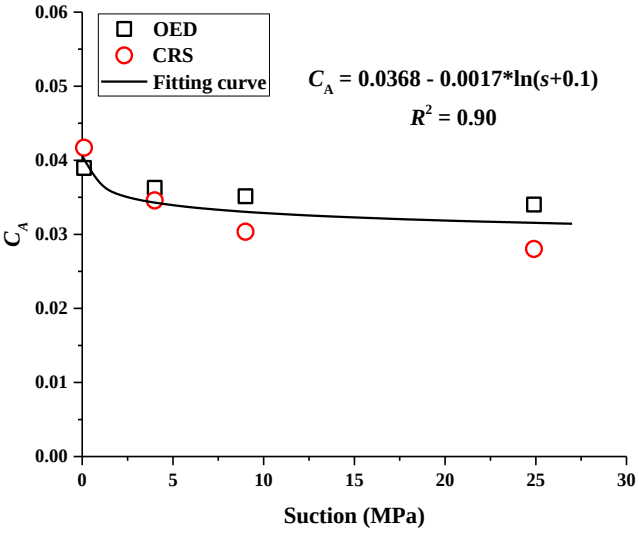

Fig. 5.28. C_A versus s for the damaged COx claystone

To model the suction effect on yield stress, Alonso and Gens (1990) described the LC curve by using two independent variables: net stress and suction. The relationship between net yield stress and suction was formulated with Eq. 5-9:

$$\frac{p_y}{p_c} = \left(\frac{p_0}{p_c}\right)^{\frac{\lambda(0)-\kappa}{\lambda(s)-\kappa}} \tag{5-9}$$

where κ is elastic parameter, p_c is a model parameter and p_y and p_0 are yield stresses at unsaturated and saturated states, respectively.

Besides, in order to consider the strain rate effect on the yield stress for unsaturated soils, Gennaro and Pereira (2013) and Qin et al. (2015) proposed Eq. 5-10 to describe the relationship between strain rate and yield stress at a given suction:

$$p_0(\dot{\varepsilon}_v) = p_0^{ref}\left(\frac{\dot{\varepsilon}_v}{\dot{\varepsilon}_{v,ref}}\right)^{C_A(s)} \tag{5-10}$$

where p_0^{ref} and $\dot{\varepsilon}_{v,ref}$ are the reference stress and the corresponding reference strain rate, respectively, $p_0(\dot{\varepsilon}_v)$ and $\dot{\varepsilon}_v$ are the present yield stress and the corresponding current strain rate, respectively.

By substituting Eq. 5-10 into Eq. 5-9, the effects of suction and strain rate can be accounted for in the modelling of LC curve for unsaturated soils with Eq. 5-11. Thus, the yield stress p_y can be calculated. As indicated before, the compression and viscous parameters were determined from the experimental results. p_c, p_0^{ref} and $\dot{\varepsilon}_{v,ref}$ could be identified by the parameter sensitivity analysis. The model parameters related to the modelling of LC curve are summarized in Table 5.2.

$$p_y = p_c\left[\frac{p_0^{ref}}{p_c}\left(\frac{\dot{\varepsilon}_v}{\dot{\varepsilon}_{v,ref}}\right)^{C_A(s)}\right]^{\frac{\lambda(0)-\kappa}{\lambda(s)-\kappa}} \tag{5-11}$$

Fig. 5.29 presents the comparison between the experimental and simulated yield stresses. Without consideration of strain rate effect, the results obtained by simulation with Eq. 5-9 are in good agreement with the experimental results obtained from OED tests, as shown in Fig. 5.29a. With the same set of parameters, the difference between simulated and experimental yield stresses in Fig. 5.29b become significant with the increase of suction, when the strain rate effect is accounted for. This is attributed to that the model parameters which are determined from the limited experimental data. More experimental results are thus needed to obtain more accurate model parameters to improve the model predictions.

Table 5.2 Model parameters for the damaged claystone

κ	$\lambda(0)$	β	r	p_c	p^{ref}	$\dot{\varepsilon}_{v,ref}$	$C_A(0)$	b
-	-	MPa^{-1}	-	MPa	MPa	s^{-1}	-	-
0.005	0.041	0.201	0.756	0.04	1.9	0.95	0.0368	0.0017

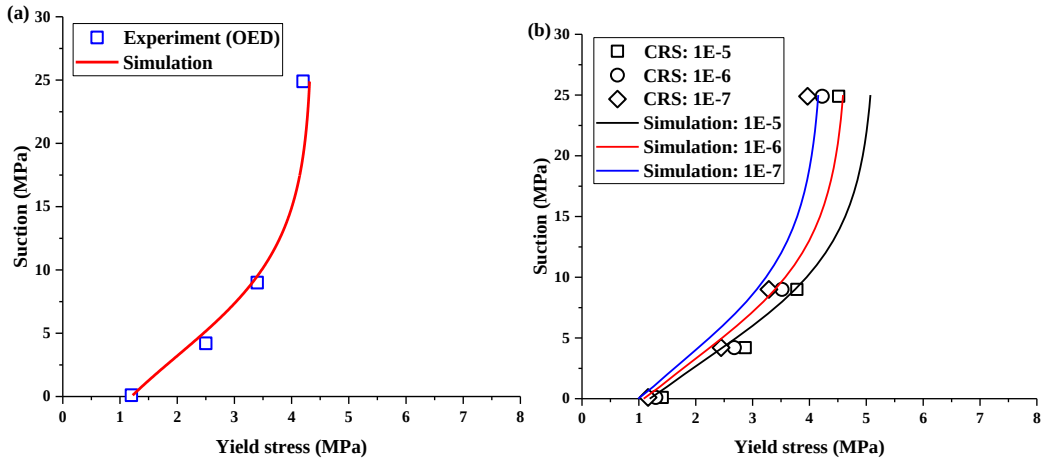

Fig. 5.30 Comparisons between experiments and simulations for LC curve: (a) without strain rate effect; (b) with strain rate effect

5.3 Conclusions

In this chapter, the hydro-mechanical behaviour of damaged COx claystone was investigated. Two experimental methods were adopted: oedometer and CRS tests with controlled-suction. In addition, CT and MIP tests were conducted aiming at investigating the microscopic properties with respect to microcracks. The results obtained allow the following conclusions to be drawn:

In oedometer tests with controlled suction, the damaged claystone shows a lower swelling strain than the intact claystone. This is attributed to the swollen clay minerals which filled the preexisting microcracks inside the damaged claystone, leading to a decrease of the swelling potential. Besides, in a standard fashion, the damaged claystone with a higher suction exhibits a lower compressibility and larger yield stress. At zero suction, the results indicate that there is a linear correlation between hydraulic conductivity and vertical stress. Compared with the intact claystone, the damaged one presents a lower compression index C_c. For C_α and C_c*, they both increase with the increase of vertical stress and with the decrease of suction, showing a significant dependency on stress and suction. A satisfactory linear relationship is observed between C_α and C_c* at each suction. The slope of the C_α - C_c curve depends on suction. It is worth noting that 16 MPa is a key stress for COx claystone, which is related to the closure of

microcracks and grain breakage, as discussed in chapter 4. Microstructure observations through CT and MIP tests indicate that the microcracks inside the damaged sample became more significant with the increase of the imposed suction after oedomter compression. This is interpreted by a lower stiffness resulting from the lower suction for the claystone grains - the microcracks were closed more easily at a given stress level. The quantitative analysis of the damaged coefficients confirms the qualitative observations on CT images.

Compared with the intact claystone investigated by Menaceur et al. (2016), the damaged claystone studied in this study exhibits a higher water contents but the similar degrees of saturation at a given suction. This is probably due to the larger initial void ratios related to the preexisting microcracks inside the damaged claystones. The results from the CRS tests show that the compression behaviour of the damaged claystone is suction-dependent. This is confirmed in terms of compression index and yield stress. Moreover, at the same suction, the yield stress increases with the increase of strain rate, which can be described with a linear correlation in a log-log plane. A viscous parameter C_A is thus obtained, which depends on suction.

Based on the experimental results obtained from OED and CRS tests, the compression and viscous parameters were determined and analysed for the damaged claystone. A formula was adopted to model the LC curve accounting for the effects of strain rate and suction. Further, the LC curve was modelled with the identified parameters. Experimental and simulated yield stress are in good agreements, validating the adopted modelling approach.

Chapter 6. Modelling of visco-plastic behaviour of COx claystone

The time dependent behaviour of unsaturated COx claystone is modelled in this chapter with consideration of the damage effect. A new constitutive model is first proposed to describe the visco-plastic behaviour of unsaturated soils. In light of the experimental results, this model incorporates suction effect in isotach concept, nonstationary flow surface theory (NSFS) and progressively hardening concept. Thus, the coupled effects of strain rate and suction under different loading paths can be described. Besides, the Bishop effective stress and the influence of suction on elasticity are also accounted for. The damage properties of COx claystone were analyzed based on MIP results, and a damage coefficient was defined accounting for the effects of suction and plastic strain. Then, the damage coefficient is incorporated in the proposed model. For the purpose of validation, a series of loading conditions were considered based on the data from the literatures and from this study. Results show that the proposed model is able to reproduce the main behaviours of unsaturated COx claystone, including swelling, rate-dependent compression/shear, creep, etc.

6.1 A visco-plastic model for unsaturated soils

In the past decades, a large amount of laboratory tests and modelling works were conducted to investigate the viscoplastic behavior of soils. For instance, triaxial tests under different confining pressures, over-consolidated ratios (OCR) and axial strain rates were carried out to analyze the rate-dependent behaviour of saturated clays at different initial states (Yin and Tong, 2011). Also, constant strain tests (CRS) were performed in oedometer on reconstituted and natural clays, allowing a unique relationship among stress, strain and strain rate to be built (Qin et al., 2015). The yield stress and shear strength are found to increase with increasing strain rate. Similarly, CRS and triaxial tests under different suctions and strain rates were carried out to understand the effect of unsaturated parameters (degree of saturation, suction etc.) on the time-dependent behaviour of partly saturated geomaterials (Wu, 2018).

Based on the experimental results, numerous empirical relations and rheological models were proposed to predict the time-dependent behaviour of soils, including creep, stress relaxation and rate effects (Liingaard et al., 2004). In addition, within the elasto-viscoplastic (EVP) frame, more general relationships between stress, strain and time (or strain rate) were constructed, for example, over-stress theory (Perzyna, 1966) and non-stationary flow surface (NSFS) concept (Qiao et al., 2016). Based on the over-stress theory and NSFS, many viscoplastic models using

different over stress functions were built to simulate the strain rate effect, creep and stress relaxation behaviour of saturated soils. Especially, 3D EVP model was derived from the generalized viscoplastic overstress theory (Qu et al., 2010). Besides, using the overstress concept, Yin et al. (2010) explored the anisotropic viscous behaviour of natural soft soils. However, the overstress-based models cannot verify the consistency condition. In other models, isotach approach proposed by Suklje (1957) was generally adopted to describe the viscosity of soils, which was incorporated into the flow yield surface theory (De Gennaro and Pereira, 2013; Qiao et al., 2016).

To date, the EVP unsaturated models are based on either the overstress theory (Wu, 2018) or the bounding surface theory (Mac et al., 2017). A constitutive model built by Wu (2018) is able to simulate the time-dependent behaviour of unsaturated Glenroy silt. However, the model still needs to be examined with more experimental results and with consideration of more stress paths. Mac et al. (2017) employed bounding surface plasticity theory to define the yield function by using viscoplastic strain as one of the variables, while neglecting the influence of strain rate on the direction of viscoplastic strain. With isotach concept, De Gennaro and Pereira (2013) extended the Barcelona Basic Model (BBM) to the effect of loading rates for chalk at different suctions. But their model cannot describe the stress relaxation phenomenon and viscoplastic effect in low stress range due to the adoption of total volumetric strain rate and single yield function.

In this study, based on the NSFS theory by Qiao et al. (2016) and the gradually hardening law by Hong et al. (2016), the model proposed by De Gennaro and Pereira (2013) is extended. This new viscoplastic constitutive model for unsaturated soils is developed within the consistency viscoplastic framework. There are two new characteristics: (1) the implication of NSFS theory enables the model to meet the loading consistency condition and to reproduce the stress relaxation phenomenon; (2) the use of a gradual hardening law allows the smooth stress-strain curves. Besides, there is no conventional pure elastic region, allowing the creep phenomenon at a very low stress to be described.

6.1.1 New characteristics and experimental evidence

For modelling the viscoplastic behaviour, the isotach approach is used to describe the relationship among stress–strain–strain rate, as shown in Fig. 6.1. The effect of strain rate on the yield stress is expressed by Eq. 6-1 (Leroueil et al., 1985):

$$\sigma_y' = f(\dot{\varepsilon}_v) \tag{6-1}$$

where σ_y' is the yield stress and $\dot{\varepsilon}_v$ is the volumetric strain rate.

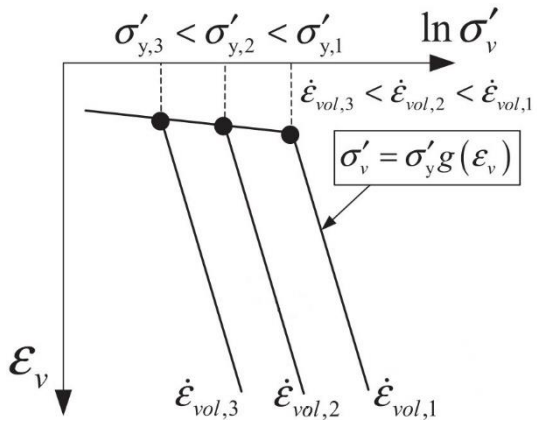

Fig. 6.1. The isotach concept (Qiao et al., 2016)

Following this approach, soils may experience both compression under constant strain rate or delayed compression under constant stress. It is worth noting that each isotach (rate line in Fig. 6.1) has an equivalent rate-dependent yield stress which is larger for a higher strain rate. By mathematically normalizing this concept, the relationship was applied in constitutive modelling by Kabbaj et al. (1986).

To describe the stress relaxation phenomenon, the relationship among stress–strain–strain rate was replaced by the stress–strain-viscoplastic strain rate (Kabbaj et al. 1985). This was further extended by Laloui et al. (2008):

$$\log\sigma_y' = A + C_\mathrm{A}\log\dot{\varepsilon}_v^{vp} \tag{6-2}$$

$$\sigma'_{y,\dot{\varepsilon}_v^{vp}} = \sigma'_{y,\dot{\varepsilon}_{v,ref}^{vp}} \left(\frac{\dot{\varepsilon}_v^{vp}}{\dot{\varepsilon}_{v,ref}^{vp}}\right)^{C_A} \tag{6-3}$$

where $\dot{\varepsilon}_v^{vp}$ is the viscoplastic volumetric strain rate. $\sigma'_{y,\dot{\varepsilon}_v^{vp}}$ is the effective yield stress at the viscoplastic volumetric strain of $\dot{\varepsilon}_v^{vp}$. $\sigma'_{y,\dot{\varepsilon}_{v,ref}^{vp}}$ is the reference effective yield stress at the reference viscoplastic volumetric strain of $\dot{\varepsilon}_{v,ref}^{vp}$.

Fig. 6.2 shows that there is a linear yield stress–strain rate relationship for highly compacted unsaturated GMZ bentonite in log–log space. The similar phenomenon was observed by De Gennaro and Pereira (2013) on unsaturated chalk. This relationship is expressed by Eq. 6-4.

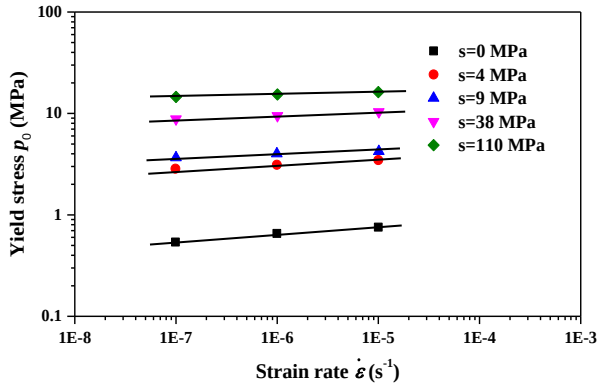

Fig. 6.2. Variation of yield stress with strain rate (data from Qin et al., 2015)

$$p_0(\dot{\varepsilon}_v) = \bar{p}_0^{ref}\left(\frac{\dot{\varepsilon}_v^{vp}}{\dot{\varepsilon}_{v,ref}^{vp}}\right)^{C_A(s)} \tag{6-4}$$

where $C_A(s)$ is the slope of the fitting line and reflects the coupling between creep and compressibility at different suctions.

It appears from Fig. 6.2 that the slope $C_A(s)$ decreases with increasing suction, which reflects the effect of suction on secondary consolidation. Besides, the collected experimental data indicate that there is a linear relationship between $C_A(s)$ and suction, as shown in Fig. 6.3. Eq. 5-6 is used to express the suction dependence of C_A.

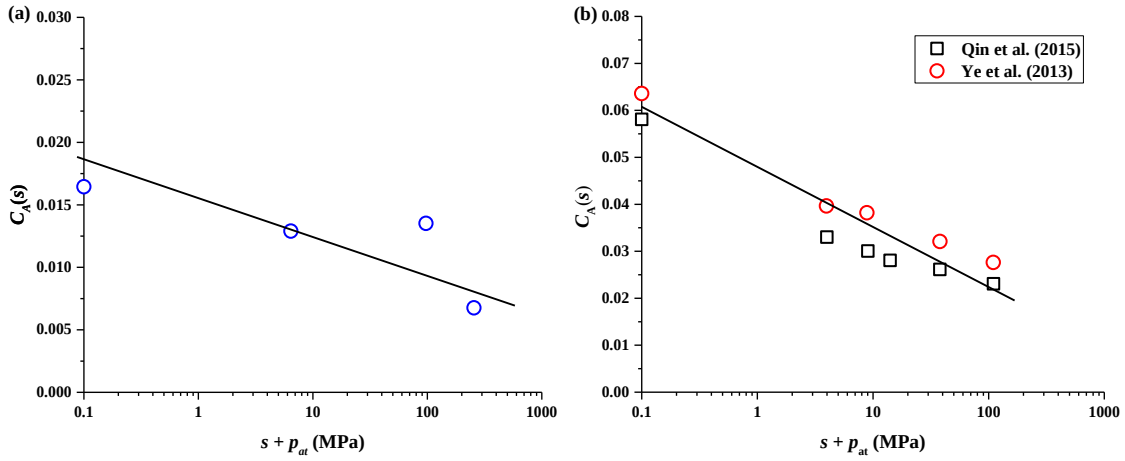

Fig. 6.3. Effect of suction on C_A: (a) rockfill (data from De Gennaro and Pereira, 2013); (b) GMZ bentonite (data from Ye et al. (2013) and Qin, et al. (2015))

The coupled effect of strain rate and suction on C_A can be described in Fig. 6.4. Qu et al. (2010) reported that there is a strain rate threshold below which the strain rate effect on the yield stress can be ignored. This is adopted in the viscoplastic modelling by Qiao et al. (2016) for saturated soils. A threshold value is also used in this study to represent the strain rate below which the rate-dependent effect disappears.

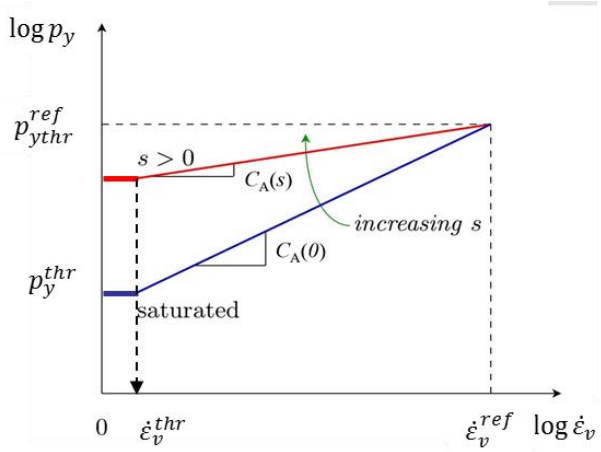

Fig. 6.4. Schematic representation of the variation of yield stress with strain rate (after De Gennaro and Pereira, 2013)

Based on the isotach concept, the strain rate effect on volume change behaviour of soils can be modelled under one dimensional or isotropic compression conditions. For the modelling in a general stress space, the nonstationary flow surface (NSFS) theory was adopted by Qiao et al. (2016) to describe the strain rate effect on the shear behaviour of saturated soils, as illustrated in Fig. 6.5. The yield surface changes with the variation of volumetric strain rate, allowing modelling the creep, relaxation and rate-dependent properties of soils. With the similar method, the creep, relaxation and rate-dependent behaviours of unsaturated soils can also be described.

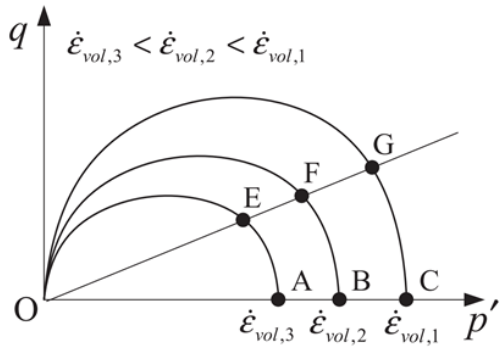

Fig. 6.5. Schematic illustration in *p'-q* plane (Qiao et al., 2016)

Moreover, inside the conventional elastic domain, the creep strain cannot occur. To address this problem, the gradual hardening concept is used in the proposed model to construct a non-purely elastic zone (Fig. 6.6), by linking the inner loading surface to the normal yield surface, as in Hong et al. (2016) and François and Laloui (2008). The progressive evolution of yield limit is described by Eqs. 6-5 and 6-6 (Hong, 2013).

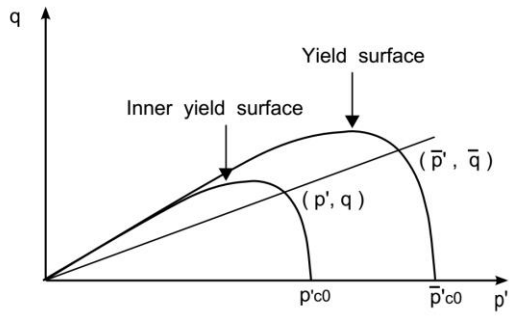

Fig. 6.6. Inner and normal yield surfaces (Hong, 2013)

$$\gamma = \frac{p'}{\bar{p}'} = \frac{q}{\bar{q}} = \frac{p'_c}{\bar{p}'_c} \tag{6-5}$$

$$\gamma = 1 + (\gamma_0 - 1)\exp(\frac{-vk}{\lambda-\kappa}\varepsilon_v^p) \tag{6-6}$$

where γ_0 is the initial value of γ which reflects the distance of the current yield state to the reference yield state, p'_c is the actual loading yield stress, $\bar{p}'_c$ is the reference yield stress on the normal consolidation line. p' and q are the actual loading yield stress, $\bar{p}'$ and $\bar{q}$ are reference stresses. k is a material parameter, ε_v^p is the plastic volumetric strain.

Thereby, the proposed model ensures: (1) a gradual hardening; (2) creep and relaxation inside the elastic domain. Thus, it can reproduce the time-dependent behaviour of soils even in low stress range.

6.1.2 Mathematical formulations of the proposed model

In the model, the strain increment is partitioned into two parts: an elastic part and a viscoplastic part, as shown in Eq. 6-7:

$$\mathrm{d}\varepsilon = \mathrm{d}\varepsilon^e + \mathrm{d}\varepsilon^{vp} \tag{6-7}$$

where $\mathrm{d}\varepsilon^e$ and $\mathrm{d}\varepsilon^{vp}$ are the elastic and viscoplastic strain increments, respectively.

To describe the stress framework of unsaturated soils, the Bishop effective stress approach is adopted to account for the combined effect of mechanical stress and suction (Bishop, 1959):

$$p' = \bar{p} + s\chi(S_r) \tag{6-8}$$

$$p'_c = \bar{p}_c + s\chi(S_r) \tag{6-9}$$

$$q' = \bar{q} \tag{6-10}$$

where $\chi(S_r)$ is the effective stress coefficient, related to the degree of saturation.

Eq. 6-11 is adopted to describe the variation of χ with S_r (Alonso et al., 2010). The water

retention curve is modelled by van Genuchten (VG) model (Eq. 6-12, van Genuchten, 1980).

$$\chi(S_r) = {S_r}^a \tag{6-11}$$

$$S_r = \left(\frac{1}{1+(\alpha_r s)^n}\right)^m \tag{6-12}$$

where a ($a > 1$) is a material parameter, and α_r, n and m are model parameters.

With the Bishop effective stress, the elastic volumetric and shear strain increments are expressed by the following equations:

$$\mathrm{d}\varepsilon_v^e = \frac{\kappa(s)}{v}\frac{\mathrm{d}p'}{p'},\ K = \frac{p'(1+e)}{\kappa(s)} \tag{6-13}$$

$$\mathrm{d}\varepsilon_q^e = \frac{\mathrm{d}q}{3G},\ G = \frac{3(1-2\nu)}{2(1+\nu)}K \tag{6-14}$$

where K and G are the elastic bulk and shear moduli, respectively; κ is the elastic slope in the lnp'-(1+e) plane and ν represents the Poisson's ratio. Note that the Poisson ratio is assumed constant in the current model, while K and G change with the variation of suction.

Considering the effect of suction on the elasticity of unsaturated soils, Eq. 6-15 is adopted to reproduce the variation of κ with suction (Adem and Vanapalli, 2015). This equation is validated with the experimental data of highly compacted GMZ bentonite (Fig. 6.7).

$$\kappa(s) = \kappa(0)[(1 - r_1)\,exp(-\beta_1 s) + r_1] \tag{6-15}$$

where $\kappa(0)$ is the elactic parameter at saturated state, $\beta_1$and r_1 are the model parameters for describing the changing rate and the smallest value of $\kappa(s)$, respectively.

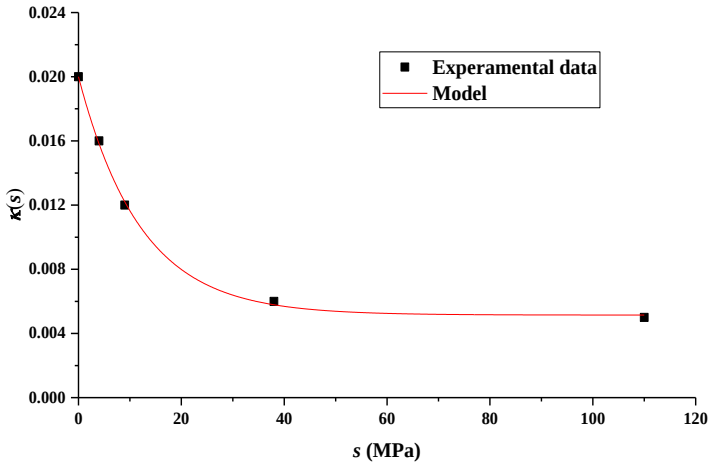

Fig. 6.7. Effect of suction on elasticity (data from Qin et al., 2015)

For the hardening law, the LC (loading collapse) curve is considered. The Eq. 6.16 recommended by Sheng et al. (2004) and Le Pense et al. (2016) is adopted for this purpose. The

yield stress contains two parts: the net yield stress part and the suction part. The evolution of the net yield stress with suction is expressed by Eq. 6-17, as proposed by Alonso and Gens (1990). By replacing the viscoplastic volumetric strain by the plastic one, the hardening law under saturated state is obtained (Eq. 6-18).

$$p'_c = \bar{p}_c + s\chi(S_r) \tag{6-16}$$

$$\frac{\bar{p}_c}{p_c} = \left(\frac{p_0^*}{p_c}\right)^{\frac{\lambda(0)-\kappa(0)}{\lambda(s)-\kappa(s)}} \tag{6-17}$$

$$p_0^* = p_0 \exp\left(\frac{v}{\lambda(0)-\kappa(0)}\varepsilon_v^{vp}\right) \tag{6-18}$$

By substituting Eqs. 6-4 and 6-18 into Eq. 6-17, the net yield stress is obtained, as follows:

$$\bar{p}_c = p_c \left[\frac{\bar{p}_{r0}^{ref}}{p_c}\left(\frac{\dot{\varepsilon}_v^{vp}}{\dot{\varepsilon}_{v,ref}^{vp}}\right)^{C_A(s)} \exp\left(\frac{v}{\lambda(0)-\kappa(0)}\varepsilon_v^{vp}\right)\right]^{\frac{\lambda(0)-\kappa(0)}{\lambda(s)-\kappa(s)}} \tag{6-19}$$

For the implication of gradual hardening law, the concept of image point is adopted to define the progressive state. The image point is obtained as a projection of the current stress state on the normal yield surface, as shown in Fig. 6.6. The stress ratio γ between the current stress point and the image point is maintained constant. In order to describe the effect of shear behaviour on the progressive hardening, Hong et al. (2016) recommended to replace ε_v^p in Eq. 6-6 with $d\varepsilon_t^{vp}$, as shown in Eq. 6-20. Meanwhile, by replacing the plastic strains with viscoplastic strains, the time effect can also be considered in this study, as follows:

$$\gamma = 1 + (\gamma_0 - 1)\exp\left(\frac{-vk}{\lambda(s)-\kappa(s)}\varepsilon_t^{vp}\right),\ d\varepsilon_t^{vp} = d\varepsilon_v^{vp} + A_d d\varepsilon_d^{vp} \tag{6-20}$$

where ε_t^{vp} is a generalized viscoplastic strain, $d\varepsilon_d^{vp}$ is the viscoplastic shear strain and A_d represents the parameter controlling the contribution of $d\varepsilon_d^{vp}$.

The modified Cam-Clay (MCC) yield function Eq. 6-21 is adopted for the yield surface. With the modification of yield surface based on the progressive hardening and NSFS, the inner yield function and normal yield functions are obtained, as expressed in Eqs. 6-22 and 6-23, respectively. The corresponding yield surfaces are schematically illustrated in Fig. 6.8. In addition, as in Alizadeh and Gatmiri (2017), the effect of cohesion on COx claystone is also neglected in this study.

$$F = q^2 - M^2 p'(p'_c - p'),\ M = \frac{6\sin\varphi'}{3-\sin\varphi'} \tag{6-21}$$

where M is the slope of the critical state line and φ' is the frictional angle.

$$F_I = q^2 - M^2 p'(p'_c - p') \tag{6-22}$$

$$F_Y = q^2 - M^2 \bar{p}'(\bar{p}'_c - \bar{p}') \tag{6-23}$$

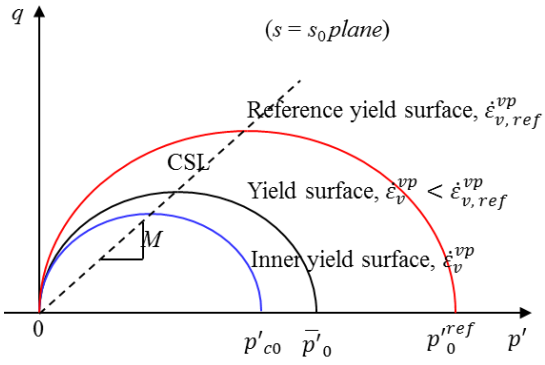

Fig. 6.8. Schematic illustration of yield surfaces

The consistency condition $dF_I = 0$ for the viscoplastic loading implies:

$$dF_I = \frac{\partial F_I}{\partial \boldsymbol{\sigma}} : d\boldsymbol{\sigma} + \frac{\partial F_I}{\partial s} ds + \frac{\partial F_I}{\partial \varepsilon_v^{vp}} d\varepsilon_v^{vp} + \frac{\partial F_I}{\partial \dot{\varepsilon}_v^{vp}} d\dot{\varepsilon}_v^{vp} = 0 \tag{6-24}$$

A non-associated flow rule is adopted as in the BBM. The visoplastic potential function is as follows:

$$G_I = \alpha_g q'^2 - M^2 p'(p'_c - p') \tag{6-25}$$

$$\alpha_g = \frac{M(M-9)(M-3)}{9(6-M)[1-\kappa(0)/\lambda(0)]} \tag{6-26}$$

where α_g is a parameter related to the stress state under zero lateral strain condition.

Thus, the viscoplastic strain is determined with Eq. 6-27 and the corresponding dilatancy is determined by Eq. 6-28.

$$d\boldsymbol{\varepsilon}^{vp} = d\lambda \frac{\partial G_I}{\partial \boldsymbol{\sigma}} \tag{6-27}$$

$$d = \frac{d\varepsilon_v^{vp}}{d\varepsilon_d^{vp}} = \frac{\partial G_I}{\partial p} \Big/ \frac{\partial G_I}{\partial q} \tag{6-28}$$

It appears from Eq. 6-24 that due to the effect of viscoplastic volumetric strain rate, the viscoplastic volumetric strain can change under constant stress and constant suction. In addition, the viscoplastic volumetric strain rate can change with time under constant volume and suction, causing variations of viscoplastic volumetric strain and stress. This correpondes to the typical stress relaxation phenomenon. By correlating the current stress state with the stress state projected on the normal yield surface based on the progressive concept, the time dependent behaviour in the low stress range can be well described by the proposed model. Besides, the softening effect is not well reproduced due to the application of this progressive concept.

6.2 Extension of the model to damage for COx claystone

Under the hydro-mechanical loadings, micro-cracks were observed inside the COx claystone at a micro scale (Wang et al., 2014, 2015), further affecting the mechanical properties. This damage effect needs to be considered in the constitutive modelling. In this section, the damage mechanism is first discussed. Then, a damage evolution law is proposed and applied in the modelling.

6.2.1 Insight into the damage of COx claystone

6.2.1.1 Damage due to hydration

As indicated in chapter 1, COx claystone is composed of clay matrix (clay minerals) and inclusions (carbonate and quartz, etc.). Wang et al. (2014) observed through ESEM that for COx claystone, micro-cracks were generated between the clay matrix and the inclusions due to hydration. Similarly, MIP results by Menaceur et al. (2016) indicated that at low suction, significant large pores appeared inside the COx claystone. The generation of the large pores are attributed to the micro-cracks induced by the swelling of clay minerals. Wang (2012) reported that the COx claystone is locally heterogeneous due to the existence of inclusion. The volume of clay matrix can swell or shrink due to the variation of humidity, while the volume of inclusions changes little, generating thus local stresses. Micro-cracks appeared along the inclusion-matrix interface in the wetting process. Besides, microcracks also appeared in the clay matrix, resulting from the swelling of clay minerals. These phenomena were evidenced by Menaceur et al., (2016) through MIP observations.

Fig. 6.9 shows the MIP results of COx claystone in the wetting process under free swelling. The detailed descriptions are presented in Table 6.1. Note that the value of 34 MPa corresponds to the initial suction. In Fig. 6.9, it is found that the detected void ratio at zero suction increased significantly and the macro-pores were significantly created due to the swelling of clay minerals, especially for the pores with a diameter larger than 1 μm. The appearance of these large pores is related to the creation of micro-cracks (Menaceur et al., 2016). Beside, from the comparisons of the PSD curves between 9 MPa suction and initial state, it appears that the curves are similar and the volume change is not significant. This is consistent with the observations by Wang et al. (2014, 2015). It is worth noting that there are some larger pores at the initial state in Fig. 6.9b, in limited quantity. This indicates that some micro-cracks may pre-exist inside the COx claystone.

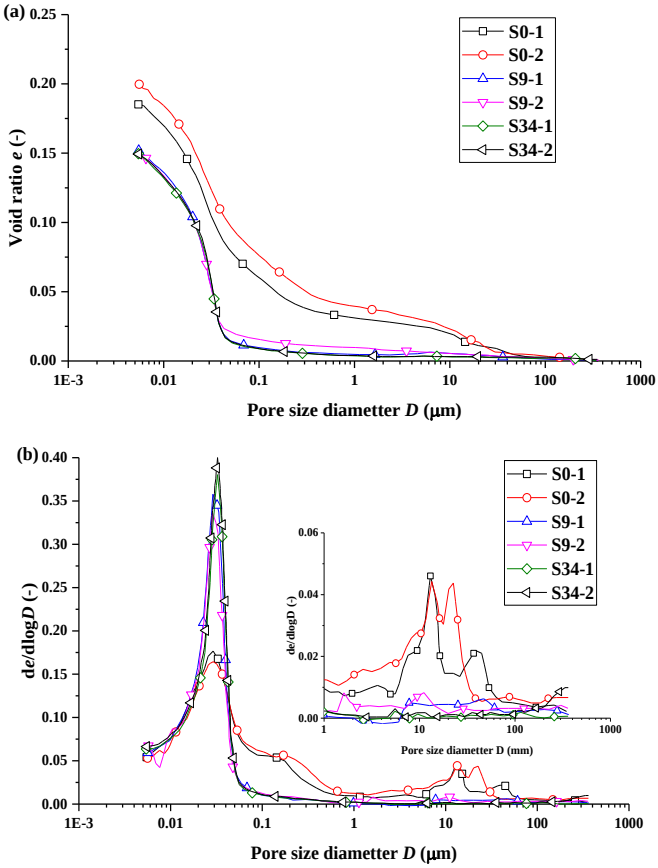

Fig. 6.9. Evolutions of the microstructures of COx claystone in the wetting process from suction 34 MPa to zero (data from Menaceur et al., 2016): (a) cumulative curve; (b) density curve

Fig. 6.10 shows the MIP results of the COx claystone in the drying process. Compared with initial state, the detected void ratios at other suctions decreased due the shrinkage of clay matrix, in agreement with the total void ratio in Table 6.1. Some larger pores were observed in Fig. 6.10b. Due to desiccation, the clay matrix shrank, causing tensile stress at the interface with the inclusions, generating micro-cracks. Moreover, the uneven shrinkage of clay matrix can also create micro-cracks, damaging thus the COx claystone.

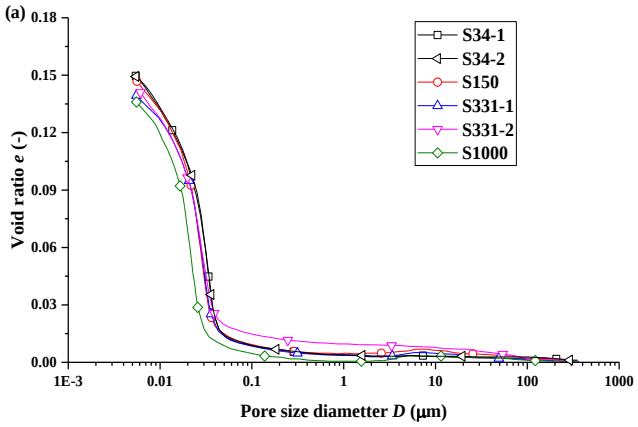

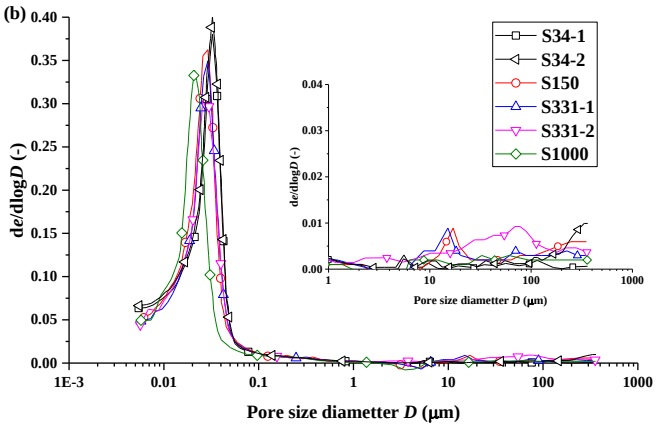

Fig. 6.10. Evolutions of the microstructure of COx claystone in the drying process from suction 34 MPa to 1000 MPa (data from Menaceur et al., 2016): (a) cumulative curve; (b) density curve

Table. 6.1 Detailed description of MIP tests at different suctions under free swelling

Test No.	Porosity	Void ratio	Testing conditions	Source
S0-1	0.220	0.281	Wetted to 0 MPa from initial state	Menaceur et al. (2016)
S0-2	0.233	0.303	Previously dried to 331 MPa, then wetted to 331 MPa	
S9-1	0.174	0.210	Wetted to 9 MPa from initial state	
S9-2	0.181	0.221	Previously dried to 331 MPa, then wetted to 9 MPa	
S34-1	0.173	0.209	Initial state	
S34-2	0.174	0.210	Initial state	Menaceur (2014)
S150	0.161	0.191	Dried to 9 MPa from initial state, then wetted to 150 MPa	Menaceur et al. (2016)
S331-1	0.154	0.182	Dried to 9 MPa from initial state	
S331-2	0.152	0.179	Previously wetted to 0 MPa, then dried to 331 MPa	
S1000	0.130	0.147	Oven dried at 105°C from initial state	Menaceur (2014)

6.2.1.2 Damage due to mechanical loading

Under mechanical loading, micro-cracks can be also generated, as evidenced by Wang et al. (2014) through ESEM observation. This damage can be explained as follows: (1) the mechanical loading can induce micro-cracks when the tensile/shear stress exceeds a certain value at the inclusion-matrix interfaces; (2) with the further increase of external stress, some coarse grains may split, creating extra micro-cracks (Wang, 2012). These micro-cracks are all

induced by plastic deformations. When the mechanical loading exceeds the elastic limit, damage occurred. The local micro-cracks increase with the increase of plastic deformation, with preferential propagation along the inclusion-matrix interfaces.

Fig. 6.11 shows the MIP results from oedometer compression at zero suction. Table 6.2 presents the detailed information of the testing conditions. It is found that at saturated state, with the increase of stress, the detected void ratio increases and the pores with a diameter larger than 1 μm also increase significantly. Menaceur (2014) reported that the volumetric strains of the oedometer samples were 4.8 and 8.3%, respectively, when the load was comprised between 56 and 113 MPa, which are significantly larger than the yield stress. Mohajerani et al. (2011) reported that a high stress resulted in significant collapse of pores but generated micro-cracks meanwhile. This mechanism is consistent with that obtained from the ESEM observation by Wang (2012). In addition, Menaceur (2014) also conducted an oedometer compression test on COx claystone at saturated state with several unloading and reloading cycles. From the compression curve, the elastic rebounding slope κ (in the $\ln\sigma_v$'- e plane) for different maximum axial stresses is determined (Fig. 6.12). With the increase of maximum axial stress, the κ increases significantly. Aversa et al. (1993) observed that a higher stress caused a more significant swelling index after unloading through the oedometer tests on Italian tectonised shales, which was attributed to the presence of discontinuities (i.e. cracks). In this sense, the increase of κ results from the generation of significant cracks due to the high stress compression. This was consistent with that reported by Mohajerani et al. (2011).

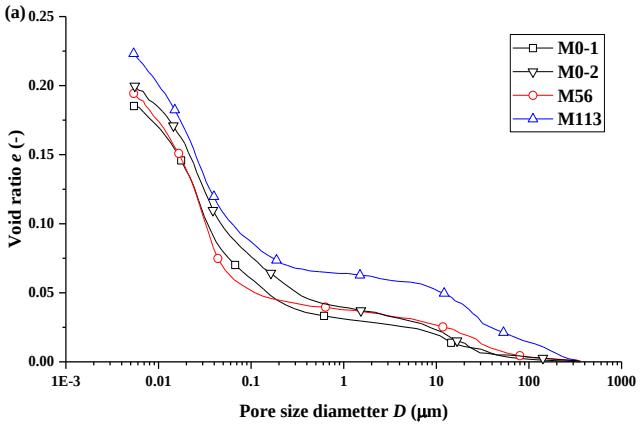

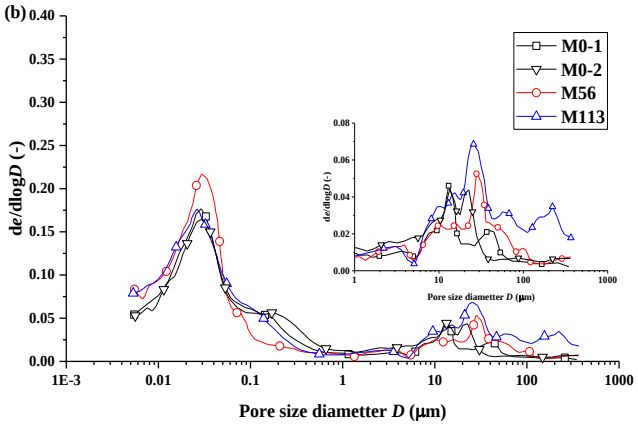

Fig. 6.11. Evolutions of the microstructures of COx claystone loaded to vertical stresses 0 MPa, 56 MPa and 113 MPa at saturated state (data from Menaceur, 2014): (a) cumulative curves; (b) density curves

Table. 6.2 Detailed description of MIP tests after oedometer compression at zero suction

Test No.	Porosity	Void ratio	Testing conditions	Source
M0-1	0.220	0.281	Wetted to zero suction under free swelling	Menaceur et al. (2016)
M0-2	0.233	0.303	Wetted to zero suction under free swelling	Menaceur (2014)
M56	0.201	0.241	Wetted to zero suction under constant volume, then loaded to 56 MPa, finally slowly unloaded to 0 MPa	
M113	0.222	0.285	Wetted to zero suction under constant volume, then loaded to 113 MPa, finally slowly unloaded to 0 MPa	

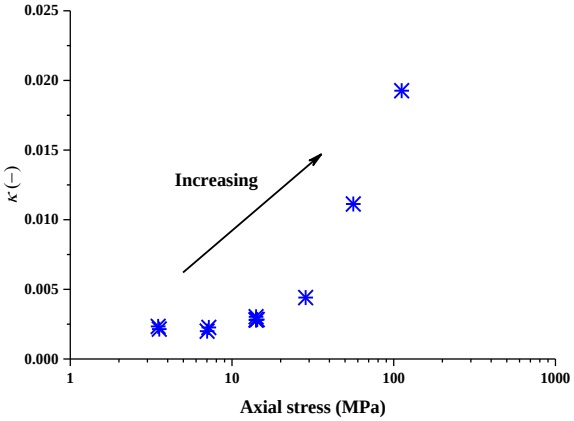

Fig. 6.12. κ determined at different maximum axial stresses

6.2.2 Modelling of damage for COx claystone

In general, the damage of geomaterials is correlated to the degradation of elastic modulus (Young's modulus E and shear modulus G). The damage coefficient D is determined with respect to the ratio of the current Young's modulus to the Young's modulus at intact state. The specific D value can be calculated with Eq. 29 based on the triaxial unloading-reloading results.

$$E_D = (1 - D)E \tag{6-29a}$$

$$G_D = (1 - D)G \tag{6-29b}$$

where E_D and G_D are the Young's and shear moduli at the current damage state, respectively, and E and G are the Young's and shear moduli at the initially intact state, respectively.

In this study, for modelling the damage of COx claystone, the damage coefficient D is defined as the ratio of cracking porosity ϕ_{crack} to the total porosity ϕ, as described in chapter 3. This definition implies that damage is physically related to the micro-cracks. MIP results are used for the determination of damage coefficient D under different test conditions. It is worth noting that for the determination of the volume of micro-cracks, the delimiting diameter 1 μm is adopted (see chapter 3 and chapter 5). This delimiting diameter allows the micro-pores and micro-cracks due to hydration to be well distinguished. Menaceur (2014) reported that the diameter of micro-cracks ranges from 7 and 100 μm.

As discussed in section 6.2.1, the damage mechanism of COx claystone is related to either hydration or mechanical loading. The MIP results in Figs. 6.9 and 6.10 indicate that the wetting/drying cycle can affect the damage extent, but in an insignificant manner. For simplicity, this effect is neglected in this study. The determined D values are presented in Fig. 6.13 for different suctions. It appears that D under free swelling decreases with the increase of suction, reflecting the suction effect on the damage level. The correlation between D and suction is given in the figure and Eq. 6-30 is proposed to describe this correlation.

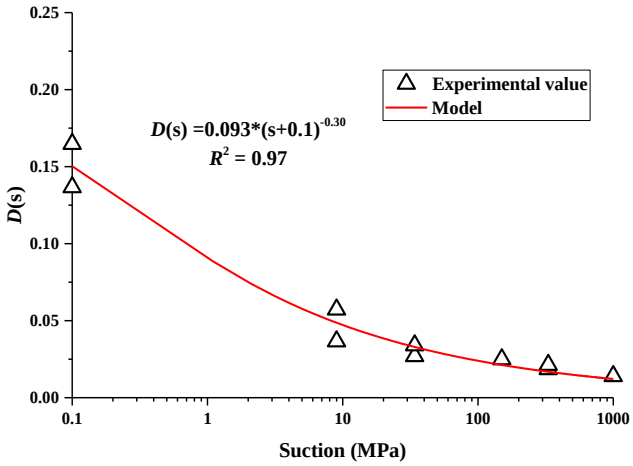

Fig. 6.13. Changes in D(s) with respect to suction

$$D(s) = \alpha_D (s + p_{atm})^{-\beta_D} \tag{6-30}$$

where α_D is a model parameter representing the damage extent at saturated state and β_D is a model parameter controlling the evolution rate of D with suction.

In addition, for the damaged COx claystone, some micro-cracks can be closed by loading, decreasing the damage extent. This phenomenon was evidenced by Zhang et al. (2011, 2015, 2019). Eq. 6-31 is proposed to describe this phenomenon by replacing suction s with Bishop effective stress p' in Eq. 6-30. The Bishop effective stress is determined with Eqs. 6-8, 6-11 and 6-12. Parameter a used in the determination of effective stress coefficient $\chi(S_r)$ is equal to 1.1. The relationship between suction and degree of saturation is fitted by VG model, as shown in Fig. 6.14. In Fig. 6.15, the data in Fig. 6.13 is replotted in terms of Bishop effective stress.

$$D(p') = \alpha_D (p')^{-\beta_D} \tag{6-31}$$

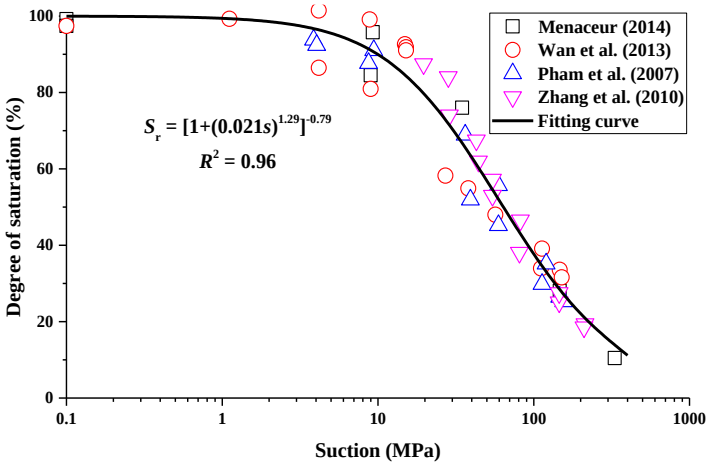

Fig. 6.14. Soil-water retention curve (SWRC) of COx claystone

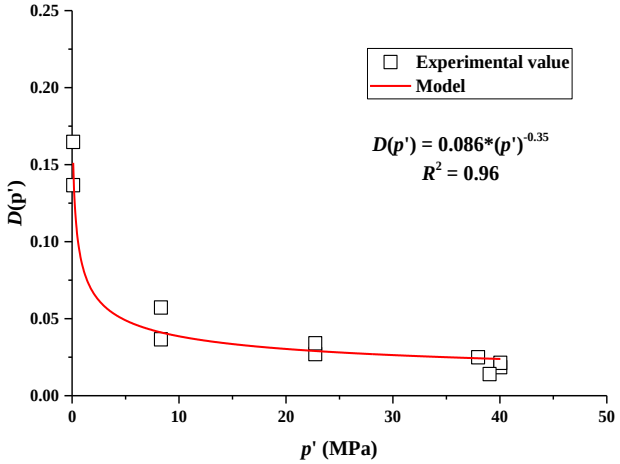

Fig. 6.15. Changes in $D(p')$ with respect to suction

In order to further consider the effect of mechanical loading, the plastic volumetric strain is adopted as the variable to describe the evolution of D at constant suction. Based on the MIP results in Fig. 6.11, the damage coefficients under different maximum stresses at zero suction are calculated. Besides, according to the corresponding compression curves obtained by Menaceur (2014), the corresponding plastic volumetric strains are determined. The elastic parameter κ is taken equal to 0.005 in the calculation of plastic volumetric strains at different maximum stresses, as recommended by Alizadeh and Gatmiri (2017). The evolution of D with the variation of plastic strain ε_v^p at saturated state is shown in Fig. 6.16. The determined D increases with the increase of ε_v^p, indicating the contribution of plastic loading to damage. The correlation is described by Eq. 6-32:

$$D(\varepsilon_v^p) = D_0 \exp(\gamma_D \varepsilon_v^p) \tag{6-32}$$

where D_0 is the damage coefficient without plastic strain and γ_D is a model parameter controlling the evolution rate of D with ε_v^p.

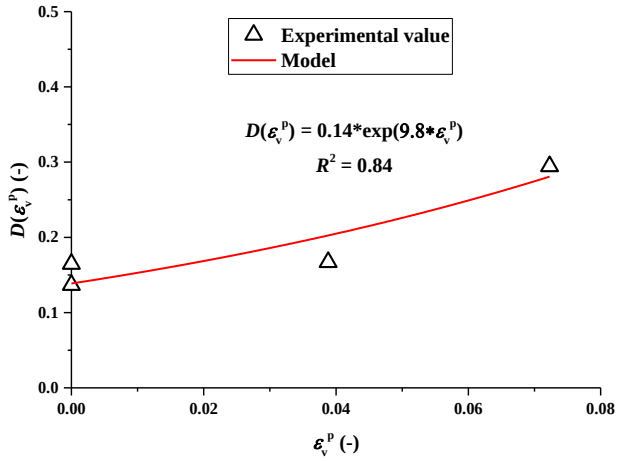

Fig. 6.16. Changes in $D(\varepsilon_v^p)$ with respect to plastic volumetric strain

Thus, if suction s and plastic volumetric strain ε_v^p are selected as the variables to describe the evolution of damage, the combined effects of hydration and mechanical loading can be accounted for. By incorporating Eqs. 6-31 and 6-32, Eq. 6-33 is obtained, allowing the combined effects to be considered. In order to consider the effect of time-dependent deformation, Eq. 6-33 is modified by replacing the plastic volumetric strain ε_v^p by the viscoplastic volumetric strain ε_v^{vp}, as shown in Eq. 6-34.

$$D(p', \varepsilon_v^p) = \alpha_D p'^{-\beta_D} \exp(\gamma_D \varepsilon_v^p) \tag{6-33}$$

$$D(p', \varepsilon_v^{vp}) = \alpha_D p'^{-\beta_D} \exp(\gamma_D \varepsilon_v^{vp}) \tag{6-34}$$

Then, by substituting Eqs. 6-29 and 6-34 into Eqs. 6-13 and 6-14, the damage effect is incorporated in the constitutive model.

6.3 Numerical calculation and determination of model parameters

For the determination of the incremental stress-strain relationship at each loading/unloading step, the elastic part can be calculated using Eqs. 6-13, 6-14, 6-29 and 6-34. The viscoplastic strains are determined by considering the consistency condition Eq. 6-24 and the viscoplastic potential Eq. 6-27. The corresponding viscoplastic multiplier $\mathrm{d}\lambda$ and hardening modulus H are expressed as follows:

$$\mathrm{d}\lambda = \frac{1}{H}\left(\frac{\partial F_I}{\partial \boldsymbol{\sigma}} : \mathrm{d}\boldsymbol{\sigma} + \frac{\partial F_I}{\partial s}\mathrm{d}s + \frac{\partial F_I}{\partial \dot{\varepsilon}_v^{vp}}\mathrm{d}\dot{\varepsilon}_v^{vp}\right) \tag{6-35}$$

$$H = -\left[\frac{\partial F_I}{\partial \gamma}\frac{\partial \gamma}{\partial \varepsilon_v^{vp}} + \frac{\partial F_I}{\partial p_c'}\frac{\partial p_c'}{\partial \varepsilon_v^{vp}}\right]\frac{\partial G_I}{\partial p'} \tag{6-36}$$

The generation of viscoplastic strain is related to the variations of net stress, suction and viscoplastic strain rate. Eq. 6-37 takes a more general form for the viscoplastic strain calculation.

$$\mathrm{d}\boldsymbol{\varepsilon}^{vp} = \lambda_1 \mathrm{d}\boldsymbol{\sigma} + \lambda_2 \mathrm{d}s\mathbf{1} + \lambda_3 \mathrm{d}\dot{\varepsilon}_v^{vp}\mathbf{1} \tag{6-37}$$

where λ_1, λ_2 and λ_3 are the partial multipliers corresponding to different loading factors.

By combining the elastic and viscoplastic strains, the incremental stress-strain matrix can be deduced. In addition, by referring to the plastic loading concept, the viscoplastic loading criteria are expressed as follows:

$$F_I(\boldsymbol{\sigma},\ s, \varepsilon_v^{vp},\ \dot{\varepsilon}_v^{vp}) = 0 \quad \text{with} \quad \mathrm{d}F_I > 0 \qquad \text{Loading} \tag{6-38a}$$

$$F_I(\boldsymbol{\sigma},\ s, \varepsilon_v^{vp},\ \dot{\varepsilon}_v^{vp}) = 0 \quad \text{with} \quad \mathrm{d}F_I = 0 \qquad \text{Neutral loading} \tag{6-38b}$$

$$F_I(\boldsymbol{\sigma},\ s, \varepsilon_v^{vp},\ \dot{\varepsilon}_v^{vp}) = 0 \quad \text{with} \quad \mathrm{d}F_I < 0 \qquad \text{Unloading} \tag{6-38c}$$

The inner yield surface varies with net stress, suction and viscoplastic volumetric strain rate and viscoplastic volumetric strain, indicating that the loading criterion is also related to these factors. When the soil reaches the reference state (Fig. 6.4), the corresponding yield surface is independent of suction. On the other hand, when the viscoplastic volumetric strain rate is below the threshold value, the corresponding yield surface is rate-independent.

Determination of model parameters:

(1) For the elastic parameters (κ and v) and the general plastic parameters (M and λ), they can be determined from triaxial and oedometer tests under different suctions. These tests also allow the determination of β_1, r_1, β, r and p_c.

(2) The hydraulic parameters (α_v, m and n) can be determined with VG model, fitting water retention curve.

(3) The viscous parameters (C_A, $\dot{\varepsilon}_{v,ref}^{vp}$, p_{r0}^{ref}) and the other hydraulic parameter (b) can be obtained from CRS tests at different suctions and from creep tests. More details can be found in Qiao et al. (2016).

(4) The damage parameters (α_D, β_D and γ_D) can be identified based on the data of damage coefficients, which are determined from the MIP results. Other parameters (k, a) can be identified by sensitivity analysis.

For COx claystone, different cores were drilled from different depths (Armand et al. 2013, 2014). The mineral compositions for these COx claystone cores drilled at different locations are different. Thus, the model parameters determined are also different. A set of model parameters adopted for COx claystone are presented in Table 6.3. In the next section, the proposed viscoplastic model is verified with the experimental data collected from different literatures. Considering the differences of claystone samples tested in the laboratory, some model parameters adopted in different simulations are slightly adjusted in a reasonable range.

Table 6.3 Model parameters for COx claystone

Elastic parameters	Unit	
$\kappa(0)$, β_1, r_1, ν	(-), (-), (-), (-)	0.005, 0, 1, 0.17
Plastic parameters		
$\lambda(0)$, β, r, M, k, A_d	(-), (MPa^{-1}), (-), (-), (-), (-)	0.041, 0.201, 0.756, 1.1, 3, 0.1
Hydraulic parameters		
p_c, m, n, α_v, a	(MPa), (-), (-), (MPa), (-)	0.04, 0.79, 1.29, 0.021, 1.1
Viscous parameters		
$C_A(0)$, b, $\dot{\varepsilon}_{v,ref}^{vp}$, p_{r0}^{ref}, $\dot{\varepsilon}_{v,thr}^{vp}$	(-), (-), (s^{-1}), (MPa) (-)	0.0368, 0.0017, 0.95, 1.9, 10^{-12}
Damage parameters		
α_D, β_D, γ_D	(-), (-), (-)	0.086, 0.35, 9.8

6.4 Verification and discussion

In this section, comparisons between simulations and experiments are presented. The proposed is then further evaluated and discussed in terms of swelling, compression, shear, creep, etc.

6.4.1 Swelling tests

Fig. 6.17 shows the comparisons of volumetric strain between the experimental results and the simulations with and without considering damage, for different suctions. Note that the experimental results were reported by Menaceur et al. (2016), obtained under free swelling condition. The suction 34 MPa corresponds to the initial state. In order to better reproduce the swelling behaviour, the adopted model parameter $\kappa(0)$ is taken equal to 0.008, different from the one in Table 6.3.

As shown in Fig. 6.17, the simulation with consideration of damage effect is in good agreement with the experimental results when suction is decreasing from the initial state, while the simulation underestimates the volume change when suction is increasing from the initial state. This is attributed to the adopted unsaturated effective stress. In the high suction range, it is difficult to estimate the contribution of suction with the effective stress coefficient χ (Nuth and Laloui, 2008; Alonso et al., 2010). In addition, comparing the simulations with and without damage, different swelling behaviours are observed. In the case without damage, the volume change is clearly underestimated. This is in accordance with the observations on other soils (Le

Pense et al., 2016; Mokni et al., 2020).

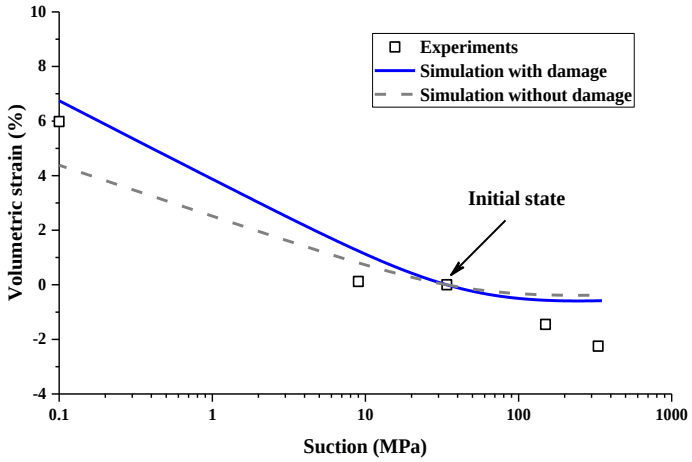

Fig. 6.17. Comparison between simulated volumetric strain and experimental ones at different suctions (experimental data from Menaceur et al., 2016)

Fig. 6.18 presents the simulated results and the experimental results for the swelling pressure under constant-volume swelling condition. Note that the experimental data is collected from Hoxha et al. (2007). At each suction, the swelling pressures show a large scatter, indicating the variability of samples. In the simulation, the model parameter a is taken equal to 20. As displayed in Fig. 6.18, the swelling pressure simulated at zero suction equals 1.13 MPa, slightly higher than the experimental one, indicating that the proposed model overestimates the swelling behaviour under the constant-volume swelling condition. Hoxha et al. (2007) pointed out that by incorporating Biot's coefficient in the unsaturated effective stress expression, the accuracy of prediction can be improved. This is not adopted in the present model. On the whole, the simulation does not seem satisfactory, but acceptable.

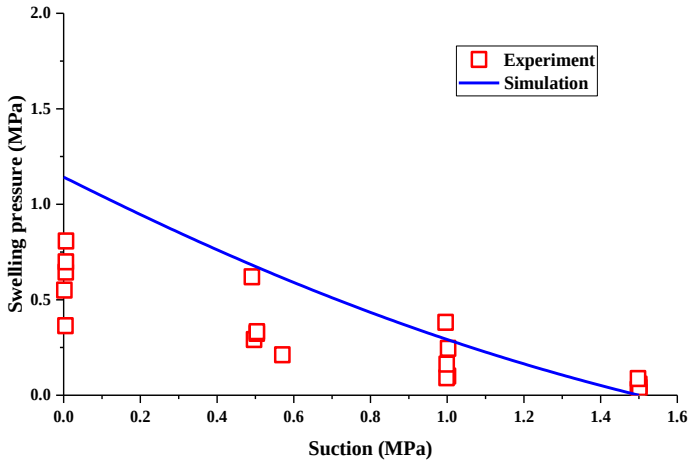

Fig. 6.18. Comparison between simulated swelling pressure and the experimental one at different suctions (experimental data from Hoxha et al., 2007)

It is worth noting that the simulated results of swelling pressure are only compared with the experimental results in a narrow range of suction. More data in a wider range of suction is needed to further verify the proposed model.

6.4.2 One-dimensional compression tests

Fig. 6.19 compares the simulations with experimental results from CRS tests on damaged COx claystone at different suctions and strain rates (see chapter 5). There are four suctions (0 MPa, 4.2 MPa, 9 MPa and 24.9 MPa) and three strain rates (1.0×10^{-7} s^{-1}, 1.0×10^{-6} s^{-1} and 1.0×10^{-5} s^{-1}). The samples tested are initially artificially damaged. In order to reproduce the effect of initial damage inside the samples, the parameter α_D used in the damage model is taken equal to 0.29, larger than the one in Table 6.3.

Fig. 6.19a shows that the simulations are in good agreement with the experimental results for different strain rates and zero suction. The yield stress increase with the increase of strain rate is well reproduced. This indicates that the proposed model can well describe the stress-strain-strain rate relationship (i.e. isotach concept). Besides, by comparing the results at different suctions (Fig. 6.19), it is found that under the same strain rate, the simulations agree well with the experimental results. The suction effect on the compressibility is also well reproduced through the compression index λ(s). Similarly, the comparisons are satisfactory for other suctions.

It is worth noting that at the end of the compression curves, the values of simulations are smaller than those from tests (e.g. suction 4.2 MPa). In chapter 3, the grain breakage effect on the compressibility of COx claystone was analyzed, showing that the compression index depends on the applied stress in the high stress range. Therefore, it is difficult to use a uniform compression index λ to describe the effect of grain breakage on the compression behaviour in the high stress range.

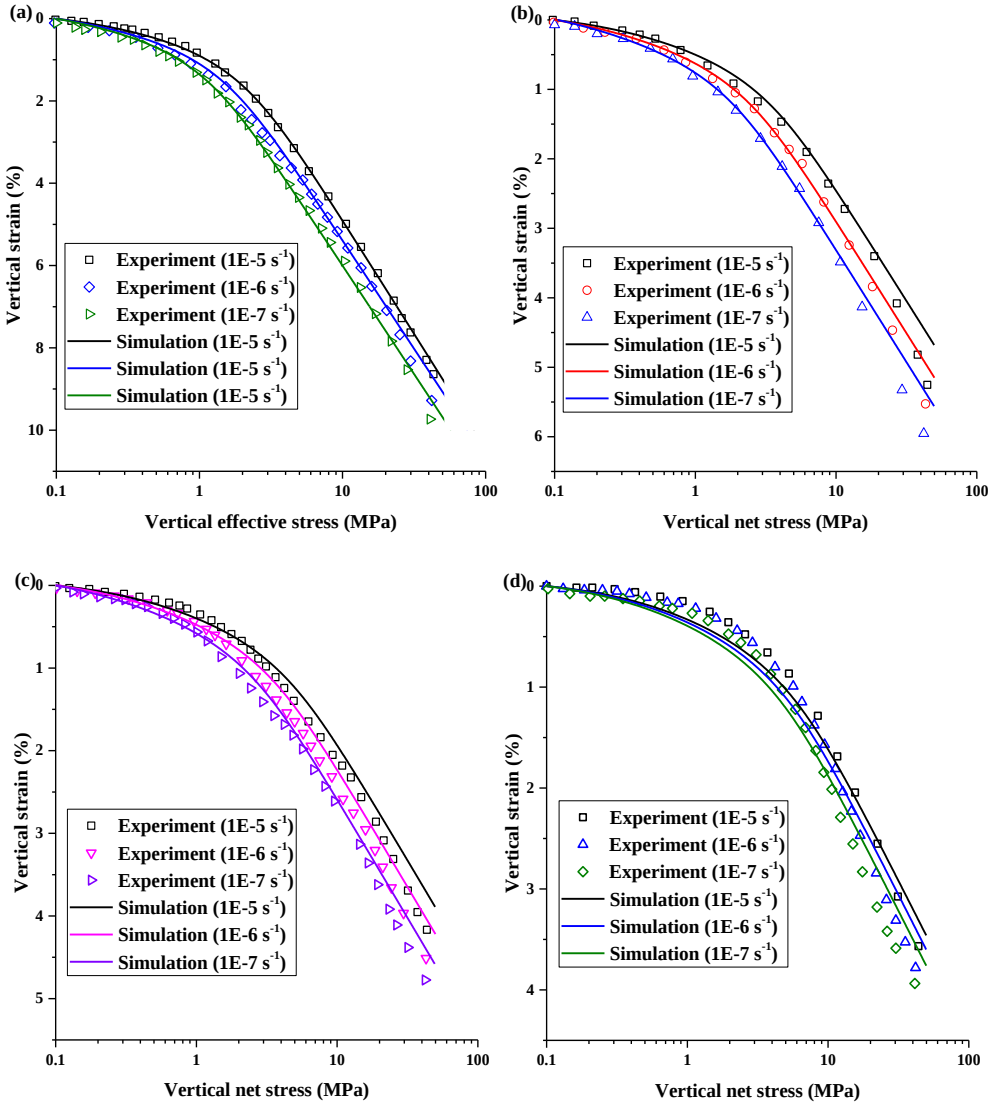

Fig. 6.19. Comparisons between simulations and CRS experiments for the damaged claystone at different strain rates and suctions: (a) suction 0 MPa; (b) suction 4.2 MPa; (c) suction 9 MPa; (d) suction 24.9 MPa

6.4.3 Triaxial shear tests

Fig. 6.20 shows the comparisons between simulations and experimental results from triaxial tests on COx claystone. The experimental data were collected from Liu et al. (2016). Three triaxial tests were conducted under constant water contents with a constant confining pressure of 12.4 MPa at a constant axial strain rate of 5×10^{-6} s^{-1}. The loading direction is perpendicular to the bedding plane. Before tests, the three triaxial samples were kept in containers with relative humidity values of 76 %, 85 % and 98 %, corresponding to suctions 37.8 MPa, 21.0 MPa and 4.2 MPa, respectively. More experimental details can be found in Liu et al. (2016).

In Fig. 6.20, the simulated results are comparable with the experimental ones with different

humidity values. A good agreement is observed, suggesting that the proposed model is able to well reproduce the evolutions of deviator stress with axial strain and lateral strain. With the increase of relative humidity, the corresponding suction decreases, leading to a lower maximum deviator stress. In addition, at the same deviator stress, the simulated lateral strain ε_3 is larger than the experimental one, whatever the relative humidity. Zhang (2019) reported that the mechanical behaviour of COx claystone is anisotropic. The direction of lateral strain is parallel to the bedding plane. At this direction, COx claystone has a higher Young's modulus, thus a lower deformation capacity (Zhang et al. 2015). For simplicity, this anisotropic feature is not considered in the present model.

Fig. 6.21 presents the simulations and experimental results of triaxial tests on COx claystone with different axial strain rates. Triaxial tests were also performed with a constant mean net stress of 12 MPa. The experimental data are collected from Liu et al. (2019). The triaxial samples tested have an initial water content of 6.2% and an initial saturation degree 90.4 %, loaded at the direction perpendicular to bedding plane. The three axial strain rates selected are 6×10^{-6} s^{-1}, 2×10^{-6} s^{-1} and 4×10^{-7} s^{-1}, respectively.

As shown in Fig. 6.21, with different axial strain rates, the comparisons between simulations and experiments are satisfactory. COx claystone presents rate-dependent shear stress-strain relationships, but relatively less significant. The simulated results also show that with the increase of strain rate, the deviator stress at the same axial strain is slightly larger, but does not change significantly, on basis of the selected model parameters. This indicates that the rate-dependent shear behaviours can also be reproduced by the present model.

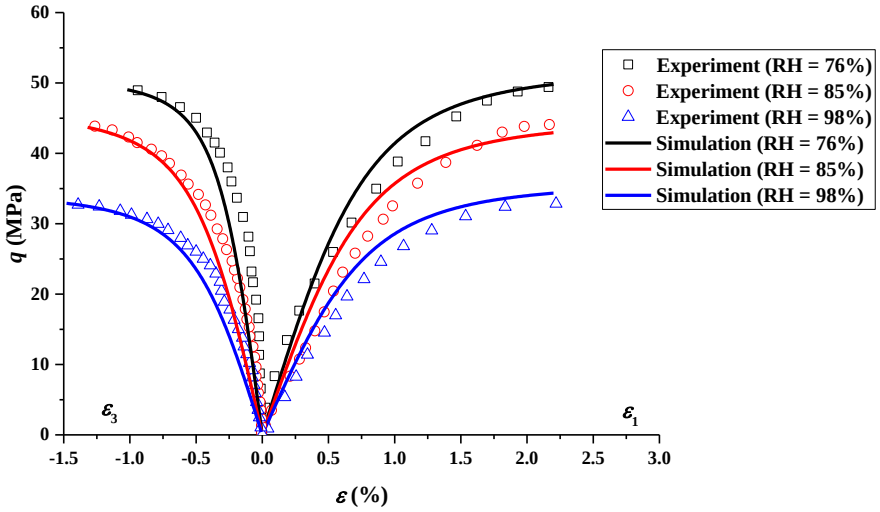

Fig. 6.20. Comparison of simulations and tests with different relative humilities (experimental data from Liu and Shao, 2016)

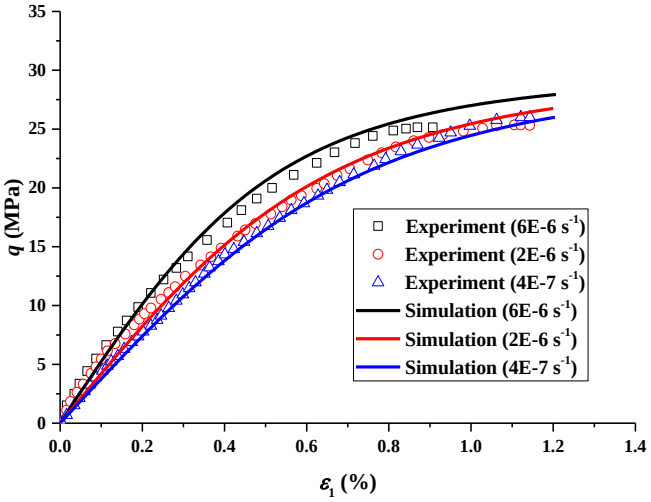

Fig. 6.21. Comparison of simulations and tests at different axial strain rates (experimental data from Liu et al., 2019)

Fig. 6.22 shows the simulated results and experimental results from a triaxial creep test on COx claystone. The tested sample had an initial degree of saturation of 57.8 % reached by imposing a relative humidity of 59 %. It was subjected to a loading at a constant axial strain rate of 2×10^{-6} s^{-1} up to a confining pressure of 12 MPa. Then, it was sheared till a deviator stress q_c = 52.3 MPa. Finally, the creep phase started by keeping the deviator stress constant.

Fig. 6.22 shows the comparisons of axial creep strains between simulation and test. It appears that the simulated axial strain before creep failure is lower than the experimental one and the test duration in simulation is shorter than that of experiment. This mainly results from the smaller simulated axial strain of 0.8 % compared to the experimental one (1.3 %) during the process where the deviator stress was loaded to 52.3 MPa. On the whole, the three phases in the creep process are reproduced correctly by the model, including the primary creep phase, the secondary creep phase and the tertiary creep phase (Fabre and Pellet, 2006). The creep failure is also well reproduced.

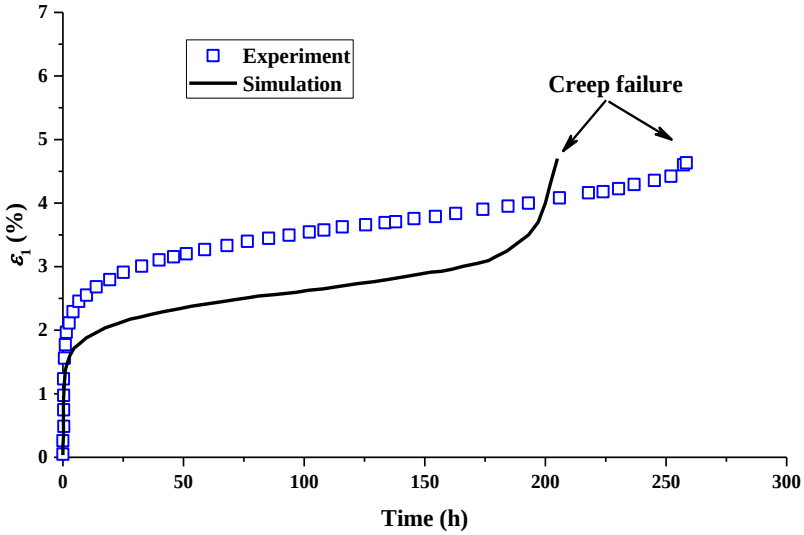

Fig. 6.22. Evolution of axial strain with time in triaxial creep test at q_c = 52.3 MPa (experimental data from Liu et al., 2018)

6.5 Conclusions

In this chapter, a EVP constitutive model is first developed to model the time dependent behaviour of unsaturated soils. Then, a damage model accounting for the volumetric proportion of micro-cracks was proposed. Combination of the two models allows the time dependent behaviours of COx claystone to be described with consideration of the damage and suction effects. The proposed model is validated based on the experimental results from the literatures and from this study.

The isotach concept was first presented with the description of strain rate on yield stress. The unique stress-strain-viscoplastic strain rate relationship adopted by Laloui et al. (2008) and Qiao et al. (2016) was also described. Incorporating the NFSF theory and the gradual hardening law, a viscoplastic model was proposed for unsaturated soils. The application of the viscous parameter $C_A(s)$ with consideration of suction effect allows the rate-dependent behaviour of unsaturated soils to be reproduced. Thus, the rate dependency, creep and stress relaxation can all be described by the proposed model.

The damage model proposed aims at describing the evolution of damage coefficient with the effective stress and plastic volumetric strain. The damage mechanism contains two aspects: hydration and mechanical loading. The damage level was identified through MIP observations on COx claystone samples at different suctions and under different loading conditions. The damage coefficient was defined as the ratio of the porosity of micro-cracks to the total porosity.

Finally, the damage model was incorporated into the unsaturated viscoplastic model. The

proposed model was validated based on the results from swelling tests, CRS tests and triaxial tests. In general, a good agreement is obtained between the simulations and tests. It is however worth noting that the model parameters are determined based on limited experimental data. Thus, the swelling pressure and the creep strain are not accurately captured by the model. Besides, the anisotropy of COx claystone is not considered.

Conclusions

The present work is devoted to the investigation of the swelling and delayed behaviours of unsaturated fractured or damaged COx claystone. The COx claystone used were drilled from the MHM URL. This site was selected for a possible geological radioactive waste disposal in France. The MHM URL was built to investigate the coupled thermo-hydro-mechanical and chemical behaviour of COx claystone, as well as to demonstrate the feasibility of constructing and operating the Cigéo project. As the fractured zones induced by the excavation of shafts and drifts play a key role in the long term safety of the repository, the time dependent behaviours related to these zones need to be clarified.

For this purpose, the preparation methods of fractured and damaged COx claystone in the laboratory were first proposed. The fractured COx claystone was prepared by sawing. Besides, a new method was proposed for the preparation of damaged COx claystone based on a novel damage criterion based on the ratio of moduli E_T/E_I. To understand the effect of grain breakage on the compressibility of COx claystone, oedometer tests were conducted on artificial sand-clay mixtures for clarifying the effect of fine fractions in the compression grain breakage processes. Oedometer tests were conducted on fractured and intact COx claystone for clarifying the effects of fracture on the hydro-mechanical behaviour. Following that, the hydro-mechanical behaviour of damaged COx claystone was investigated. Two experimental methods were adopted: oedometer and CRS tests with controlled-suction. In addition, CT and MIP tests were conducted for investigating the microscopic properties with respect to micro-cracks. Finally, for the modelling of time dependent behaviour of unsaturated COx claystone, an EVP model was proposed with consideration of the suction and damage effects.

Based on the analyses and discussions of the obtained results, the following conclusions are drawn:

Fractured COx claystone

In the laboratory, the cylindrical sample of COx claystone was first drilled from the COx core with the drilling machine. Then, by sawing the claystone cylinder, triaxial and intact oedometer samples were obtained with the target dimensions. For the preparation of fractured claystone, intact oedometer samples were sawed into two parts, either in thinner disks or in semicircles. The thickness of the corresponding fracture depends on the roughness of the contact surfaces between the two parts, which can be controlled by polishing the surfaces with a sand paper.

Swelling and self-sealing properties

The existence of fracture decreases the swelling strain of claystone and this phenomenon depends on the infiltration path and the orientation of fracture. At the end of the swelling process, test on horizontally fractured sample with filter paper exhibited a higher vertical strain compared to that on vertically fractured sample, while the vertical strains of tests on fractured samples without filter paper are closer. The vertical strains in both cases are smaller than that of test on intact sample. Due to the existence of filter paper, water infiltrated in to fractures faster and the sample swelled faster. This indicates that the infiltration path can affect the global swelling rate of fractured claystone. The self-sealing of fracture is mainly attributed to the swelling and clogging of COx claystone grains in the fracture zone. The self-sealing process can be divided into three stages: (i) closure - the swelling of claystone near the fracture surface induces fracture closure with the expansion of clay minerals; (ii) clogging - the claystone grains disaggregate and clog the fracture zone; (iii) homogenization - the macro-pores between the disaggregated claystone grains collapse by the further swelling of claystone farther from the fracture zone.

Compression and creep properties

Due to the weaker mechanical properties of the filled fracture zone, lower compression coefficient a, higher compression index C_c* and higher secondary consolidation coefficient C_α are observed for the fractured claystone, defining a higher compressibility and creep than the intact one. The compression and creep behaviours depend on the stress level and the orientation of fracture. With the increase of vertical stress, both C_α and C_c* show a three-stage relationship. Compared to the test on vertically fractured sample, the test on horizontally fractured sample exhibited a slightly larger C_α and C_c*. Comparison of hydraulic conductivities between fractured and intact claystone indicates that the hydraulic conductivity can be partially recovered due to the collapse of macro-pores in the filled fracture zone. This is also confirmed by analysing the evolution of consolidation coefficients c_v with stress.

All the fractured and intact samples present a uni-modal pore size distribution mode as in initial state. The dimension of macro-pores in the closed fracture depends on the fracture orientation (i.e. different initial fracture size). The results also confirm that the initial hydration path scarcely affect the closure of fracture after compression, and the pre-existing fracture cannot be closed completely even under the combined effects of hydration and high stress compression. It is worth noting that the stress 16 MPa represents an important stress level. Beyond this stress

level, the fracture effect can be neglected, but the compressibility increases further due to grain breakage. These findings clearly show the effect of fracture on the swelling, compression, permeability and creep of COx claystone.

Effect of grain breakage on compression behaviour under high stress

For natural COx claystone, Opalinus and Teguline clays, all can be regarded as mixtures of clay minerals and granular grains. The variation of C_c* exhibits an uncommon two-stage phenomenon: with the increase of vertical stress, C_c^* first increases slightly and then rapidly after a critical stress. This two-stage change of C_c^* can be attributed to the grain breakage phenomenon which which has been also evidenced by several authors so far (Klinkenberg et al., 2009; Wang, 2012) through image analysis.

The results obtained on the artificial sand-clay mixtures including pure sand and pure clay not only confirm the effect of grain breakage but also evidence the influence of clay fractions. The compression behaviour of these soils can be roughly distinguished into three zones according to the fine fractions. At low fine fractions, the compression behaviour is governed by grain breakage. At high fine fractions, the pore collapse of fines becomes dominating. At medium fine fractions, both pore collapse and grain breakage occur: pore collapses first, allowing grains to be well in contact either directly (grain-grain contacts) or indirectly (grain-fine-grain contacts) to activate the grain breakage phenomenon upon further loading. Thus, the compression behaviour of sand-clay mixtures is governed by both sand grain breakage and collapse of pore in the clay matrix, depending on the sand-clay ratios and stress levels. This is consistent with the identified compression behaviour of natural fine-grained soils.

Damaged COx claystone

For the preparation of damaged samples, triaxial tests were first performed. The shear modulus G and Young's modulus E were determined and then used to analyze the damage properties. It was observed that both the shear modulus and Young's modulus decreased slightly with the increase of deviator stress. The degradation of mechanical parameters indicates that damage was indeed generated inside the triaxial sample. For a practical reason, the tangent Young's modulus E_T was used to analyze the evolution of damage during shearing. Through the analysis and discussion on E_T obtained in this study and other works, it is found that the average ratio $E_{T,0.9}/E_I$ 0.22 is a good criterion to characterise the sample damage corresponding to 0.9 q_{max}. This criterion was further validated by analysing the proportion of micro-crack volume through

X-ray tomography and MIP tests. Indeed, when the triaxial sample was loaded to the ratio E_T/E_I 0.22, significant micro-cracks were generated. Based on this criterion, an experimental procedure was proposed to prepare damaged samples used in oedometer tests and in CSR tests with controlled suction.

Swelling, compression and creep behaviours

In oedometer tests with controlled suction, the damaged claystone shows a lower swelling strain than the intact claystone. This is attributed to the swollen clay minerals which filled the preexisting micro-cracks inside the damaged claystone, leading to a decrease of the swelling potential. Besides, in a standard fashion, the damaged claystone with a higher suction exhibits a lower compressibility and larger yield stress. At zero suction, the results indicate that there is a linear correlation between hydraulic conductivity and vertical stress. Compared with the intact claystone, the damaged one presents a lower compression index C_c. For C_α and C_c*, they both increase with the increase of vertical stress and with the decrease of suction, showing a significant dependency on stress and suction. A satisfactory linear relationship is observed between C_α and C_c* at each suction. The slope of the C_α - C_c curve depends on suction. It is worth noting that 16 MPa is a key stress for COx claystone, which is related to the closure of micro-cracks and grain breakage. Microstructure observations through CT and MIP tests indicate that the micro-cracks inside the damaged sample became more significant with the increase of the imposed suction after oedometer compression. This is explained by a lower stiffness resulting from the lower suction for the claystone grains - the micro-cracks were closed more easily at a given stress level. The quantitative analysis of the damaged coefficients confirms the qualitative observations on CT images.

Compared with the intact claystone investigated by Menaceur et al. (2016), the damaged claystone studied in this study exhibits a higher water contents but the similar degrees of saturation at a given suction. This is probably due to the larger initial void ratios related to the preexisting micro-cracks inside the damaged claystone. The results from the CRS tests show that the compression behaviour of the damaged claystone is suction-dependent. This is confirmed in terms of compression index and yield stress. Moreover, at the same suction, the yield stress increases with the increase of strain rate, which can be described with a linear correlation in a log-log plane. A viscous parameter C_A is thus obtained, which depends on suction.

Based on the experimental results obtained from OED and CRS tests, the compression and viscous parameters were determined and analysed for the damaged claystone. A formula was adopted to model the LC curve accounting for the effects of strain rate and suction. Further, the LC curve was modelled with the identified parameters. Experimental and simulated yield stress are in good agreements, validating the adopted approach.

Modelling the unsaturated visco-plastic behaviour of COx claystone

The isotach concept was first presented with the description of strain rate on yield stress. The unique stress-strain-viscoplastic strain rate relationship adopted by Laloui et al. (2008) and Qiao et al. (2016) was also described. Incorporating the NFSF theory and the gradual hardening law, a viscoplastic model was proposed for unsaturated soils. The application of the viscous parameter $C_A(s)$ with consideration of suction effect allows the rate-dependent behaviour of unsaturated soils to be reproduced. Thus, the rate dependency, creep and stress relaxation can all be described by the proposed model.

The damage model proposed aims at describing the evolution of damage coefficient with the effective stress and plastic volumetric strain. The damage mechanism contains two aspects: hydration and mechanical loading. The damage level was identified through MIP observations on COx claystone samples at different suctions and under different loading conditions. The damage coefficient was defined as the ratio of the porosity of micro-cracks to the total porosity.

Finally, the damage model was incorporated into the unsaturated viscoplastic model. The proposed model was validated based on the results from the swelling tests, CRS tests and triaxial tests, as well as the results from literatures. In general, a good agreement is obtained between the simulations and tests. It is however worth noting that the model parameters are determined based on limited experimental data. Thus, the swelling pressure and the creep strain are not accurately captured by the model. Besides, the anisotropy of COx claystone is not considered. In these aspects, the proposed model needs to be further improved in the future.

Perspectives

In this study, the factors influencing the hydro-mechanical behaviour of fractured/damaged COx claystone, including grain breakage, facture orientation and size, suction, strain rate, damage, etc., were investigated. Several other aspects can be further investigated in the future:

- The present investigation on the fracture effect can be extended to the thermal effect. Indeed, the thermal expansion and contraction of COx claystone can affect the closure and opening of fractures. It appears important to investigate this effect in the context of geological nuclear waste disposal.

- The experimental investigations have been conducted at a small scale in the laboratory. Considering the extension zone with larger fractures, they need to be extended to a larger scale.

- More investigations with consideration of different initial damage extents of COx claystone can be conducted with the damage criterion proposed in this study.

- The proposed constitutive model needs to be further improved by taking into account the anisotropic and softening properties.

- As COx claystone with different inclusion contents can exhibit different behaviours, the natural variability in terms of mineralogy of COx claystone needs to be studied in more depth. The proposed constitutive model can also be implemented in a numerical code for field tests analyses.

REFERENCES

Abdallah, Y. (2019). Compaction Banding in High-porosity Carbonate Rocks. PhD thesis, Ecole Nationale des Ponts et Chaussées, Université Paris-Est, Champs-sur-Marne, France.

Adachi, T., & Okano, M. (1974). A constitutive equation for normally consolidated clay. Soils and Foundations, 14(4), 55-73.

Adachi, T., & Oka, F. (1982). Constitutive equations for normally consolidated clay based on elasto-viscoplasticity. Soils and foundations, 22(4), 57-70.

Adachi, T., Oka, F., & Mimura, M. (1987). Mathematical structure of an overstress elasto-viscoplastic model for clay. Soils and Foundations, 27(3), 31-42.

Adem, H. H., & Vanapalli, S. K. (2015). Prediction of the modulus of elasticity of compacted unsaturated expansive soils. International Journal of Geotechnical Engineering, 9(2), 163-175.

AFNOR. (2005). Geotechnical Investigating and Testing, Laboratory Testing of Soils, Part 5: Incremental Loading Oedometer Test. XP CEN ISO/TS 17892-5.

Agus, S.S., Leong, E.C., and Rahardjo, H. (2001) Soil-water characteristic curve of Singapore residual soils. Geotechnical and Geological Engineering, 19: 285-309.

Agus, S. S., & Schanz, T. (2003). Vapour equilibrium technique for tests on a highly compacted bentonite-sand mixture. In Proceedings of the international conference on problematic soils, Nottingham, United Kingdom (Vol. 2003, pp. 467-474).

Alonso, E.E., Gens, A. and Josa, A. (1990). A constitutive model for partially saturated soils. Géotechnique, 40(3), pp.405-430.

Alonso, E.E., Pereira, J.M., Vaunat, J. and Olivella, S. (2010). A microstructurally based effective stress for unsaturated soils. Géotechnique, 60(12), pp.913-925.

Alizadeh, A., & Gatmiri, B. (2017). An elasto-plastic damage model for argillaceous geomaterials. Applied Clay Science, 135, 82-94.

Anagnostopoulos, C. A., & Grammatikopoulos, I. N. (2009). A new model for the prediction of secondary consolidation index of low and medium plasticity clay soils. European Journal of Scientific Research, 34(4), 542-549.

ANDRA, D. (2005). Argile, Référentiel du site de Meuse/Haute Marne. CRP ADS, 4.

ANDRA, 2005, Dossier (2005). Evolution phénoménologique du stockage géologique. Rapport Andra no. C.RP.ADS.04.0025, France.

ANDRA (2012), Référentiel du comportement THM des formations sur le site de Meuse/ Haute-Marne. D.RP. AMFS.1 2.0024.

Arifin, Y.F., 2008. Thermo-hydro-mechanical behaviour of compacted bentonite-sand mixtures: an experimental study. Th`ese Bauhaus-University Weimar, Weimar.

Armand, G., Noiret, A., Zghondi, J., & Seyedi, D. M. (2013). Short-and long-term behaviours of drifts in the Callovo-Oxfordian claystone at the Meuse/Haute-Marne Underground Research Laboratory. Journal of Rock Mechanics and Geotechnical Engineering, 5(3), 221-230.

Armand, G., Leveau, F., Nussbaum, C., de La Vaissiere, R., Noiret, A., Jaeggi, D., Landrein P., & Righini, C. (2014). Geometry and properties of the excavation-induced fractures at the Meuse/Haute-Marne URL drifts. Rock Mechanics and Rock Engineering, 47(1), 21-41.

Armand, G., Djizanne, H., Zghondi, J., de La Vaissière, R., Talandier, J., & Conil, N. (2016). Inputs from in situ experiments to the understanding of the unsaturated behaviour of Callovo-Oxfordian claystone. In E3S Web of Conferences (Vol. 9, p. 03004). EDP Sciences.

Armand, G., Conil, N., Talandier, J., & Seyedi, D. M. (2017). Fundamental aspects of the hydromechanical behaviour of Callovo-Oxfordian claystone: from experimental studies to model calibration and validation. Computers and Geotechnics, 85, 277-286.

ASTM, D2435-96. (1996). Standard Test Method for One-Dimensional Consolidation Properties of Soils. ASTM International.

ASTM, D4186-06. (2007). Standard Test Method for One-dimensional Consolidation Properties of Soils Using Controlled-strain Loading, 4.

ASTM, D4546-14. (2014). Standard test methods for one-dimensional swell or collapse of soils. ASTM Book of Standard Specifications, Designation: D, 4546-14.

Auvray, C., Arnold, G., & Armand, G. (2015). Experimental study of elastic properties of different constituents of partially saturated argillite using nano-indentation tests. Engineering Geology, 191, 61-70.

Aversa, S., Evangelista, A., Leroueil, S., Picarelli, L. (1993). Some aspects of the mechanical behaviour of structured soils and soft rocks. In: Anagnostopoulos, editor. Geotechnical engineering of hard soils–soft rocks. Rotterdam: Balkema.

Bandis, S. C., Lumsden, A. C., & Barton, N. R. (1983). Fundamentals of rock joint deformation. In International Journal of Rock Mechanics and Mining Sciences & Geomechanics Abstracts (Vol. 20, No. 6, pp. 249-268). Pergamon.

Barbour, S. L., & Fredlund, D. G. (1989). Mechanisms of osmotic flow and volume change in clay soils. Canadian Geotechnical Journal, 26(4), 551-562.

Bauer-Plaindoux, C., Tessier, D., & Ghoreychi, M. (1998). Propriétés mécaniques des roches argileuses carbonatées : importance de la relation calcite-argile. Comptes Rendus de l'Académie des Sciences-Series IIA-Earth and Planetary Science, 326(4), 231-237.

Belmokhtar, M. (2017). Contributions à l'étude du comportement thermo-hydro-mécanique de l'argilite du Callovo-Oxfordien (France) et de l'argile à Opalinus (Suisse) (Doctoral dissertation).

Belmokhtar, M., Delage, P., Ghabezloo, S., & Conil, N. (2018). Drained triaxial tests in low-permeability shales: application to the Callovo-Oxfordian claystone. Rock Mechanics and Rock Engineering, 51(7), 1979-1993.

Bemer, E., Longuemare, P., & Vincké, O. (2004). Poroelastic parameters of Meuse/Haute Marne argillites: effect of loading and saturation states. Applied Clay Science, 26(1-4), 359-366.

Bésuelle, P., Viggiani, G., Lenoir, N., Desrues, J. and Bornert, M. (2006). X-ray Micro CT for Studying Strain Localization in Clay Rocks under Triaxial Compression. In: Advances in X-Ray Tomography for Geo-materials, J. Desrues et al. Eds, ISTE, London, 35–52.

Bian, H., Zhang, X., & Shao, J. (2017). A coupled elastoplastic and visco-plastic damage model for hard clay and its application for the underground gallery excavation. Underground Space, 2(1), 60-72.

Biot, M. A. (1941). General theory of three-dimensional consolidation. Journal of applied physics, 12(2), 155-164.

Biot, M. A. (1955). Theory of elasticity and consolidation for a porous anisotropic solid. Journal of Applied Physics, 26, 182–185.

Biot, M. A. (1973). Nonlinear and semilinear rheology of porous solids. Journal of Geophysical Research, 78(23), 4924–4937.

Bishop, A. W. (1959). The principle of effective stress. Teknisk ukeblad, 39, 859-863.

Bishop, A. W., & Blight, G. E. (1963). Some aspects of effective stress in saturated and partly saturated soils. Géotechnique, 13(3), 177–197.

Blackwell, P. S., Ringrose-Voase, A. J., Jayawardane, N. S., Olsson, K. A., McKenzie, D. C., & Mason, W. K. (1990). The use of air-filled porosity and intrinsic permeability to air to characterize structure of macropore space and saturated hydraulic conductivity of clay soils. Journal of Soil Science, 41(2), 215-228.

Blatz, J.A., Graham, J., and Chandler, N.A. (2002) Influence of suction on the strength and stiffness of compacted sand-bentonite. Canadian Geotechnical Journal, 39(5): 1005-1015.

Blümling, P., Bernier, F., Lebon, P., & Martin, C. D. (2007). The excavation damaged zone in clay formations time-dependent behaviour and influence on performance assessment. Physics and Chemistry of the Earth, Parts A/B/C, 32(8-14), 588-599.

Bock, H., Dehandschutter, B., Martin, C. D., Mazurek, M., De Haller, A., Skoczylas, F., & Davy, C. (2010). Self-sealing of fractures in argillaceous formations in the context of geological disposal of radioactive waste.

Bolt, G. H. (1956). Physico-chemical analysis of the compressibility of pure clays. Geotechnique, 6(2), 86-93.

Bornert, M., Vales, F., Gharbi, H., & Nguyen Minh, D. (2010). Multiscale full-field strain measurements for micromechanical investigations of the hydromechanical behaviour of clayey rocks. Strain, 46(1), 33-46.

Boulin, P. F., Angulo-Jaramillo, R., Daian, J. F., Talandier, J., & Berne, P. (2008). Pore gas connectivity analysis in Callovo-Oxfordian argillite. Applied clay science, 42(1-2), 276-283.

Braun, P., Ghabezloo, S., Delage, P., Sulem, J., & Conil, N. (2019). Determination of multiple thermo-hydro-mechanical rock properties in a single transient experiment: application to Shales. Rock Mechanics and Rock Engineering, 52(7), 2023-2038.

Braun, P. (2019). Thermo-hydro-mechanical behavior of the Callovo-Oxfordian claystone: Effects of stress paths and temperature changes. Doctoral dissertation, University of Paris-Est.

Bui, T. A., Wong, H., Deleruyelle, F., & Zhou, A. (2016). Constitutive modelling of the time-dependent behaviour of partially saturated rocks. Computers and Geotechnics, 78, 123-133.

Bui, T. A., Wong, H., Deleruyelle, F., Xie, L. Z., & Tran, D. T. (2017). A thermodynamically consistent model accounting for viscoplastic creep and anisotropic damage in unsaturated rocks. International Journal of Solids and Structures, 117, 26-38.

Carter, T. G., Castro, S. O., Carvalho, J. L., Hattersley, D., Wood, K., Barone, F. S., Yuen D., & Giraldo, C. M. K. (2010). Tunnelling Issues with Chilean tertiary volcaniclastic rocks. In Mir conference.

Casagrande, A. (1936). The determination of pre-consolidation load and it's practical significance. In Proc. Int. Conf. Soil Mech. Found. Eng. Cambridge, Mass., 1936 (Vol. 3, p. 60).

Cernica, J. N. (1995). Geotechnical engineering: soil mechanics.

Chen, L., Wang, J., Liu, Y., Collin, F., & Xie, J. (2012). Numerical thermo-hydro-mechanical modeling of compacted bentonite in China-mock-up test for deep geological disposal. Journal of Rock Mechanics and Geotechnical Engineering, 4(2), 183-192.

Chen, L., Liu, Y. M., Wang, J., Cao, S. F., Xie, J. L., Ma, L. K., Zhao, X.G., Liu, J. (2014). Investigation of the thermal-hydro-mechanical (THM) behaviour of GMZ bentonite in the China-Mock-up test. Engineering geology, 172, 57-68.

Chiarelli, A. S., Shao, J. F., & Hoteit, N. (2003). Modeling of elastoplastic damage behaviour of a claystone. International Journal of plasticity, 19(1), 23-45.

Coleman, J. D. (1962). Stress strain relations for partly saturated soil. Corespondence to Geotechnique, 12(4), 348-350.

Collins, I. F., & Houlsby, G. T. (1997). Application of thermomechanical principles to the modelling of geotechnical materials. Proceedings of the Royal Society of London. Series A: Mathematical, Physical and Engineering Sciences, 453(1964), 1975-2001.

Conil, N., Talandier, J., Djizanne, H., de La Vaissière, R., Righini-Waz, C., Auvray, C., Molot, G., & Armand, G. (2018). How rock samples can be representative of in situ condition: A case study of Callovo-Oxfordian claystones. Journal of Rock Mechanics and Geotechnical Engineering, 10(4), 613-623.

Coussy, O. (2004). Poromechanics. John Wiley & Sons.

Crisci, E., Ferrari, A., Giger, S. B., & Laloui, L. (2019). Hydro-mechanical behaviour of shallow Opalinus Clay shale. Engineering Geology, 251, 214-227.

Cui, Y. J., & Delage, P. (1996). Yielding and plastic behaviour of an unsaturated compacted silt. Géotechnique, 46(2), 291-311.

Cui, Y. J., Nguyen, X. P., Tang, A. M., & Li, X. L. (2013). An insight into the unloading/reloading loops on the compression curve of natural stiff clays. Applied clay science, 83, 343-348.

Cuisinier, O., & Masrouri, F. (2004). Testing the hydromechanical behaviour of a compacted swelling soil. Geotechnical Testing Journal, 27(6), 598-606.

Dao, L. Q., Cui, Y. J., Tang, A. M., Pereira, J. M., Li, X. L., & Sillen, X. (2015). Impact of excavation damage on the thermo-hydro-mechanical properties of natural Boom Clay. Engineering Geology, 195, 196-205.

Dao, L. Q. (2015). Étude du comportement anisotrope de l'argile de Boom (Doctoral dissertation, Université Paris-Est).

Dardé, B. (2019). Experimental and numerical study of the hydromechanical behaviour of bentonite pellet-powder mixtures (Doctoral dissertation, Université Paris-Est).

David, C., Robion, P., & Menéndez, B. (2007). Anisotropy of elastic, magnetic and microstructural properties of the Callovo-Oxfordian argillite. Physics and Chemistry of the Earth, Parts A/B/C, 32(1-7), 145-153.

Davy, C. A., Skoczylas, F., Barnichon, J. D., & Lebon, P. (2007). Permeability of macro-cracked argillite under confinement: gas and water testing. Physics and Chemistry of the Earth, Parts A/B/C, 32(8-14), 667-680.

Debure, M., Tournassat, C., Lerouge, C., Madé, B., Robinet, J. C., Fernández, A. M., & Grangeon, S. (2018). Retention of arsenic, chromium and boron on an outcropping clay-rich rock formation (the Tégulines Clay, eastern France). *Science of the total environment* **642**, 216-229.

De Gennaro, V., Delage, P., Cui, Y. J., Schroeder, C., & Collin, F. (2003). Time-dependent behaviour of oil reservoir chalk: a multiphase approach. Soils and foundations, 43(4), 131-147.

De Gennaro, V., & Pereira, J. M. (2013). A viscoplastic constitutive model for unsaturated geomaterials. Computers and Geotechnics, 54, 143-151.

de La Vaissière, R., Armand, G., & Talandier, J. (2015). Gas and water flow in an excavation-induced fracture network around an underground drift: a case study for a radioactive waste repository in clay rock. Journal of Hydrology, 521, 141-156.

Deng, Y. F., Cui, Y. J., Tang, A. M., Li, X. L., & Sillen, X. (2012). An experimental study on the secondary deformation of Boom clay. Applied Clay Science, 59, 19-25.

Delage, P., & Lefebvre, G. (1984). Study of the structure of a sensitive Champlain clay and of its evolution during consolidation. Canadian Geotechnical Journal, 21(1), 21-35.

Delage, P., & Pellerin, F. M. (1984). Influence de la lyophilisation sur la structure d'une argile sensible du Québec. Clay Minerals, 19(2), 151-160.

Delage, P., Howat, M. D., & Cui, Y. J. (1998). The relationship between suction and swelling properties in a heavily compacted unsaturated clay. Engineering geology, 50(1-2), 31-48.

Delage, P. (2007). Microstructure features in the behaviour of engineered barriers for nuclear waste disposal. In Experimental unsaturated soil mechanics (pp. 11-32). Springer, Berlin, Heidelberg.

Delage, P. (2010). A microstructure approach to the sensitivity and compressibility of some Eastern Canada sensitive clays. Géotechnique, 60(5), 353-368.

Delage, P. (2013). On the thermal impact on the excavation damaged zone around deep radioactive waste disposal. Journal of Rock Mechanics and Geotechnical Engineering, 5(3), 179-190.

Delage, P, Menaceur, H, Tang, A.M, Talandier J. (2014). Suction effects in deep Callovo-Oxfordian claystone specimen. Géotechnique Letter, 3(2):84–88.

Delay, J., Vinsot, A., Krieguer, J.M., Rebours, H., Armand, G. (2007). Making of the underground scientific experimental programme at the Meuse/Haute-Marne underground research laboratory, North Eastern France. Physics and Chemistry of the Earth, 32, 2-18.

Delay, J., Lebon, P., & Rebours, H. (2010). Meuse/Haute-Marne centre: next steps towards a deep disposal facility. Journal of Rock Mechanics and Geotechnical Engineering, 2(1), 52-70.

Delville, A., & Laszlo, P. (1990). The origin of the swelling of clays by water. Langmuir, 6(7), 1289-1294.

Di Donna, A., Charrier, P., Salager, S., & Bésuelle, P. (2019). Self-sealing capacity of argillite samples. In E3S Web of Conferences (Vol. 92, p. 03005). EDP Sciences.

di Prisco, C., & Imposimato, S. (1996). Time dependent mechanical behaviour of loose sands. Mechanics of Cohesive-frictional Materials: An International Journal on Experiments, Modelling and Computation of Materials and Structures, 1(1), 45-73.

Dormieux, L., Lemarchand, E., & Coussy, O. (2003). Macroscopic and micromechanical approaches to the modelling of the osmotic swelling in clays. Transport in porous media, 50(1-2), 75-91.

Eberhardt, E., Stead, D., Stimpson, B., & Read, R. S. (1998). Identifying crack initiation and propagation thresholds in brittle rock. Canadian geotechnical journal, 35(2), 222-233.

Eisenberg, M., & Yen, C. F. (1981). A theory of multiaxial anisotropic viscoplasticity.

Espitia, J. M., & Caicedo, B. (2014). Mechanical behaviour of unsaturated argillaceous rocks under uniaxial compression through acoustic emission. In 6th International Conference on Unsaturated Soils, UNSAT (pp. 1597-1603).

Espitia, J. M., Caicedo, B., & Vallejo, L. (2017). Effect of suction and stress on Poisson's ratio of argillaceous rocks. Géotechnique Letters, 7(1), 53-59.

Fabre, G., & Pellet, F. (2006). Creep and time-dependent damage in argillaceous rocks. International Journal of Rock Mechanics and Mining Sciences, 43(6), 950-960.

Fairhurst, C., & Damjanac, B. (1996). The excavation damage zone—an international perspective. In proceedings of the excavation disturbed zone workshop on designing the excavation disturbed zone for a nuclear repository in hard rock. Winnipeg.

Fairhurst, C. (2004). Nuclear waste disposal and rock mechanics: contributions of the Underground Research Laboratory (URL), Pinawa, Manitoba, Canada. International Journal of Rock Mechanics and Mining Sciences, 41(8), 1221-1227.

Favero, V., Ferrari, A., & Laloui, L. (2016). On the hydro-mechanical behaviour of remoulded and natural Opalinus Clay shale. Engineering Geology, 208, 128-135.

Feia, S., Ghabezloo, S., Bruchon, J. F., Sulem, J., Canou, J., & Dupla, J. C. (2014). Experimental evaluation of the pore-access size distribution of sands. Geotechnical Testing Journal, 37(4), 613-620.

Feldkamp, L. A., Davis, L. C., & Kress, J. W. (1984). Practical cone-beam algorithm. Josa a, 1(6), 612-619.

Ferreira, T., & Rasband, W. (2012). ImageJ user guide. ImageJ/Fiji, 1, 155-161.

Ferrari, A., Favero, V., Marschall, P., & Laloui, L. (2014). Experimental analysis of the water retention behaviour of shales. International Journal of Rock Mechanics and Mining Sciences, 72, 61-70.

François, B., & Laloui, L. (2008). ACMEG ‐ TS: A constitutive model for unsaturated soils under non ‐ isothermal conditions. International journal for numerical and analytical methods in geomechanics, 32(16), 1955-1988.

Fredlund, D. G., & Morgenstern, N. R. (1977). Stress state variables for unsaturated soils. Journal of Geotechnical and Geoenvironmental Engineering, 103(ASCE 12919).

Fredlund, D. G., & Rahardjo, H. (1993). Soil mechanics for unsaturated soils. New York: John Wiley & Sons.

Gaucher G, Robelin C, Matray JM, Négrel G, Gros Y, Heitz JF, Vinsot A, Rebours H, Cassagnabère, Bouchet A. (2004). ANDRA underground research laboratory: interpretation of the mineralogical and geochemical data acquired in the Callovian-

Oxfordian formation by investigative drilling. Physics and Chemistry of the Earth 29: 55-77.

Gasc-Barbier, M., Chanchole, S., & Bérest, P. J. A. C. S. (2004). Creep behaviour of Bure clayey rock. Applied Clay Science, 26(1-4), 449-458.

Gens, A. (1996). Constitutive modelling: application to compacted soils. In PROCEEDINGS OF THE FIRST INTERNATIONAL CONFERENCE ON UNSATURATED SOILS/UNSAT'95/PARIS/FRANCE/6-8 SEPTEMBER 1995. VOLUME 3.

Gens, R., Lalieux, P., De Preter, P., Dierckx, A., Bel, J., Boyazis, J. P., & Cool, W. (2003). The Second Safety Assessment and Feasibility Interim Report (SAFIR 2 Report) on HLW Disposal in Boom Clay: Overview of the Belgian Programme. MRS Online Proceedings Library Archive, 807.

Ghoreychi, M. (1997). Comportement rhéologique et couplages thermo-hydro-mécaniques dans les argilites de l'est: Expériences macroscopiques et analyses microscopiques. Proceedings of Journées Scientifiques CNRS/ANDRA Etude de l'Est du Bassin Parisien, 109-128.

Ghoreychi, M. (1999). Comportement thermo-hydro-mécanique des argilites de l'est et son incidence sur les ouvrages souterrains. Dans « Etude pour la faisabilité des stockages de déchets radioactifs » Actes des Journées scientifiques ANDRA. Nancy, 7, 8 et 9 décembre 1999. EDP Sciences Ed, 397-418.

Giot, R., Auvray, C., & Talandier, J. (2019). Self-sealing of claystone under X-ray nanotomography. Geological Society, London, Special Publications, 482(1), 213-223.

Goodman, R. E. (1976). Methods of geological engineering in discontinuous rocks (No. BOOK).

Graham, J., Crooks, J. H. A., & Bell, A. L. (1983). Time effects on the stress-strain behaviour of natural soft clays. Géotechnique, 33(3), 327-340.

Gratier, J. P., Jenatton, L., Tisserand, D., & Guiguet, R. (2004). Indenter studies of the swelling, creep and pressure solution of Bure argillite. Applied Clay Science, 26(1-4), 459-472.

Guayacán-Carrillo, L. M., Sulem, J., Seyedi, D. M., Ghabezloo, S., Noiret, A., & Armand, G. (2016). Analysis of long-term anisotropic convergence in drifts excavated in Callovo-Oxfordian claystone. Rock Mechanics and Rock Engineering, 49(1), 97-114.

Guayacan-Carrillo, L. M., Ghabezloo, S., Sulem, J., Seyedi, D. M., & Armand, G. (2017). Effect of anisotropy and hydro-mechanical couplings on pore pressure evolution during tunnel excavation in low-permeability ground. International Journal of Rock Mechanics and Mining Sciences, 97, 1-14.

Guerra, A. M., Mokni, N., Delage, P., Cui, Y. J., Tang, A. M., Aimedieu, P., ... & Bornert, M. (2017). In-depth characterisation of a mixture composed of powder/pellets MX80 bentonite. Applied Clay Science, 135, 538-546.

Guerra, A. M. (2018). Experimental and numerical characterizations of the hydro-mechanical behaviour of a heterogeneous material: pellet/powder bentonite mixture (Doctoral dissertation).

Guerra, A. M., Cui, Y. J., He, Y., Delage, P., Mokni, N., Tang, A. M., ... & Bernier, F. (2019). Characterization of water retention, compressibility and swelling properties of a pellet/powder bentonite mixture. Engineering Geology, 248, 14-21.

Guéry, A. A. C., Cormery, F., Shao, J. F., & Kondo, D. (2008). A micromechanical model of elastoplastic and damage behaviour of a cohesive geomaterial. International Journal of Solids and structures, 45(5), 1406-1429.

Hinchberger, S. D., & Rowe, R. K. (1998). Modelling the rate-sensitive characteristics of the Gloucester foundation soil. Canadian Geotechnical Journal, 35(5), 769-789.

Hong, P. Y. (2013). Development and explicit integration of a thermo-mechanical model for saturated clays (Doctoral dissertation).

Hong, P. Y., Pereira, J. M., Tang, A. M., & Cui, Y. J. (2016). A two-surface plasticity model for stiff clay. Acta Geotechnica, 11(4), 871-885.

Houben, M. E., Desbois, G., & Urai, J. L. (2014). A comparative study of representative 2D microstructures in Shaly and Sandy facies of Opalinus Clay (Mont Terri, Switzerland) inferred form BIB-SEM and MIP methods. Marine and Petroleum Geology, 49, 143-161.

Hu, D. W., Zhang, F., Shao, J. F., & Gatmiri, B. (2014). Influences of mineralogy and water content on the mechanical properties of argillite. Rock mechanics and rock engineering, 47(1), 157-166.

Huang, Y., Xie, S. Y., & Shao, J. F. (2014). An experimental study of crack growth in claystones. European journal of environmental and civil engineering, 18(3), 307-319.

Hujeux, J. C. (1979). Calcul numérique de problèmes de consolidation élastoplastique (Doctoral dissertation).

IAEA (2009). Classification of radioactive waste. General safety guide. IAEA Safety Standards GSG-1, 68.

Jia, Y., Song, X. C., Duveau, G., Su, K., & Shao, J. F. (2007). Elastoplastic damage modelling of argillite in partially saturated condition and application. Physics and Chemistry of Earth, 32, 656–666.

Kabbaj, M., Oka, F., Leroueil, S., & Tavenas, F. (1986). Consolidation of natural clays and laboratory testing. In Consolidation of soils: Testing and evaluation. ASTM International.

Karaborni, S., Smit, B., Heidug, W., Urai, J., & Van Oort, E. (1996). The swelling of clays: molecular simulations of the hydration of montmorillonite. Science, 271(5252), 1102-1104.

Karim, M. R., & Gnanendran, C. T. (2014). Review of constitutive models for describing the time dependent behaviour of soft clays. Geomechanics and Geoengineering, 9(1), 36-51.

Khalili, N., & Khabbaz, M. H. (1998). A unique relationship for χ for the determination of the shear strength of unsaturated soils. Geotechnique, 48(5), 681-687.

Khalili, N., Geiser, F., & Blight, G. E. (2004). Effective stress in unsaturated soils: Review with new evidence. International journal of Geomechanics, 4(2), 115-126.

Khalili, N., Habte, M. A., & Valliappan, S. (2005). A bounding surface plasticity model for cyclic loading of granular soils. International journal for numerical methods in engineering, 63(14), 1939-1960.

Khalili, N., Habte, M. A., & Zargarbashi, S. (2008). A fully coupled flow deformation model for cyclic analysis of unsaturated soils including hydraulic and mechanical hystereses. Computers and Geotechnics, 35(6), 872-889.

Kim, Y. T., & Leroueil, S. (2001). Modeling the viscoplastic behaviour of clays during consolidation: application to Berthierville clay in both laboratory and field conditions. Canadian Geotechnical Journal, 38(3), 484-497.

Klinkenberg, M., Kaufhold, S., Dohrmann, R., & Siegesmund, S. (2009). Influence of carbonate microfabrics on the failure strength of claystones. Engineering Geology, 107(1-2), 42-54.

Komine, H., & Ogata, N. (2003). New equations for swelling characteristics of bentonite-based buffer materials. Canadian Geotechnical Journal, 40(2), 460-475.

Kowalski, S. J. (2003). Characterization of drying processes. In Thermomechanics of Drying Processes (pp. 24-30). Springer, Berlin, Heidelberg.

Kutter, B. L., & Sathialingam, N. (1992). Elastic-viscoplastic modelling of the rate-dependent behaviour of clays. Géotechnique, 42(3), 427-441.

Ladd, C. C. (1971). Settlement analyses for cohesive soils. Massachusetts Inst. of Technology, Department of Civil Engineering.

Laird, D. A., Shang, C., & Thompson, M. L. (1995). Hysteresis in crystalline swelling of smectites. Journal of colloid and interface science, 171(1), 240-245.

Laloui, L., Leroueil, S., & Chalindar, S. (2008). Modelling the combined effect of strain rate and temperature on one-dimensional compression of soils. Canadian Geotechnical Journal, 45(12), 1765-1777.

Lambe, T.W., Whitman, R.V., 1979. *Soil Mechanics*. Wiley and Sons.

Lambe, T. W., & Whitman, R. V. (1991). Soil mechanics (Vol. 10). John Wiley & Sons.

Lee, K. L., & Farhoomand, I. (1967). Compressibility and crushing of granular soil in anisotropic triaxial compression. Canadian geotechnical journal, 4(1), 68-86.

Lemaitre, J., & Chaboche, J. L. (1994). Mechanics of solid materials. Cambridge university press.

Lenoir, N., Bornert, M., Desrues, J., Bésuelle, P., & Viggiani, G. (2007). Volumetric digital image correlation applied to X-ray microtomography images from triaxial compression tests on argillaceous rock. Strain, 43(3), 193-205.

Lerouge, C., Robinet, J. C., Debure, M., Tournassat, C., Bouchet, A., Fernández, A. M., Flehoc, C., Guerrot., C., Kars, M., Lagroix, F., Landrein, P., Madé, B., Negrel, P., Wille, G., & Claret, F., (2018). A deep alteration and oxidation profile in a shallow clay aquitard: Example of the Tégulines Clay, East Paris Basin, France. Geofluids, 2018.

Leroueil, S., Kabbaj, M., Tavenas, F., & Bouchard, R. (1985). Stress–strain–strain rate relation for the compressibility of sensitive natural clays. Géotechnique, 35(2), 159-180.

Leroueil, S. (1996). Importance of strain rate and temperature effects in geotechnical engineering. Measuring and modeling time dependent soil behaviour.

Leroueil, S. (2006). The Isotache approach. Where are we 50 years after its development by Professor Šuklje? 2006 Prof. Šuklje's Memorial Lecture. In Proceedings of the XIII Danube-European Conference on Geotechnical Engineering, Ljubljana, Slovenia (Vol. 2, pp. 55-88).

Le, T. T. (2008). Comportement thermo-hydro-mécanqiue de l'argile de Boom (Doctoral dissertation, Paris Est).

Le Pense, S., Arson, C., & Pouya, A. (2016). A fully coupled damage-plasticity model for unsaturated geomaterials accounting for the ductile–brittle transition in drying clayey soils. International Journal of solids and structures, 91, 102-114.

Liingaard, M., Augustesen, A., & Lade, P. V. (2004). Characterization of models for time-dependent behaviour of soils. International Journal of Geomechanics, 4(3), 157-177.

Liu, Z. B., Xie, S. Y., Shao, J. F., & Conil, N. (2015). Effects of deviatoric stress and structural anisotropy on compressive creep behaviour of a clayey rock. Applied Clay Science, 114, 491-496.

Liu, Z., & Shao, J. (2016). Moisture effects on damage and failure of Bure claystone under compression. Géotechnique Letters, 6(3), 182-186.

Liu, Z., Shao, J., Xie, S., & Conil, N. (2017). Triaxial Creep Induced Gas Permeability Change and Elastic Modulus Variation in Callovo-Oxfordian Argillite. In Poromechanics VI (pp. 1037-1044).

Liu, Z., Shao, J., Xie, S., Conil, N., & Zha, W. (2018). Effects of relative humidity and mineral compositions on creep deformation and failure of a claystone under compression. International Journal of Rock Mechanics and Mining Sciences, 103, 68-76.

Liu, Z., Shao, J., Xie, S., Conil, N., & Talandier, J. (2019). Mechanical behaviour of claystone in lateral decompression test and thermal effect. Rock Mechanics and Rock Engineering, 52(2), 321-334.

Lloret, A., Villar, M. V., Sanchez, M., Gens, A., Pintado, X., & Alonso, E. E. (2003). Mechanical behaviour of heavily compacted bentonite under high suction changes. Géotechnique, 53(1), 27-40.

Mac, T. N., Shahbodagh, B., & Khalili, N. (2017). A bounding surface viscoplastic constitutive model for unsaturated soils. In Poromechanics VI (pp. 1045-1052).

Marcial D, Delage P, Cui YJ, (2002). On the high stress compression of bentonites. Canadian Geotechnical Journal 39 (4): 812–820.

Mata, C., Romero, E., & Ledesma, A. (2002). Hydro-chemical effects on water retention in bentonite-sand mixtures. In Proceedings of the 3rd international conference on unsaturated soils (Vol. 1, pp. 107-112).

Mayor, J. C., García-Siñeriz, J. L., Alonso, E., Alheid, H. J., & Blumbling, P. (2005). Engineered barrier emplacement experiment in Opalinus Clay for the disposal of radioactive waste in underground repositories (No. ENRESA--02/05). Empresa Nacional de Residuos.

Mazars, J. (1984). Application de la mécanique de l'endommagement au comportement non linéaire et à la rupture du béton de structure. THESE DE DOCTEUR ES SCIENCES PRESENTEE A L'UNIVERSITE PIERRE ET MARIE CURIE-PARIS 6.

Menaceur, H. (2014). Comportement thermo-hydro-mécanique et microstructure de l'argilite du Callovo-Oxfordien. PhD thesis, Ecole Nationale des Ponts et Chaussées, Université Paris-Est, Champs-sur-Marne, France (in French).

Menaceur, H., Delage, P., Tang, A. M., & Conil, N. (2015). The thermo-mechanical behaviour of the Callovo-Oxfordian claystone. International Journal of Rock Mechanics and Mining Sciences, 78, 290-303.

Menaceur, H., Delage, P., Tang, A. M., & Talandier, J. (2016). The status of water in swelling shales: an insight from the water retention properties of the Callovo-Oxfordian claystone. Rock Mechanics and Rock Engineering, 49(12), 4571-4586.

Meier, P., Trick, T., Blümling, P., & Volckaert, G. (2000). Self-healing of fractures within the EDZ at the Mont Terri Rock Laboratory: results after one year of experimental work. In Proceedings of international workshop on geomechanics, hydromechanical and thermohydro-mechanical behaviour of deep argillaceous rocks: Theory and experiment (Vol. 2000, pp. 267-274). Swets & Zeitlinger.

Mesri, G., & Godlewski, P. M. (1977). Time and stress-compressibility interrelationship. ASCE J Geotech Eng Div, 103(5), 417-430.

Mesri, G., Lo, D. O. K., & Feng, T. W. (1994). Settlement of embankments on soft clays. In Proceedings of the Conference on Vertical and Horizontal Deformations of Foundations and Embankments. ASCE Geotechnical Special Publication 40, 8–56.

Mesri, G., & Vardhanabhuti, B. (2009). Compression of granular materials. Canadian Geotechnical Journal, 46(4), 369-392.

Mitchell, J. K., (1993). Fundamentals of Soil Behaviour, John Wiley&Sons. Inc., New York, 437p.

Mitchell, J. K., & Soga, K. (2005). Fundamentals of soil behaviour (Vol. 3). New York: John Wiley & Sons.

Mohajerani, M. (2011). Etude expérimentale du comportement thermo-hydro-mécanique de l'argilite du Callovo-Oxfordien (Doctoral dissertation).

Mohajerani, M., Delage, P., Monfared, M., Tang, A. M., Sulem, J., & Gatmiri, B. (2011). Oedometric compression and swelling behaviour of the Callovo-Oxfordian argillite. International Journal of Rock Mechanics and Mining Sciences, 48(4), 606-615.

Mohajerani, M., Delage, P., Sulem, J., Monfared, M., Tang, A. M., & Gatmiri, B. (2014). The thermal volume changes of the Callovo–Oxfordian claystone. Rock mechanics and rock engineering, 47(1), 131-142.

Mokni, N., Molinero Guerra, A., Cui, Y. J., Delage, P., Aimedieu, P., Bornert, M., & Tang, A. M. (2020). Modelling the long-term hydro-mechanical behaviour of a bentonite pellet/powder mixture with consideration of initial structural heterogeneities. Géotechnique, 70(7), 563-580.

Monkul, M. M., & Ozden, G. (2007). Compressional behaviour of clayey sand and transition fines content. Engineering Geology, 89(3-4), 195-205.

Montes, H. G., Duplay, J., Martinez, L., Escoffier, S., & Rousset, D. (2004). Structural modifications of Callovo-Oxfordian argillite under hydration/dehydration conditions. Applied Clay Science, 25(3-4), 187-194.

Muhammed, R. D., Canou, J., Dupla, J. C., & Tabbagh, A. (2018). Evaluation of local soil-pile friction in saturated clays under cyclic loading. Soils and Foundations, 58(6), 1299-1312.

Mun, W., & McCartney, J. S. (2017). Roles of particle breakage and drainage in the isotropic compression of sand to high pressures. Journal of Geotechnical and Geoenvironmental Engineering, 143(10), 04017071.

Nakata, Y., Kato, Y., Hyodo, M., Hyde, A. F., & Murata, H. (2001). One-dimensional compression behaviour of uniformly graded sand related to single particle crushing strength. Soils and foundations, 41(2), 39-51.

NEA (2008). Moving forward with geological disposal of radioactive waste, a collective statement by the NEA Radioactive Waste Management Commitee (RWMC). Technical report, OECD – Nuclear Energy Agency.

Nguyen, X. P. (2013). Étude du comportement chimico-hydro-mécanique des argiles raides dans le contexte du stockage de déchets radioactifs (Doctoral dissertation).

Niandou, H., Shao, J. F., Henry, J. P., & Fourmaintraux, D. (1997). Laboratory investigation of the mechanical behaviour of Tournemire shale. International Journal of Rock Mechanics and Mining Sciences, 34(1), 3-16.

Nicksiar, M., & Martin, C. D. (2012). Evaluation of methods for determining crack initiation in compression tests on low-porosity rocks. Rock Mechanics and Rock Engineering, 45(4), 607-617.

Nuth, M., & Laloui, L. (2008). Effective stress concept in unsaturated soils: Clarification and validation of a unified framework. International journal for numerical and analytical methods in Geomechanics, 32(7), 771-801.

OECD/NEA (1995). The environmental and ethical basis of geological disposal of long- lived radioactive wastes. ïA collective opinion of the Radioactive Waste Management Committee of the OECD Nuclear Energy Agency. Technical report, OECD – Nuclear Energy Agency.

Oldecop, L. A., & Alonso, E. E. (2007). Theoretical investigation of the time-dependent behaviour of rockfill. Géotechnique, 57(3), 289-301.

Olszak, W., & Perzyna, P. (1966). 'On elastic-viscoplastic soils, rheology and soil mechanics. In International Union of Theoretical and Applied Mechanics Symposium, Grenoble.

Olszak, W., and Perzyna, P. (1970). Stationary and nonstationary viscoplasticity, McGraw-Hill, New York.

Perzyna, P. (1963). The constitutive equations for rate sensitive plastic materials. Quarterly of applied mathematics, 20(4), 321-332.

Perzyna, P. (1966). Fundamental problems in viscoplasticity. In Advances in applied mechanics (Vol. 9, pp. 243-377). Elsevier.

Pham, Q. T., Vales, F., Malinsky, L., Minh, D. N., & Gharbi, H. (2007). Effects of desaturation-resaturation on mudstone. Physics and Chemistry of the Earth, Parts A/B/C, 32(8-14), 646-655.

Phillips, A., and Wu, H. C. (1973). A theory of viscoplasticity. International Journal of Solids and Structures, 9, 15–30.

Pimentel, E. (2015). Existing methods for swelling tests–a critical review. Energy Procedia, 76(1), 96-105.

Priol, G., De Gennaro, V., Delage, P., & Servant, T. (2007). Experimental investigation on the time dependent behaviour of a multiphase chalk. In Experimental Unsaturated Soil Mechanics (pp. 161-167). Springer, Berlin, Heidelberg.

Qi, S., Cui, Y. J., Chen, R. P., Wang, H. L., Lamas-Lopez, F., Aimedieu, P., Dupla, J. C., Canou, J., & Saussine, G. (2020). Influence of grain size distribution of inclusions on the mechanical behaviours of track-bed materials. Géotechnique, 70(3), 238-247.

Qin, P. J., Ye, W. M., Chen, Y. G., Chen, B., & Cui, Y. J. (2015). Influence of strain-rate on hydromechanical behaviour of highly compacted GMZ01 bentonite. Engineering Geology, 195, 85-92.

Qiao, Y., Ferrari, A., Laloui, L., & Ding, W. (2016). Nonstationary flow surface theory for modeling the viscoplastic behaviours of soils. Computers and Geotechnics, 76, 105-119.

Qu, G., Hinchberger, S. D., & Lo, K. Y. (2010). Evaluation of the viscous behaviour of clay using generalised overstress viscoplastic theory. Geotechnique, 60(10), 777-789.

Rao, S. M., & Shivananda, P. (2005). Role of osmotic suction in swelling of salt-amended clays. Canadian Geotechnical Journal, 42(1), 307-315.

Rao, S. M., Thyagaraj, T., & Thomas, H. R. (2006). Swelling of compacted clay under osmotic gradients. Geotechnique, 56(10), 707-713.

Rampino, C., Mancuso, C., & Vinale, F. (2000). Experimental behaviour and modelling of an unsaturated compacted soil. Canadian Geotechnical Journal, 37(4), 748-763.

Ren, X., Zhao, Y., Deng, Q., Kang, J., Li, D., & Wang, D. (2016). A relation of hydraulic conductivity-void ratio for soils based on Kozeny-Carman equation. Engineering Geology, 213, 89-97.

Revil, A., Grauls, D., & Brévart, O. (2002). Mechanical compaction of sand/clay mixtures. Journal of Geophysical Research: Solid Earth, 107(B11), ECV-11.

Rezania, M., Bagheri, M., & Mousavi Nezhad, M. (2020). Creep and consolidation of a stiff clay under saturated and unsaturated conditions. Canadian Geotechnical Journal, 57(5), 728-741.

Robinet, J. C. (2008). Minéralogie, porosité et diffusion des solutés dans l'argilite du Callovo-Oxfordien de Bure (Meuse, Haute-Marne, France) de l'échelle centimétrique à micrométrique (Doctoral dissertation, Poitiers).

Robinet, J. C., Sardini, P., Coelho, D., Parneix, J. C., Prêt, D., Sammartino, S., ... & Altmann, S. (2012). Effects of mineral distribution at mesoscopic scale on solute diffusion in a clay-rich rock: Example of the Callovo-Oxfordian mudstone (Bure, France). Water Resources Research, 48(5).

Romero, E., Gens, A., & Lloret, A. (2003). Suction effects on a compacted clay under non-isothermal conditions. Géotechnique, 53(1), 65-81.

Romero, E., & Simms, P. H. (2008). Microstructure investigation in unsaturated soils: a review with special attention to contribution of mercury intrusion porosimetry and environmental scanning electron microscopy. Geotechnical and Geological engineering, 26(6), 705-727.

Romero Morales, E. E., Musso, G., & Jommi, C. (2012). Experimental techniques for multi-scale description of soil fabric and its dual pore network.

Rothfuchs, T., Jockwer, N., & Zhang, C. L. (2007). Self-sealing barriers of clay/mineral mixtures–The SB project at the Mont Terri Rock Laboratory. Physics and Chemistry of the Earth, Parts A/B/C, 32(1-7), 108-115.

Russell, A. R., & Khalili, N. (2006). A unified bounding surface plasticity model for unsaturated soils. International Journal for Numerical and Analytical Methods in Geomechanics, 30(3), 181-212.

Samarasinghe, A. M., Huang, Y. H., & Drnevich, V. P. (1982). Permeability and consolidation of normally consolidated soils. Journal of the Geotechnical Engineering Division, 108(6), 835-850.

Sammartino S, Bouchet A, Prêt D, Parneix JC, Tevissen E (2003). Spatial distribution of porosity and minerals in clay rocks from the Callovo–Oxfordian formation (Meuse/Haute-Marne, Eastern France)—implications on ionics species diffusion and rock sorption capability. Applied Clay Science 23 (1–4): 157–166.

Samingan, A. S. (2005). An Experimental Study on Hydro-mechanical Characteristics of Compacted Bentonite Sand Mixtures. Universitätsverl.

Sánchez, M., Gens, A., do Nascimento Guimarães, L., & Olivella, S. (2005). A double structure generalized plasticity model for expansive materials. International Journal for numerical and analytical methods in geomechanics, 29(8), 751-787.

Saiyouri, N., Hicher, P. Y., & Tessier, D. (1998). Microstructural analysis of highly compacted clay swelling.

Saiyouri, N., Hicher, P. Y., & Tessier, D. (2000). Microstructural approach and transfer water modelling in highly compacted unsaturated swelling clays. Mechanics of Cohesive-frictional Materials: An International Journal on Experiments, Modelling and Computation of Materials and Structures, 5(1), 41-60.

Saiyouri, N., Tessier, D., & Hicher, P. Y. (2004). Experimental study of swelling in unsaturated compacted clays. Clay minerals, 39(4), 469-479.

Sarout, J., Molez, L., Guéguen, Y., & Hoteit, N. (2007). Shale dynamic properties and anisotropy under triaxial loading: Experimental and theoretical investigations. Physics and Chemistry of the Earth, Parts A/B/C, 32(8-14), 896-906.

Sarout, J., & Guéguen, Y. (2008). Anisotropy of elastic wave velocities in deformed shales: Part 1—Experimental results. Geophysics, 73(5), D75-D89.

Schanz, T., Agus, S. S., & Tscheschlok, G. (2004). Determination of hydro-mechanical properties of Trisoplast®. Research Rep. Bo-015/03. Laboratory of Soil Mechanics, Bauhaus-University Weimar, Weimar, Germany.

Sekiguchi, H. (1985). Macrometric approaches-static-intrinsically time-dependent. Constitutive Laws of Soils, Proc. Discussion Session 1A, 11th ICSMFE, 1985, 66-98.

Sekiguchi, H. (1985). Macrometric approaches-static-intrinsically time-dependent. Constitutive Laws of Soils, Proc. Discussion Session 1A, 11th ICSMFE, 1985, 66-98.

Seyedi, D. M., Armand, G., & Noiret, A. (2017). “Transverse Action”–A model benchmark exercise for numerical analysis of the Callovo-Oxfordian claystone hydromechanical response to excavation operations. Computers and Geotechnics, 85, 287-305.

Sheahan, T. C., & Watters, P. J. (1997). Experimental verification of CRS consolidation theory. Journal of geotechnical and geoenvironmental engineering, 123(5), 430-437.

Sheng, D., Sloan, S. W., & Gens, A. (2004). A constitutive model for unsaturated soils: thermomechanical and computational aspects. Computational Mechanics, 33(6), 453-465.

Shipton, B., & Coop, M. R. (2012). On the compression behaviour of reconstituted soils. Soils and Foundations, 52(4), 668-681.

Shipton, B., & Coop, M. R. (2015). Transitional behaviour in sands with plastic and non-plastic fines. Soils and Foundations, 55(1), 1-16.

Suklje, L. (1957). The analysis of the consolidation process by the isotaches method. In Proc. 4th ICSMFE (Vol. 1, pp. 200-206).

Tatsuoka, F., Ishihara, M., DI, B. H., & Kuwano, R. (2002). Time-dependent shear deformation characteristics of geomaterials and their simulation. Soils and foundations, 42(2), 103-129.

Terzaghi, K. (2004). Geotechnical investigation and testing-Laboratory testing of soil-Part 5: Incremental loading oedometer test 2. W3C XML, 1, 2006.

Tsang, C. F., Bernier, F., & Davies, C. (2005). Geohydromechanical processes in the Excavation Damaged Zone in crystalline rock, rock salt, and indurated and plastic clays—in the context of radioactive waste disposal. International Journal of Rock Mechanics and Mining Sciences, 42(1), 109-125.

Valès, F., Minh, D. N., Gharbi, H., & Rejeb, A. (2004). Experimental study of the influence of the degree of saturation on physical and mechanical properties in Tournemire shale (France). Applied Clay Science, 26(1-4), 197-207.

Van Geet, M., Bastiaens, W., & Ortiz, L. (2008). Self-sealing capacity of argillaceous rocks: review of laboratory results obtained from the SELFRAC project. Physics and Chemistry of the Earth, Parts A/B/C, 33, S396-S406.

Van Genuchten, M. T. (1980). A closed-form equation for predicting the hydraulic conductivity of unsaturated soils. Soil science society of America journal, 44(5), 892-898.

Viggiani, G., Besuelle, P., & Desrues, J. (2013). X-ray micro tomography as a tool for studying localized damage/deformation in clay rock (No. NEA-RWM-CLAYCLUB--2013-1).

Wang, J. (2010). High-level radioactive waste disposal in China: update 2010. Journal of Rock Mechanics and Geotechnical Engineering, 2(1), 1-11.

Walker, L. K. (1985). Secondary compression in the shear of clays. Golden Jubilee of the International Society for Soil Mechanics and Foundation Engineering: Commemorative Volume, 123.

Wan, M., Delage, P., Tang, A. M., & Talandier, J. (2013). Water retention properties of the Callovo-Oxfordian claystone. International Journal of Rock Mechanics and Mining Sciences, 64, 96-104.

Wang, L. (2012). Micromechanical experimental investigation and modelling of strain and damage of argillaceous rocks under combined hydric and mechanical loads. PhD thesis, Ecole Polytechnique, Paris.

Wang, L. L., Bornert, M., Héripré, E., Yang, D. S., & Chanchole, S. (2014). Irreversible deformation and damage in argillaceous rocks induced by wetting/drying. Journal of Applied Geophysics, 107, 108-118.

Wang, L., Bornert, M., Héripré, E., Chanchole, S., Pouya, A., & Halphen, B. (2015). Microscale insight into the influence of humidity on the mechanical behaviour of mudstones. Journal of Geophysical Research: Solid Earth, 120(5), 3173-3186.

Wang, H. L., Cui, Y. J., Lamas-Lopez, F., Calon, N., Saussine, G., Dupla, J. C., Canou, J., Aimedieu, P., & Chen, R. P. (2018). Investigation on the mechanical behaviour of track-bed materials at various contents of coarse grains. Construction and Building Materials, 164, 228-237.

Wang, Q., Tang, A. M., Cui, Y. J., Delage, P., & Gatmiri, B. (2012). Experimental study on the swelling behaviour of bentonite/claystone mixture. Engineering Geology, 124, 59-66.

Wang, Q., Tang, A. M., Cui, Y. J., Delage, P., Barnichon, J. D., & Ye, W. M. (2013). The effects of technological voids on the hydro-mechanical behaviour of compacted bentonite–sand mixture. Soils and Foundations, 53(2), 232-245.

Wang, Y. (2016). Investigating the thermo-hydro-mechanical properties of lime-treated fine-grained soils (Doctoral dissertation).

Wei, X., Duc, M., Hattab, M., Reuschlé, T., Taibi, S., & Fleureau, J. M. (2017). Effect of decompression and suction on macroscopic and microscopic behaviour of a clay rock. Acta Geotechnica, 12(1), 47-65.

Wersin, P., Curti, E., & Appelo, C. A. J. (2004). Modelling bentonite–water interactions at high solid/liquid ratios: swelling and diffuse double layer effects. Applied Clay Science, 26(1-4), 249-257.

Wileveau, Y., Cornet, F. H., Desroches, J., & Blumling, P. (2007). Complete in situ stress determination in an argillite sedimentary formation. Physics and Chemistry of the Earth, Parts A/B/C, 32(8-14), 866-878.

Wileveau, Y., & Bernier, F. (2008). Similarities in the hydromechanical response of Callovo-Oxfordian clay and Boom Clay during gallery excavation. Physics and Chemistry of the Earth, Parts A/B/C, 33, S343-S349.

Wittke, W. (1984). Felsmechanik – Grundlagen für wirtschaftliches Bauern im Fels, Springer-Verlag.

Wood, D. M. (1990). Soil behaviour and critical state soil mechanics, Cambridge University Press, Cambridge, U.K.

Wright, H. (2001). Rôle de la minéralogie, de la texture et de la structure dans la déformation et la rupture des argilités de l'est. PhD thesis, Ecole Nationale des Ponts et Chaussées, Marne-la-vallée, France (in French).

XP CEN ISO/TS 17892-8. (2005). Reconnaissance et essais géotechniques — Essais de laboratoire sur les sols - Partie 8 : Essai triaxial non consolidé non drainé.

Yang, D., Bornert, M., Chanchole, S., Wang, L., Valli, P., & Gatmiri, B. (2011). Experimental investigation of the delayed behaviour of unsaturated argillaceous rocks by means of digital image correlation techniques. Applied clay science, 54(1), 53-62.

Yang, D., Chanchole, S., Valli, P., & Chen, L. (2013). Study of the anisotropic properties of argillite under moisture and mechanical loads. Rock mechanics and rock engineering, 46(2), 247-257.

Yao, Y. P., Niu, L., & Cui, W. J. (2014). Unified hardening (UH) model for overconsolidated unsaturated soils. Canadian geotechnical journal, 51(7), 810-821.

Ye, W. M., Lai, X. L., Wang, Q., Chen, Y. G., Chen, B., & Cui, Y. J. (2014). An experimental investigation on the secondary compression of unsaturated GMZ01 bentonite. Applied clay science, 97, 104-109.

Yin, Z. Y., Chang, C. S., Karstunen, M., & Hicher, P. Y. (2010). An anisotropic elastic–viscoplastic model for soft clays. International Journal of Solids and Structures, 47(5), 665-677.

Yin, J. H., & Tong, F. (2011). Constitutive modeling of time-dependent stress–strain behaviour of saturated soils exhibiting both creep and swelling. Canadian Geotechnical Journal, 48(12), 1870-1885.

Yoshida, H., Aoki, K., Semba, T., Ota, K., Amano, K., Hama, K., ... & Tsubota, K. (2000). Overview of the stability and barrier functions of the granitic geosphere at the Kamaishi Mine: relevance to radioactive waste disposal in Japan. In Developments in geotechnical engineering (Vol. 84, pp. 159-170). Elsevier.

Yven, B., Sammartino, S., Geraud, Y., Homand, F., & Villieras, F. (2007). Mineralogy, texture and porosity of Callovo-Oxfordian argillites of the Meuse/Haute-Marne region (eastern Paris Basin). Mémoires de la Société géologique de France, 178(1), 73-90.

Zeng, T., Shao, J. F., & Yao, Y. (2019). An upscaled model for elastoplastic behaviour of the Callovo-Oxfordian argillite. Computers and Geotechnics, 112, 81-92.

Zhang, C., & Rothfuchs, T. (2004). Experimental study of the hydro-mechanical behaviour of the Callovo-Oxfordian argillite. Applied Clay Science, 26(1-4), 325-336.

Zhang, C. L., & Rothfuchs, T. (2008). Damage and sealing of clay rocks detected by measurements of gas permeability. Physics and Chemistry of the Earth, Parts A/B/C, 33, S363-S373.

Zhang, C. L. (2009). Self-sealing of fractures in argillites under repository conditions. In International conference and workshop in the framework of the EC TIMODAZ and THERESA projects.

Zhang, C. L., Czaikowski, O., & Rothfuchs, T. (2010). Thermo-hydro-mechanical behaviour of the Callovo-Oxfordian clay rock. Final Report of the BURE-HAUPT/EC-TIMODAZ Project, GRS-266. Gesellschaft für Anlagenund Reaktorsicherheit (GRS), Cologne, Germany.

Zhang, C. L. (2011). Experimental evidence for self-sealing of fractures in claystone. Physics and Chemistry of the Earth, Parts A/B/C, 36(17-18), 1972-1980.

Zhang, C. L. (2013). Sealing of fractures in claystone. Journal of Rock Mechanics and Geotechnical Engineering, 5(3), 214-220.

Zhang, C. L., Czaikowski, O., Rothfuchs, T., & Wieczorek, K. (2013). Thermo-hydro-mechanical processes in the nearfield around a HLW repository in argillaceous formations. Vol. I. Laboratory investigations (No. GRS--312). Gesellschaft fuer Anlagen-und Reaktorsicherheit mbH (GRS).

Zhang, C. L., Armand, G., & Conil, N. (2015). Investigation on the anisotropic mechanical behaviour of the Callovo-Oxfordian clay rock. Final report.

Zhang, C. L. (2016). The stress–strain–permeability behaviour of clay rock during damage and recompaction. Journal of Rock Mechanics and Geotechnical Engineering, 8(1), 16-26.

Zhang, C. L., Conil, N., & Armand, G. (2017). Thermal effects on clay rocks for deep disposal of high-level radioactive waste. Journal of Rock Mechanics and Geotechnical Engineering, 9(3), 463-478.

Zhang, C. L., Armand, G., Conil, N., & Laurich, B. (2019). Investigation on anisotropy of mechanical properties of Callovo-Oxfordian claystone. Engineering Geology, 251, 128-145.

Zhang, F., Cui, Y., Zeng, L., Robinet, J. C., Conil, N., & Talandier, J. (2018). Effect of degree of saturation on the unconfined compressive strength of natural stiff clays with consideration of air entry value. Engineering Geology, 237, 140-148.

Zhang, F., Cui, Y. J., Zeng, L., & Conil, N. (2019). Anisotropic features of natural Teguline clay. Engineering Geology, 261, 105275.

Zhang, F., Ye, W. M., Wang, Q., Chen, Y. G., & Chen, B. (2019). An insight into the swelling pressure of GMZ01 bentonite with consideration of salt solution effects. Engineering Geology, 251, 190-196.

Zhang, F., Cui, Y. J., Conil, N., & Talandier, J. (2020). Assessment of swelling pressure determination methods with intact Callovo-Oxfordian claystone. Rock Mechanics and Rock Engineering, 53(4), 1879-1888.

Zhang, F., Xie, S. Y., Hu, D. W., Shao, J. F., & Gatmiri, B. (2012). Effect of water content and structural anisotropy on mechanical property of claystone. Applied Clay Science, 69, 79-86.

Zhang, F., Hu, D. W., Xie, S. Y., & Shao, J. F. (2014). Influences of temperature and water content on mechanical property of argillite. European journal of environmental and civil engineering, 18(2), 173-189.

Zheng, L., Rutqvist, J., Liu, H. H., Birkholzer, J. T., & Sonnenthal, E. (2014). Model evaluation of geochemically induced swelling/shrinkage in argillaceous formations for nuclear waste disposal. Applied clay science, 97, 24-32.

Zhou, H., Jia, Y., & Shao, J. F. (2008). A unified elastic–plastic and viscoplastic damage model for quasi-brittle rocks. International Journal of Rock Mechanics and Mining Sciences, 45(8), 1237-1251.

Zuo, L., & Baudet, B. A. (2015). Determination of the transitional fines content of sand-non plastic fines mixtures. Soils and Foundations, 55(1), 213-219.